Metallurgical Characterization of Self Catalytic Structural Materials for Sulfuric Acid Decomposition

by

David Andrés Rigual

B.S. Marine Engineering Systems
United States Merchant Marine Academy, 2003

SUBMITTED TO THE DEPARTMENT OF NUCLEAR SCIENCE AND ENGINEERING
IN PARTIAL FULFULLMENT OF THE REQUIREMENTS FOR THE DEGREE OF

MASTER OF SCIENCE IN NUCLEAR ENGINEERING
AT THE
MASSACHUSETTS INSTITUTE OF TECHNOLOGY
(June 2005)
MAY 2005

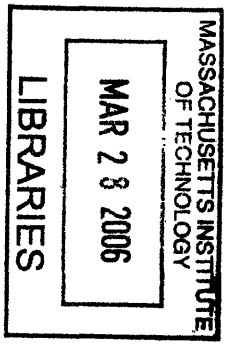

Signature of Author: _____
Department of Nuclear Science and Engineering
May 20, 2005

Certified By: _____
Ronald G. Ballinger
Associate Professor of Nuclear Science and Engineering
Associate Professor of Materials Science and Engineering
Thesis Supervisor

Certified By: _____
Michael Driscoll
Professor Emeritus of Nuclear Science and Engineering
Thesis Reader

Accepted By: _____
Jeffrey Coderre
Associate Professor of Nuclear Science and Engineering
Chairman, Department Committee for Graduate Students

Metallurgical Characterization of Self Catalytic Structural Materials for Sulfuric Acid Decomposition

by

David Andrés Rigual

Submitted to the Department of Nuclear Science and Engineering
on May 20, 2005 in Partial Fulfillment of the
Requirements for the Degree of Master of Science in
Nuclear Engineering

ABSTRACT

Eight heats of material with base alloy chemistries of Alloys 800 HT or 617 with platinum additions of 2, 5, 15, or 30 wt% have been characterized according to their microstructural features. The goals of characterization were to determine metallurgical stability for service as self-catalytic structural materials. The results presented herein will be useful to the development of a material for the construction of a heat exchanger designed for sulfuric acid decomposition. This type of heat exchanger is a key component to hydrogen generation by the thermochemical sulfur-iodine water-splitting process, a future technology that promises efficient hydrogen production if coupled to a Generation IV nuclear reactor heat source.

Characterization of each material was carried out in the cast and wrought conditions with optical and SE microscopy, electron dispersive spectrometry, chemical composition analysis, and thermodynamic modeling. Materials have been characterized according to grain size and morphology, precipitate features, twinning characteristics, and platinum composition effects.

Results indicate that platinum and carbon compositions have the greatest effect on the development of microstructural features. Increasing platinum compositions in both base alloy chemistries fosters the presence of annealing twins, which indicates that platinum additions reduce stacking fault energy within the alloy systems. Platinum additions appear to cause the development of larger grain structures as well as increase corrosion resistance.

With the exception of the Alloy 800 HT – 30 wt% Pt system, the alloy systems characterized herein were melted with carbon contents between 1.2 – 3.6 times higher than the maximum specified compositions for the base chemistries. Excessive inter and intra-granular carbide precipitation resulted, which leads to compromised corrosion resistance and mechanical properties. Inter-granular attack due to sensitization is observed in the Alloy 800 HT – 2, 5 wt% Pt systems. SEM micrographs of the Alloy 617 – Pt systems show that these systems are less prone to inter-granular attack.

The grain structures of each base alloy – Pt system are much finer than those of the respective base alloy systems included for comparison. Fine grain structures are

detrimental to overall ductility and high temperature creep strength. On average, the Alloy 800 HT – Pt systems developed larger grains than the Alloy 617 – Pt systems.

A two phase microstructure that resembles pearlite developed in the Alloy 617 – 30 wt% Pt system. This alloy system will be excluded from further characterization for self catalytic structural application due to expected poor mechanical and corrosion resistance properties. The most important microstructural improvements for the development of a self-catalytic structural material include a reduction of carbon content and an increase in grain size. Further characterization of catalytic, corrosion resistance, and mechanical properties are required for selection of the optimum platinum addition to the base chemistries of Alloys 800 HT and 617 for sulfuric acid decomposition service.

Thesis Supervisor: Ronald G. Ballinger
Title: Associate Professor of Nuclear Science and Engineering
Associate Professor of Materials Science and Engineering

iii. Acknowledgements

I would like to take the opportunity to thank many individuals for their contributions to my education over the last two years. First of all, and most importantly, I give my God and Creator thanks and credit for the fruits of my labor. Without Him I would be nothing. Secondly I would like to thank Professor Ron Ballinger, my advisor, for the patient instruction and kind encouragement that has brought me to this point. Thank you for coming down to my level on so many occasions to share your knowledge that has defined my graduate education. I will always remember the anecdotes that you would share with me on matters of life and work. My personal favorite was when you told me not to let my alligator mouth get in front of my humming bird ass.

I would like to thank the many people who have helped me take giant leaps of progress in my research along the way. I thank Pete Stahle for the war stories, the heat it and beat it solutions, and the right attitude. Jeongyoun Lim, I thank you for teaching me how to work in the lab, and for always being there for me when I needed help. Mike Short, I thank you for helping me in the final hour. I am grateful to the PSFC machinists who work in NW 21 for their assistance with machining and welding. One of the most helpful people to my research progress is Nate Eisinger of the Special Metals Corporation. Thank you for letting me use your equipment and for giving me a tour of the facilities. I am especially grateful to Professor Krystyn Van Vliet of the Materials Science and Engineering department. Your insightful comments on the results of my work were very helpful to the overall quality of my thesis. Thank you for going out of your way to help me.

I would like to thank all of my friends who shared their common experiences with me over the last two years. Jane I will never forget how important you are to me, especially because of what we went through together in the early days. Last but not least, I want to thank my loving Ma and Pa. The support that you have provided me has helped me tremendously. I want to thank you most of all for the guidance that you have provided and for listening when I needed you to.

iv. Table of Contents

v. List of Figures

vi. List of Tables

1. Introduction

1.1. Effects of Power Generation and Hydrogen Production Practices

Currently 86% of the world's energy is supplied by fossil fuel combustion [24]. Measured trends in global warming and the finite supply of oil reserves have lead to increases in renewable and alternative energy R&D. The use of hydrogen as an energy carrier has the potential to reduce greenhouse gas emissions and reliance on oil through clean technology production. Current hydrogen production practice, however, uses fossil fuels as raw material. 95% of the hydrogen used within the US is produced by the steam methane reforming process, which accounts for a release of 74 million tons of CO_2 per year into the atmosphere [42]. In the petroleum industry hydrogen is used to remove sulfur from petroleum products, open benzene rings, and break long chain hydrocarbons. In the chemical industry hydrogen is used to produce fertilizers as well as to produce anhydrous ammonia.

1.2. Benefits of Clean Hydrogen Production from the SI process

Beyond current industrial processing applications, hydrogen has many benefits as an energy carrier. Hydrogen can be readily stored or transported and its combustion products are only water and heat. Furthermore, hydrogen has lower losses compared to electricity when transported over long distance for energy conversion [27]. The production of hydrogen via a water splitting process would eliminate greenhouse gasses released by current production practices and has the potential to reduce greenhouse gas emissions from the transportation sector. Generation IV nuclear technology promises the benefit of operational temperatures in the range required for various electrolytic and thermochemical water splitting processes, one of the most promising of which is the Sulfur-Iodine (SI) thermochemical water splitting process. The SI process can be thought of as a chemical engine that generates H_2 and O_2 from H_2O by combining high

temperature endothermic and low temperature exothermic chemical reactions where sulfuric acid and iodine are used as chemical catalysts [24, 25]. The SI process has the ability to generate hydrogen with a thermal efficiency between 45 – 55 % with the use of a high temperature gas cooled reactor (HTGR) as a heat source [24, 25]. The basic reactions of the SI process are as follows [24, 26]:

$$\mathbf{H_2SO_4 \rightarrow \frac{1}{2}\, O_2 + SO_2 + H_2O} \qquad (1.1)$$

ΔG = -137 kJ / mol, ΔH = 371 kJ /mol

$$\mathbf{I_2 + SO_2 + 2\, H_2O \rightarrow H_2SO_4 + 2\, HI} \qquad (1.2)$$

ΔG = -41 kJ / mol, ΔH = -216 kJ / mol

$$\mathbf{2\, HI \rightarrow I_2 + H_2} \qquad (1.3)$$

ΔG = 24 kJ / mol, ΔH = 12 kJ / mol

Note: Gibbs free energy and enthalpy changes are given for the following reaction temperatures with respect to equations 1 – 3: 830 °C, 120 °C, and 320 °C

As can be seen from the Gibbs free energy of formation, the reaction shown in Equation 1.1 is highly endothermic. For efficient conversion this reaction requires a temperature in the range of 800 - 900 °C as well as a catalytic surface to proceed [24]. Furthermore, the corrosive nature of the sulfuric acid decomposition process requires careful materials selection in order to ensure safe system operation. The sulfuric acid decomposition process can be analyzed as set of three reactions shown accordingly [26]:

$$\mathbf{H_2SO_4\,(l) \rightarrow H_2SO_4\,(g)} \qquad (1.4)$$

$$\mathbf{H_2SO_4\,(g) \leftrightarrow H_2O\,(g) + SO_3\,(g)} \qquad (1.5)$$

$$\mathbf{SO_3\,(g) \rightarrow SO_2\,(g) + \tfrac{1}{2}O_2\,(g)} \qquad (1.6)$$

The reaction shown in Equation 1.4 occurs reversibly between the liquid and gas phases at 100 °C. The reactions shown in equations 1.5 and 1.6 are endothermic. The decomposition of sulfuric acid into water and sulfur trioxide occurs nearly completely

between 350 – 500 °C [25, 26]. The decomposition of sulfur trioxide into sulfur dioxide and oxygen requires the presence of a solid catalyst as well as an operational temperature range of 800 – 900 °C [26]. The challenges posed in the decomposition of sulfuric acid (Equation 1.1) are therefore reduced to the decomposition of sulfur trioxide (Equation 1.6). The reactions shown in equations 1.2 and 1.3 pose less of an engineering challenge because they require relatively lower temperatures.

1.3. Materials R&D needs for Sulfuric Acid Decomposition

Each reaction in the SI process has been demonstrated individually. The process itself has not been demonstrated in an integrated fashion nor have the economics of the cycle been proven viable [24]. However, with the current state of knowledge the SI cycle is entirely feasible. Favorable thermodynamic modeling results and bench scale demonstrations are sufficient for a preliminary design [24]. Reaction 1.1 would take place within a shell and tube heat exchanger in which the process side would be packed with a catalytic material such as platinum. Such an approach, however, would limit the cycle's efficiency due to an appreciable pressure drop across the process side of the heat exchanger. The development of self-catalytic constructional alloys would preclude the need to pack the process side of the heat exchanger with a supported catalyst because the heat exchanger itself could be constructed from a material that would satisfy the catalytic requirements of the decomposition process. The end goal of such a development effort would be to develop an alloy consisting of the base chemistry of a pre-existing alloy with platinum addition to enhance the catalytic activity of the surface. Such an alloy would be deemed effective if it met several criteria including: metallurgical stability at service temperature, excellent high temperature mechanical properties, and efficient catalysis [28].

1.4. Research Objectives

The purpose of the research results presented in this thesis is to determine the feasibility of the development of a self catalytic structural alloy for sulfuric acid decomposition. Eight special alloys, four based on Alloy 800 HT and four based on Alloy 617, were melted with platinum additions of 2, 5, 15, and 30 weight percent.

1.4.1. Metallurgical Characterization

The focus of the research conducted herein is on the metallurgical characterization of the alloy chemistries listed above. The most important goal of this work was to determine any form of metallurgical instability present within each material characterized. These materials will undergo further evaluation of mechanical and catalytic properties in later work beyond the scope of this thesis. Each heat of material was received in the cast condition from the Special Metals Corporation. Optical microscopy was performed on each cast material at several low levels of magnification. Wrought and heat treated structures were developed from each cast material for characterization by optical microscopy, scanning electron microscopy (SEM), and electron dispersive spectrometry (EDS). All optical microscopy was carried out in both the etched as well as the un-etched conditions whereas further characterization was carried out only in the etched condition. Precipitate models were developed for each material from chemical composition results in order to rationalize microscopy and EDS results. Thermodynamic modeling was carried out with JMat Pro, version 3.0 [48]. Materials were characterized according to several observations made regarding their respective microstructures. Grain morphology was examined and grain size calculations were performed on each wrought material for comparison to the respective base alloy grain characteristics. Precipitates were characterized according to their chemistry, morphology, size, density, and distribution. Each microstructure was also examined for the presence of elemental segregation.

1.4.2. Preliminary Design of a Catalysis Effectiveness Loop

In addition to microstructural characterization, a preliminary design of a catalysis effectiveness loop has been completed and is included as Appendix A. This work begins with reactant selection and flow rate calculations for various operational temperatures. Several reactants were available as options including various weight percent sulfuric acid aqueous solutions and sulfur trioxide. Flow rate calculations were completed for each possible reactant species at various operational temperatures in order to determine the best reactant that would produce measurable conversion at an optimal flow rate. Following reactant selection and flow rate calculations the reactant supply and configuration was selected from two possible options. Criteria for design decisions included safety concerns, ease of design, and cost. Fortunately, the safest options were generally the easiest and cheapest to design. The analysis of reaction products will be performed by a gas chromatograph that has already been purchased and received from the vendor. Detailed AutoCAD drawings of the proposed catalysis effectiveness loop have been completed with a parts list. Vendor and pricing information is included on the parts list in order to facilitate procurement and construction.

2. Metallurgical Structure Theory

The materials studied herein were received in the as cast form from Special Metals Inc. Metallurgical analysis was performed to determine the suitability of these materials for construction of corrosion resistant high service temperature tubes. This application requires the materials to be converted into a wrought form for characterization. Prior to understanding the wrought structures developed within the heats of base alloy + Pt chemistry, it is important to consider the solidification structures that develop from the melt process. A comparison of the solidification and post melt processing microstructures is beneficial to understanding the effects of each stage of microstructure development.

2.1. Cast Structures

Solidification usually occurs by one of two mechanisms, or a combination of both. These include the nucleation and growth of either single phase primary crystals or of polyphase crystals. In general the latter mechanism is more predominant than the former.

Solidification of single phase primary crystals within a melt takes place differently at the mold/metal interface than it does further into the melted region. At the interface the heat transfer rate is higher than at any other point in the melt due to the relatively lower temperature of the mold. This large heat flux causes small grains to nucleate on the mold walls and grow at random orientations, which forms an outer equiaxed zone. A second stage of development begins when these grains become dendritic and grow along preferred crystallographic directions (<001> for cubic materials) [1]. The preferred direction of growth is determined by the heat flux during cooling. The dendritic grains that grow in a direction opposite to the heat flux dominate the solid/liquid interface thereby eliminating other grains with random growth directions. The resulting solidification structure resembles a zone of columnar dendritic grains around the outer edge of the melt.

Within the inner region of the melt, solidification begins with heterogeneous nucleation on impurities or dissimilar particles. Heterogeneous nucleation is a more energetically favorable process than homogenous nucleation because the latter mechanism allows for the nucleated grain to form with a much lower surface energy. Once nucleation occurs a grain will grow within the melt to form an equiaxed dendritic structure. The melted medium acts as a heat sink for the grains as they grow. As grains get larger they release latent heat to the surrounding medium until a condition of thermal equilibrium is reached and the entire melt is solidified. It is worthy to note that grain growth occurs in the direction of the heat flux within the medium of the melt, whereas grain growth in the outer columnar region occurs in a direction opposite to the heat flux. The transition from directionally solidified columnar grains at the metal / mold interface to the internal equiaxed structure is shown very well in Figure 2.1:

Fig 2.1: Transition from directionally solidified columnar grains at the mold/metal interface to an internal equiaxed grain structure, Cast Alloy 617 – 5 wt% Pt, 50 X, glyceregia – 1020 sec

Nucleation and growth of polyphase crystals is the dominant solidification process found in pure eutectic alloy systems [1]. This form of solidification is expected to play a minor role in the solidification processes of the heats of materials characterized herein. Binary phase diagrams of platinum with each of the major alloying elements

found in In-617 and Alloy 800 HT indicate that the heats of base alloy + Pt are very likely peritectic alloys [2]. Peritectic alloys form dendrites similar to single phase primary crystals during solidification [1].

2.2. Development of Wrought Structures

Cast structures developed from the solidification process provide information regarding macroscopic phase stability of the alloy systems. However, the base alloy + Pt systems studied herein must be converted to wrought structures for complete characterization as they would be used in such a form in future service conditions. Wrought structure development was carried out by imparting either hot or cold work into the material followed by an annealing process. The annealing process allows for the worked material to undergo the sequential processes of recovery, recrystallization, and grain growth.

2.2.1. Recovery

Recovery occurs within a temperature range below the recrystallization temperature of the material. Recovery is aptly named so because it signifies the recovery of material properties such as hardness, ductility, strength and electrical resistivity. During recovery internal stresses are relieved by two separate mechanisms including annihilation and polygonization of the structure caused by deformation. Annihilation occurs when like dislocations of opposite signs recombine. Annihilation of dislocations can occur via both glide along their slip planes and climb in directions perpendicular to their slip planes due to the elevated annealing temperature. Polygonization is a process in which internal features align themselves in a pattern that minimizes energy in the system. Polygonization is driven by a reduction of the strain energy of dislocations as they align themselves into lower energy configurations. Dislocations move via both glide and climb during polygonization. A result of polygonization is the formation of sub-boundaries that

separate sub-grains. The rate at which recovery occurs decreases as the strain energy within the material that drives the process is expended.

2.2.2 Recrystallization

As annealing continues beyond the recovery process a secondary, and larger, energy release occurs through the process of recrystallization. The kinetics of recrystallization are roughly given by Equation 2.1 [3].

$$\frac{1}{\tau} = Ae^{-Q_r/RT} \qquad (2.1)$$

where: $1/\tau$ = recrystallization rate when 50% of the structure is recrystallized.

R = 8.37 J / mol-K

Q_r = Recrystallization activation energy (J / mol)

T = Temperature (K)

Equation 2.1 is only a rough approximation because the recrystallization activation energy changes as the driving force for recrystallization is expended. The above equation holds over a wide annealing temperature range, which indicates that relatively small changes in annealing temperature reflect large changes in annealing time required for a specified amount of recrystallization. For practical purposes a temperature is usually specified for complete recrystallization of a material within a given timeframe (generally one hour). This temperature is called the recrystallization temperature and it is usually between 30% – 50% of the material's melting temperature [3].

It is important to note that the recrystallization temperature is dependent on the recrystallization activation energy. This energy is a function of the amount of cold work performed on the material, which acts as the driving force for the recrystallization process. Following recovery the polygonized internal structure retains the internal energy required to carry out recrystallization. Energy is released through the elimination of sub-boundaries resulting in the formation of nuclei that will grow or diminish depending on their size relative to the critical size for growth [3].

Another predominant theory for grain nucleation involves the expansion of a pre-existing grain into a grain with a higher defect density. The volume swept out in such an expansion forms a bulge in the grain boundary between the two grains. This region is relatively free of defects and will separate to form the nucleus of a new grain if it meets the critical size criterion for growth [3]. Other theories for nucleation exist, any number of which may apply to different cases for recrystallization of different materials. There exist two commonalities, however, in all recrystallization nucleation mechanisms. Nucleation only occurs in regions of high defect density near high angle grain boundaries. As mentioned before, the driving process for recrystallization comes from the stored energy in defects. Furthermore, in order for nucleation to occur atomic diffusion must occur. High angle grain boundaries facilitate atomic diffusion because they are more mobile than lower angle grain boundaries [3].

The result of recrystallization is a new grain structure that has not yet begun to coarsen. The average grain size prior to grain growth depends on the ratio between the nucleation and growth rates. When nucleation occurs more rapidly than growth a finer grain structure is produced. The nucleation and growth rates themselves are controlled by the recrystallization activation energy, which in turn is controlled by the degree of cold work performed on the material prior to annealing. As the degree of prior cold work increases, the resulting recrystallization grain structure becomes finer. This trend is in agreement with the requirement for nucleation to occur in regions of high defect density. As defect density increases due to increasing cold work, more nucleation sites are formed. The result is that the nucleation rate increases while the growth rate is held constant. There exists a critical amount of cold work below which recrystallization will not occur. This critical value varies with the type of cold work induced. For example, when cold work is induced along slip plane directions that facilitate glide the critical amount of cold work is much higher than when the same material is deformed in shear via torsion [3].

The effects of temperature and initial cold work are among the most significant in determining the recrystallized grain structure of a material. Two other variables are the purity of the material as well as the initial grain size. Impurities interact with moving grain boundaries in much the same was as they do with moving dislocations. Their grain

boundary pinning effect during nucleation is most significant at low concentrations and must be overcome by raising the recrystallization temperature. It is not expected that impurities will play a large role in altering annealing procedures for the base alloy + Pt materials that are to be treated following cold working. The multi-elemental composition of these materials renders impurity effects on recrystallization immeasurable.

Initial grain size is a more important consideration in determining the recrystallization grain size. As cold work is applied grain boundaries provide resistance to deformation. As a result cold work produces a higher defect concentration in regions surrounding grain boundaries compared to interior grain regions. Therefore, cold work tends to create more defects in materials with finer grain structures due to their larger grain boundary areas. The requirement for nucleation to occur in regions with relatively high defect density results in higher nucleation rates for cold worked materials with fine pre-cold work grain structures. This behavior results in fine recrystallized grain structures. The cast materials of base alloy + Pt have a dendritic structure rather than a wrought grain structure. The size of the dendrites can be correlated to a large grain structure when considering the effects of initial grain size on recrystallized grain structure. The relatively low inner dendritic boundary area in the cast materials is an indication that the recrystallized grain structure will be very large. Therefore, each cast sample may require a second reduction in area followed by a second annealing process in order to reduce the final grain structure to values consistent with base alloy standards.

2.2.3 Grain Growth

Following recrystallization there still exists within the material enough energy from the initial cold working process to induce further transformations to the metallurgical structure. This energy is stored in the form of excessive grain boundary surface energy and dissipates through grain growth. The behavior of a grain during the growth phase is dependent on its size relative to the critical size for growth. All grain boundaries exhibit some degree of convexity. During growth, grain boundary migration takes place in the direction of the center of curvature. Grains below the critical size for

growth possess convex boundaries, which leads to their eventual consumption by larger grains with concave boundaries.

A first order approximation for grain growth kinetics can be derived from relations applied to general cellular growth. Following recrystallization, the rate of change of the average grain diameter (D) can be approximately given by Equation 2.2 [3].

$$\frac{dD}{dt} = \frac{K}{D} \tag{2.2}$$

where: K = constant

D = average grain diameter

By integrating the above equation and assuming that the initial grain diameter is given by D_o leads to Equation 2.3 [3]:

$$D^2 - D_o^2 = Kt \tag{2.3}$$

This equation can be further simplified by assuming that the initial grain size is relatively insignificant compared to the final grain size, thus:

$$D = kt^{1/2} \tag{2.4}$$

where: $k = \sqrt{K}$

Equation 2.4 can only be applied to ideal grain growth conditions under which no variables exist that may inhibit the coarsening process [3]. Experimental isothermal grain growth data, however, tends to correspond to an equation of a similar form, where:

$$D = kt^n \tag{2.5}$$

The exponent (n) in Equation 2.5 varies between 0 and ½, and is largely dependent on composition and annealing temperature [3]. Increasing purity and higher

annealing temperatures generally reflect larger values in n. Impurities affect grain coarsening via different mechanisms depending on their form within a material. Minority elements in solid solution introduce an elastic stress field into the crystal lattice if a significant size disparity exists. The resulting stress field acts as a diffusion potential that drives impurity atoms to the grain boundaries where stresses may be relieved due to lattice misfit. A greater density of impurity elements on grain boundaries produces a pinning effect on grain boundary migration. In order to migrate, grain boundaries must pull along the solid solution impurity atmospheres that form around them [3]. The effect of raising annealing temperature, however, weakens the grain boundary pinning effect by increasing lattice vibration intensity within the grain boundary solute regions. Impurities in the form of inclusions interact differently to retard grain boundary migration. Grain boundaries are able to migrate through inclusions by pulling away from them when the surface tension force induced by grain boundary curvature is great enough in magnitude to exceed the pinning force induced by inclusions [3]. Larger particles tend to have a smaller effect on grain boundary pinning because the drag of a particle is inversely proportional to the particle radius. Increased temperature promotes the coalescence of inclusions to form larger particles, which reduces grain boundary pinning forces. Increased temperature also promotes the dissolution of inclusions throughout the matrix, thereby reducing concentrations at grain boundaries.

The end result of cold working and subsequent annealing is a wrought microstructure ideally characterized by homogenized grains. The existence of grains themselves indicates that there is an upper limit to grain size during the growth process. This limit is attained by free surface and impurity effects. The materials studied herein will not be reduced to such a thickness where free surface effects play a significant role in producing a limiting grain size. Only impurity effects will be considered. The driving force for grain growth is given by Equation 2.6 [3].

$$\eta = 2\frac{\gamma}{R} \qquad (2.6)$$

where: η = Driving force / unit area

γ = Grain boundary surface tension

R = Grain boundary radius of curvature

Grain growth terminates when the driving force per unit area is equal to the retarding force induced by inclusions. This retarding force, given by Equation 2.7, is equal to the restraining force of a single particle multiplied by the number of particles per unit area [3].

$$\eta = 2\frac{\gamma}{R} = n_s \pi r \gamma \qquad (2.7)$$

where: n_s = particles / unit area

r = particle radius

By assuming that the all inclusions are uniform in size, perfectly spherical, and uniformly distributed throughout the microstructure, it is possible to derive the limiting grain boundary radius of curvature, which was originally proposed by Zener [3]. The total number of inclusions that pin grain boundary migration lie within a volume defined by the inclusion diameter and the total grain boundary area, A. This volume will hold $2n_v$Ar inclusions, where n_v is defined as the number of inclusions per unit volume. The Zener relation is derived as follows [3]:

$$n_s = 2n_v r \qquad (2.8)$$

$$n_v = \frac{\xi}{\frac{4}{3}\pi r^3} \qquad (2.9)$$

where: = Volume fraction of inclusions

Substitution and cancellation of the above equations leads to the Zener relation:

$$R = \frac{4}{3}\frac{r}{\xi} \qquad (2.10)$$

The extensive assumptions made in determining this relationship introduces a significant amount of error in its accuracy; nevertheless, this relation indicates that impurities induce a limiting grain size within the microstructure during the annealing process.

3. Development and Metallurgy of Alloys 800 HT & 617

3.1. Alloy 800 HT

3.1.1. Development of Alloy 800 HT

Alloy 800, a predominantly Fe-Ni-Cr alloy, was first developed in the 1950's by the Special Metals Corporation under the trade name Incoloy® 800. This alloy was developed to address a need for a low nickel content material designed for continuous service in high temperature corrosive environments. At the time, nickel was considered to be a strategic material [8]. From experimental practice it was found that Alloy 800 with carbon content in the upper range of specified limits (0.01 - 0.1% C) possessed improved creep and rupture properties than lower carbon material. This observation lead to the development of Alloy 800 H, which is differentiated from Alloy 800 by more restrictive carbon content (0.05-0.10% C) and a minimum specified grain size of ASTM 5 or coarser [8]. Alloy 800 HT is the latest addition to the 800 series of alloyed materials, and was originally introduced by the Special Metals Corporation under the trade name Incoloy® 800 HT. This material was originally introduced to the market partly as a response to competition from manufacturers of Alloy 800 H. Alloy 800 HT retains higher creep and rupture strength properties over commercial Alloy 800 H with more restricted carbon content (0.06-0.10%C) and more restricted Al + Ti contents (0.85-1.20% Al + Ti vs. 0.3-1.2% Al + Ti for Alloy 800 H) [8]. Alloys 800, 800 H, and 800 HT have approximately equal corrosion resistance due to their nickel and chromium content. The high chromium content promotes the formation of a passivating chrome-oxide based film, which is enhanced by high nickel content [8].

The main difference between each of the individual alloys within the 800 family stems from the effect of temperature on their respective mechanical properties. Alloy 800 possesses more favorable mechanical properties at room temperature and during short exposure to high temperature environments [8]. Annealing treatment and restricted

chemistry specifications yield improved rupture strength and creep properties in Alloys 800 H and 800 HT over Alloy 800 during continuous high temperature service. These materials are approved for service up to 982 °C by the ASME Boiler and Pressure Vessel Code [8]. Additionally, Alloys 800, 800 H and 800 HT are used widely throughout the nuclear industry due to their relatively low neutron cross sections for absorption [8].

3.1.2. Metallurgical Structure of Alloy 800 HT

Like Alloy 800 H, Alloy 800 HT is specified to have an ASTM grain size of 5 or coarser [5]. This requirement is met by a solution annealing process at 1149 °C for 1 – 2 hrs. The nominal weight percent chemistry of Alloy 800 HT is provided in Table 3.1 below [6, 8]:

Table 3.1		**Composition of Alloy 800 HT**		
Fe	39.5% min	S	0.015% max	
Ni	30.0 – 35.0%	Si	1.0% max	
Cr	19.0 – 23.0%	Cu	0.75% max	
C	0.06 – 0.10%	Al	0.15 - 0.60%	} 0.85 - 1.20% Total
Mn	1.5% max	Ti	0.15 - 0.60%	

The dominant Fe-Ni-Cr chemistry of Alloys 800 H and 800 HT form solid solution strengthened austenitic microstructures. High temperature mechanical properties are enhanced by the addition of minor alloying elements through precipitation strengthening. Titanium carbides, titanium nitrides, carbonitrides, and chromium carbides are common precipitates in Alloy 800 H and 800 HT microstructures. Of those listed above, MC type carbides have the greatest high temperature strengthening effect on Alloy 800 / 800 HT microstructures [21]. Heat treatment has no effect on the first three of the above mentioned precipitates because they are stable below the melting point of Alloy 800 H and 800 HT. $Cr_{23}C_6$ precipitates, however, precipitate between 540 -760 °C. Like other austenitic alloys, Alloy 800, 800 H and 800 HT are susceptible to sensitization within a certain temperature range (540 - 760°C), which can lead to intergranular attack due to grain boundary chromium depletion [6, 8, 20]. γ' precipitation (FCC, $Ni_3(Al, Ti)$)

strengthening is possible in the 800 family of alloys by annealing between 565 °C and 621 °C for periods of time in excess of 100 hours.

3.2. Alloy 617

3.2.1. Development of Alloy 617

Alloy 617 was developed by the Special Metals Corporation under the trade name Inconel® 617 as a material with exceptional high temperature creep and corrosion resistance. Gas turbine application has lead to current Alloy 617 processing techniques that optimize both Low Cycle Fatigue resistance (LCF) and high temperature creep resistance. Like Alloys 800 and 800HT, Alloy 617 is one of a few materials with allowable design stresses specified by the ASME Boiler and Pressure Vessel Code for operation up to 982 °C [7]. The alloy is used predominantly in the solution annealed condition in order to obtain the coarse grain structure required for high temperature creep resistance. Post processing solution annealing is usually performed at 1177 °C for approximately 1 hour followed by air or faster cooling [5, 7].

Alloy 617 possesses excellent corrosion resistance properties. Oxidation resistance is enhanced by nickel, molybdenum, chromium and aluminum additions. The latter elements, in particular, promote the formation of a thin surface oxide region that forms rapidly upon exposure to high temperatures. This film continues to grow until it reaches approximately 1 – 2 mils in thickness [7]. The oxide region increases spalling resistance and is sufficiently porous to allow for the formation of a chromium oxide film on the surface of the material [7].

3.2.2. Metallurgical Structure of Alloy 617

Alloy 617 is a Ni-Cr-Co-Mo alloy, the composition of which is given in Table 3.2 below [7]:

Table 3.2		Composition of Alloy 617			
Ni	44.5% min	C	0.05% - 0.15%	Ti	0.6% max
Cr	20.0 – 24.0%	Fe	3.0% max	Cu	0.5% max
Co	10.0 – 15.0%	Mn	1.0% max	B	0.006% max
Mo	8.0 – 10.0%	Si	1.0% max		
Al	0.8%-1.5%	S	0.015% max		

Alloy 617 has a coarse grained microstructure with a typical grain size of ASTM 4 or 5. The alloy consists of an austenitic FCC nickel matrix in which chromium, cobalt, and molybdenum are dissolved as solute elements. Substitutional solid solution strengthening, provided mainly by cobalt and molybdenum additions, enhances the high temperature creep resistance of the alloy [7]. Coarse precipitates of titanium nitrides and MC carbides are present within the alloy prior to any annealing process. The high melting temperature of these precipitates prevents them from solutionizing during the annealing process. The annealing process, however, does cause any $M_{23}C_6$ or M_6C originally present to dissolve until reheating at a lower temperature. During high temperature service conditions, the primary precipitates within the matrix include titanium nitrides, MC (TiC) carbides and M_6C ($Mo_3Cr_2(Ni,Co)C$). Secondary precipitates include $M_{23}C_6$ ($Cr_{21}Co_2C_6$), M_6C, and γ' (Ni_3Al). The stable discrete intergranular $M_{23}C_6$ precipitates have been identified as principal strengthening agents within the Alloy 617 system. The degree of secondary precipitation of $M_{23}C_6$ is strongly influenced by the degree of primary precipitation because the primary precipitates act as nucleation sites for secondary precipitation. Alloy 617 is relatively stable at temperatures up to 982 °C due to the lack of formation of the brittle sigma, mu, chi or laves phases. Some γ' precipitates can precipitate from ageing between 649 -760 °C, which causes a limited increase in hardness and strength and a corresponding decrease in ductility and

toughness. These changes in mechanical properties, however, are not significant enough to qualify as serious embrittlement [5].

3.3. Precipitate structures in Alloys 800 HT and 617

3.3.1. γ' Precipitation Strengthening

γ' is a FCC type $L1_2$ ordered coherent intermetallic precipitate with a stoichiometric composition of A_3B. This crystal structure of this type of coherent precipitate is commonly referred to as a superlattice. Precipitation of γ' within the Alloy 800HT and 617 microstructures occurs upon ageing and is rather limited in comparison to its presence within other alloyed systems due to low concentration of B type atoms (Al, Ti). Nevertheless, γ' precipitation provides a contribution to the strength of Alloy 800HT and 617 systems over a wide range of temperatures. The coherent nature of γ' precipitates preclude the need for looping to occur during dislocation migration. Such interactions are favorable in that they prevent the eventual cutting of precipitates under significant deformation, which would mitigate their strengthening effects. Strengthening by coherent precipitates that form super lattice crystal structures is provided by the resolution of edge dislocations within precipitates as they pass through. This requires excess energy over normal dislocation migration owing to the localized misfits within the precipitate lattices. A diagram of the γ' $L1_2$ ordered structure is shown in Figure 3.1 below:

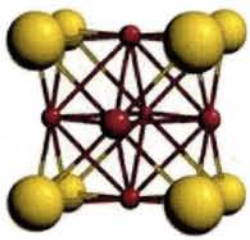

Fig 3.1: Diagram of $L1_2$ crystal lattice, courtesy of the Naval Reactors Laboratory [18]

3.3.2. Carbide Formation and Effects

Carbide precipitation within Alloy 800HT and 617 microstructures improves creep rupture resistance and high temperature rupture strength. There are three main types of carbide precipitates that form within the above mentioned alloys, which include MC, $M_{23}C_6$, and M_6C. MC type carbides have FCC crystal structures that form with a coarse random script morphology. MC type carbides precipitate with a discrete heterogeneous distribution within the matrix. Additionally, MC type carbides provide effective precipitate strengthening at high temperatures. These carbides may form either inter-granularly or trans-granularly and have little or no orientation with the matrix. MC type carbides are among some of the most stable compounds found in nature. MC carbides begin to slowly decompose at approximately 980 °C, which allows them to provide a source of carbon for the precipitation of the M_6C and $M_{23}C_6$ [19].

$M_{23}C_6$ type carbides are found to be profuse within Alloys 617 and 800 HT due to their high chromium content. Precipitation of $M_{23}C_6$ type carbides begins between 760 – 980 °C and occurs predominantly along grain boundaries; precipitation has also been found to occur along twin boundaries and stacking faults as well. $M_{23}C_6$ carbides will nucleate on the TCP σ phase because of a similar complex crystal structure. When molybdenum is present, as in the Alloy 617 system, $M_{23}C_6$ is composed of $Cr_{21}Mo_2C_6$. Nickel, cobalt, and iron have all been found to substitute for chromium within the $M_{23}C_6$ carbide phase of many alloy systems. The large size and inter-granular precipitation of $M_{23}C_6$ provides for effective grain boundary pinning at high temperatures; however, precipitation of $M_{23}C_6$ has lead to inter-granular attack due to chromium depletion of grain boundaries [19].

Precipitation of M_6C type carbides will only occur when there is sufficient molybdenum or tungsten present within the matrix to replace the chromium in other carbides. M_6C type carbides will therefore form within the Alloy 617 microstructure, but not within the microstructure of the Alloy 800 HT system. M_6C carbides precipitate between 815 – 980 °C. The slightly higher upper temperature range of M_6C type carbides over $M_{23}C_6$ carbides allows them to more effectively control grain size in wrought alloys. During slow cooling following a solution anneal the initial precipitation of intergranular

M_6C type carbides will act as nucleation sites for secondary precipitation of $M_{23}C_6$ type carbides. M_6C type carbides may range in formula from M_3C to $M_{13}C$ depending on the constitution of the alloy matrix; however, typical M_6C formulas include $(Ni,Co)_3Mo_3C$, and $(Ni,Co)_2W_4C$. M_6C morphology occurs as discrete blocky particles that are usually found along grain boundaries. The crystal structure of M_6C type carbides varies widely across the range of carbides that fall within this category; however, all of these structures are complex cubic [19].

Several different carbide reactions have been identified to occur over a variety of temperature regimes. The most significant carbide reaction in many alloy systems is the formation of $M_{23}C_6$ and γ' according to the following reaction [19]:

$$MC + \gamma \rightarrow M_{23}C_6 + \gamma' \qquad (3.1)$$

Equation 3.1 would be applied to the systems under investigation accordingly [7, 8, 19]:

Alloy 617: $(Ti, Mo)C + (Ni, Cr, Al, Ti) \rightarrow Cr_{21}Mo_2C_6 + Ni_3(Al,Ti)$

Alloy 800HT: $TiC + (Ni, Cr, Al, Ti) \rightarrow Cr_{23}C_6 + Ni_3(Al, Ti)$

The stoichiometric balance of Equation 3.1 is not satisfied because it serves as a rough approximation of a common metallographic observation. Nevertheless, this reaction is still regarded as important to the production of blocky $M_{23}C_6$ carbides and γ'. As mentioned previously the $M_{23}C_6$ type carbide is important to inhibiting grain boundary sliding. The γ' that forms around $M_{23}C_6$ carbides as a result of the reaction shown in Equation 3.1 adds ductility and creep resistance to the grain boundary region [19].

M_6C carbide can form in a similar manner according to the following reaction [19]:

$$MC + \gamma \rightarrow M_6C + \gamma' \qquad (3.2)$$

The reaction shown in Equation 3.2 would occur within the Alloy 617 system accordingly [7, 19]:

$(Ti,Mo)C+ (Ni, Co, Al, Ti) \rightarrow Mo_3(Ni,Co)_3C + Ni_3(Al,Ti)$

The formation of one carbide phase from another is also possible according to the following reaction [19]:

$$M_6C + M' \rightarrow M_{23}C_6 + M'' \qquad (3.3)$$

The reaction shown in Equation 3.3 would occur within the Alloy 617 system accordingly [7, 19]:

$Mo_3(Ni,Co)_3C + Cr \leftrightarrow Cr_{21}Mo_2C_6 + (Ni,Co,Mo)$

The precipitation of $M_{23}C_6$ carbides on stacking faults and twins was previously mentioned. Such a reaction would occur accordingly [19]:

$$\gamma_1 \rightarrow M_{23}C_6 + \gamma_2 \qquad (3.4)$$

An example of the reaction shown in Equation 3.4 is as follows:

$(Ni, Co, Cr, Mo, C) \rightarrow Cr_{21}Mo_2C_6 + (Ni,Co)$

4. Effects of Platinum Addition to Alloys 800 HT & 617

4.1. Solubility of Platinum

An estimate of approximate, qualitative, elemental solubility in terminal solid solution systems can be predicted according to several criteria known as the Hume-Rotherey rules for solubility [4]. These criteria, as applied to transition group elements, include the Atomic Size Factor, the electronegative valency effect, and relative valency effects. The most important solubility criteria is known as the Atomic Size Factor, which states that atomic diameter differences greater than 15% between the solute and solvent transition group atoms will limit solubility of the solute species to only a few atomic percent. The evaluation of the atomic size factor should be done with consideration to the fact that the atomic size difference between the solute and solvent atoms is related to their distance of closest approach. Therefore, evaluation of the metallic diameter difference between the solute and solvent atoms should determine whether or not the atomic size factor criterion is met for a particular example [4]. Tables 4.1 and 4.2 show the atomic size factor solubility criterion evaluation for platinum in alloys 800 HT and 617, respectively [22, 30 - 34]:

Table 4.1		
Atomic Size Factor Evaluation of Pt in Alloy 800 HT		
Element	**Met. Diameter (Angstroms)**	**% Diff from the Avg Metallic Dia. Of Alloy 800 HT elements**
Iron	2.52	0.53%
Nickel	2.50	1.32%
Chromium	2.58	1.84%
Platinum	2.70	6.58%

Table 4.2		
Atomic Size Factor Evaluation of Pt in Alloy 617		
Element	**Met. Diameter (Angstroms)**	**% Diff from the Avg Metallic Dia. Of Alloy 617 elements**
Nickel	2.50	4.58%
Chromium	2.58	1.53%
Cobalt	2.50	4.58%
Molybdenum	2.90	10.69%
Platinum	2.70	3.05%

Tables 4.1 and 4.2 both show that platinum meets the atomic size factor criterion for solubility in both Alloys 800 HT and 617 because the metallic diameter size difference between the platinum atom and the major alloyed elements does not exceed 15% in either case.

The relative electronegative valency effect is another important criterion for transition group elemental solubility. In general, it has been found that the free energy of formation of a stable intermetallic compound decreases with increasing electronegativity difference between solute and solvent atoms. Therefore, a greater electronegativity difference between the solute and solvent atoms increases the tendency to form a stable intermetallic compound at the expense of a terminal solid solution [4]. Tables 4.3 and 4.4 show the Pauling electronegativity values for each of the major species in Alloys 800 HT and 617 with platinum [35 - 40].

Table 4.3	
Electronegativity of Major Alloyed Elements in Alloy 800 HT with Platinum	
Element	**Pauling Electronegativity (eV)**
Iron	1.83
Nickel	1.91
Chromium	1.66
Platinum	2.28

Table 4.4	
Electronegativity of Major Alloyed Elements in Alloy 617 with Platinum	
Element	**Pauling Electronegativity (eV)**
Nickel	1.91
Chromium	1.66
Cobalt	1.88
Molybdenum	2.16
Platinum	2.28

The greatest electronegativity differences for the Alloy 800 HT and 617 systems are both $\Delta_{Pt\text{-}Cr}$ = 0.62 eV. The typical coherent γ' intermetallic precipitates that form within Alloy 800 HT and 617 systems are comprised of either nickel and aluminum, or nickel and titanium. The electronegativity difference between nickel and aluminum, and nickel and titanium are 0.30 eV and 0.37 eV. These low values relative to the difference between platinum and chromium indicate that the possibility exists for the formation of a stable Pt – Cr intermetallic compound. Furthermore, it should be taken into consideration that the elemental electronegativity difference for incoherent intermetallic compounds will be higher than that for coherent intermetallic compounds. This indicates that any Pt-Cr compounds that do form will most likely be incoherent.

The solubility of a group VIB element, such as chromium, in a group VIII element, such as platinum, is greater than the solubility of a group VIII element in a group VI B element. This preferable solubility is related to the Hume-Rothery relative valency effects. Metallic bonding within the transition group is stronger than those of other groups because bonding involves both the sub-valent d obitals as well as the valent s orbitals. The d orbital of the group VIII element is too filled to provide the significant d orbital function necessary for metallic bonding with group VI B elements. The lower degree of d orbital filling in group VI B elements precludes a similar restriction on the solubility of group VI B elements in group VIII solvents [4].

The size factor and relative valency effect rules for solubility are satisfied for the addition of platinum to alloy 800 HT and 617 systems. However, the electronegative valency effect indicates that a stabilized Pt-Cr intermetallic phase is likely within these alloy systems. Further investigation into the possibility of the precipitation of such a phase has been carried out by phase diagram inspection. The binary Pt-Cr phase diagram indicates that 9 – 44 wt% platinum in chromium at a temperature 1050 °C will lead to partitioning of chromium between a solid solution and a Cr_3Pt phase [2]. The materials characterized were water quenched from a solution anneal at 1050 °C. Table 4.5 gives the chromium and Cr_3Pt phase composition at 1050 °C with additions of 2, 5, 15, and 30 wt% platinum in a pure binary system. The values shown in Table 4.5 were calculated by applying the lever rule to the binary Pt-Cr phase diagram [2].

Table 4.5		
Cr and Cr3Pt Composition of Binary Pt-Cr system at 1050 C		
Pt wt % addition	%Cr	%Cr3Pt
2	100.0%	0.0%
5	100.0%	0.0%
15	81.2%	18.8%
30	37.6%	62.4%

The Cr_3Pt phase has an A15 crystal lattice strukturbericht designation [2]. If found to be present in the Alloy 800 HT / 617 + Pt systems, the non-cubic crystal lattice structure of the Cr_3Pt precipitate could lead to significant lattice mismatch that would compromise the mechanical properties of the respective microstructures. Further inspection of binary phase diagrams between Pt and the remaining major alloyed elements in Alloys 800 HT and 617 shows no new phases that should precipitate by platinum addition [2].

4.2. Review of Platinum Metallurgy Literature

The research conducted herein involves the study of wrought and cast structures of solid solution strengthened nickel-cobalt and iron-nickel base alloyed systems with significant platinum additions. A recent literature review of platinum alloy metallurgy indicates that this research effort is a first of its kind. Six major literature sources were identified that treat the topic of platinum alloy metallurgy for industrial purposes in the most closely related manner to the research involved herein [9-14]. The literature indicates that concurrent efforts are ongoing in both South Africa ([12 – 14]) and Germany ([9 – 11]) in the study of pure binary, ternary, and quarternary platinum alloys in the cast form. Additional sources reviewed involve collaborative French and Italian surface science studies of various binary platinum alloy systems, the results of which indicate a consistent platinum enrichment of the first monatomic (111) face surface layers [5-17]. The examination techniques utilized, and resulting findings of these works may be useful for the characterization of the alloys studied herein.

German and South African research efforts are concentrated on the development of a new platinum group of super alloys with higher melting points, but similar mechanical, microstructural and corrosion resistance properties to cast precipitate strengthened nickel base super alloys used in high temperature service applications. The development of such materials will allow for higher temperature operation of power conversion cycles, which will lead to an overall increase in net thermal efficiency. The most promising direct application will be for use in gas turbines.

Currently, there are a number of nickel base super alloys (NBSA) that are widely used in gas turbine applications for their exceptional high temperature mechanical and corrosion resistance properties. In such applications, NBSAs are exposed to aggressive environments at temperatures up to 1100 °C (0.85 T_{melt}). These materials consist of an austenitic γ nickel matrix strengthened by a high volume fraction (~70%) of finely dispersed $L1_2$ cubic γ' ($Ni_3(Al,Ti)$), and γ" ($Ni_3(Nb,Ta)$) precipitates. Good coherency between the precipitates and the matrix, due to similar crystal structures, results in low interfacial surface energy. This prevents precipitate coarsening at high temperature, which results in retention of creep resistance and yield strength at temperature [19]. Precipitate volume fraction is controlled by additions of elements that make up the precipitate phases. Corrosion resistance properties are enhanced by aluminum and chromium additions. These elements form protective surface oxides that are stable at high temperature.

High temperature platinum group super alloy research is a fairly new area of study. The oldest literature source from German and South African research efforts is from 1999 [13]. The initial stages of these works have focused on simple binary, ternary, and quarnary cast systems where minor alloying additions are added to an FCC platinum matrix. The possibility of the development of such systems is largely founded on the similar size, crystal lattice, and electron structures of platinum and nickel [9].

In the work of Cornish (2003), binary Pt – X systems, where X = Ti, Ta, Nb, Al, were investigated for phase stability, melting point, hot corrosion resistance, high thermal conductivity, low thermal expansion, and low density [9]. Ternary additions of Rh, Ru and Ni were later added for solid solution strengthening effects. Samples were annealed at 1350 °C and subjected to stepped isothermal oxidation and hardness testing. Ternary

systems from these elements that were found to produce intermetallic precipitates with crystal structures other than the $L1_2$ form were excluded from further study. It was found that only Pt-Al-X systems demonstrated acceptable oxidation resistance. The Pt_3Al precipitate formed in Pt-Al-X base systems was found to undergo a transformation from the $L1_2$ structure to the tetragonal DO'_c structure at lower temperatures. This lead to the evaluation of ternary additions of Ti, Cr, Ru, Ta, and Ir for their stabilizing effect on the $L1_2$ crystal structure of Pt_3Al precipitates. Ternary systems consisting of Cr, Ru and Ti additions to Pt-Al systems demonstrated the best oxidation resistance of all systems evaluated for $L1_2$ structure Pt_3Al precipitate stability. The combinations of ternary systems were down-selected to 86Pt-10Al-4Cr and 86Pt-10Al-4Ru for further study for quarternary system development. Cr and Ru additions to the base Pt-Al system were found to give good stabilization of the $L1_2$ structure of the Pt_3Al precipitates and good solid solution strengthening, respectively. An 85Pt-7Al-3Cr-5Ru quarternary system was developed and annealed for 96 hours at several temperatures ranging from 1150 °C – 1450 °C in order to investigate the effect of heat treatment on the microstructure. The annealing process at 1450 °C produced the optimal microstructure with precipitates so finely dispersed that their existence could only be determined by XRD.

The superior oxidation resistance of Pt-Al-X systems was confirmed by Yamabe-Mitarai (2004) [11]. Additional ternary systems consisting of Pt-X-Z, where X = Al Nb Ta Ti and Z = Ni Ru Cr Re, were studied for stability of $L1_2$ precipitates. The stability of several $L1_2$ compounds, including Pt_3Ti Pt_3Cr Pt_3In Pt_3Ga Pt_3Sn and Pt_3Al, were evaluated for their temperature dependence. Only Pt_3Al was found to show strong temperature dependence. The superior oxidation resistance and the dependence of precipitate formation on temperature for the Pt-Al-X systems lead to their selection for further development over the other alloy systems considered. Ternary additions of Ti, Ta, Cr, Ni, Nb, and Sc were all found to have a stabilizing effect on the $L1_2$ structured Pt_3Al precipitates. Tensile creep tests were performed on Pt-Al-Cr and Pt-Al-Ru alloys. Results showed higher rupture strength than commercial ODS alloys. These findings indicate that Pt base ternary alloys can be developed with better mechanical properties than ODS alloys in high temperature service applications [11].

The results of the work presented by Vorberg (2004) focus predominantly on Cr concentration effects on $\gamma - \gamma'$ lattice misfit and γ' precipitation, and heat treatment cooling regimes on γ' precipitate morphology [10]. The principle Pt alloy systems studied in this work consisted of Pt-Al-Cr-Ni systems of variable concentrations. A study of the effect of heat treatment cooling regimes on γ' precipitation was conducted with a 78.5Pt-12.5Al-3Cr-6Ni heat of material. Samples were annealed for 12 hours at 1500 °C and subjected to water quenching, air cooling, and furnace cooling prior to metallographic analysis by SEM technique. The quenched sample contained less than 3% volume fraction of precipitates that may have formed between furnace removal and quenching. The air cooled sample had a microstructure consisting of approximately 30% volume fraction of partially aligned 200 nm diameter precipitates. The chemical composition of the precipitates in the air cooled and water quenched microstructures could not be determined due to the small precipitate sizes. The furnace cooled sample had a bimodal precipitate size distribution consisting of a total of approximately 34 % volume fraction. One group of precipitates was characterized by a maximum diameter of 200 nm while the second group consisted of coarsened precipitates with an approximate average diameter of 3 microns. The chemical composition of the coarsened precipitates was analyzed to be approximately 74.3Pt-20Al-1.9Cr-3.8Ni, indicating a partitioning of only Al to the precipitate phase. The effect of Cr concentration dependence on γ' precipitation was studied by comparing a ternary Pt base system with a quarternary Pt base system including Cr addition. Heats of 82Pt-12Al-6Ni and 76Pt-12Al-6Ni-6Cr were homogenized at 1500 °C for 12 hours followed by air cooling. The ternary system contained approximately 22 % volume fraction of 100 nm edge cuboidal precipitates. The Cr bearing quarternary system contained approximately 50 % volume fraction of 500 nm diameter spherical precipitates. Heats of 78.5Pt-12.5Al-3Cr-6Ni and 76Pt-12Al-6Cr-6Ni were examined by XRD analysis for γ- γ' lattice misfit (δ) , where $\delta = (a_{\delta'} - a_{\delta}) / a_{\delta}$. The former heat was found to have a lattice misfit of approximately $-3*10^{-3}$, while the latter heat was found to have a lattice misfit of approximately $-1*10^{-3}$. Preferable partitioning of Cr atoms, which are relatively smaller than Al or Pt, to the matrix causes the lattice parameter of the matrix to decrease more than the lattice parameter of the precipitates. This leads to an overall decrease in the absolute value of the γ- γ' lattice

misfit. The relevant findings from Vorberg (2004) are as follows: Faster heat treatment cooling regimes result in smaller precipitates. Increasing Cr content increases precipitate size and volume fraction, and decreases lattice misfit.

The work presented in Hill (2001) covers a wide assessment of Pt base ternary alloys for high temperature service. Several combinations of Pt-X-Z systems were first considered [12]. Secondary X elements, which included Al Ti Ta and Nb, were selected because they form the characteristic γ' Pt_3X phase found in precipitate strengthened NBSAs. Ternary Z elements, which included Ru Ni and Re, were selected as stabilizing elements for the γ' phase and for their solid solution strengthening effect on the γ Pt matrix. Targeted ternary system ratios were determined by first investigating binary X-Z systems in which ternary additions to the alloy were targeted. If second phase structures precipitated from these systems, the corresponding X-Z ratios were eliminated from the ternary Pt-X-Z systems to prevent the formation of undesirable phases. Eight ternary systems were identified for further investigation, including: Pt-Al-Ni, Pt-Al-Ru, Pt-Al-Re, Pt-Ti-Ru, Pt-Ti-Re, Pt-Ta-Ru, Pt-Ta-Re, and Pt-Nb-Ru. Three heats of each system were melted based on the Pt_3X eutectic, X poor and X rich compositions from the corresponding Pt-X phase diagrams. Each system was characterized according to microstructure phase distribution and morphology, relative resistance to oxidation, room temperature hardness, and resistance to cracking around hardness indentations. The Pt-Al-Z systems were singled out for further investigations based on their superior resistance to oxidation due to the formation of a protective alumina oxide (Al_2O_3) film. The absence of such a protective film resulted in internal oxidation of the remaining ternary systems. Pt-Al-Ni and Pt-Al-Ru systems were further down selected for analysis. The three heats of both of these systems appeared to be single phase in the as-cast condition. Two phase microstructures were identified after annealing at 1350 °C for 66 hours; however, coherency was not established and it was determined that further refinement of heat treatment and composition would be required to develop a microstructure with optimal cast NBSA characteristics.

The most important conclusive results presented by Hill (2001) involve the selection of Pt-Al-Z systems for further study in the development of high temperature Pt base cast ternary alloys with similar NBSA precipitate strengthened microstructures.

Continued research efforts by the same research group are presented in Hill (2002) [14]. The investigation objectives of the research efforts described therein include: determination of element Z partitioning between the γ Pt matrix and the γ' Pt_3Al precipitate phase, development of a fine distribution of γ' precipitates within the γ matrix, effects of element Z on the γ - γ' interface, XRD analysis of element Z effect on γ' crystal structure stability, and preliminary assessment of mechanical properties by room temperature hardness tests. Ternary Z elements included Ti, Ta, Cr, Ni, Mo, Re, Ru, and W. Ru and Re partitioned fully to the γ Pt matrix. W, Ni, Cr and Mo partitioned mostly to the γ matrix, but showed some solubility in γ' precipitates. These elements show the most promise as solid solution strengtheners because, with limited solubility in the γ' phase, they have little effect on the γ' structure and γ - γ' phase boundaries. The low temperature DO_c' γ' structure was observed in the Pt-Al-(Ni,W) systems. XRD analysis of the γ' microstructure in the Pt-Al-(Cr,Mo) systems could not be determined; however, no martensitic laths were observed in these structures, which could indicate that the cuboidal FCC $L1_2$ γ' structure could have been stabilized. Ti and Ta partitioned nearly evenly between the γ matrix and the γ' precipitates. Ternary additions of Ti, Ta, Cr, Ni and Re produced fine two phase γ - γ' microstructures characteristic of precipitate strengthened NBSAs; however, the coherency of these structures is not reported. Low γ' aluminum concentration of approximately 10 at% indicates that precipitation of γ' within these systems probably occurred during heat treatment rather than eutectically due to the fact that eutectic Pt_3Al contains approximately 20 at% Al. Following annealing at 1350 °C for 96 hours, hardness testing indicated a hardness of 400 HV or better for all systems except those containing Ni and Cr. Solid solution strengthening effects of these ternary additions may therefore be limited. Nevertheless, based on adequate solubility, stabilized γ' crystal structure, and two phase γ - γ' morphology, ternary additions to Pt-Al-Z systems were down-selected to Ti, Ta, and Cr for further development of high temperature platinum base cast ternary alloys.

A brief treatment of martensitic transformations in Pt-Al and Pt-Fe systems is presented by Biggs (1999) [13]. The work presented therein is mainly concerned with the study of martensitic transformations in Pt-Ti systems. The introduction, however, indicates that γ' Pt_3Al may undergo martensitic transformations to γ'_1 Pt_3Al and then to

γ'_2 Pt_3Al. It is also indicated that Pt-Fe systems containing approximately 25 at% Pt undergo a martensitic transformation from disordered FCC to BCC at a transformation temperature between 30 °C and 300 °C.

Collaborative French and Italian surface composition studies of binary Pt-X systems began in the early 1980s and continued through the early 1990s [15 – 17]. The most encompassing and exhaustive report on Pt-X surface composition is presented by Gauther (1992) [17]. In this work low energy electron diffraction (LEED) analysis is used to determine the surface structure and the composition profile vs. depth for (111) surfaces of 80Pt – 20(Fe, Co, Ni) alloy systems. LEED analysis was chosen because it provides an accurate analysis of the structure and chemical composition of the first 2 – 4 monatomic surface layers. Characteristic differences were identified between the Ni/Co and the Fe bearing heats of material. The first monatomic surface layer in all three systems were nearly 100 at% Pt enriched. The platinum composition profile vs. depth for the Pt-Fe system decays to the bulk monotonously. The platinum composition profile for the Pt-(Ni,Co) systems decay in an oscillatory manner across the first three monatomic surface layers to the bulk composition. These differences are partially attributable to lower order – disorder transition temperatures on Ni and Co alloy phase diagrams than on Fe alloy phase diagrams, which results in substitutionally disordered Pt-(Ni,Co) systems and a substitutionally ordered Pt-Fe system [17]. Table 4.6 presents the composition vs. depth profiles, inter-atomic distances, and lattice parameters for each of the binary platinum alloys studied.

Table 4.6						
Alloy	Composition (at % Pt)			Inter-Layer		Lattice
	1st layer	2nd layer	3rd layer	1st - 2nd	2nd - 3rd	Parameter (A)
Pt-Ni	99	30	87	2.180	2.180	3.845
Pt-Co	100	48	89	2.219	2.239	3.855
Pt-Fe	96	88	85	2.279	2.238	3.900

It can be seen from Table 4.6 that the substitutionally disordered alloys produce damped oscillatory platinum segregation profiles. Considering that the pure platinum lattice parameter of 3.92 A is larger than any of those above, it follows that a decrease in the platinum concentration within the second monatomic layer relieves strain within the

top layer of the disordered alloys [17]. A decrease in Pt concentration within the second monatomic layer of the Pt-Fe system, however, is not energetically favorable. The strain field of the surface layer induced by Pt – Fe size differences does not provide sufficient energy to break Pt – Fe chemical bonds in the second monatomic layer, which are strengthened by the chemically ordered state of the system [17]. Certain similarities exist for each of the FCC structured binary systems studied. Only (111) faces of each binary system were examined for LEED analysis. All examined surfaces showed little interlayer relaxation with no stacking faults, and typical ABC stacking [17].

The development of high temperature precipitate strengthened cast Pt alloy systems has yielded many useful insights towards the development of heat resistant wrought self-catalytic materials of alloy 617 / 800 HT + Pt chemistry. The base alloy chemistry of these materials, however, are different than the materials developed by the German and South African research groups in that they are predominantly substitutionally solid solution strengthened and carbide precipitate strengthened alloys. It is hoped that the microstructures of the alloys characterized herein will be similar to those of their base chemistry, but findings from the literature reported above may indicate that this will not be the case. The development of precipitate strengthened Pt alloy systems first began by identifying those elements that would readily form a coherent stabilized precipitate phase within an FCC γ Pt matrix; the elements identified include: Al, Cr, In, Ga, Sn, Ti, Ta, and Nb [9, 11, 12]. According to tables 3.1 and 3.2 above, the base chemistry of alloys 800 HT and 617 contain minor additions of Al and Ti, and significant additions of Cr. Inspection of binary Pt-Cr phase diagrams indicates that Pt additions in the range of 66 – 96 wt% could lead to precipitation of a $L1_2$ stabilized terminal Pt_3Cr phase within the matrix of either base alloy 617 or 800 HT material [2]. Such a coherent phase would provide beneficial high temperature precipitation solid solution strengthening. However, the current investigations require the additions of 2 – 30 wt % platinum to Alloys 800 HT and 617. Platinum concentrations within such a range in binary Pt-Cr systems leads to the precipitation of a Cr_3Pt phase that has a non cubic A15 type crystal structure. The presence of such a precipitate may have deleterious effects on the mechanical properties of the cubic structured matrix due to significant lattice

mismatch. By phase diagram inspection, it does not appear that any other significant phases will precipitate within alloy 617 / 800 HT + Pt systems [2].

The direct results of surface science studies of Pt-X binary systems do not appear to be as useful for the development of wrought 617/ 800 HT + Pt alloy systems. Surface enrichment of Pt reported by Gauthier (1992) applies only to (111) faces. The alloy 617/800 HT + Pt materials developed for characterization are wrought polycrystalline materials that should not exhibit general macroscopic Pt enrichment due to non uniform crystalline surface orientation.

5. Procedures

Four heats each of Alloy 800 HT + Pt chemistry, and Alloy 617 + Pt chemistry were received from Special Metals Inc. of Huntington, WV. Platinum additions were made to the base alloys in nominal amounts of 2 wt%, 5 wt%, 15 wt%, and 30 wt%. The diameter and thickness of the received cast buttons of Alloy 800 HT + Pt chemistry were 3.8 cm and 0.953 cm, respectively. The cast buttons of Alloy 617 + Pt chemistry were approximately 3.18 cm wide and 0.64 cm thick. Images of the microstructures, in the as cast and wrought form, were developed via optical and electron microscopy. The wrought microstructure images are compared with corresponding images of commercial Alloys 800 HT and Inconel 617 to facilitate the identification of significant alterations within the microstructure due to the effects of added platinum. Specimens of commercial Alloy 800 HT and Inconel 617 material were provided by Metalmen Inc. of New York, NY, and Special Metals Inc., respectively.

5.1. Commercial Alloy and Cast Specimen Preparation

5.1.1. Sectioning

Each button of Alloy 800 HT+ Pt chemistry was sectioned with a hacksaw into three segments to form an inner segment with a width of approximately 1.0 inches. The Alloy 617 + Pt buttons were sectioned with a high speed precision abrasive cutoff wheel to produce center sections approximately 1.9 cm in width. The outer two segments of each button were used to prepare micrographs of the as cast microstructure. A very coarse surface was produced from hacksawing; however, due to low heat input during the sectioning process, an unaltered as cast microstructure was attainable with sufficient grinding and polishing. Figure 5.1 shows a received and sectioned button of Alloy 800 HT – Pt material for reference.

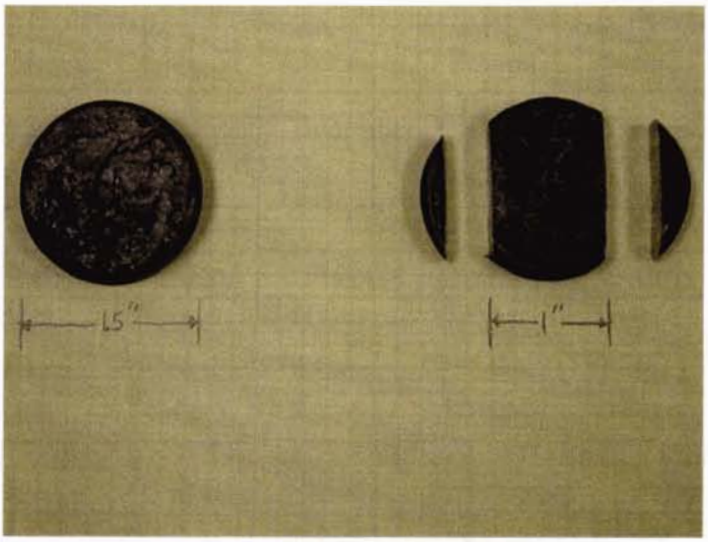

Fig 5.1: As received and sectioned buttons of Alloy 800HT + Pt chemistries

The wrought commercial Alloy 800 HT material received from Metalmen Inc. was 1.27 cm D x 1.27 cm L, and therefore required no sectioning prior to mounting. The commercial Inconel 617 from Special Metals, Inc. was received in sheet form. A 1.27 cm x 0.64 cm specimen of sheet stock was cut with a low speed diamond saw in order to mount for analysis.

5.1.2. Mounting

One outer segment of each sectioned Alloy 800 HT + Pt cast button was mounted with cold setting epoxy resin in a 3.18 cm D cylindrical mold. Room temperature Epocure resin was mixed with hardener in proportions of 5:1 to prepare the epoxy compound for specimen mounting. The mixture was poured into molds over the samples and hardened in a period of 10 hrs. One outer segment of each sectioned Alloy 617 + Pt cast button, as well as the specimen of commercial Inconel 617, was mounted via hot pressing with copper powder in a 3.18 cm D cylindrical mold. The specimen of commercial Alloy 800 HT was mounted via hot pressing with bakelite in a 3.18 cm D cylindrical mold. A variety of sample mounting materials were used for the cast specimens in order to gain wider experience with sample mounting techniques.

5.1.3. Grinding and Polishing

Samples were mechanically ground and polished according to the procedure outlined in tables 5.1 and 5.2:

Table 5.1	Grinding and Polishing Procedures for Cast Alloy 800 HT – Pt Systems, and Wrought Commercial Alloy 800 HT				
Cast Alloy 800 HT + Pt			Wrought Commercial Alloy 800HT		
Grinding					
Grit	**Pressure (lbs)**	**Time (sec)**	**Grit**	**Pressure (lbs)**	**Time (sec)**
60	6	5400	180	5	600
180	5	1800	240	5	480
240	5	900	320	5	360
320	5	600	400	5	300
400	5	300	600	5	240
600	5	240			
Polishing					
Microns	**Pressure (lbs)**	**Time (sec)**	**Microns**	**Pressure (lbs)**	**Time (sec)**
6	5*	120	6	5*	120
1	3*	120	1	3*	120
0.5	3*	60	0.5	3*	60

Table 5.2	Grinding and Polishing Procedures for Cast Alloy 617 – Pt Systems, and Wrought Commercial Alloy 617				
Cast Alloy 617 + Pt			Wrought Commercial Inconel 617		
Grinding					
Grit	**Pressure (lbs)**	**Time (sec)**	**Grit**	**Pressure (lbs)**	**Time (sec)**
180	6	1800	180	6	600
240	5	900	240	5	480
320	5	600	320	5	360
400	5	360	400	5	300
600	5	300	600	5	240
Polishing					
Microns	**Pressure (lbs)**	**Time (sec)**	**Microns**	**Pressure (lbs)**	**Time (sec)**
6	5*	120	6	5*	120
1	3*	120	1	3*	120
0.5	3*	60	0.5	3*	60

*Pressure is an estimate because samples were polished by hand against a rotating wheel

5.1.4. Etching

Initial etching practice involved the use of glyceregia (3 parts glycerol, 3 parts HCl, 1 part HNO_3) on the sample of cast Alloy 800 HT + 2% Pt material. Though glyceregia works well as a mild etchant for Fe-Ni base super alloys, it created corrosion artifacts on the surface of the above mentioned material within 10 seconds [23]. In order to gain more control over the etching process, the sample of 2% Pt material was re-polished and etched with a weak version of glyceregia (12 parts glycerol, 3 parts HCl, 1 part HNO_3). The weaker etchant allowed for the development of a high quality as-cast microstructure image of the sample of 2% Pt material by slowing the etching process. The same weak etchant was used to etch the sample of 5% Pt material and produced good results for imaging. For the cast materials containing 15% and 30% Pt the etchant was weakened again by a factor of 2 (24 parts glycerol, 3 parts HCl, 1 part HNO_3).

The commercial Alloy 800 HT was etched with glyceregia. Initially the material was etched at 30 second intervals to prevent over etching of the microstructure; however, the interval was extended to 2 minutes due to the slow etching effect. The material required a total of 10 minutes of etching in order to reveal the grain boundary structure for imaging.

Etching procedures for the cast Alloy 617 + Pt chemistries were determined on the presumption that these materials would be more corrosion resistant than Alloy 800 HT + Pt. This presumption was made on the basis that Inconel 617 is predominantly a Ni base system whereas Alloy 800 HT is predominantly a Fe base system, where both alloys have appreciable yet nearly equal Cr concentrations. Initially a ½ strength glyceregia based solution (6 parts glycerol, 3 parts HCl, 1 part HNO_3) was used to etch the cast Alloy 617 + 2%Pt; however, after 3000 seconds of etch time no visible effects were observable with the naked eye or at 100 X optical magnification. The etchant strength was increased to the specified composition of glyceregia (3 parts glycerol, 3 parts HCl, and 1 part HNO_3), which revealed the as-cast structure of the Alloy 617 + 2%Pt material after 780 seconds of etch time. The lengthy time required to produce a quality microstructure for imaging indicated that full strength glyceregia could be used to effectively etch the remaining cast Alloy 617 + Pt chemistries. Etching of each material

occurred in 2 minute intervals interrupted with ultrasonic cleansing in an ethanol bath in order to periodically monitor microstructure development via optical magnification at 100 X. The commercial Inconel 617 was etched according to the same procedure used to etch the corresponding platinum bearing materials. The etch times and etchants used on each of the materials studied herein are included in tables 5.3 and 5.4 below:

Table 5.3			
Wrought commercial Alloy 800 HT and Cast Alloy 800 HT + Pt			
% Pt	**Etchant Chemistry**	**Etch time** (sec)	**Reference Figure**
0	3 glycerol, 3 HCl, 1 HNO3	900	6.2
2	12 glycerol, 3 HCl, 1 HNO3	210	6.5
5	12 glycerol, 3 HCl, 1 HNO3	200	6.22
15	24 glycerol, 3 HCl, 1 HNO3	510	6.39
30	24 glycerol, 3 HCl, 1 HNO3	1380	6.56

Table 5.4			
Wrought commercial Alloy 617 and Cast Alloy 617 + Pt			
% Pt	**Etchant Chemistry**	**Etch time** (sec)	**Reference Figure**
0	3 glycerol, 3 HCl, 1 HNO3	1230	6.71
2	3 glycerol, 3 HCl, 1 HNO3	780	6.74
5	3 glycerol, 3 HCl, 1 HNO3	1020	6.90
15	3 glycerol, 3 HCl, 1 HNO3	1500	6.106
30	3 glycerol, 3 HCl, 1 HNO3	480	6.122

5.2. Wrought Specimen Preparation

5.2.1. Cold Working and Annealing

Wrought structures were developed from each of the cast buttons. For safety reasons, the relatively small size of each sectioned cast material precluded the option of direct cold working. Each of the larger middle portions of the cast materials were TIG spot welded with Inconel 617 filler rod into cut out sections of plate stock. Plate stock of the base chemistry of each material was utilized for the respective samples. Once welded into place, each plate and sample assembly was milled to uniform thickness to facilitate rolling operations. Figure 5.2 shows the final geometry of the specimen + plate assemblies prepared for cold working and annealing operations.

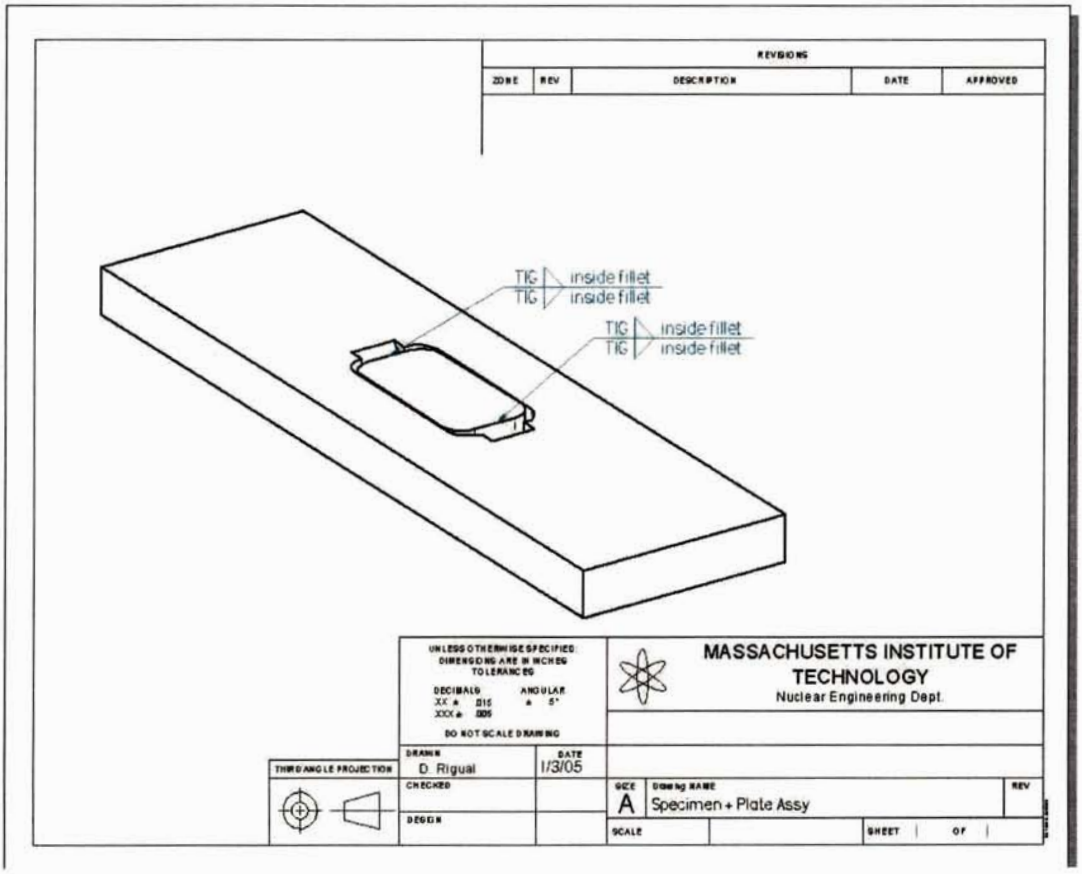

Fig 5.2: Cast specimen + plate stock welded assembly.

Large dendrites observed in the cast material indicated that an extensive amount of cold work, with an intermediate anneal, would be needed to fully develop wrought structures. Each cast material + plate stock assembly was rolled to a 75% reduction in area. At 50 % reduction an intermediate anneal was performed on each material at 1050 °C for 30 minutes followed by water quenching. After the final rolling to 75 % reduction in area, each material was annealed again at 1050°C for 30 minutes followed by water quenching. Following cold working and annealing, each material was removed from its respective plate stock by water jet cutting.

5.2.2. Sectioning

Four small sections of each wrought material were cut from the bulk with a high speed precision saw. The first section was sent to Luvak Inc. for chemical composition analysis. The remaining sections were set aside for metallographic analysis.

5.2.3. Mounting

Three sections of each heat of material were mounted for metallographic analysis in order to characterize the respective microstructures in the rolling plane as well as in the two orthogonal planes to the rolling plane. For reference purposes, the rolling direction has been defined as the y direction of the xy plane in a typical Cartesian coordinate system. The specimen mounted in the xz plane shows the rolling direction projected orthogonally out of the plane of view. The specimen mounted in the yz plane shows a side cut of the rolled plane. Prior to mounting, a type 316L SS wire was spot welded to each specimen in order to allow for ease of electrolytic etching, as well as to establish continuity when imaged in the SEM. Each specimen was mounted with a quick curing cold setting epoxy resin in 3.18 cm D cylindrical molds. Room temperature Epokwik resin was mixed with hardener in proportions of 5:1 to prepare the epoxy compound for specimen mounting. The mixture was poured into molds over the samples and hardened in a period of 2 hrs. Epoxy mounting was chosen for its excellent corrosion resistance

compared to hot pressed copper mounting compound in the electrolytic etching environment.

5.2.4. Grinding and Polishing

The wrought samples were mechanically ground and polished according to the procedure outlined in Table 5.5:

Table 5.5	Grinding and Polishing Procedures for Wrought Alloy 800 HT – Pt Systems, and Wrought Alloy 617 – Pt systems				
Wrought Alloy 800 HT + Pt			Wrought Alloy 617 + Pt		
Grinding					
Grit	**Pressure (lbs)**	**Time (sec)**	**Grit**	**Pressure (lbs)**	**Time (sec)**
60	5	720	60	5	600
180	5	480	180	5	360
240	5	360	240	5	360
320	5	360	320	5	360
400	5	360	400	5	360
600	5	360	600	5	360
Polishing					
Micron	**Pressure (lbs)**	**Time (sec)**	**Micron**	**Pressure (lbs)**	**Time (sec)**
6	5*	300	6	5*	300
1	3*	300	1	3*	300
0.5	3*	60	0.5	3*	120

*Pressure is an estimate because samples were polished by hand against a rotating wheel

5.2.5. Etching

The results of chemical etching of the cast materials produced acceptable microstructures for imaging analysis; however, it was determined that the quality of microstructure evaluation could be improved upon with an electrolytic etching process. Chemical etching of the cast microstructures produced certain areas that were severely over etched while other areas were not etched at all. It has been shown that electrolytic etching establishes a more uniform etching effect than chemical etching techniques [23].

Additionally, following the initial setup, electrolytic etching requires less time than chemical etching, which is extremely beneficial considering that three times as many wrought structures than cast structures are involved in this research.

Unfortunately, no experience has been published in the literature regarding etching materials similar to those studied herein. As a starting point each sample was etched according to procedures developed at the Special Metals Corporation for etching Alloys 800 HT and 617 [43]. The base chemistry Alloy 800 HT materials were etched in a Nital Electrolyte (95 % Methanol, 5 % Nitric acid). The base chemistry Alloy 617 materials were initially etched in a 10% Oxalic acid ($C_2H_2O_4$) aqueous solution. The results of the Alloy 617 – 2 wt% Pt etching indicated that a stronger etchant might be needed to fully reveal the microstructural features of the base Alloy 617 materials with higher platinum concentration. 3 ml of hydrochloric acid were added to the 10% Oxalic acid aqueous solution to strengthen the electrolyte.

The goals of etching were to adequately reveal the grain structure of each material, the precipitates formed, any other features that might have been produced during cold working and annealing, and to prevent over darkening of the surfaces etched. Etching procedures varied from material to material based on experience gained throughout the course of etching. Certain samples were imaged following both an intermediate and a final etching process. The etching procedures used for each base Alloy 800 HT and Alloy 617 material are shown in tables 5.6 and 5.7 respectively. The listed second etching procedures for particular materials indicate additional etching performed on these materials. Micrograph images were recorded between etching steps for these materials. For instance, the sample of Alloy 617 + 5 wt% Pt material was imaged following etching for 4 seconds with a 1.5 VDC potential and then was imaged again following an additional 2 seconds of etching with a 1.5 VDC potential. Reference figures are indicated so that the reader may find corresponding micrographs of the etching procedures performed on each material.

Table 5.6					
Electrolytic etching procedures of wrought base Alloy 800HT + Pt					
Nom. Pt composition	**Plane**	**Etchant**	**VDC**	**Etch Time (s)**	**Reference Figure**
2 wt%	xy	Nital	3	6	B.8
2 wt%	xy	Nital	1.5	10	6.9
2 wt%	xz	Nital	1.5	8	6.10
2 wt%	xz	Nital	1	15	B.9
2 wt%	yz	Nital	1.5	4	6.11
2 wt%	yz	Nital	1	10	B.10
5 wt%	xy	Nital	3	6	6.26
5 wt%	xy	Nital	1.5	10	B.23
5 wt%	xz	Nital	1.5	5	6.27
5 wt%	xz	Nital	1	5	B.24
5 wt%	yz	Nital	1.5	5	6.28
5 wt%	yz	Nital	1	4	B.25
15 wt%	xy	Nital	3	5	6.43
15 wt%	xy	Nital	1.5	15	B.37
15 wt%	xz	Nital	1.5	4	6.44
15 wt%	xz	Nital	1	5	B.38
15 wt%	yz	Nital	1.5	4	6.45
15 wt%	yz	Nital	1	5	B.39
30 wt%	xy	Nital	3	5	6.60
30 wt%	xz	Nital	1.5	5	6.61
30 wt%	xz	Nital	1.5	10	B.52
30 wt%	yz	Nital	1.5	4	6.62

Table 5.7					
Electrolytic etching procedures of wrought base Alloy 617 + Pt chemistries					
Nom. Pt composition	**Plane**	**Etchant**	**VDC**	**Etch Time (s)**	**Reference Figure**
2 wt%	xy	10 Oxalic Acid, 90 H2O	3	4	6.78
2 wt%	xz	10 Oxalic Acid, 90 H2O	1.5	6	6.79
2 wt%	yz	10 Oxalic Acid, 90 H2O	1.5	4	6.80
5 wt%	xy	10 Oxalic Acid, 90 H2O, 3 HCl	1.5	4	6.94
5 wt%	xy	10 Oxalic Acid, 90 H2O, 3 HCl	1.5	2	B.82
5 wt%	xz	10 Oxalic Acid, 90 H2O, 3 HCl	1	3	6.95
5 wt%	yz	10 Oxalic Acid, 90 H2O, 3 HCl	1	3	6.96
15 wt%	xy	10 Oxalic Acid, 90 H2O, 3 HCl	1.5	6	6.111
15 wt%	xz	10 Oxalic Acid, 90 H2O, 3 HCl	1	7	6.112
15 wt%	yz	10 Oxalic Acid, 90 H2O, 3 HCl	1	4	6.113
30 wt%	xy	10 Oxalic Acid, 90 H2O, 3 HCl	1.5	12	6.128
30 wt%	xz	10 Oxalic Acid, 90 H2O, 3 HCl	1.5	8	6.129
30 wt%	yz	10 Oxalic Acid, 90 H2O, 3 HCl	1.5	6	6.130

5.3. *Imaging and Characterization Procedures*

5.3.1. Optical Microscopy

Images were recorded via optical microscopy for all materials prior to and following the development of the cast and wrought microstructures via etching. A series of black and white images were recorded for each cast material at 50 X, 100 X, and 200 X levels of magnification. Micrographs were taken of wrought materials at magnifications of 100 X, 200 X, and 500 X. The range of magnification for the wrought materials was shifted to a higher level because the details of the wrought structures were finer than the cast structures. Images taken at 200 X and 500 X provide the best details of microstructural features and are included in Chapter 6 for microstructural evaluation. Images at lower magnification are included for reference in appendix B. No images were taken above 100 X for the 100 % Alloy 800 HT material that is included for comparison. Images of this material are included in Chapter 6 at 100 X magnification. From the recorded images several initial observations could be made regarding the nature of the respective microstructures. In order to roughly determine particle sizes a scale is included with each image. All grain size measurements were conducted using the linear intercept measurement method [46]. The details of the image observations are included in the results section of this report.

5.3.2. Scanning Electron Microscopy

SEM micrographs were developed at 500 X, 1300 X, 2500 X, and 3000 X to explore finer details of each microstructure that are not evident with optical means. A complete set of images is included in Appendix B. SEM analysis was conducted at the Special Metals Corporation where images were recorded via both SEI and Backscatter Electron Imaging (BEI) at 1300 X and 3000 (in some cases, micrographs were only taken at either 1300 X or 3000 X). SEI mode imaging primarily revealed topological features of each microstructure following etching. BEI mode imaging was used to determine

elemental segregation within the respective microstructures via differences in image contrast. These images are included in Chapter 6 for microstructural evaluation. All samples were sputter-coated with palladium and carbon painted prior to imaging.

5.3.3. Energy Dispersive Spectrometry

EDS analysis was performed on the matrix, precipitates, and in some cases the grain boundaries of each microstructure evaluated herein. The purpose of EDS analysis is to understand grain boundary and precipitate chemistry relative to the matrix. The effective spot size for EDS analysis is approximately 3 microns due to the depth and volume of the region below the surface of the material from which X-Ray information is obtained. Every effort was made to perform EDS analysis on regions larger than 3 microns due to the volume within the matrix below the electron beam from which X-ray information is obtained. In some cases, precipitates were so profuse that EDS analysis of the matrix had to be performed over areas with relatively fewer precipitates, which provided the best minimization of precipitate spectrum associated error. EDS analysis of grain boundary chemistry was performed on the largest grain boundary regions, such as 3 grain intersection points, in order to minimize the matrix spectrum associated error. It was not possible to observe light element peaks, such as carbon. Therefore, EDS spectra for matrix and precipitates are compared on the basis of transition metal composition. An EDS dot map was developed for the microstructures of the Alloy 617 – 5 and 15 wt% Pt materials.

5.3.4. Grain size measurement

Grain size measurement calculations were performed in each mounted plane relative to the rolling direction of each wrought material. Measurements were completed with the linear intercept method on 500 X optical micrographs. All of the micrographs used for linear intercept grain size calculations are included for reference in Appendix B with their corresponding grain size calculation spread sheets.

The linear intercept method for grain size calculation rests on assumptions that are necessary to apply a 2-D representation to a 3-D structure. Therefore, some inaccuracy is expected in the value of the calculated grain size with this measurement technique. Figure 5.3 shows a typical example of the structure from which the analysis was performed. As seen in Figure 5.3 for the case of Alloy 800 HT, linear projections were imposed at random orientations on an image of each wrought microstructure for which the grain size was measured. Each projection was labeled according to its length across the microstructure (L) and the number of times it intersects a grain boundary (I).

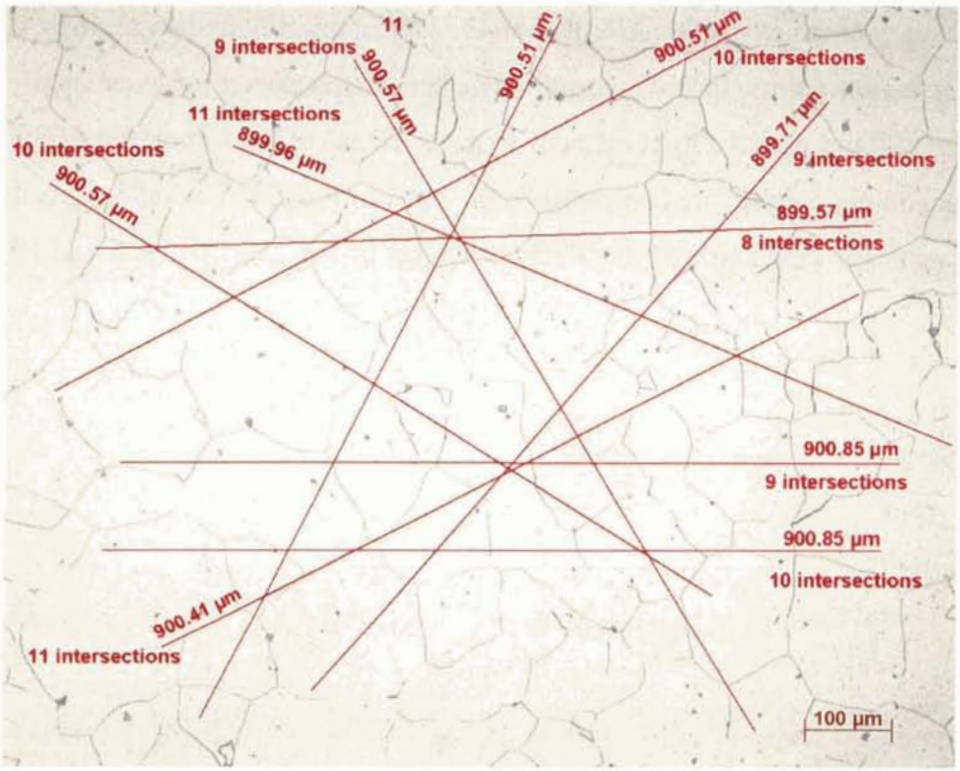

Fig. 5.3: Linear intercept grain measurement applied to Alloy 800 HT, 100X, glyceregia etch

The following set of equations was utilized for calculating grain size:

$$N_{avg} = \Sigma (I / L) / x \qquad (5.1)$$

I = Number of intercepts

L = Length

x = number of projections

$$N_{avg} = S_v / 2 \qquad (5.2)$$

S_v = Surf Area / Unit Vol

$$N_{avg} = (1/2) [(4\pi r^2) / (4/3\pi r^3)] \qquad (5.3)$$

$N_{avg} = 3 / 2r = 3 / D$

$$D = 3 / N_{avg} = 3L / I \qquad (5.4)$$

D = Average grain size

The grain size calculation for the commercial Alloy 800 HT material is given in Table 5.8:

Table 5.8			
Grain size calculation for Alloy 800 HT			
Projection	**Length (microns)**	**# intercepts**	**Grain size (microns)**
1	900.57	10	270
2	899.96	11	240
3	900.57	9	300
4	900.51	11	250
5	900.51	10	270
6	899.71	9	300
7	899.57	8	340
8	900.85	9	300
9	900.85	10	270
10	900.41	11	250
AVG grain size			**280**

For the case of the supplied base chemistry materials of Alloy 800 HT and In-617, the calculated grain sizes can be validated by comparing them to the respective manufacturer's grain size measurement specified in an ASTM grain size number. The ASTM grain size number (G) corresponds to the number of grains observed in a square inch at 100 X magnification when entered into the following formula [29]:

$$n = 2^{G-1} \qquad (5.5)$$

n = # grains / in^2 @ 100X

G = ASTM grain size

The commercial Alloy 800 HT material has a manufacturer's specified grain size of 2.5. This corresponds to a grain diameter of 190 μm across when the following relations are utilized:

$$m = 10{,}000 * n \qquad (5.6)$$

m = # grains / in^2

$$D = (4/\pi)\,(1/m)^{1/2}\,(25{,}400\ \mu m / in) \qquad (5.7)$$

D = average grain size

The % difference between the manufacturers measured grain size and the grain size measured in the laboratory for the commercial Alloy 800 HT material is 45%. The comparison is cited as percent difference rather than by percent error because the value reported by the manufacturer is not assumed to be 100% accurate; however, the manufacturer's value is most likely much more accurate than the value measured in the laboratory.

The large percent difference between the two reported grain size measurements can be accounted for by errors introduced in the etching process. The random grain structure of each material, due in part to non-uniform etching, introduced difficulties with developing an accurate grain size measurement. To compensate for this problem, ten projections were imposed over each image at random orientations in order to increase the

precision of N_{avg} values. These values, however, are relatively inaccurate because non-uniform etching results in large values for calculated grain size by reducing N_{avg}.

5.3.5. Chemical Composition Analysis

Alloy 617 - Pt materials were analyzed for carbon, titanium, aluminum, chromium, cobalt, molybdenum, manganese, silicon, phosphorous, sulfur, boron, iron, copper, platinum, and nickel [44]. Alloy 800 HT – Pt materials were analyzed for all of the above elements with the exceptions of cobalt, molybdenum, boron, and phosphorous [44]. Analysis of carbon and sulfur content was performed by combustion infrared detection [44]. All other elemental analysis was performed by direct current plasma emission spectroscopy [44].

5.3.6. Microstructural Evaluation

The most important microstructural properties characterized were related to grain structure, precipitate type, chemistry and morphology, and twinning characteristics. Microstructures were also evaluated for the presence of any obvious phase segregation revealed by scanning electron microscopy, as well as resistance to etching due to platinum induced cathodic protection. Particle sizing and distribution was carried out subjectively due to the lack of imaging analysis software.

The micrographs developed of each of the three planes relative to the rolling direction were very useful in characterizing grain size and morphology of each alloyed system. Grain boundary size measurements have been completed in each plane to determine the amount of texturing present following the working and annealing processes as well as to establish the overall grain size within each respective alloy system.

Precipitates were characterized according to their size, distribution, density, morphology, and chemistry relative to the matrix. Micrographs of the three planes relative to the rolling direction of each alloyed system show the effect of cold working on precipitate distribution. In addition to EDS semi-quantitative analysis, the observed

precipitate densities are compared to precipitate models of each alloyed system to aid in determining whether or not they are carbides. JMat Pro thermodynamic models, performed at the Special Metals Corporation, were developed for precipitate density vs. temperature within each alloyed system based on chemical composition analysis. The lack of a platinum database for the JMat Pro program required the assumption that all platinum was equivalent to nickel. The similar electronic structure and electronegativity between platinum and nickel indicates that this assumption most likely introduces only limited error. Additionally, literature sources indicate that nickel and platinum are not major elements in carbide precipitates [19]. As mentioned above, JMat Pro plots show precipitate density as a function of temperature for each alloy. Therefore each alloy was analyzed at the 1050 °C (1925 °F) isotherm as this was the temperature at which each wrought material was annealed prior to water quenching.

Optically developed micrographs of each heat of material were examined for the presence of twinning in addition to the above mentioned characteristics. Qualitative twin boundary characteristics were observed to determine the effect of platinum concentration on twinning within each alloy system. Twin boundaries were also characterized according to their resemblance to either annealing or deformation twin appearance as such observations point to the possible crystal structure of the respective alloy systems.

Etching was performed on each material with the intention of adequately revealing the grain structure, twinned structures, as well as any precipitates that may have nucleated and coarsened. Some materials required longer etching times or stronger etchants to reveal such structures. Preliminary observations of each microstructure showed different levels of uniform surface darkening within certain regions as well as areas that did not etch at all. Consequently, the goals of the metallographic microstructural characterization of the alloy systems studied herein were extended to include the effects of platinum on increasing corrosion resistance.

6. Results

6.1. Alloy 800 HT

Optical micrographs of the unetched and etched microstructure of commercial Alloy 800 HT are shown in figures 6.1 and 6.2, respectively. These figures are provided for comparison with the Alloy 800 HT – Pt materials included herein. The calculated grain size of 280 microns for the commercial Alloy 800 HT material is also included for comparison with the measured values of the respective Alloy 800 HT – Pt materials.

6.1.1. Optical Micrographs of Wrought Structure

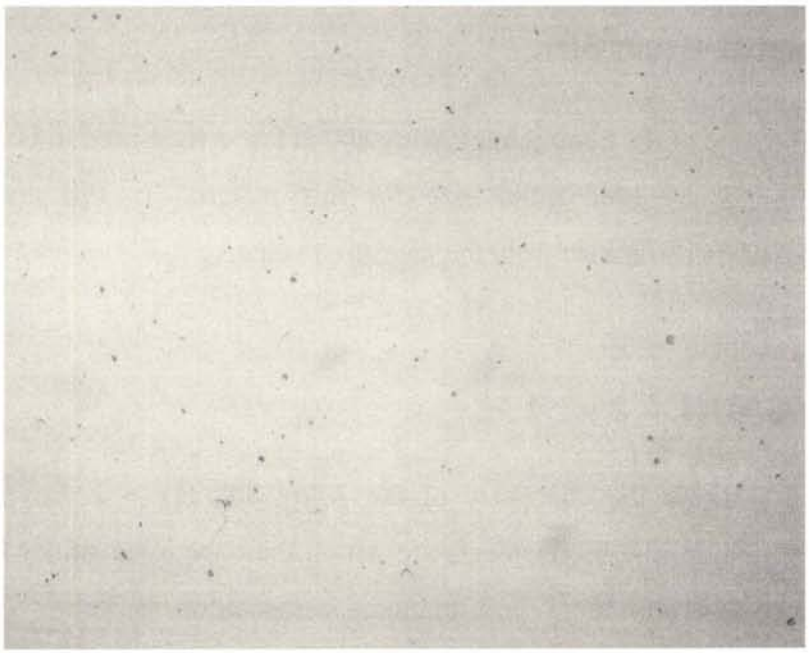

Fig 6.1: Precipitates within the microstructure of Alloy 800 HT, 100 X

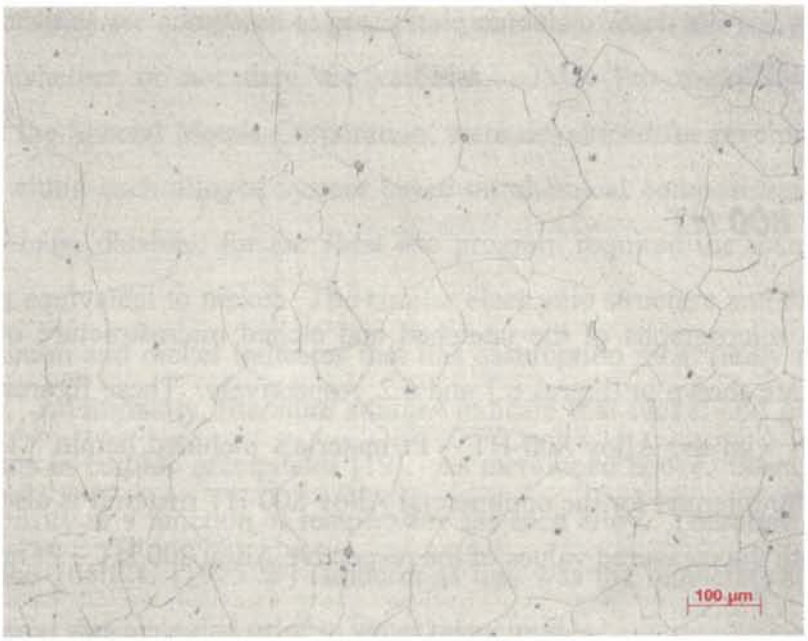

Fig 6.2: Grain and precipitate structure of commercial Alloy 800 HT, 100 X, glyceregia - 900 sec

6.1.2. Calculated Grain Size

The grain size of the commercial Alloy 800 HT was measured to be 280 microns. The manufacturer's specified grain size for this material is 190 microns, which corresponds to a 45 % difference from the measured value.

6.2. Alloy 800HT – 2 wt% Pt

Table 6.1 shows the chemistry of the Alloy 800 HT – 2 wt% Pt alloy and indicates that all major alloying elements are within their specified values for Alloy 800 HT. The combined aluminum and titanium composition is below the combined minimum value specified for Alloy 800 HT. The platinum concentration of 2.10% is nearly equal to the specified nominal composition. With the exception of carbon, all tramp and minor alloying elements are within their specified values. The carbon content of this alloy is 2.2 times higher than the maximum allowed carbon content of Alloy 800 HT. This is expected to result in extensive carbide precipitation.

Figure 6.3 shows the results of the JMat Pro thermodynamic model for this material. At 1050 °C (1925 °F) the Alloy 800 HT – 2 wt % microstructure is expected to have carbide compositions of 3% $M_{23}C_6$, 3% M_7C_3, and 1% MC. The remaining microstructure is predicted to be an austenite matrix.

Figure 6.4, a micrograph of the cast unetched microstructure at 200 X, shows a fine distribution of precipitates that are approximately 1 micron in diameter. Coarsened precipitates that are approximately 3 - 5 microns in diameter are also present. These larger precipitates have pulled slightly during mechanical polishing, which caused "comet tail" tracks through the matrix. This indicates that these precipitates are harder than the matrix. Figure 6.5, a micrograph of the same cast microstructure in the etched condition at 200 X, shows a large dendritic structure typical of cast alloys. The smaller precipitates observed in Figure 6.4 are found to be intra-dendritic in Figure 6.5.

Micrographs of the unetched wrought microstructure at 200 X are included for the xy rolling plane and the orthogonal xz and yz planes in figures 6.6 – 6.8. These micrographs show the same size and density of precipitate features as observed in figures 6.4 and 6.5; however, figures 6.6 – 6.8 show that the precipitates are strung out in the direction of rolling. Figures 6.9 – 6.11, which are optical micrographs of the etched microstructure at 200 X, show a uniform fine grain structure in each plane imaged relative to the plane of rolling. These micrographs reveal fine darkened intra-granular regions that may either be precipitates or pits formed during the etching process. Figures 6.12 – 6.14 are optical micrographs of the etched wrought structure at 500X. Figures 6.12 – 6.14 reveal the definite presence of inter-granular precipitates by higher magnification. Figure 6.14, in particular, shows strung inter-granular carbides that exhibit a pinning effect on the grain boundaries.

A problem associated with the etching procedure was that the grain structure could not be fully revealed without creating excessive etching artifacts. Figures 6.12 – 6.14 best exemplify the compromise that had to be made between adequately revealing the grain structure without causing excessive etching artifacts. Table 6.2 gives the calculated grain size for each of the three planes imaged above. Nearly equal grain sizes in each plane indicate a uniform grain structure throughout the microstructure. The average grain size of 22 microns is very small compared to the manufacturer's specified

grain size of 190 microns for the commercial specimen of Alloy 800 HT shown in Figure 6.2.

SEI mode scanning electron micrographs at 1300X and 3000 X are shown in figures 6.15 and 6.16, respectively. These micrographs clearly reveal topological features of the Alloy 800 HT – 2 wt% Pt material. Figures 6.15 and 6.16 show that etch induced pitting initiates on or around precipitate sites. Precipitates that have not pitted appear to be topographically raised from the matrix. Figure 6.17 shows that the raised precipitate structures from figure 6.16 have a slightly darker contrast than the matrix when imaged with backscatter electrons. This indicates that the raised precipitates viewed in SEI mode have a lower average atomic number. This is evidence that the precipitates are probably carbides. Figure 6.17 also shows very dark contrast in the corresponding pitted regions of Figure 6.16. These darkened regions do not indicate anything about composition. They are simply a result of deep pits relative to the matrix surface.

Figures 6.18 and 6.19 shows EDS analysis results of the matrix and raised precipitate features shown in figures 6.15 and 6.16, respectively. Figure 6.18 indicates relative peak heights consistent with the compositional analysis results reported in Table 6.1. Figure 6.19 shows a significantly higher chromium peak than Figure 6.18. This is a strong indication that the precipitates are $Cr_{23}C_6$ or Cr_7C_3 type carbides, especially in light of the JMat Pro precipitate model results and the typical composition of each type of carbide predicted by the model. The presence of other major alloying element peaks in Figure 6.19 can be explained by x-rays generated from the matrix surrounding the precipitates due to the 3 micron spot size.

6.2.1. Chemical Composition and JMat Pro Precipitate Model

Table 6.1			
Composition of Alloy 800 HT - 2 wt% Pt			
Element	**Wt %**	**Element**	**Wt%**
Carbon	0.222	Sulfur	0.003
Titanium	0.35	Iron	42.7
Aluminum	0.22	Copper	0.28
Chromium	19.9	Platinum	2.10
Manganese	0.77	Nickel	30.7
Silicon	0.20	Ref. [44]	

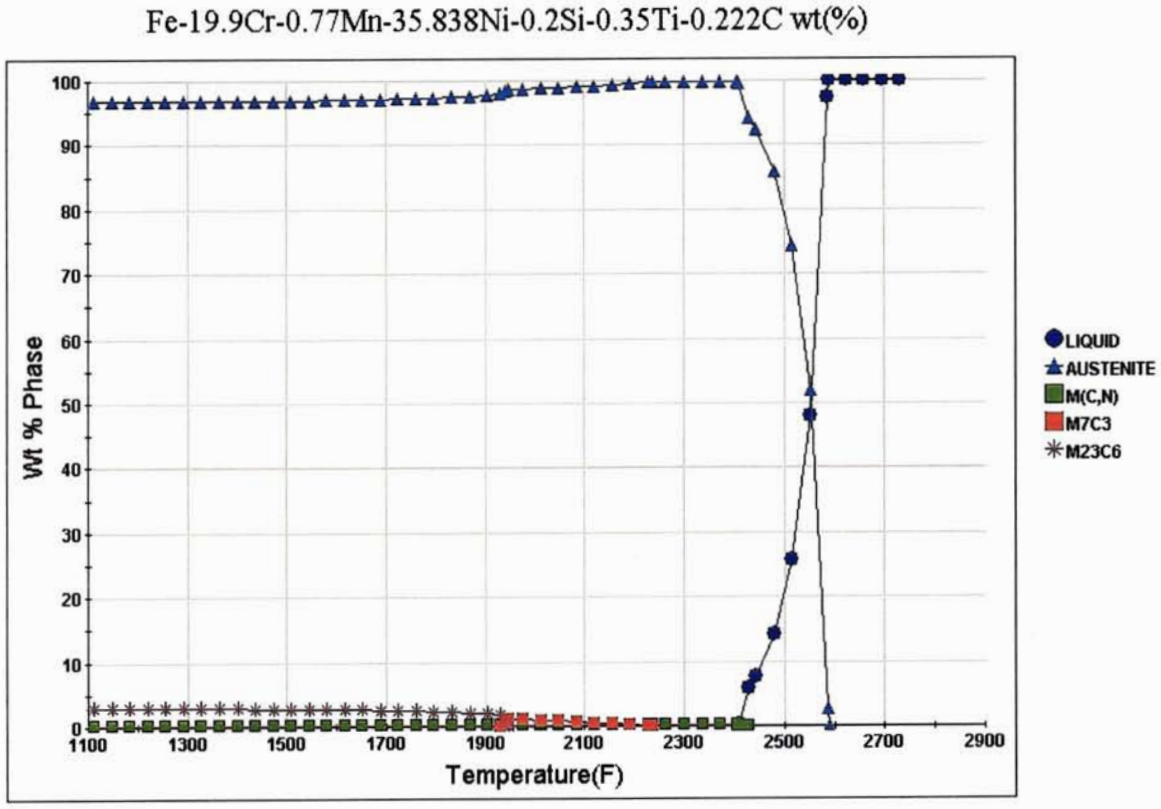

Fig 6.3: JMat Pro thermodynamic precipitate model for Alloy 800 HT – 2 wt% Pt alloyed system

6.2.2. Optical Micrographs of Cast Structure

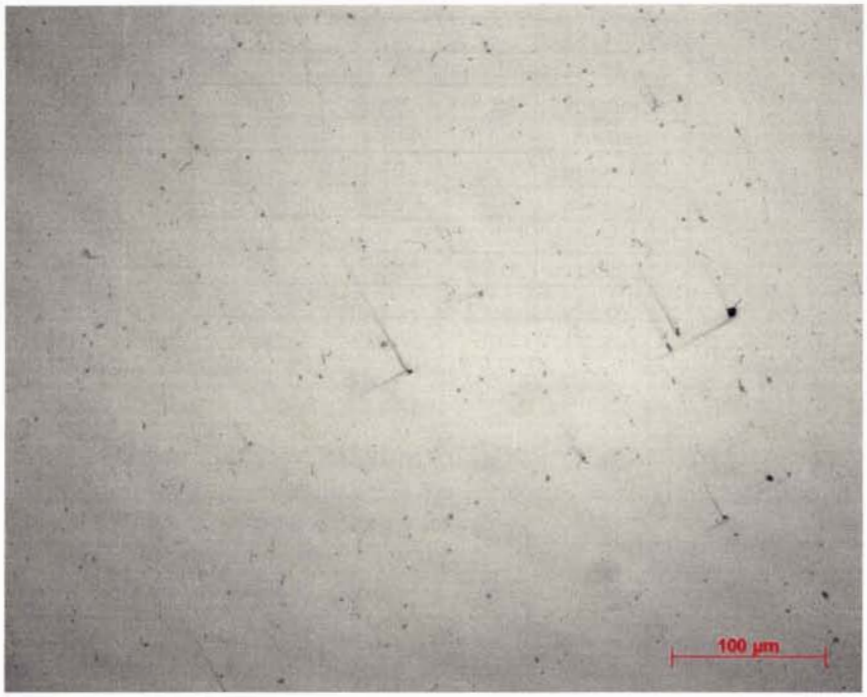

Fig 6.4: Precipitate features of cast Alloy 800 HT - 2 wt% Pt, 200 X

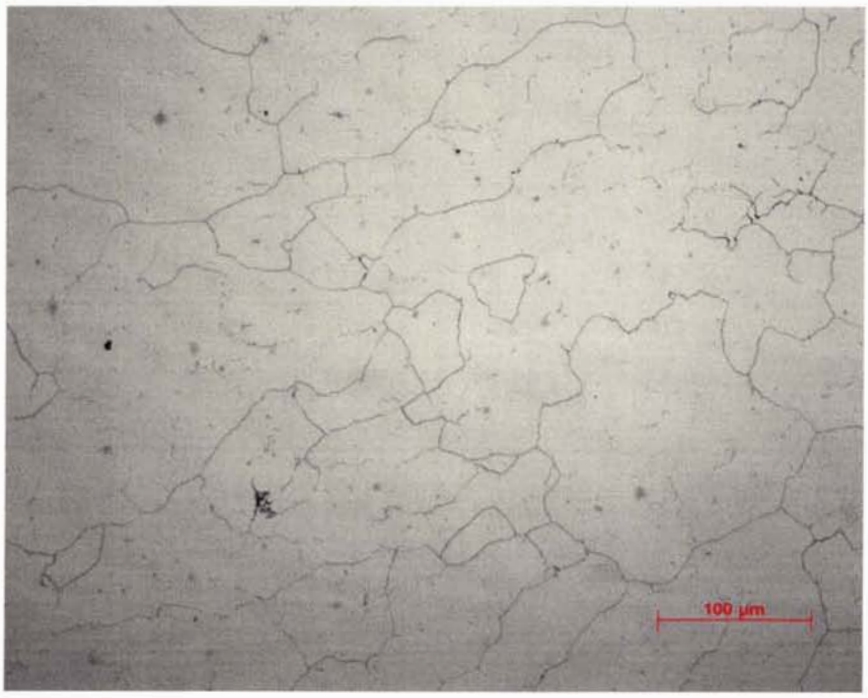

Fig 6.5: Dendrite and precipitate features of cast Alloy 800 HT - 2 wt% Pt, 200 X, weak glyceregia - 210 sec

6.2.3. Optical Micrographs of Wrought Structure

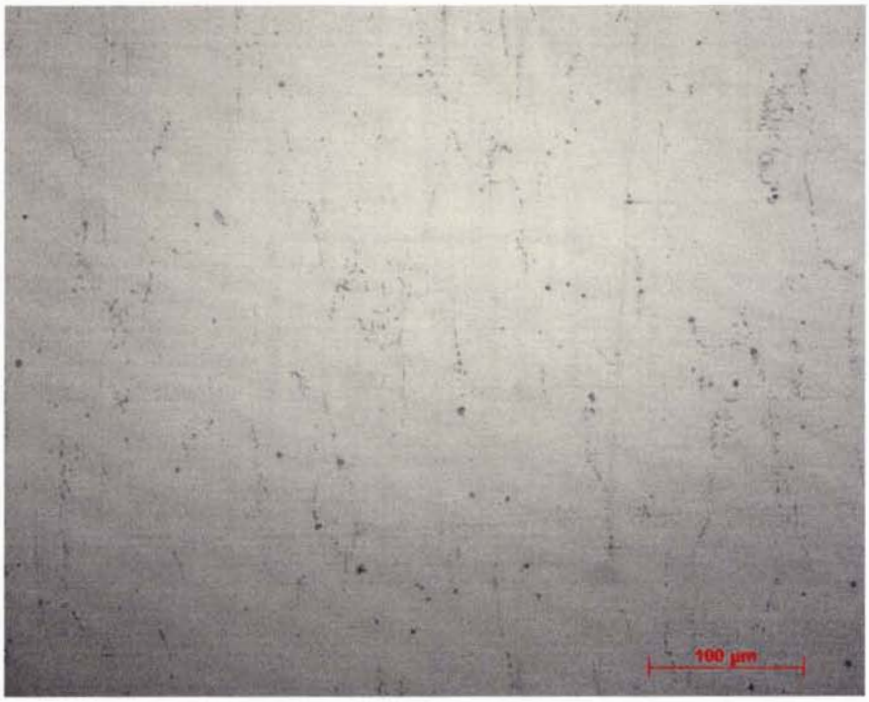

Fig 6.6: Precipitate features of wrought Alloy 800 HT – 2 wt% Pt, xy plane, 200 X

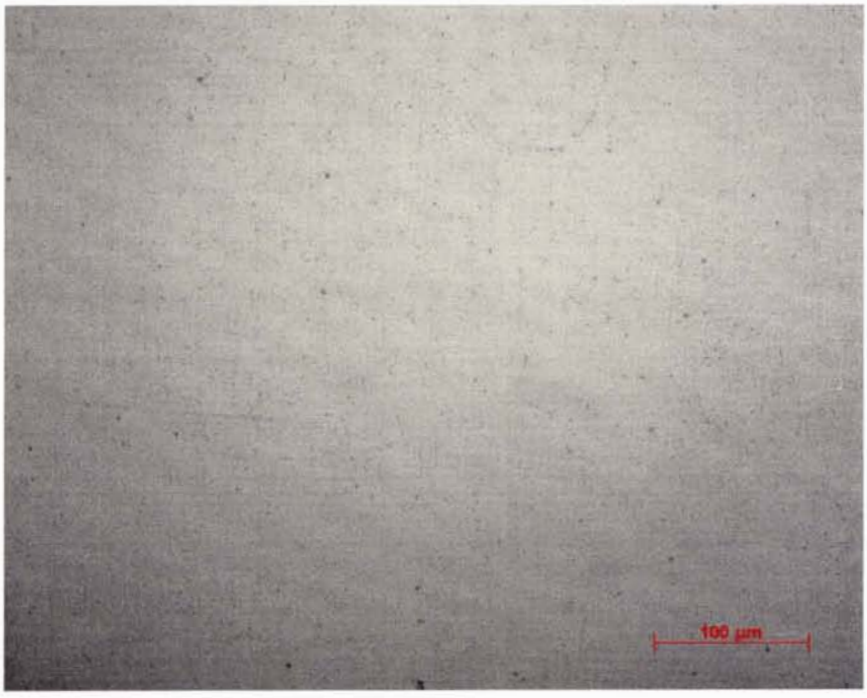

Fig 6.7: Precipitate features of wrought Alloy 800 HT – 2 wt% Pt, xz plane, 200 X

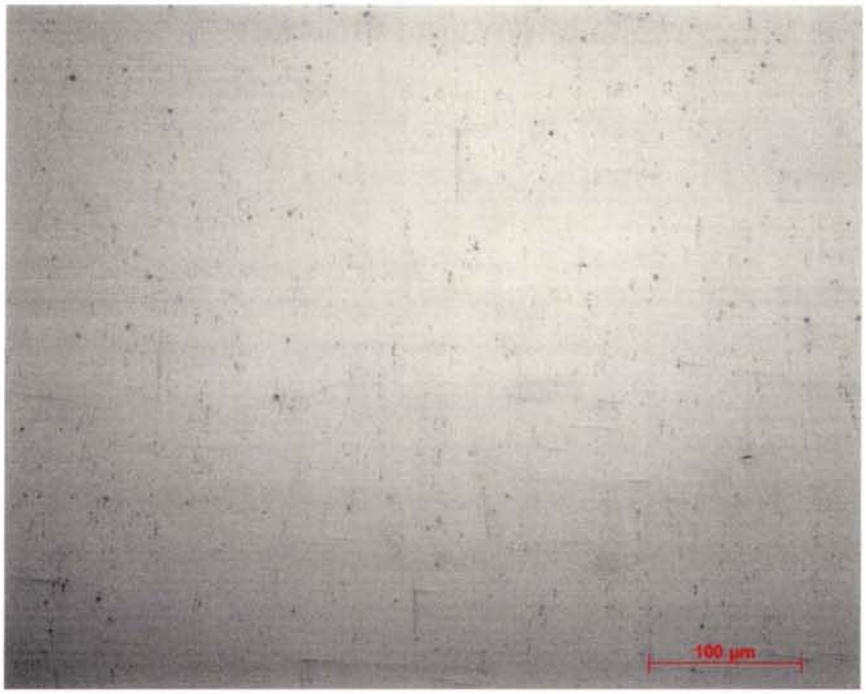

Fig 6.8: Precipitate features of wrought Alloy 800 HT - 2 wt% Pt, yz plane, 200 X

Fig 6.9: Precipitate features and grain structure of wrought Alloy 800 HT - 2 wt% Pt, xy plane, 200 X, Nital, 3 VDC - 6 sec, 1.5 VDC – 10 sec

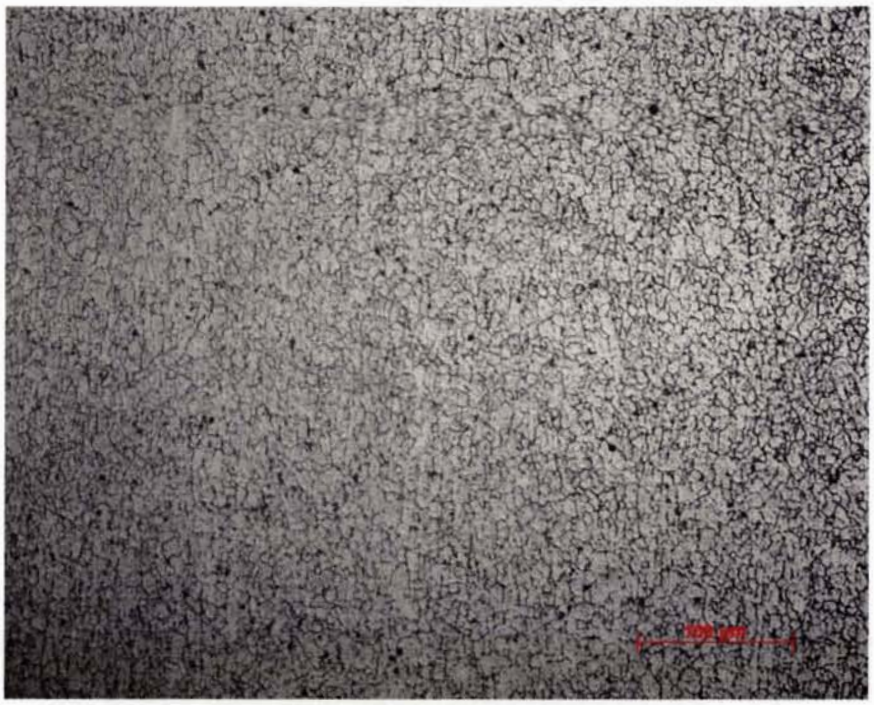

Fig 6.10: Precipitate features and grain structure of wrought Alloy 800 HT - 2 wt% Pt, xz plane, 200 X, Nital, 1.5 VDC - 8 sec

Fig 6.11: Precipitate features and grain structure of wrought Alloy 800 HT- 2 wt% Pt, yz plane, 200 X, Nital, 1.5 VDC - 4 sec

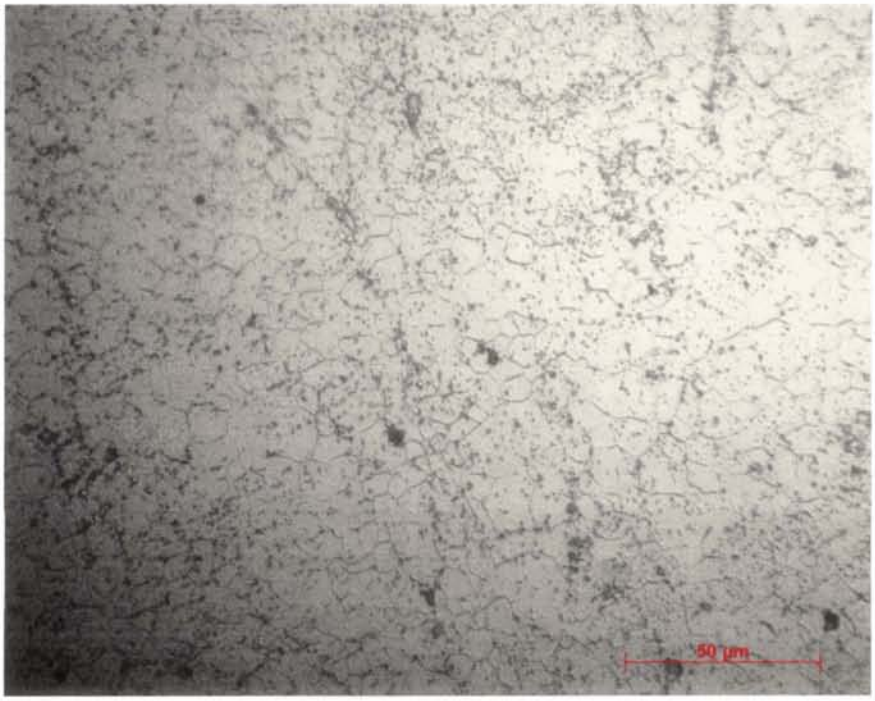

Fig 6.12: Precipitate features and grain structure wrought Alloy 800 HT - 2 wt% Pt, xy plane, 500 X, Nital, 3 VDC - 6 sec

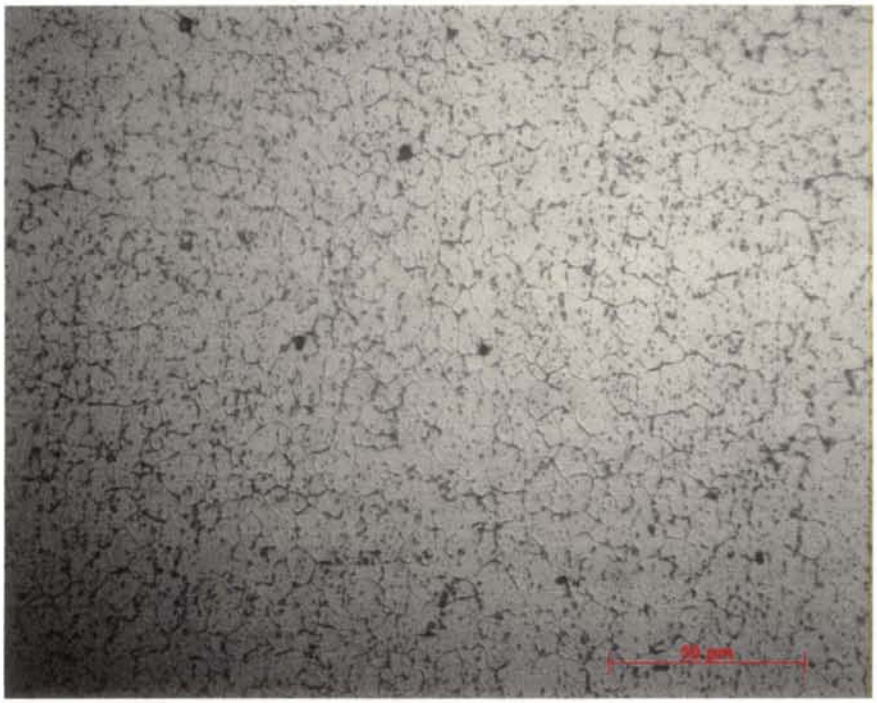

Fig 6.13: Precipitate features and grain structure of wrought Alloy 800 HT - 2 wt% Pt, xz plane, 500 X, Nital, 1.5 VDC - 8 sec

Fig 6.14: Precipitate features and grain structure of wrought Alloy 800 HT- 2 wt% Pt, yz plane, 500 X, Nital, 1.5 VDC - 4 sec

6.2.4. Calculated Grain Size

Table 6.2	
Calculated grain sizes for Alloy 800 HT - 2 Wt % Pt	
Plane	**Diameter (microns)**
xy	21
xz	22
yz	22
Average	**22**

6.2.5. Scanning Electron Micrographs of Wrought Structure

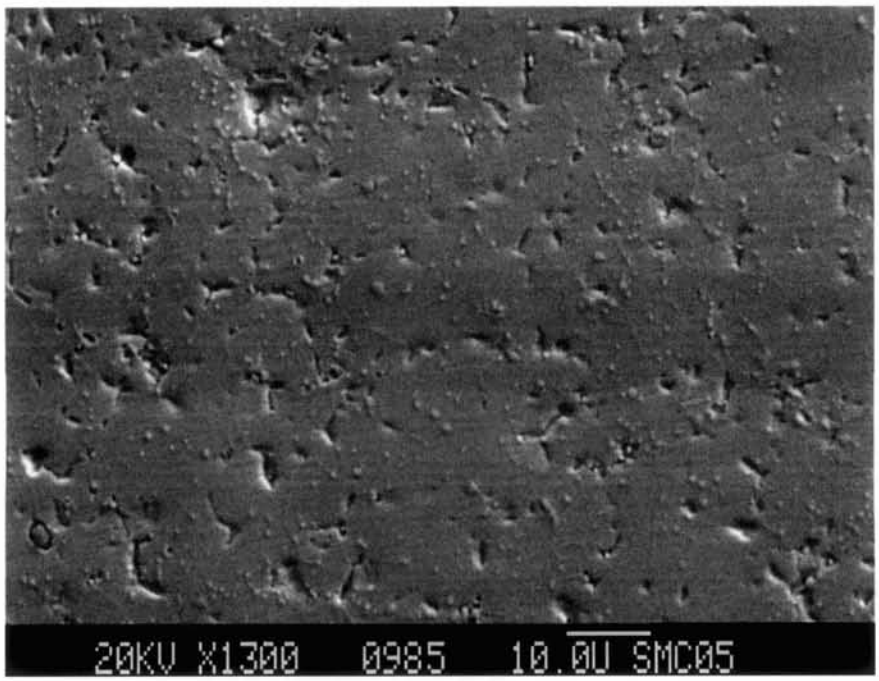

Fig 6.15: Pit sites and precipitate features of wrought Alloy 800 HT - 2 wt% Pt, Secondary Electron Image, 1300 X

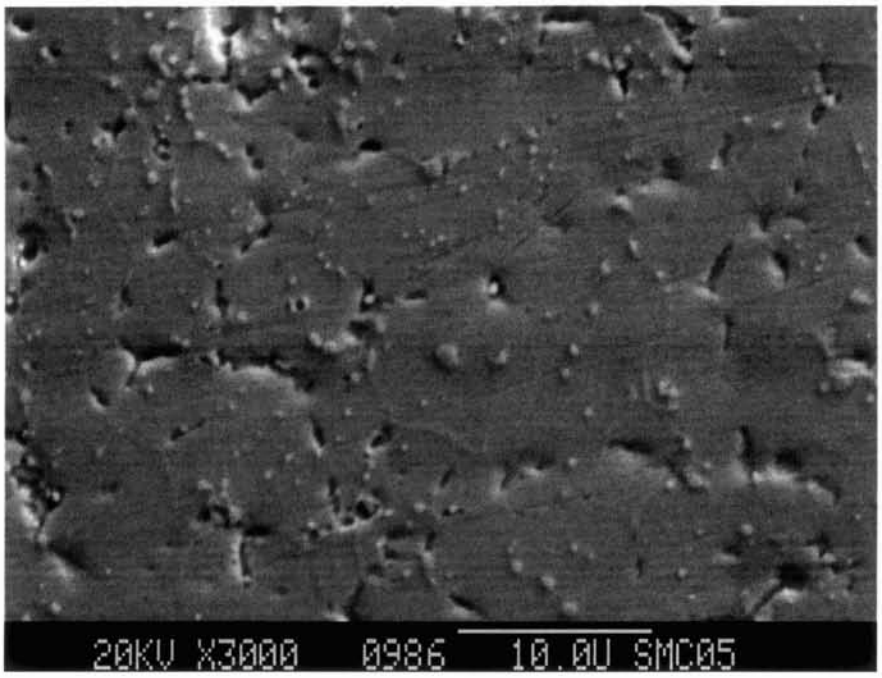

Fig 6.16: Pit sites and precipitate features of wrought Alloy 800 HT - 2 wt% Pt, Secondary Electron Image, 3000 X

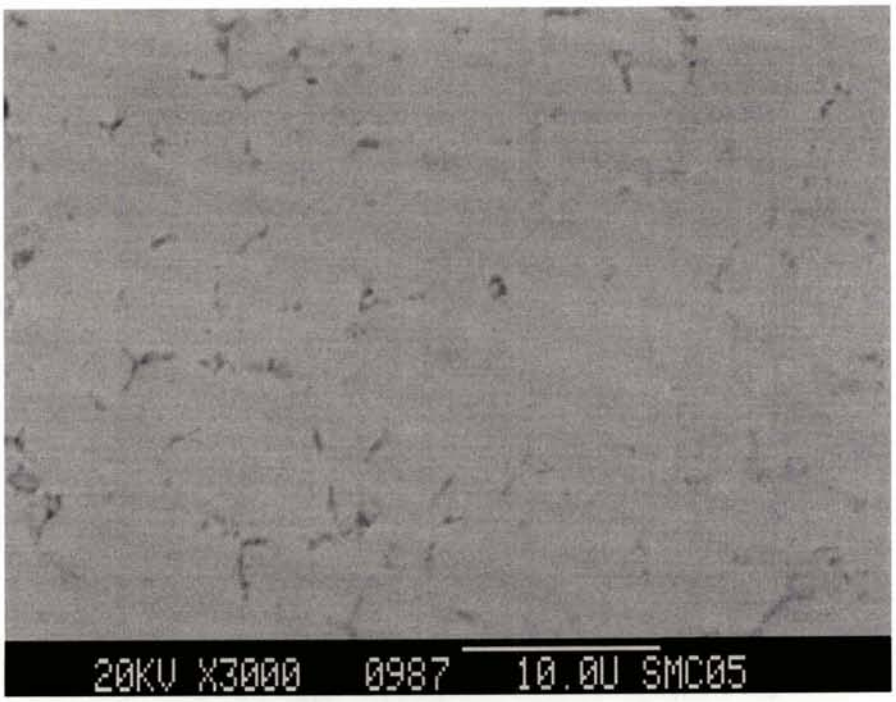

Fig 6.17: Slight contrast of precipitate features of wrought Alloy 800 HT - 2 wt% Pt, pits appear much darker than the matrix, Backscatter Electron Image, 3000 X

6.2.6. Electron Dispersive Spectrometry of Wrought Structure Features

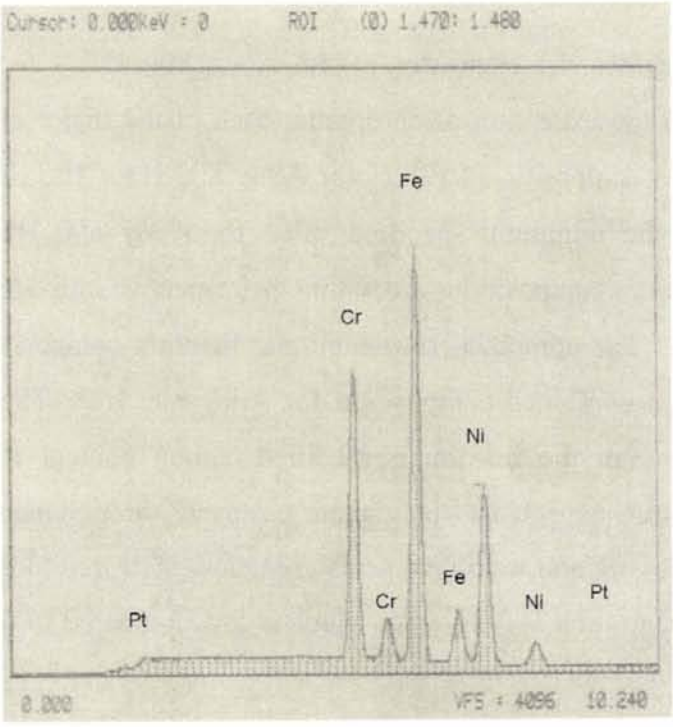

Fig 6.18: Element peak heights for matrix are consistent with compositional analysis of wrought Alloy 800 HT – 2 wt% Pt

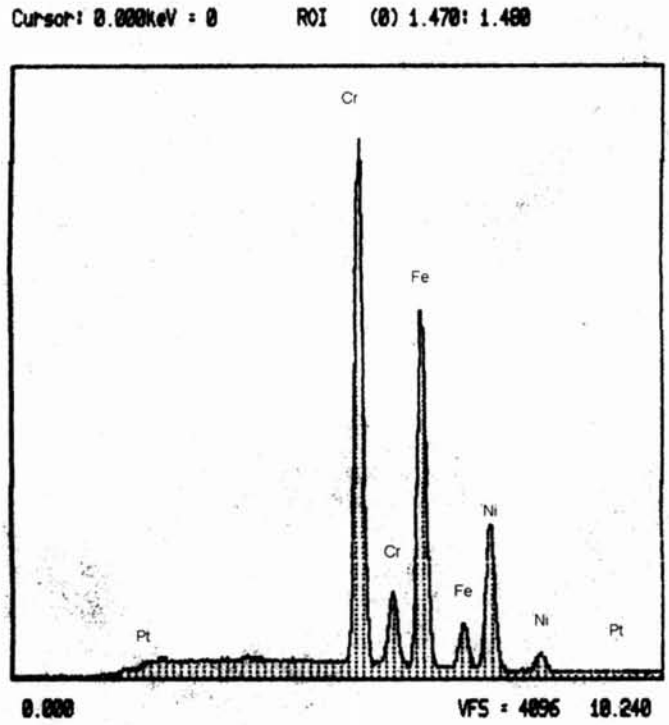

Fig 6.19: High chromium peak for precipitate in wrought Alloy 800 HT – 2 wt% Pt

6.3. *Alloy 800HT – 5 wt% Pt*

Table 6.3 shows the chemistry of the Alloy 800 HT – 5 wt% Pt alloy and indicates that, with the exception of chromium, each of the major alloying elements is within the specified compositional values for Alloy 800 HT. The chromium content is only 0.1% below the minimum specified value for Alloy 800 HT. The individual aluminum and titanium compositions are within the respective individual specified values for Alloy 800 HT. The combined aluminum and titanium compositions, however, are below the minimum combined composition for Alloy 800 HT. The carbon content is 2.02 times higher than the maximum specified carbon content for Alloy 800 HT. Carbides are therefore expected to precipitate profusely throughout the microstructure. All other minor alloying and tramp elements are below their minimum specified values. The platinum concentration is 4.29 wt%, which is low compared to the nominal desired composition of 5 wt%.

Figure 6.20 gives the results of the JMat Pro thermodynamic model for this material. At 1050 °C (1925 °F) the microstructure of the Alloy 800 HT – 5 wt% Pt system is predicted to be comprised of 2% M_3C_7 and 1% MC type carbides. The rest of the microstructure is predicted to be an austenite matrix

Figure 6.21, a micrograph of the cast unetched microstructure at 200 X, shows a fine distribution of precipitates that are approximately 1 micron in diameter. Coarsened precipitates with diameters of approximately 3 – 5 microns are also present. Very few of the precipitates appear to have pulled from the matrix during mechanical polishing. Figure 6.22, a micrograph of the same cast microstructure in the etched condition at 200 X, shows that all of the precipitates that formed during the casting process are intra-dendritic. The etched microstructure of the Alloy 800 HT – 5 wt% system has large dendritic boundaries characteristic of cast metal alloy microstructures.

Figures 6.22 – 6.24 are micrographs of the unetched wrought microstructures at 200 X in the xy, xz, and yz planes. These micrographs show the same precipitate features from the cast structure strung out in the direction of rolling. Figures 6.22 and 6.23, micrographs of the unetched microstructure in the xy and xz planes, show additional precipitate features. These precipitates are larger, blockier, and lighter in contrast than other precipitates. Additionally, these precipitates have pulled more from the matrix than others, which indicates that they are harder. From the above mentioned observations, it is likely that these precipitates are T, CN. T, CN are not expected to have a significant effect on the stability of the microstructure due to their large size, stability, and low volume fraction. Micrographs of the same wrought microstructures at 200 X in the etched condition are shown in figures 6.26 – 6.28. These micrographs are most beneficial in showing a uniform grain size in each plane relative to the direction of rolling. Figures 6.26 – 6.28 each reveal small intra-granular pits or precipitates that require further examination at higher magnification. Micrographs at 500 X, shown in figures 6.26 – 6.31, show the same intra-granular pits or precipitates viewed at 200 X in larger detail without revealing their true nature. Figure 6.29 reveals the presence of some annealing twins.

As in the case of Alloy 800 HT – 2 wt% Pt, grain boundaries could not be fully revealed without over-etching of the sample surface. Figures 6.29 – 6.31 show the

compromise that had to be made between adequately revealing the grain structure without over-etching. Table 6.4 indicates nearly equal grain size for each plane of the wrought microstructure imaged. The average grain size of 21 microns is very fine compared to the manufacturer's specified grain size of 190 microns of the commercial Alloy 800 HT material.

SEI mode scanning electron micrographs at 1300 X and 3000 X are shown in figures 6.32 and 6.33, respectively. These micrographs reveal topological features of the Alloy 800 HT – 5 wt% Pt material. Figures 6.32 and 6.33 show that pit formation initiated on or around precipitate sites as in the case of the Alloy 800 HT – 2 wt % Pt material. Precipitates that are not pitted appear to be topologically raised from the matrix. Figure 6.34, a BEI mode micrograph, only shows contrast difference between pitted features and the matrix. Figure 6.34, therefore, cannot be used to conclusively determine any elemental composition differences between the matrix and precipitates.

Figures 6.35 and 6.36 give EDS analysis results for the matrix and precipitates, respectively. Figure 6.35 shows peak heights consistent with the alloy composition reported in Table 6.3. Figure 6.36 shows a much higher chromium peak than Figure 6.35. In light of the JMat Pro precipitate model results discussed above and the typical composition of carbides and EDS analysis results, it is very likely that the precipitates are Cr_3C_7 type carbides. The presence of other major alloying element peaks in figure 6.36 can be explained by x-ray information reflected from the matrix around the precipitates due to a spot size of 3 microns.

6.3.1. Chemical Composition and JMat Pro Precipitate Model

Table 6.3			
Composition of Alloy 800 HT - 5 wt% Pt			
Element	**Wt %**	**Element**	**Wt%**
Carbon	0.202	Sulfur	0.004
Titanium	0.32	Iron	42.4
Aluminum	0.22	Copper	0.26
Chromium	18.9	Platinum	4.29
Manganese	0.73	Nickel	30.8
Silicon	0.18	Ref [44]	

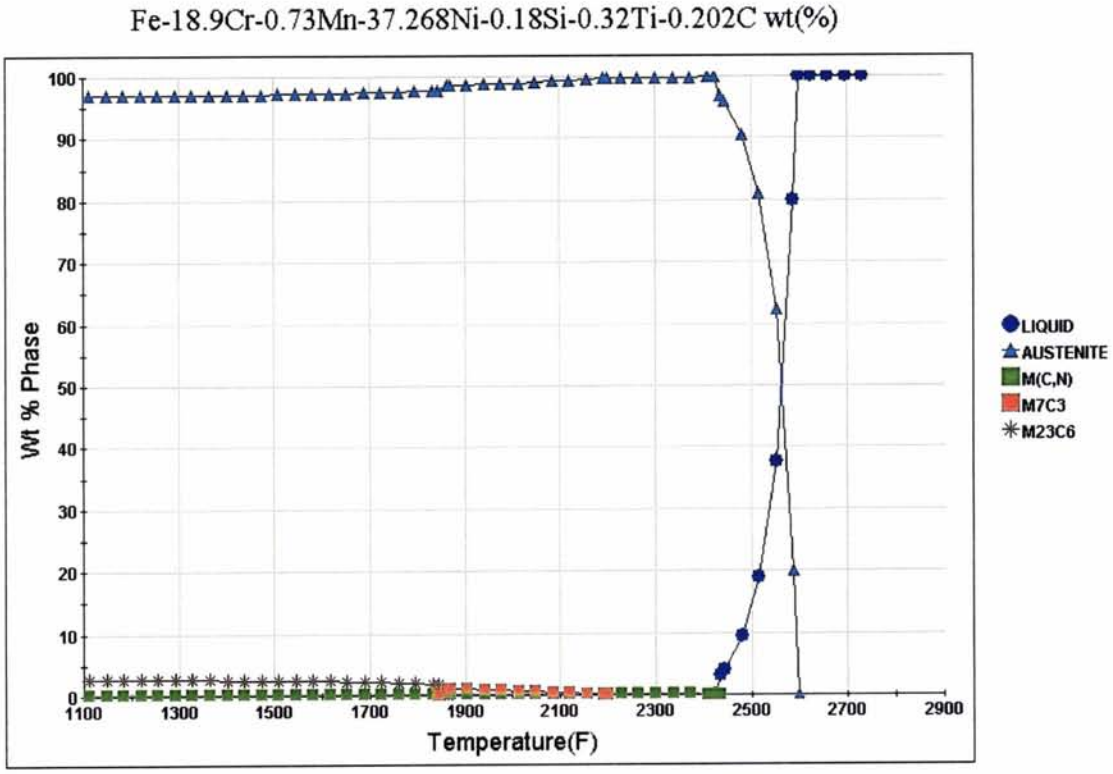

Fig 6.20: JMat Pro thermodynamic precipitate model for Alloy 800 HT – 5 wt% Pt alloyed system

6.3.2. Optical Micrographs of Cast Structure

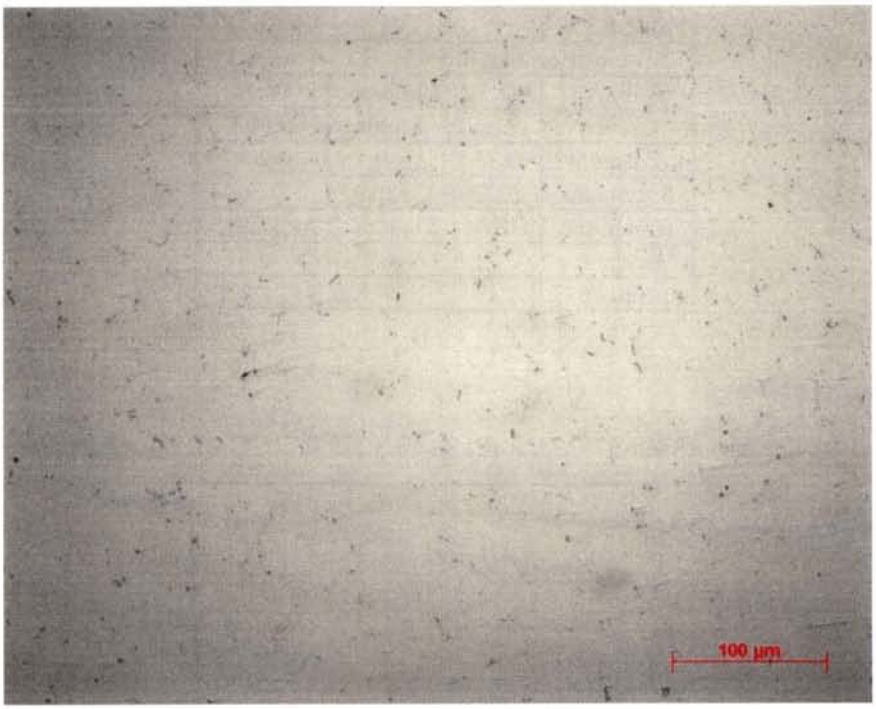

Fig 6.21: Precipitate features of cast Alloy 800 HT - 5 wt% Pt, 200 X

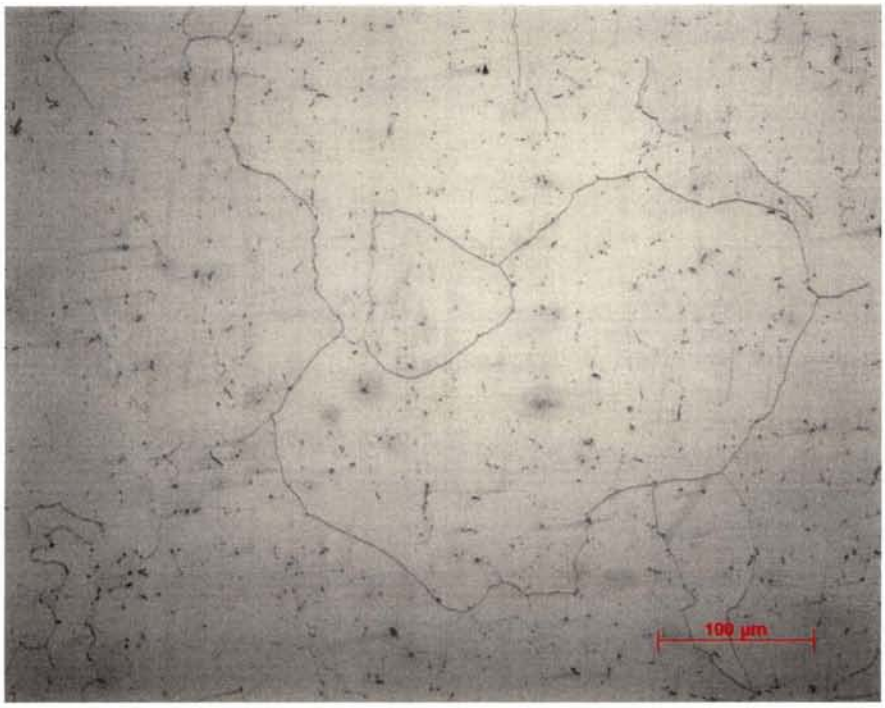

Fig 6.22: Dendrite and precipitate features of cast Alloy 800 HT - 5 wt% Pt, 200 X, weak glyceregia - 200 sec

6.3.3. Optical Micrographs of Wrought Structure

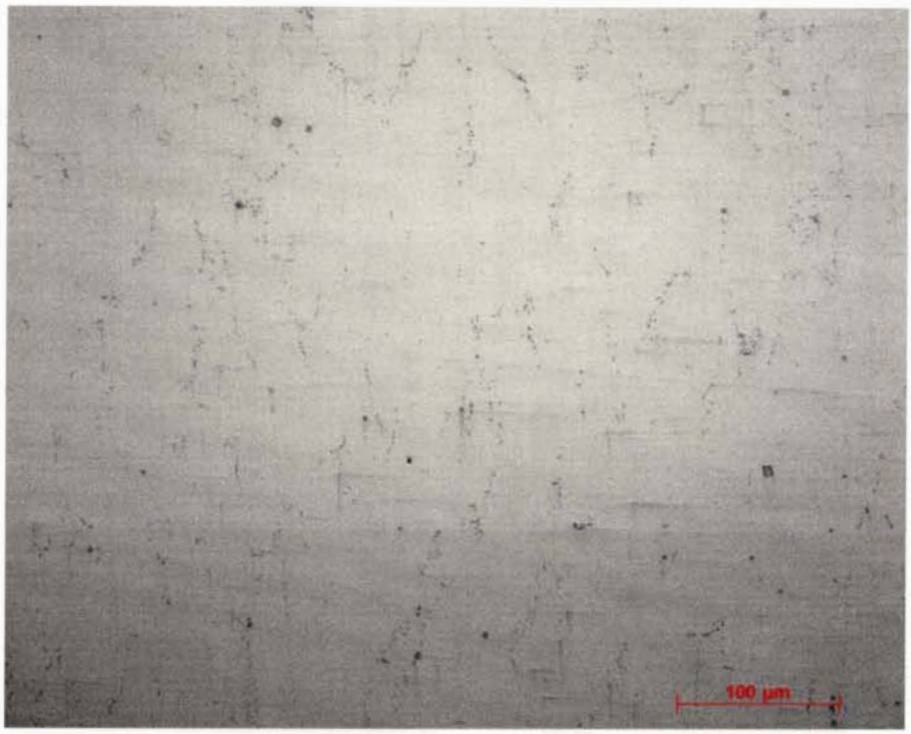

Fig 6.23: Precipitate features of wrought Alloy 800 HT – 5 wt% Pt, xy plane, 200 X

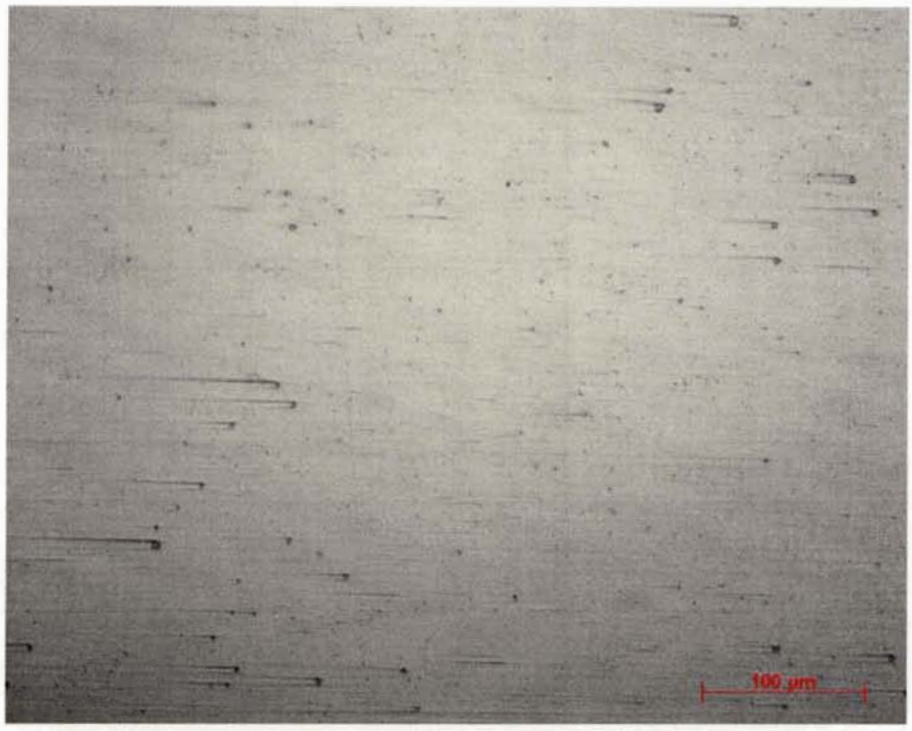

Fig 6.24: Precipitate features of wrought Alloy 800 HT – 5 wt% Pt, xz plane, 200 X

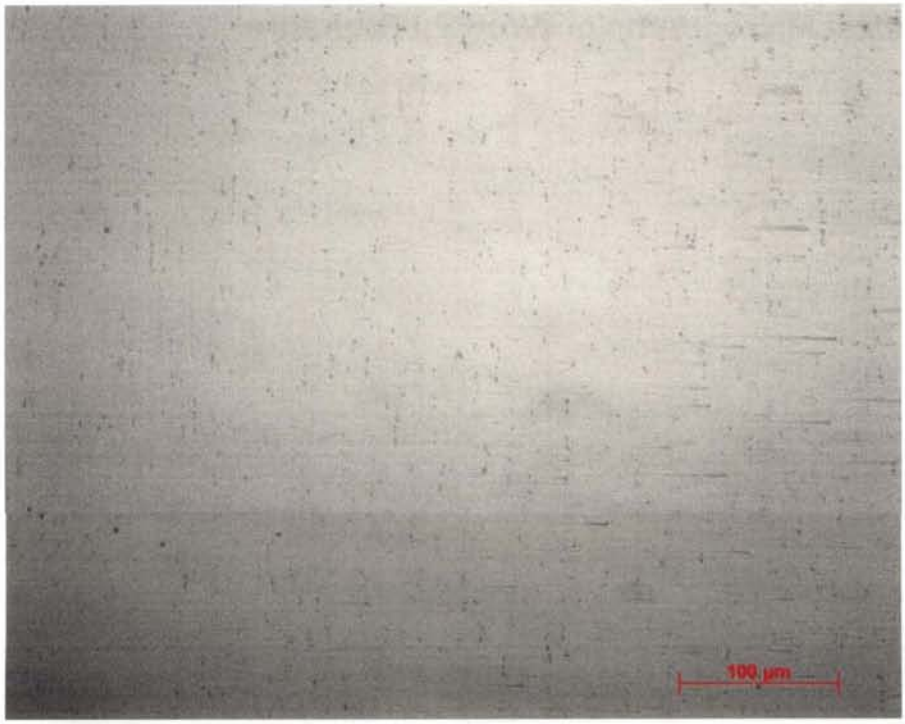

Fig 6.25: Precipitate features of wrought Alloy 800 HT – 5 wt% Pt, yz plane, 200 X

Fig 6.26: Precipitate features and grain structure of wrought Alloy 800 HT - 5 wt% Pt, xy plane, 200 X, Nital, 3 VDC - 6 sec

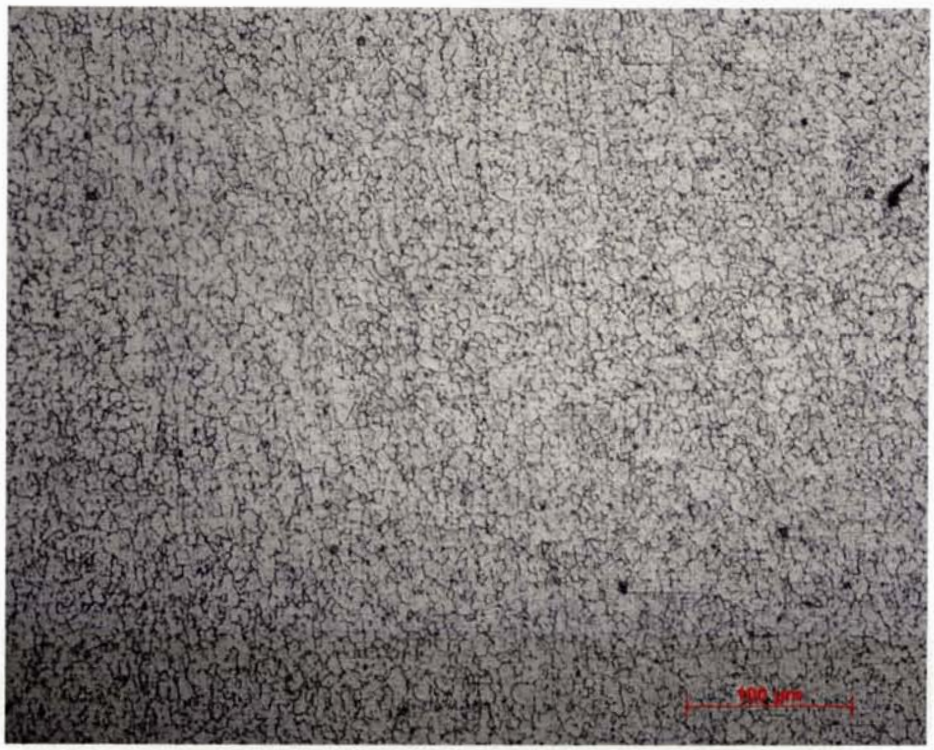

Fig 6.27: Precipitate features and grain structure of wrought Alloy 800 HT - 5 wt% Pt, xz plane, 200 X, Nital, 1.5 VDC - 5 sec

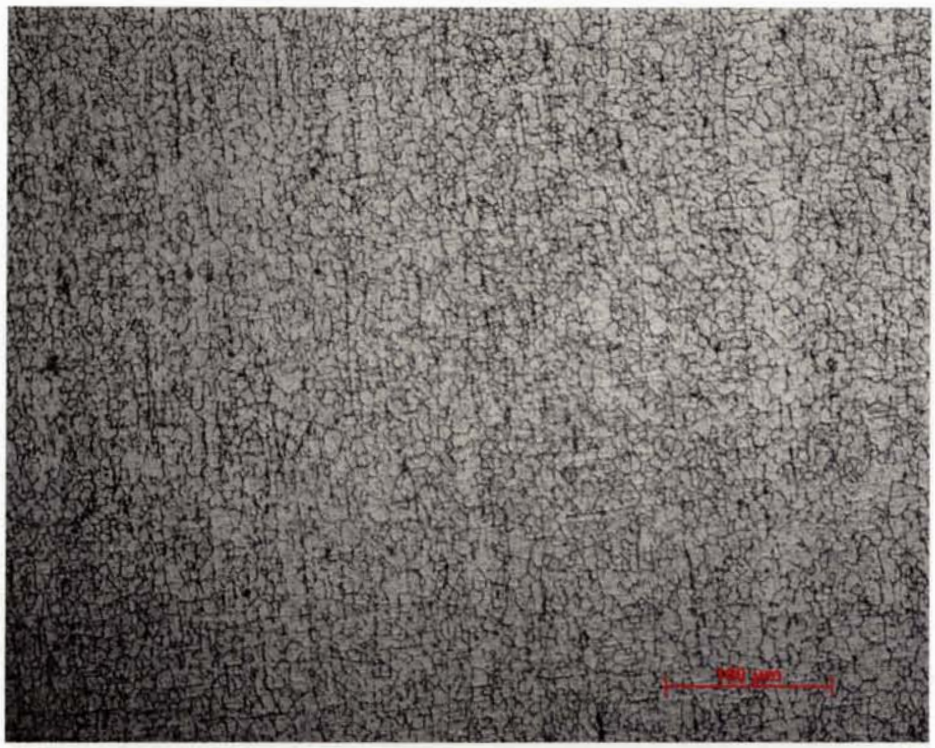

Fig 6.28: Precipitate features and grain structure of wrought Alloy 800 HT - 5 wt% Pt, yz plane, 200 X, Nital, 1.5 VDC - 5 sec

Fig 6.29: Precipitate features, annealing twins, and grain structure of wrought Alloy 800 HT - 5 wt% Pt, xy plane, 500 X, Nital, 3 VDC - 6 sec

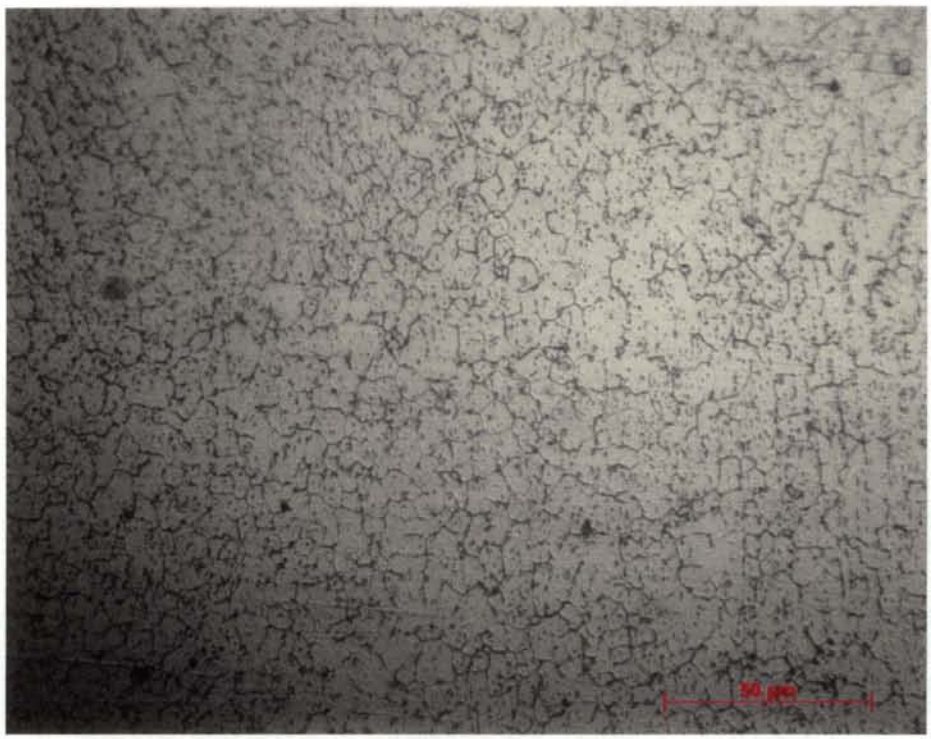

Fig 6.30: Precipitate features and grain structure of wrought Alloy 800 HT - 5 wt% Pt, xz plane, 500 X, Nital, 1.5 VDC - 5 sec

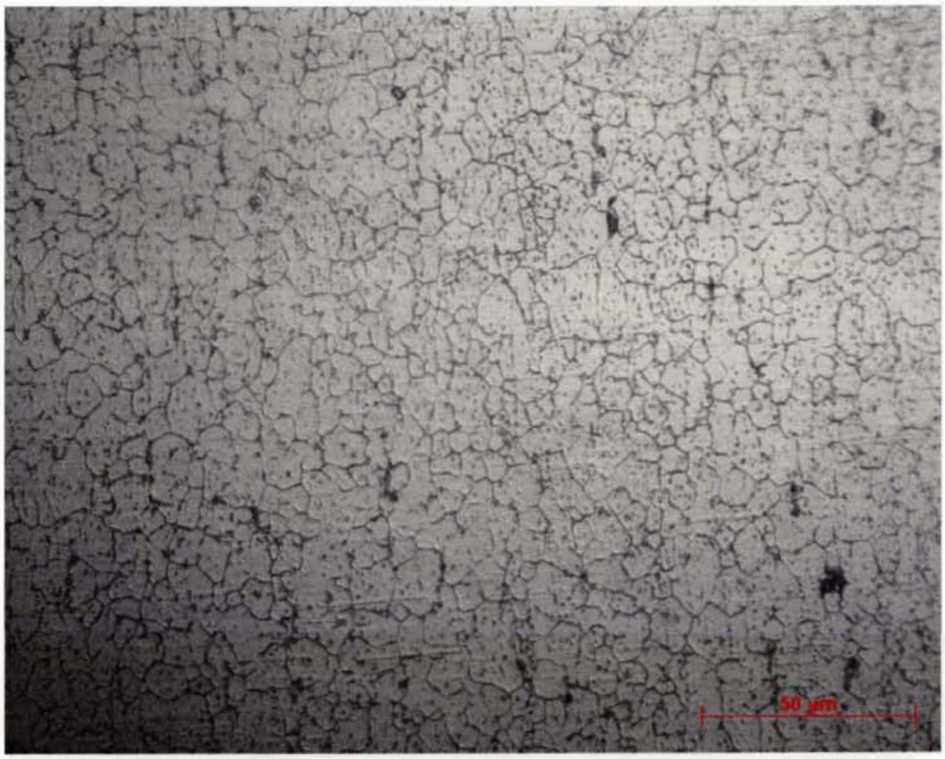

Fig 6.31: Precipitate features and grain structure of wrought Alloy 800 HT - 5 wt% Pt, yz plane, 500 X, Nital, 1.5 VDC - 5 sec

6.3.4. Calculated Grain Size

Table 6.4	
Calculated grain sizes for Alloy 800 HT - 5 Wt % Pt	
Plane	**Diameter (microns)**
xy	21
xz	22
yz	21
Average	**21**

6.3.5. Scanning Electron Micrographs of Wrought Structure

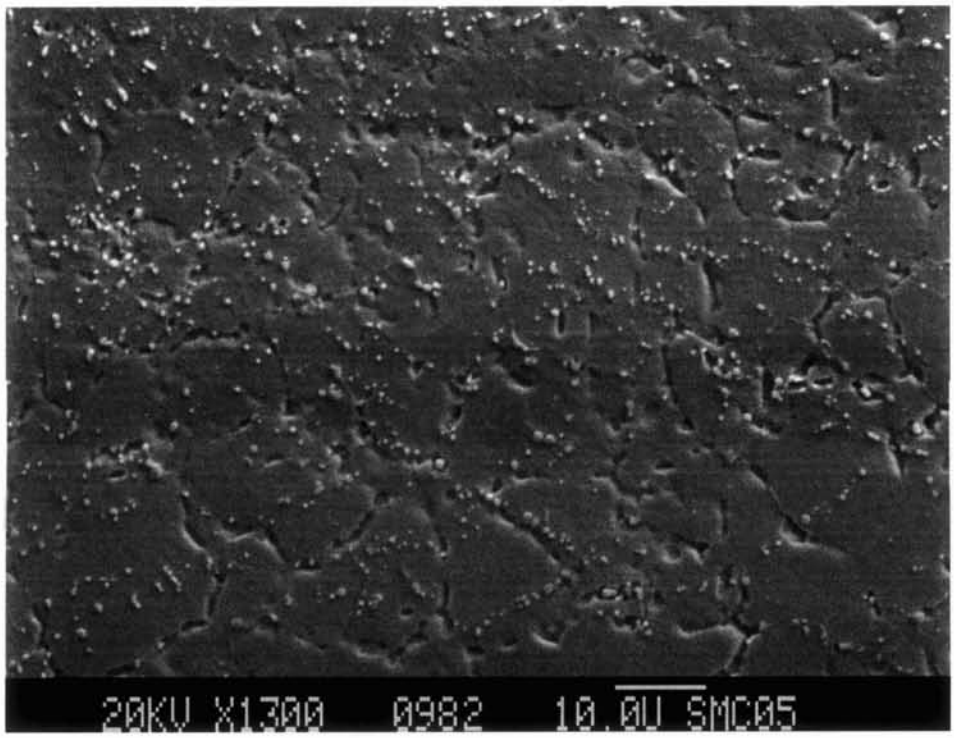

Fig 6.32: Pit sites and precipitate features of wrought Alloy 800 HT - 5 wt% Pt, Secondary Electron Image, 1300 X

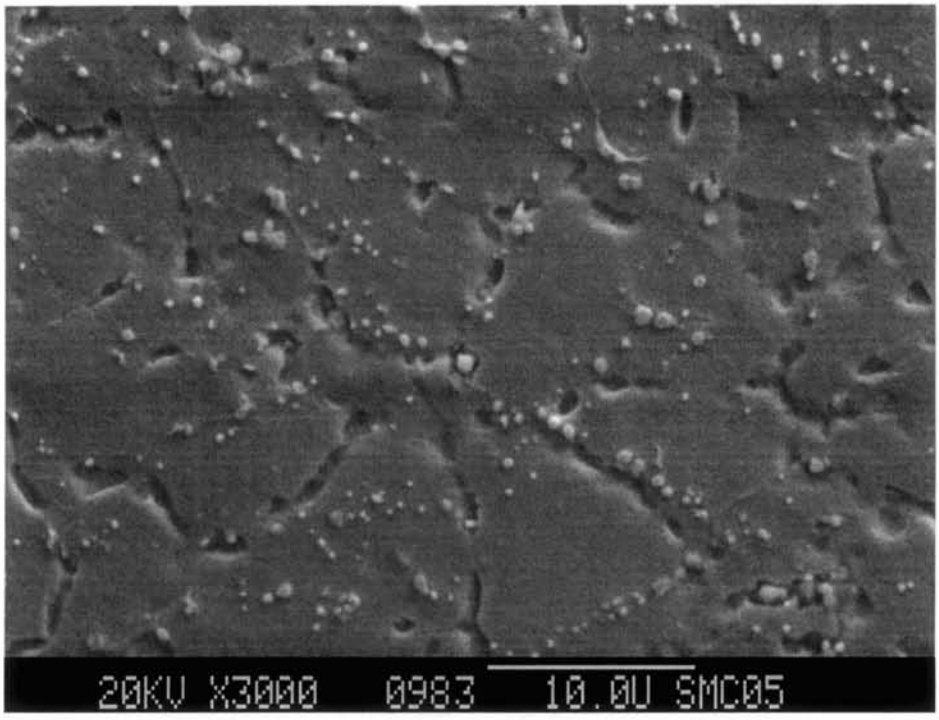

Fig 6.33: Pit sites and precipitate features of wrought Alloy 800 HT - 5 wt% Pt, Secondary Electron Image, 3000 X

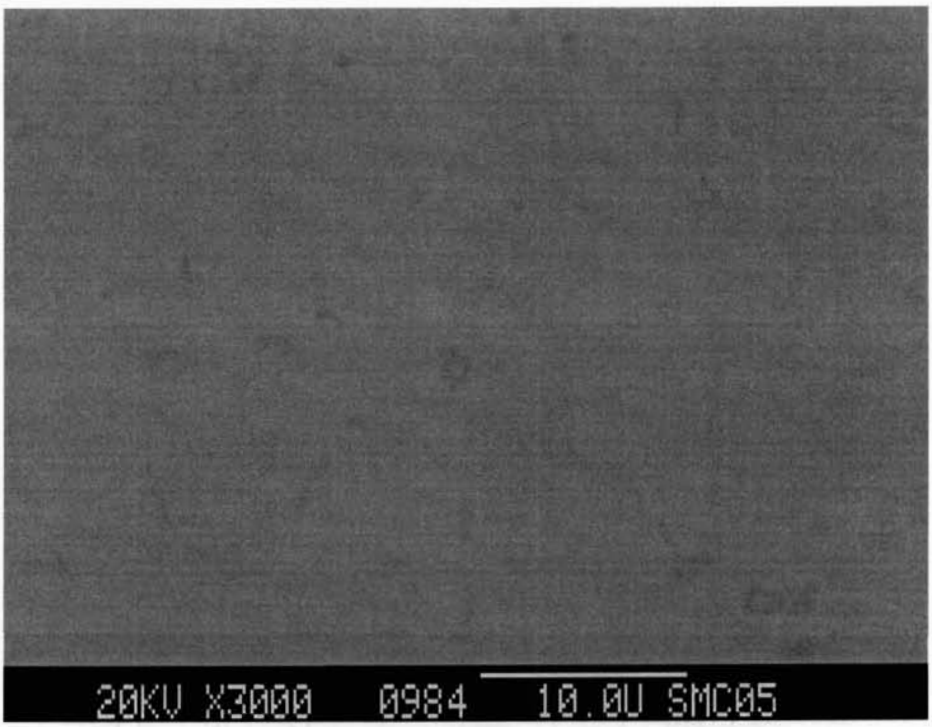

Fig 6.34: No contrast difference between precipitates and matrix for wrought Alloy 800 HT - 5 wt% Pt, slight contrast for pitted regions, Backscatter Electron Image, 3000 X

6.3.6. Electron Dispersive Spectrometry of Wrought Structure Features

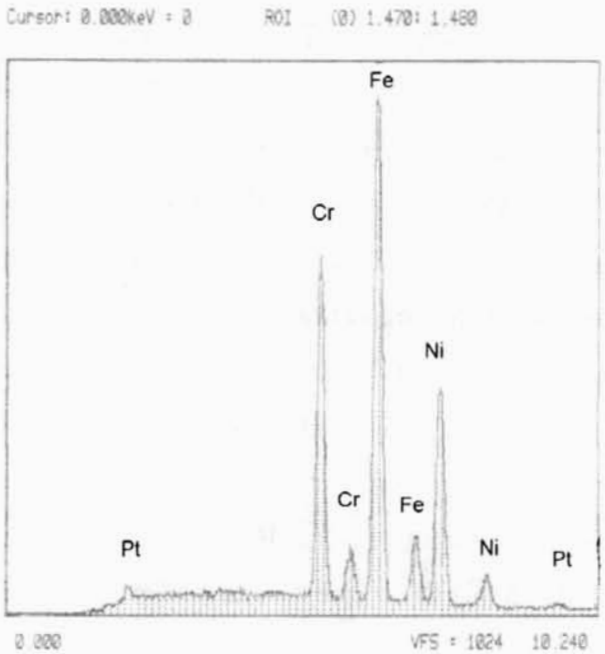

Fig 6.35: Element peak heights for matrix are consistent with compositional analysis of wrought Alloy 800 HT – 5 wt% Pt

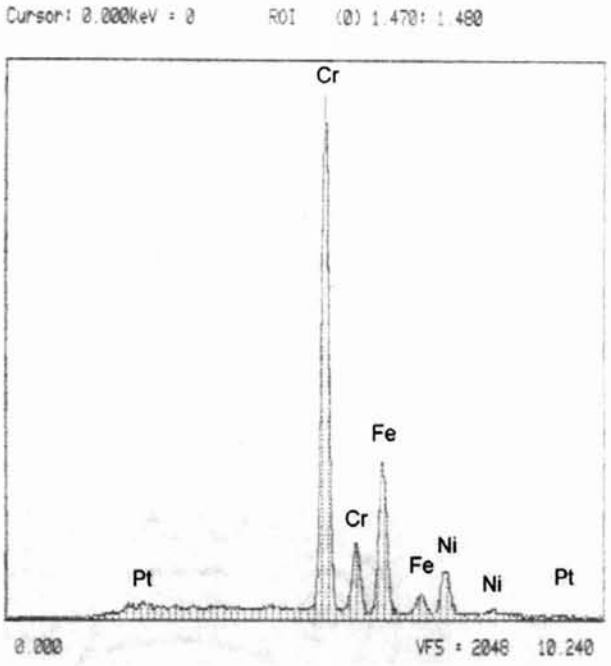

Fig 6.36: High chromium peak for precipitate in wrought Alloy 800 HT – 5 wt% Pt

6.4. *Alloy 800HT – 15 wt% Pt*

Table 6.5 shows the chemistry of the Alloy 800 HT – 15 wt% Pt alloy and indicates that the composition of each major alloying element is slightly lower than the specifications for commercial Alloy 800 HT. This discrepancy is expected considering that the platinum composition of the Alloy 800 HT – 15 wt% Pt system is reported as 13.5 wt%. Titanium and aluminum concentrations are each within the specified values for Alloy 800 HT. The combined composition of aluminum and titanium, however, is below the combined specified value for Alloy 800 HT. With the exception of carbon, all minor alloying and tramp elements are below their specified values. The carbon content of the Alloy 800 HT – 15 wt% Pt system is 1.71 times higher than the maximum specified value for Alloy 800 HT, which indicates that carbides should have precipitated profusely throughout the microstructure.

Figure 6.37 gives the results of the JMat Pro thermodynamic model for this material. At 1050 °C (1925 °F) the microstructure of the Alloy 800 HT – 15 wt% Pt

system is predicted to be comprised of approximately 1% M_3C_7 and less than 1% MC type carbides. The rest of the microstructure is predicted to be an austenite matrix

Figure 6.38, a micrograph of the cast unetched microstructure at 200 X, shows a fine distribution of 1 micron size precipitates. A more diffuse distribution of coarsened 3 – 5 micron size precipitates appear within the cast unetched microstructure as well. Figure 6.39, a micrograph of the cast microstructure in the etched condition, shows signs of preferential etching between large dendrites. Figure 6.39 reveals that some of the larger precipitates have pulled from the matrix during mechanical polishing. The "comet tail" tracks left behind by these pulled precipitates indicate that they are harder than the matrix.

Optical micrographs of the wrought unetched microstructure at 200 X are included for the xy, xz, and yz planes in figures 6.40 – 6.42. Figures 6.40 and 6.41, micrographs of the xy and xz planes, respectively, show that the precipitates have strung out in the direction of rolling. Figure 6.42, a micrograph of the xz plane, is not as useful for demonstrating the effects of rolling on precipitate orientation due to excessive polishing artifacts. Micrographs of the etched wrought structure at 200 X are shown in figures 6.43 – 6.45. These micrographs reveal a very different grain structure from the previously discussed alloys. At 200 X there appears to be significant contrast differences between individual grains. Micrographs of the wrought microstructure at 500 X, shown in figures 6.46 – 6.48, reveal significant annealing twin formation throughout the microstructure. The presence of annealing twins has a camouflaging effect on the grain structure.

The applied etching technique did not adequately reveal the grain structure via optical microscopy due to the camouflaging effect of annealing twins. Etching for times longer than those used to produce the optical micrographs shown above quickly causes a uniform darkening of the surface that shows very little microstructural detail. An example of an over-etched surface is shown in Figure B.42 of Appendix B. Table 6.6 indicates a nearly equal grain size in each plane of the microstructure imaged. The overall measured grain size was 25 microns, which again is very small compared to the manufacturer's specified grain size of 190 microns for the commercial Alloy 800 HT material.

Figure 6.46, an SEI mode scanning electron micrograph of the wrought microstructure at 3000 X, reveals the true grain structure that was not visible via optical microscopy. The presence of twinning is not as apparent with SEM microscopy. Figure 6.49 shows a decorated grain structure that appears to have a much smaller grain size than the measured value of 25 microns. A corresponding BEI mode micrograph shown in Figure 6.50 reveals the decorated grain boundaries with significantly lighter contrast than the matrix. Due to its higher atomic number compared to the other elements within the matrix, it is possible that a heavier element, such as platinum, segregated from the matrix to the grain boundaries. Segregation of platinum in the form of discrete precipitation on grain boundaries, however, is highly unlikely. If the platinum had exceeded the solubility limit within the base Alloy 800 HT chemistry, either grain boundaries would have become enriched or a second phase would have precipitated intra-granularly. Figure 6.49 shows the presence of profusely distributed 0.1 – 1 micron size intra-granular precipitates within the wrought microstructure. Backscatter imaging of these precipitates indicates a different composition from the matrix due to contrast differences.

Figures 6.51 - 6.53 show the results of EDS analysis performed on the matrix, the grain boundaries and precipitates, respectively. Figure 6.51 shows elemental peak heights within the matrix that are consistent with the composition of the alloy chemistry reported in Table 6.5. Figures 6.52 and 6.53 show a nearly equal spectrum to the matrix. These poor results can only be attributed to the fact that the effective EDS spot size of 3 microns is much larger than any grain boundary or precipitate region that could be analyzed.

6.4.1. Chemical Composition and JMat Pro Precipitate Model

Table 6.5			
Composition of Alloy 800 HT - 15 wt% Pt			
Element	**Wt %**	**Element**	**Wt%**
Carbon	0.171	Sulfur	0.004
Titanium	0.32	Iron	38.3
Aluminum	0.20	Copper	0.18
Chromium	18.5	Platinum	13.5
Manganese	0.72	Nickel	27.5
Silicon	0.14	Ref [44]	

Fe-18.5Cr-0.72Mn-41.649Ni-0.14Si-0.32Ti-0.171C wt(%)

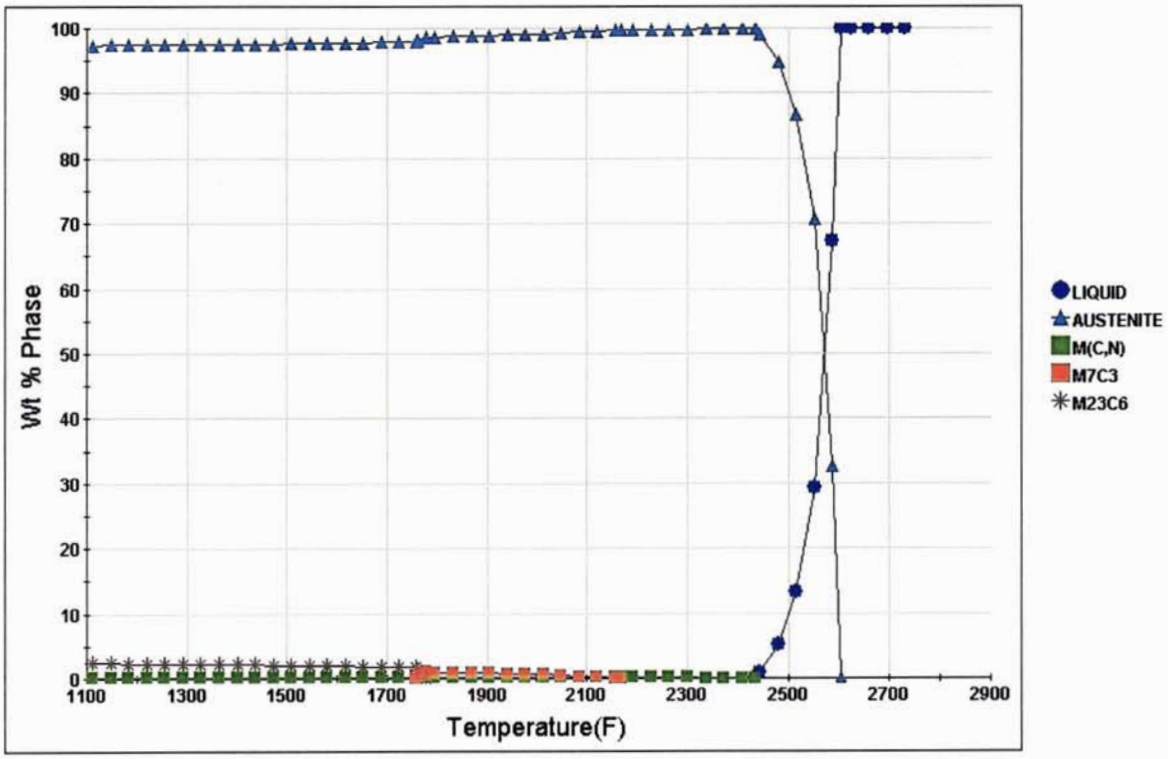

Fig 6.37: JMat Pro thermodynamic precipitate model for Alloy 800 HT – 15 wt% Pt alloyed system

6.4.2. Optical Micrographs of Cast Structure

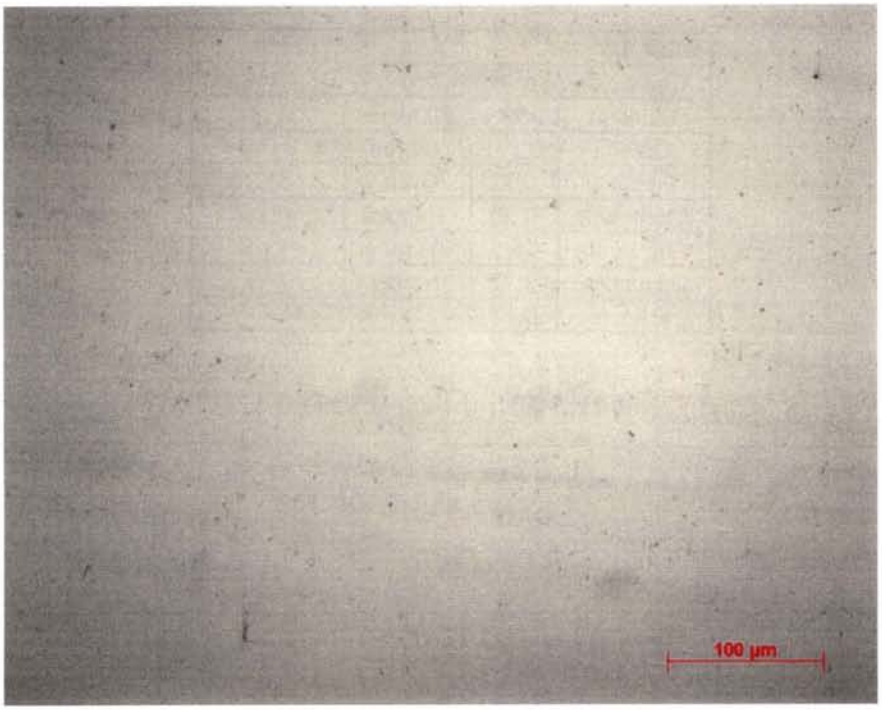

Fig 6.38: Precipitate features of cast Alloy 800 HT - 15 wt% Pt, 200 X

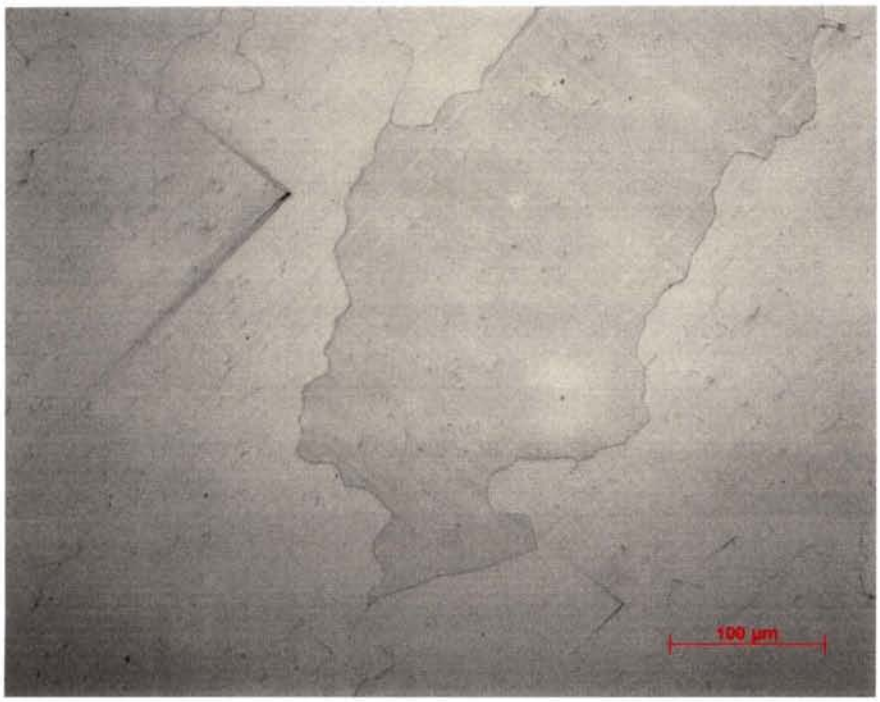

Fig 6.39: Dendrite and precipitate features of cast Alloy 800 HT - 15 wt% Pt, 200 X, weak glyceregia - 510 sec

6.4.3. Optical Micrographs of Wrought Structure

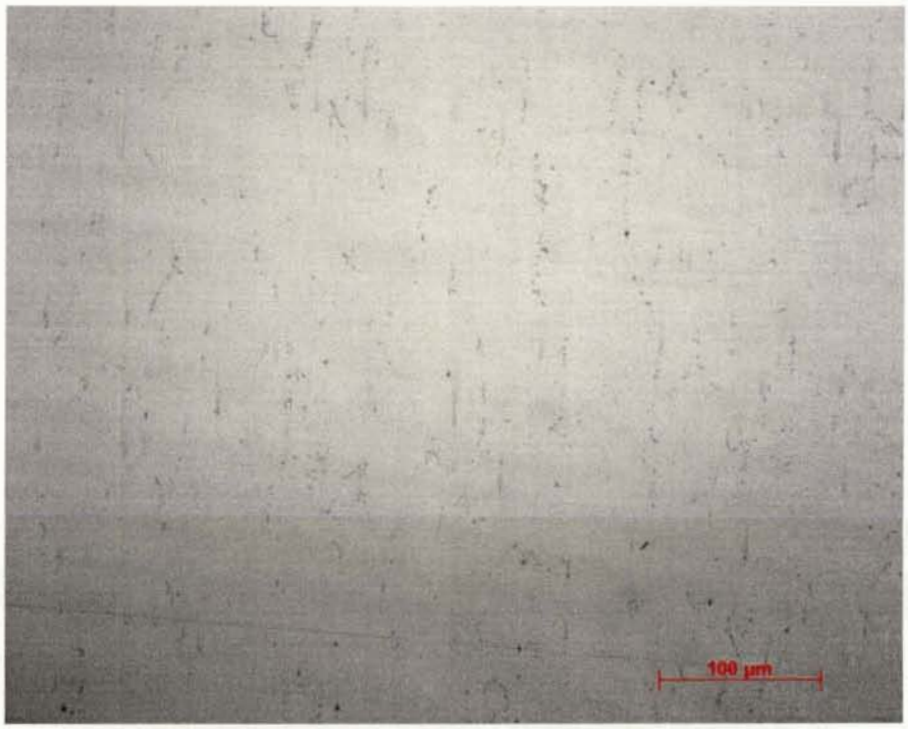

Fig 6.40: Precipitate features of wrought Alloy 800 HT – 15 wt% Pt, xy plane, 200 X

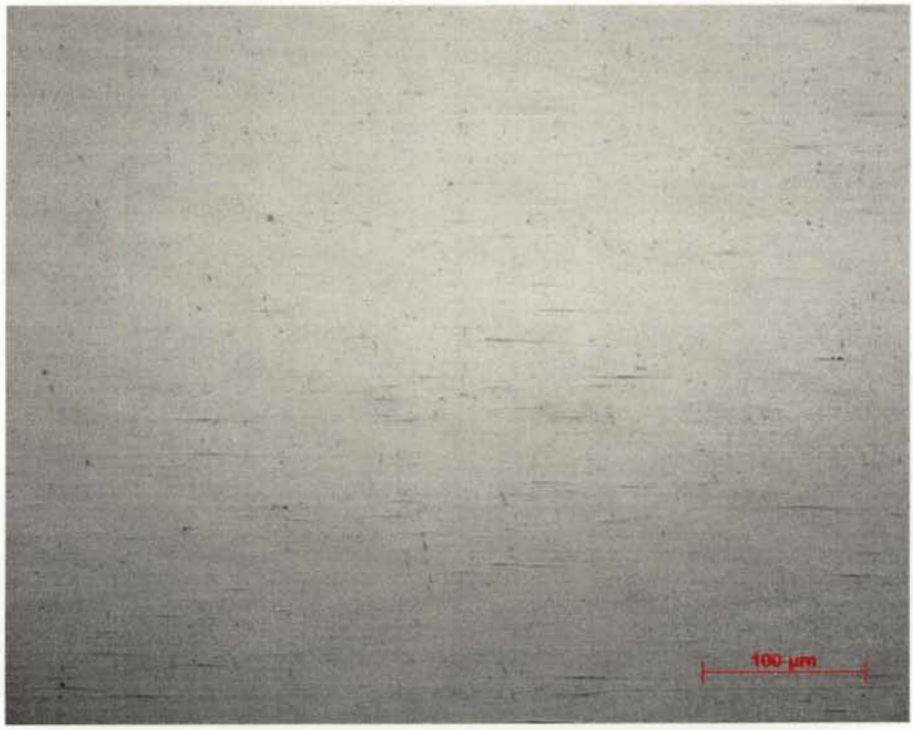

Fig 6.41: Precipitate features of wrought Alloy 800 HT – 15 wt% Pt, xz plane, 200 X

Fig 6.42: Precipitate features of wrought Alloy 800 HT – 15 wt% Pt, yz plane, 200 X

Fig 6.43: Precipitate features and grain structure of wrought Alloy 800 HT - 15 wt% Pt, xy plane, 200 X, Nital, 3 VDC - 5 sec

Fig 6.44: Precipitate features and grain structure of wrought Alloy 800 HT - 15 wt% Pt, xz plane, 200 X, Nital, 1.5 VDC - 4 sec

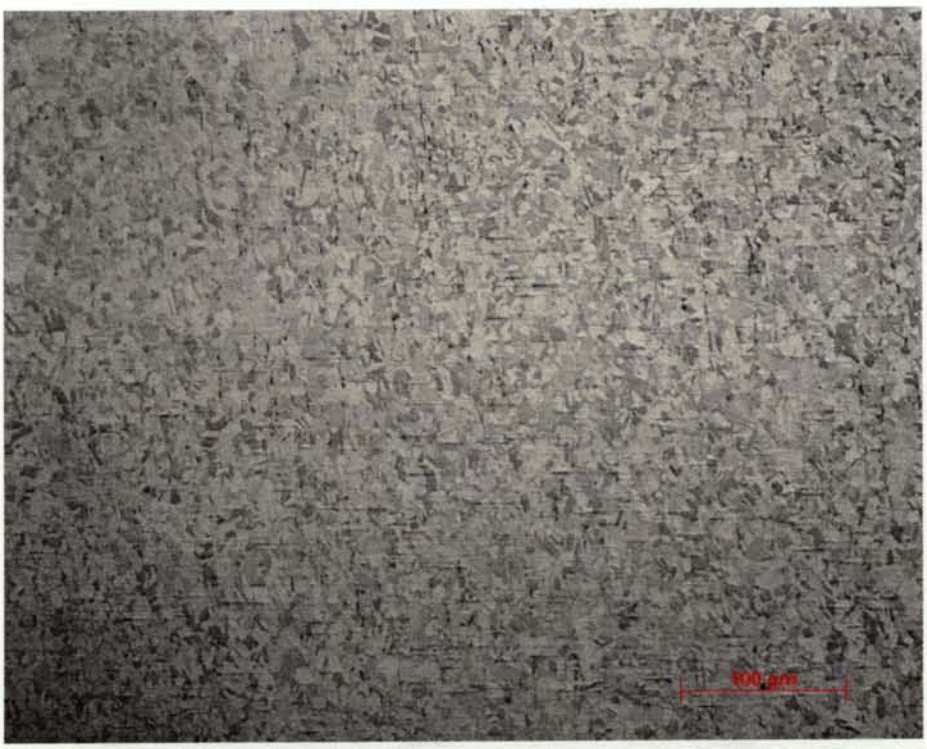

Fig 6.45: Precipitate features and grain structure of wrought Alloy 800 HT - 15 wt% Pt, yz plane, 200 X, Nital, 1.5 VDC - 4 sec

Fig 6.46: Precipitate features, annealing twins, and grain structure of wrought Alloy 800 HT - 15 wt% Pt, xy plane, 500 X, Nital, 3 VDC - 5 sec

Fig 6.47: Precipitate features, annealing twins, and grain structure of wrought Alloy 800 HT - 15 wt% Pt, xz plane, 500 X, Nital, 1.5 VDC - 4 sec

Fig 6.48: Precipitate features, annealing twins, and grain structure of wrought Alloy 800 HT - 15 wt% Pt, yz plane, 500 X, Nital, 1.5 VDC - 4 sec

6.4.4. Calculated Grain Size

Table 6.6	
Calculated grain sizes for Alloy 800 HT - 15 Wt % Pt	
Plane	**Diameter (microns)**
xy	26
xz	24
yz	24
Average	**25**

6.4.5. Scanning Electron Micrographs of Wrought Structure

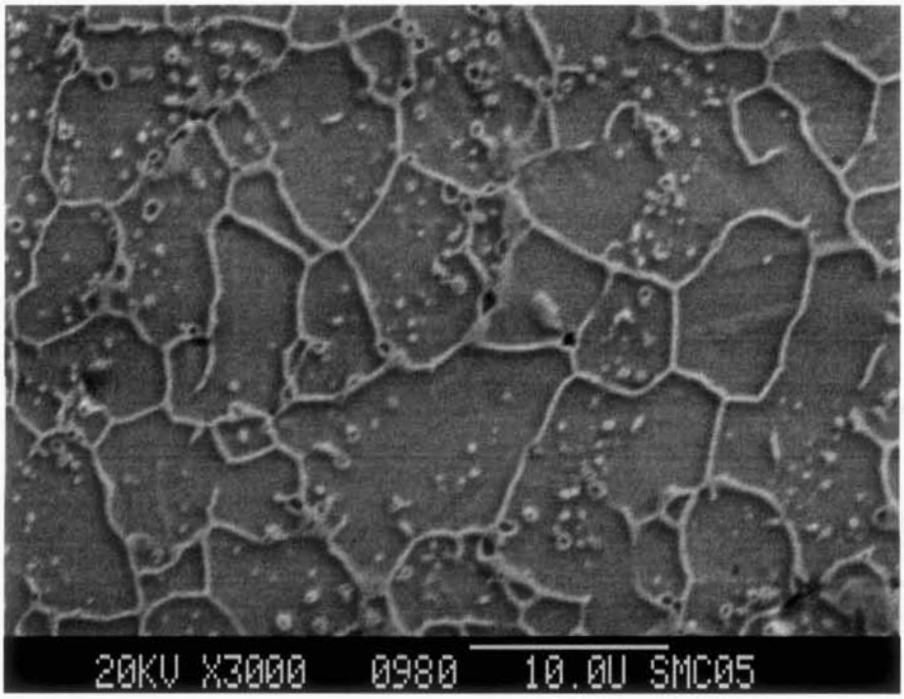

Fig 6.49: Decorated grain boundaries and precipitate features of wrought Alloy 800 HT - 15 wt% Pt, Secondary Electron Image, 3000 X

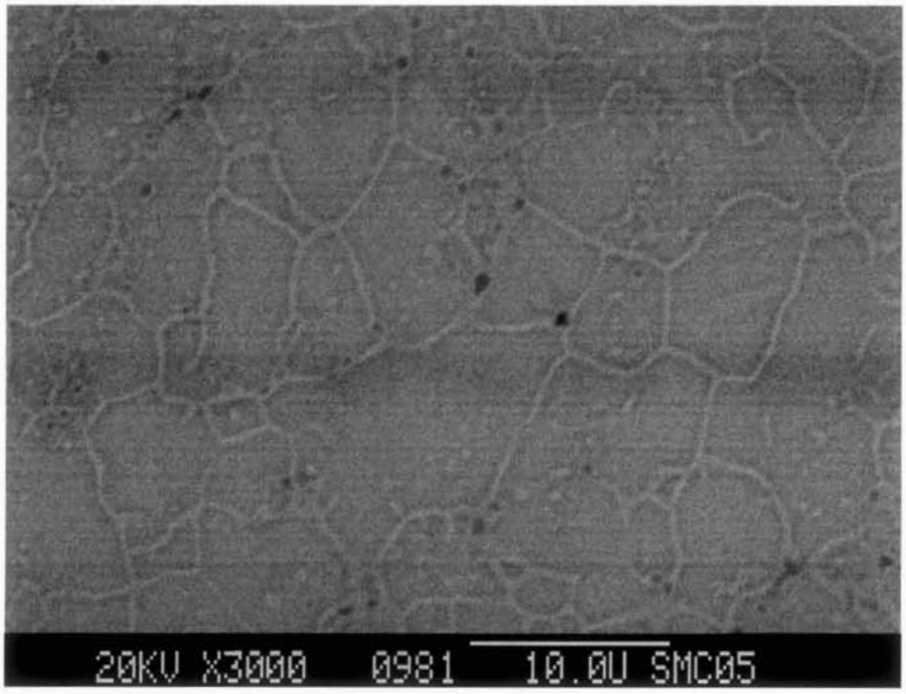

Fig 6.50: Decorated grain boundaries and precipitate features of wrought Alloy 800 HT - 15 wt% Pt, Backscatter Electron Image, 3000 X

6.4.6. Electron Dispersive Spectrometry of Wrought Structure Features

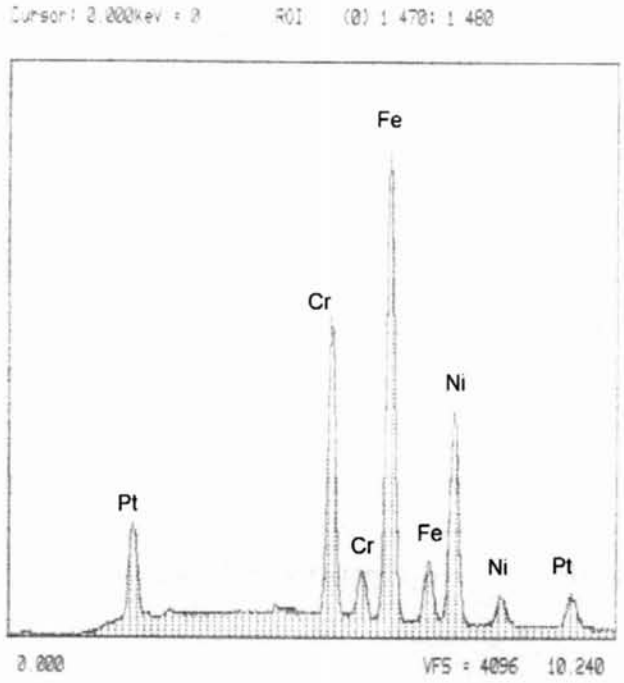

Fig 6.51: Element peak heights for matrix are consistent with compositional analysis of wrought Alloy 800 HT – 15 wt% Pt

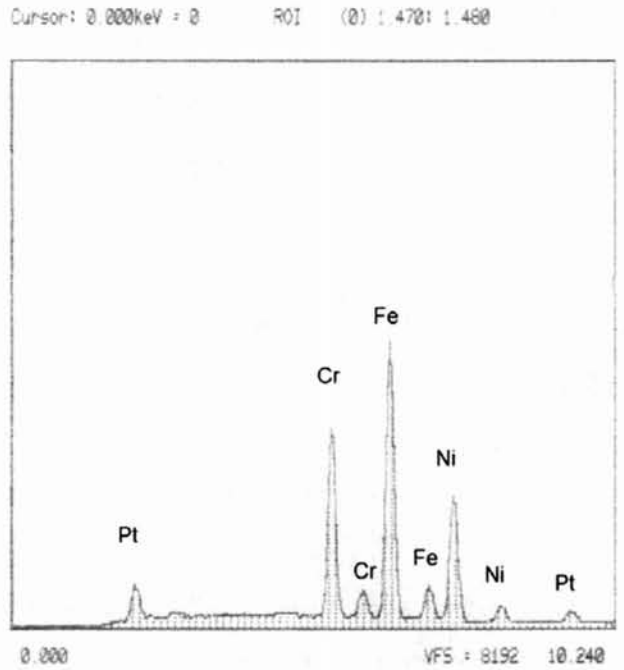

Fig 6.52: Element peak heights for the grain boundary are similar to those of the matrix of wrought Alloy 800 HT – 15 wt% Pt

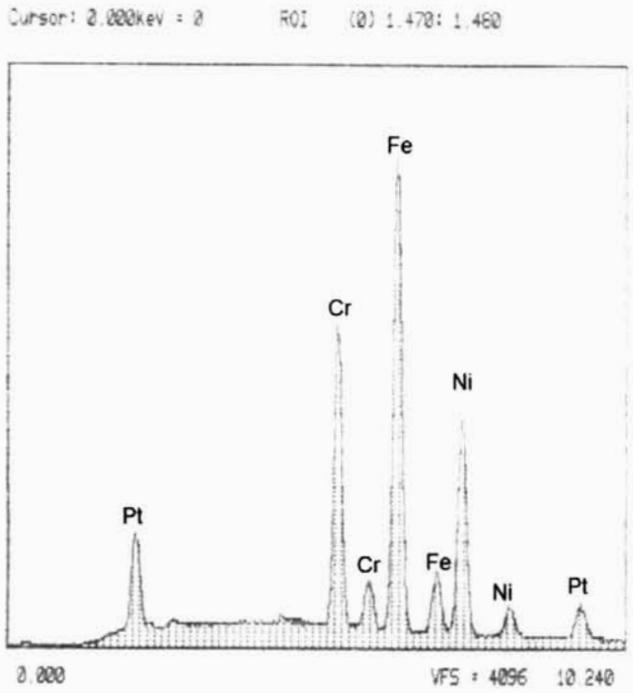

Fig 6.53: Element peak heights for the precipitates are similar to those of the matrix of wrought Alloy 800 HT – 15 wt% Pt

6.5. *Alloy 800HT – 30 wt% Pt*

Table 6.7 shows the chemistry of the Alloy 800 HT – 30 wt% Pt alloy and indicates a uniform depletion of major alloying elements below specified values for Alloy 800 HT. This makes sense considering the addition of a platinum composition of 28.3 wt%. All minor alloying and tramp element compositions are below the maximum specified values for Alloy 800 HT. The combined aluminum and titanium composition is, again, below the minimum specified combined composition for Alloy 800 HT. The overall composition indicates a relatively clean melt. The carbon content is 0.04% lower than the minimum specified compositional value for Alloy 800 HT.

Figure 6.54 gives the results of the JMat Pro thermodynamic model of this material. At 1050 °C (1925 °F) the microstructure of the Alloy 800 HT – 30 wt% Pt system is predicted to be comprised of less than 1% MC type carbides. The rest of the microstructure is predicted to be an austenite matrix

Figure 6.55, an optical micrograph of the cast unetched microstructure at 200 X, shows an extremely profuse distribution of 1 micron size precipitates. Figure 6.55 also

shows that only a very few number of coarsened 3 – 5 micron sized precipitates are present within the microstructure. Figure 6.56, an optical micrograph of the cast microstructure in the etched condition at 200 X, shows circular regions around a few precipitates that were not attacked by the etching process. A possible explanation of this behavior is that the precipitates are cathodically protecting the surrounding matrix. Preferential etching between dendritic and twinned regions is also apparent in Figure 6.56. These observations indicate that the high platinum concentration may have induced segregation away from the more heavily etched regions.

Optical micrographs of the wrought unetched microstructure at 200 X are shown for the xy, xz, and yz planes in figures 6.57 – 6.59. The effect of precipitate stringing in the direction of rolling is barely visible in these micrographs due to the very low precipitate density. Figure 6.58, an unetched micrograph of the xz plane, shows significant precipitate pulling induced by mechanical polishing, which indicates that the existing precipitates are harder than the matrix. Optical micrographs of the wrought microstructure in the etched condition at 200 X are shown in figures 6.60 – 6.62. These micrographs indicate a uniform grain structure between each of the three planes imaged. Figures 6.60 – 6.62 also reveal a significant number of annealing twins within the microstructure as well as a larger grain size. Micrographs recorded at 500 X, shown in figures 6.63 – 6.65, provide the best optical details of the wrought microstructure. Small features that are either precipitates or pits appear to be much brighter than the surrounding matrix in figures 6.60 – 6.65. These features appear to be strung out in the direction of rolling, which indicates that if they are indeed pits they were formed on or around precipitate sites.

The etching technique reveals very large regions of annealing twins without adequately revealing the grain structure. Further etching beyond the level shown in the above optical micrographs produces a uniformly darkened region that shows very little detail of the microstructure. An example of over-etching is shown in Figure B.57 of Appendix B. Table 6.8 displays a fairly uniform grain size in each imaged plane of the microstructure. The average grain size was measured to be 51 microns, which is very close to the minimum specified grain size of 63.5 microns for commercial Alloy 800 HT.

The grain size calculations performed on this alloy system, however, contain a significant amount of error due to subjectivity induced by an inadequately revealed grain structure.

Figure 6.66, an SEI mode scanning electron micrograph at 3000 X, shows no decoration of grain boundaries as in the case of Alloy 800 HT – 15 wt% Pt. Figure 6.66 shows that pitting occurred at precipitate sites, and that nearly all precipitates were pit sites. Pit edges appear to be very abrupt, which indicates that the matrix region around precipitates is very well cathodically protected by the high platinum concentration. Figure 6.66 reveals a very flat uniform matrix surface. No grain boundary or twinning structures are apparent with secondary electron imaging. A corresponding BEI mode micrograph shown in Figure 6.67 verifies no elemental segregation to grain boundaries. Some contrast difference within the matrix is apparent. The morphology of these contrast regions appears more like differences in oxide layer structure induced by etching rather than differences in composition. Precipitate sites appear to be heavily pitted by dark BEI contrast.

Figures 6.68 and 6.69 show the results of EDS analysis performed on the matrix as well as on what appeared to be the pitted precipitate features. EDS analysis of the matrix produced peaks that are consistent with the compositional analysis results reported in Table 6.7. EDS analysis results of the pitted precipitate features predictably resulted in peaks that were nearly identical to the matrix spectrum. This only verifies that the observed features are in fact pits.

6.5.1. Chemical Composition and JMat Pro precipitate model

Table 6.7			
Composition of Alloy 800 HT - 30 wt% Pt			
Element	**Wt %**	**Element**	**Wt%**
Carbon	0.056	Sulfur	0.004
Titanium	0.27	Iron	32.1
Aluminum	0.15	Copper	0.16
Chromium	15.3	Platinum	28.3
Manganese	0.53	Nickel	23.0
Silicon	0.13	Ref [44]	

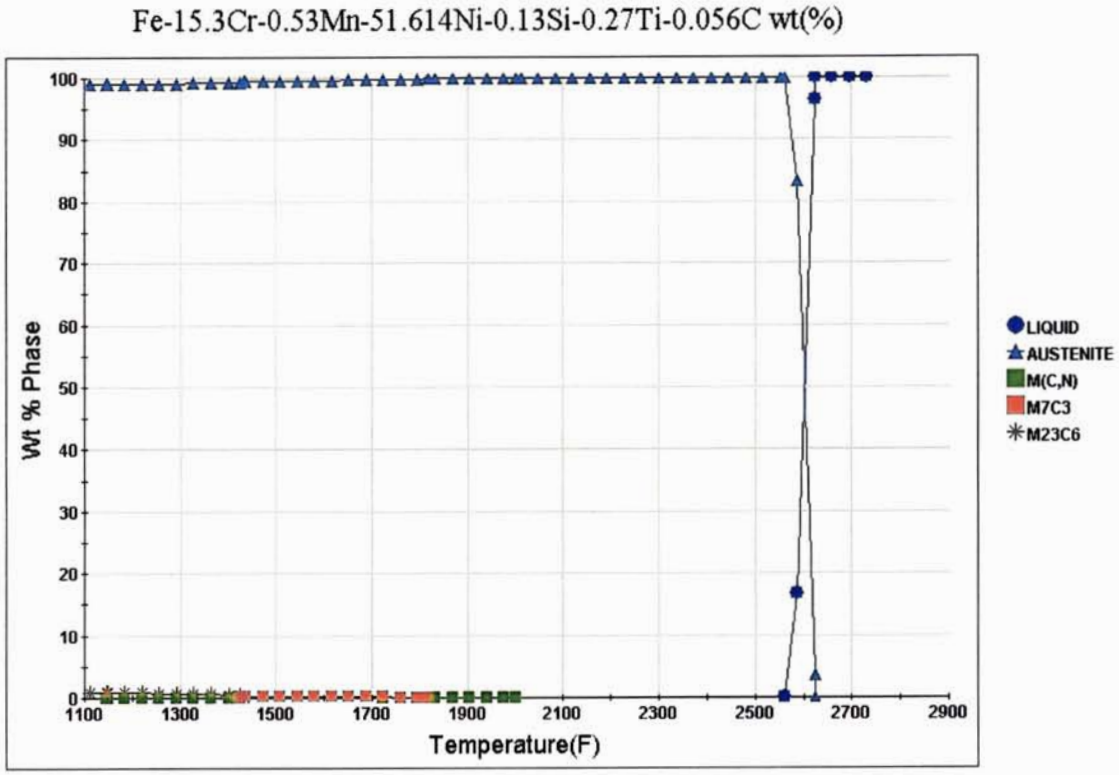

Fig 6.54: JMat Pro thermodynamic precipitate model for Alloy 800 HT – 30 wt% Pt alloyed system

6.5.2. Optical Micrographs of Cast Structure

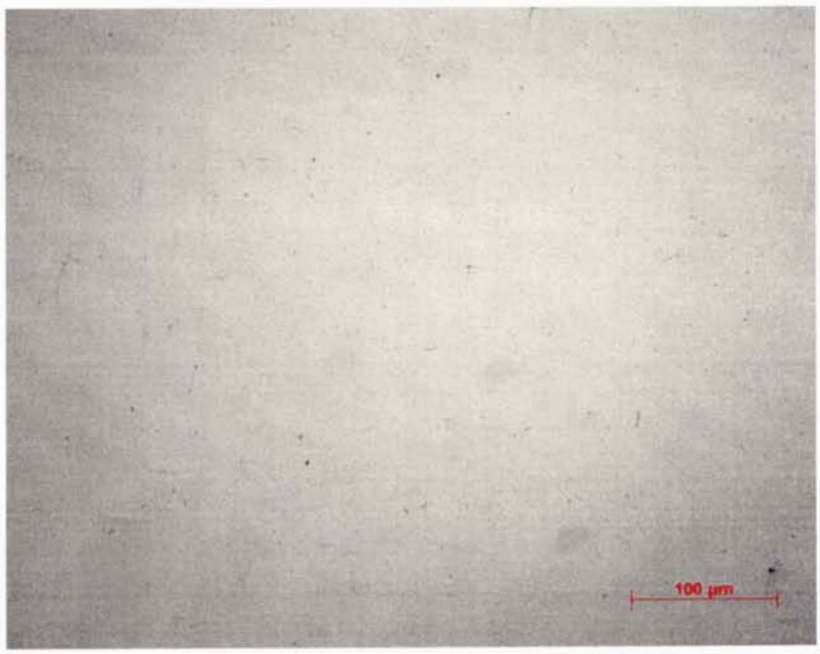

Fig 6.55: Precipitate features of cast Alloy 800 HT - 30 wt% Pt, 200 X

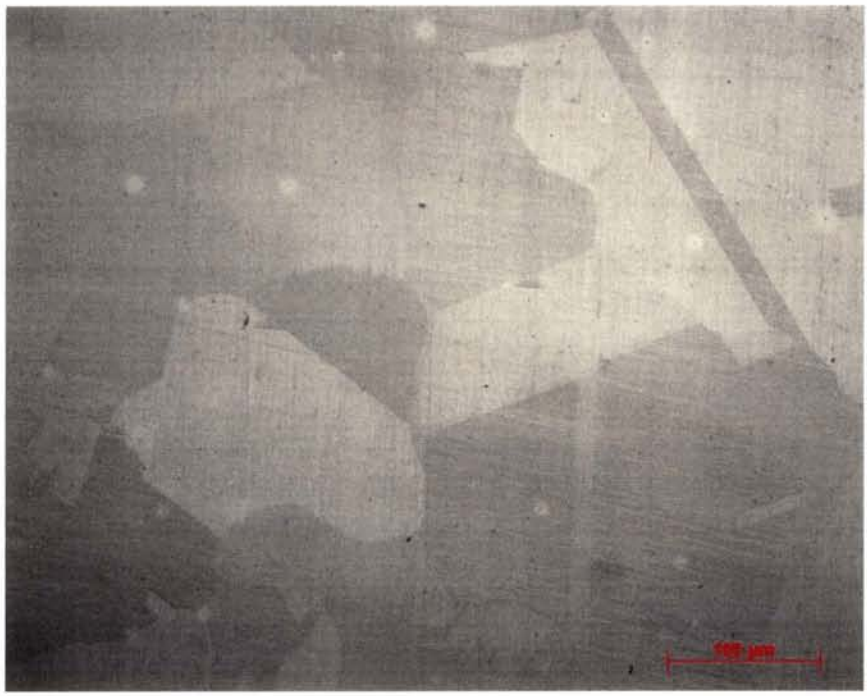

Fig 6.56: Dendrite structure and precipitate features of cast Alloy 800 HT - 30 wt% Pt, 200 X, weaker glyceregia - 1380 sec

6.5.3 Optical Micrographs of Wrought Structure

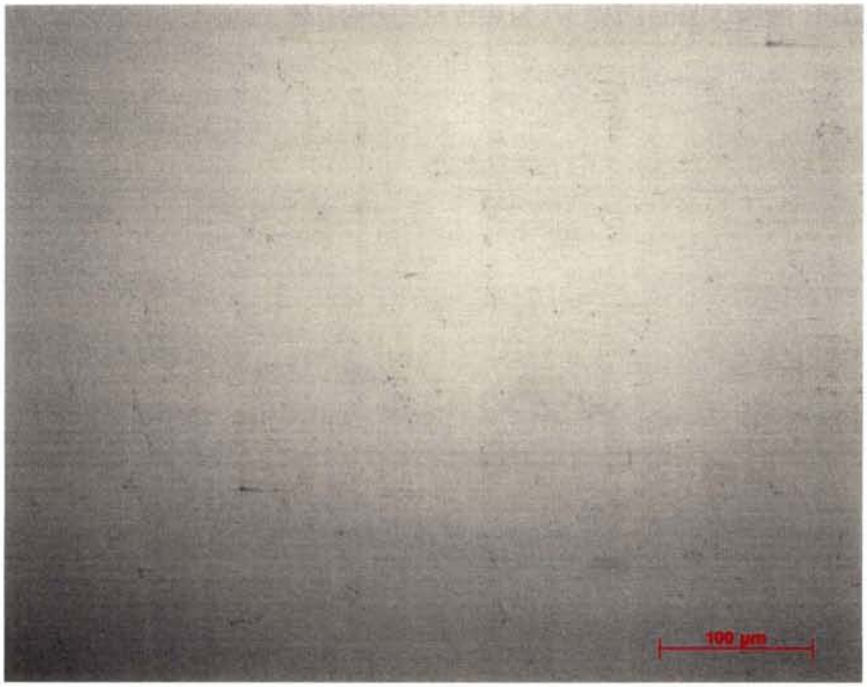

Fig 6.57: Precipitate features of wrought Alloy 800 HT – 30 wt% Pt, xy plane, 200 X

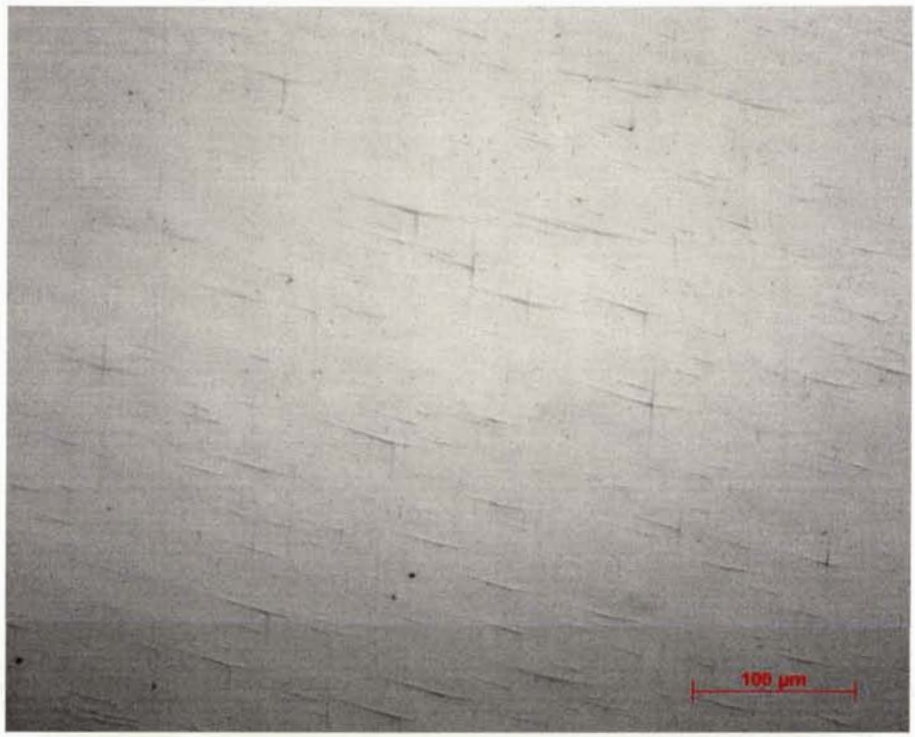

Fig 6.58: Precipitate features of wrought Alloy 800 HT – 30 wt% Pt, xz plane, 200 X

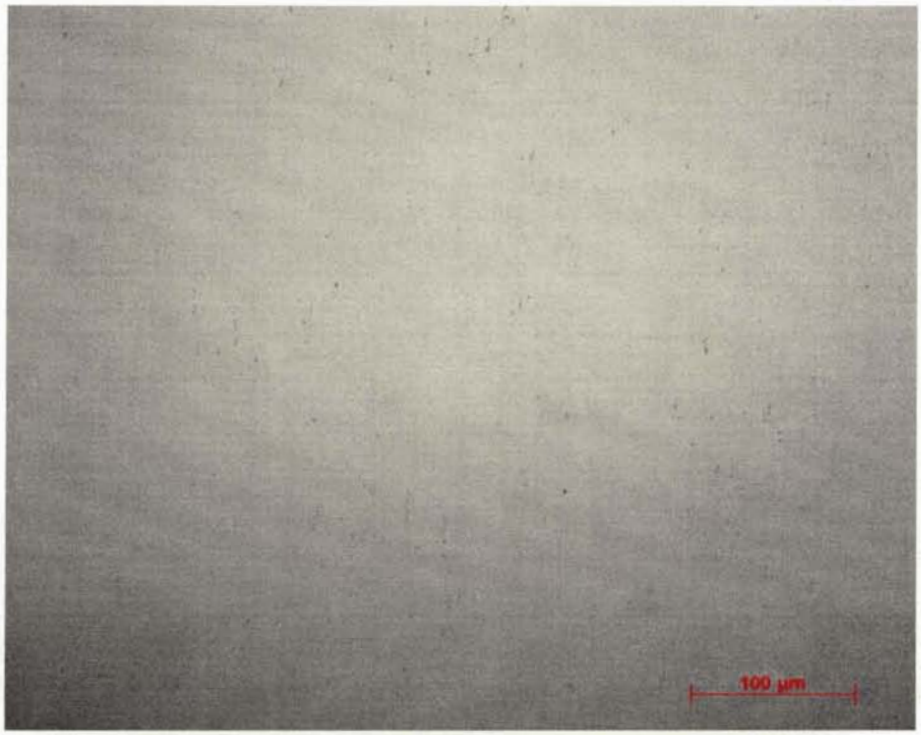

Fig 6.59: Precipitate features of wrought Alloy 800 HT – 30 wt% Pt, yz plane, 200 X

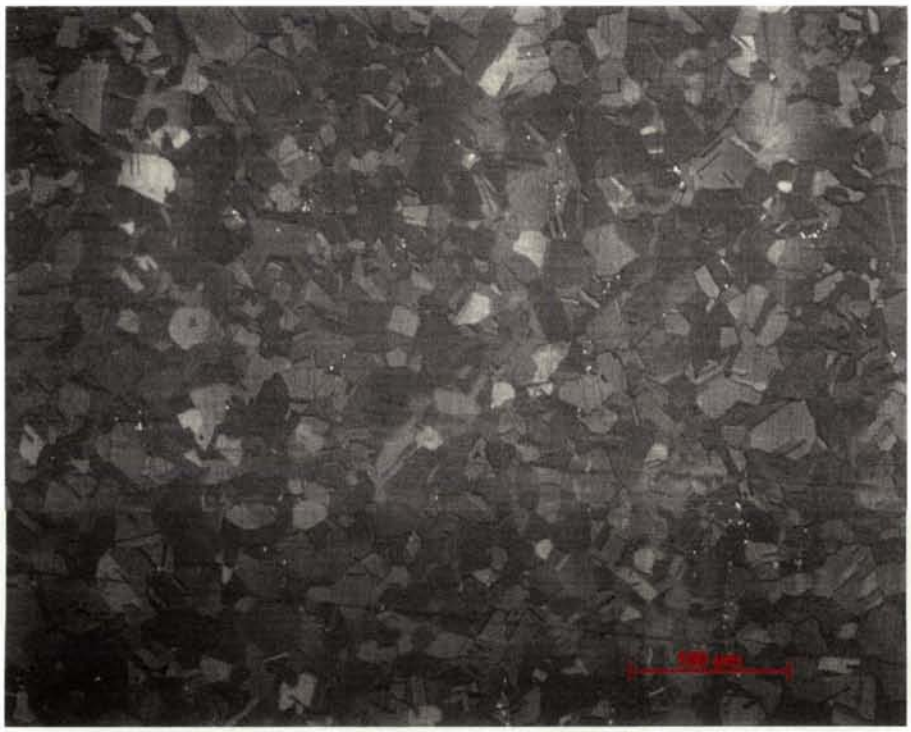

Fig 6.60: Grain structure, annealing twins and precipitate features of wrought Alloy 800 HT - 30 wt% Pt, xy plane, 200 X, Nital, 3 VDC - 5 sec

Fig 6.61: Grain structure, annealing twins and precipitate features of wrought Alloy 800 HT - 30 wt% Pt, xz plane, 200 X, Nital, 1.5 VDC - 5 sec

Fig 6.62: Grain structure, annealing twins and precipitate features of wrought Alloy 800 HT - 30 wt% Pt, yz plane, 200 X, Nital, 1.5 VDC - 4 sec

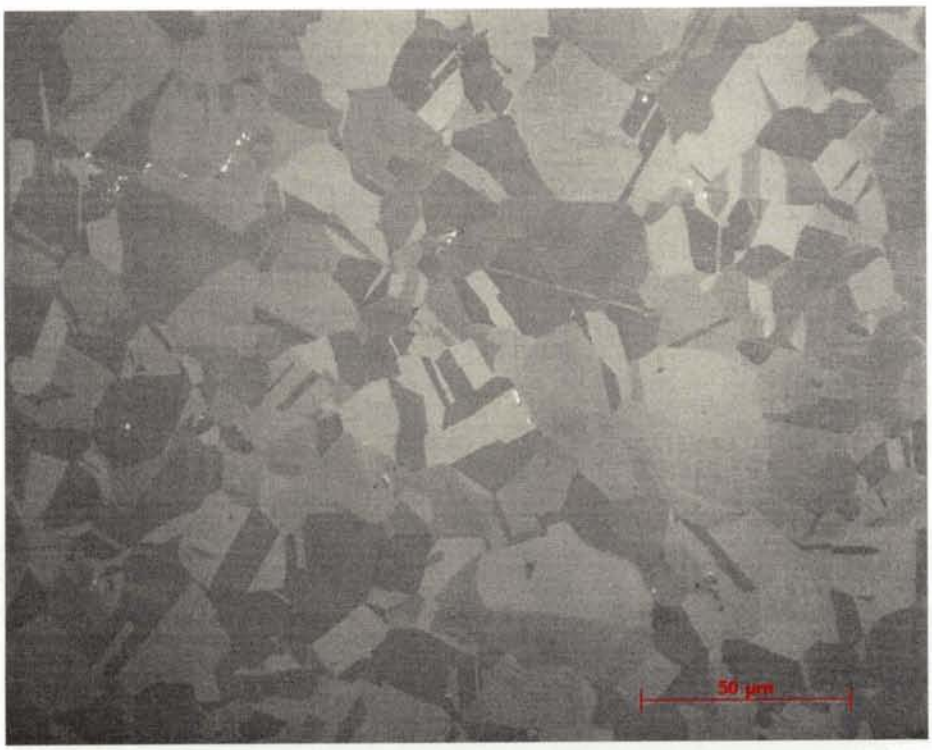

Fig 6.63: Grain structure, annealing twins and precipitate features of wrought Alloy 800 HT - 30 wt% Pt, xy plane, 500 X, Nital, 3 VDC - 5 sec

Fig 6.64: Grain structure, annealing twins and precipitate features of wrought Alloy 800 HT - 30 wt% Pt, xz plane, 500 X, Nital, 1.5 VDC - 5 sec

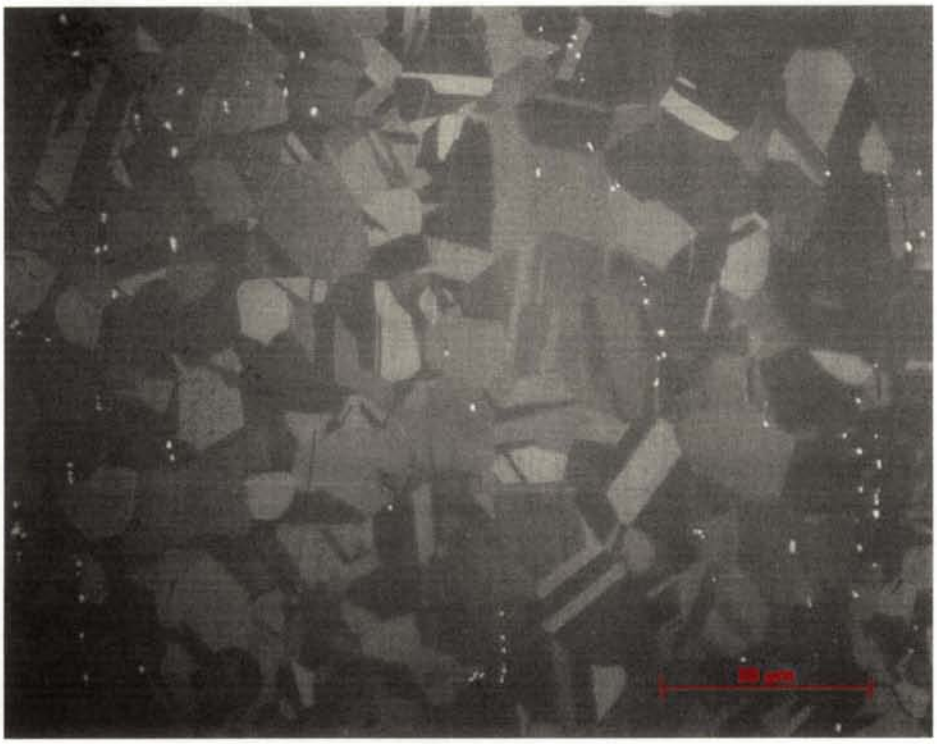

Fig 6.65: Grain structure, annealing twins and precipitate features of wrought Alloy 800 HT - 30 wt% Pt, yz plane, 500 X, Nital, 1.5 VDC - 4 sec

6.5.4. Calculated Grain Size

Table 6.8	
Calculated grain sizes for Alloy 800 HT - 30 Wt % Pt	
Plane	**Diameter (microns)**
xy	51
xz	49
yz	54
Average	**51**

6.5.5. Scanning Electron Micrographs of Wrought Structure

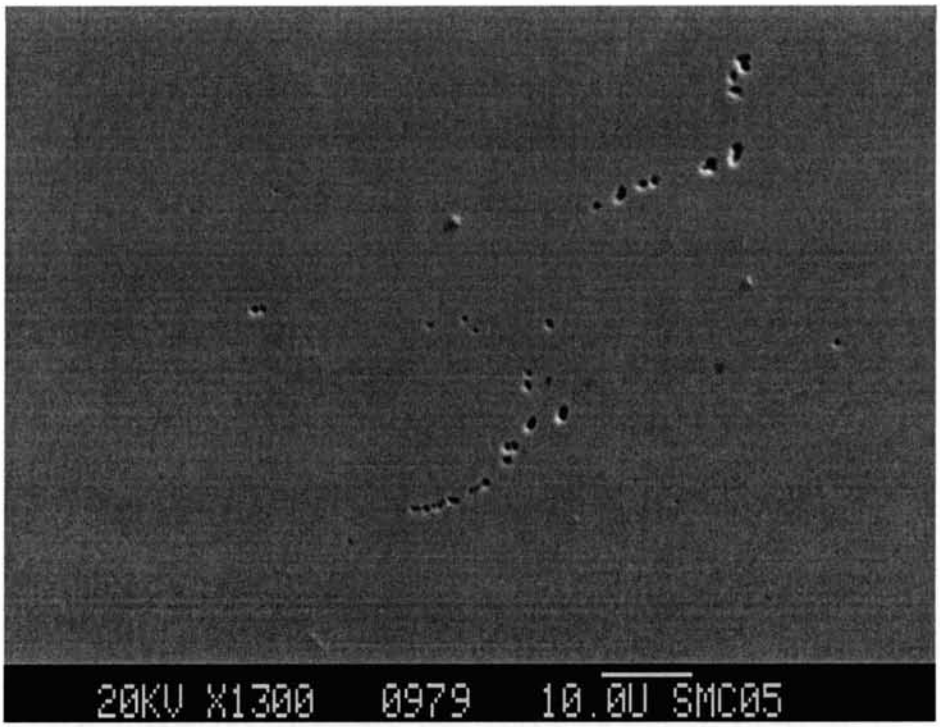

Fig 6.66: Pitted precipitate sites of wrought Alloy 800 HT - 30 wt% Pt, Secondary Electron Image, 1300 X

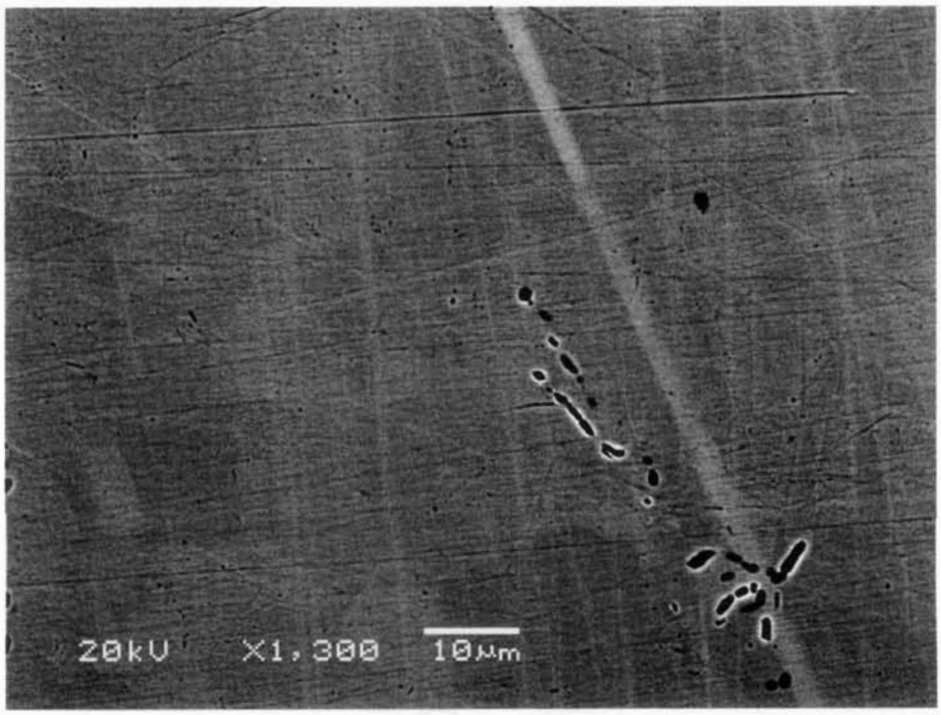

Fig 6.67: Pitted precipitate sites of wrought Alloy 800 HT - 30 wt% Pt, Backscatter Electron Image, 1300 X

6.5.6. Electron Dispersive Spectrometry of Wrought Structure Features

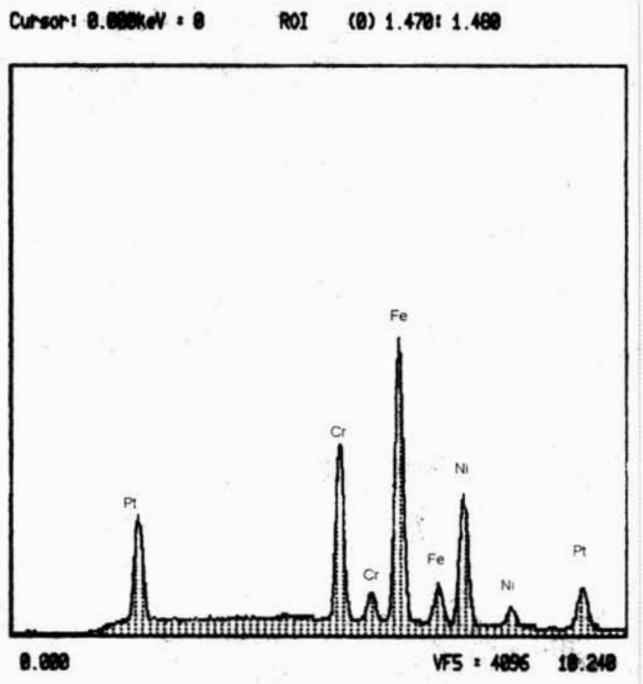

Fig 6.68: Element peak heights for matrix are consistent with compositional analysis of wrought Alloy 800 HT – 30 wt% Pt

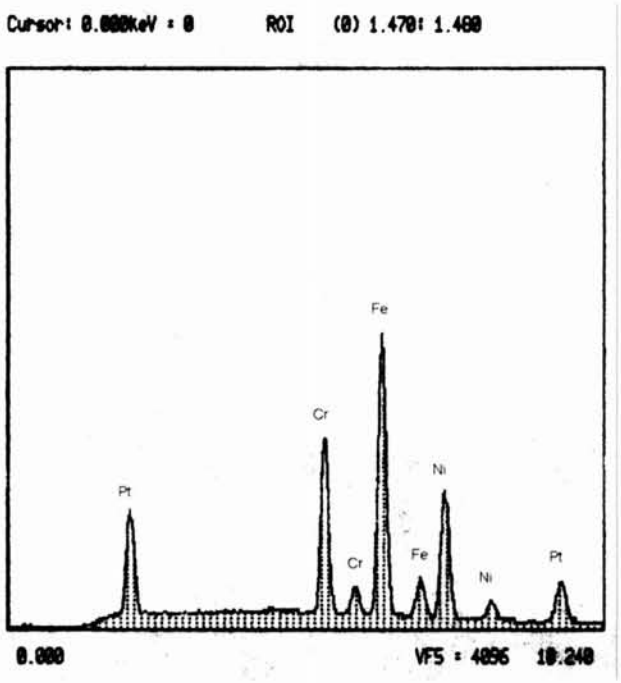

Fig 6.69: Element peak heights for pitted precipitate sites are similar to the matrix for wrought Alloy 800 HT – 30 wt% Pt

6.6. *Alloy 617*

Optical micrographs of the unetched and etched microstructure of commercial Alloy 617 are shown in figures 6.70 and 6.71, respectively. These figures are provided for comparison with the Alloy 617 – Pt materials included herein. The calculated grain size of 110 microns for the commercial Alloy 617 material is also included for comparison with the measured values of the respective Alloy 617 – Pt material.

6.6.1. Optical Micrographs of Wrought Structure

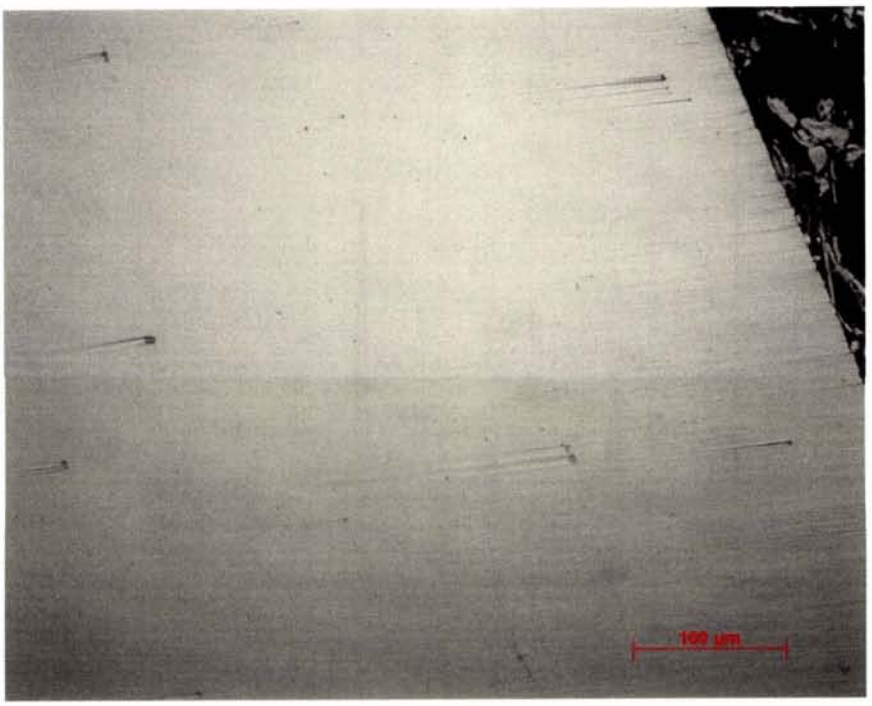

Fig 6.70: Alloy 617 HT, 200 X

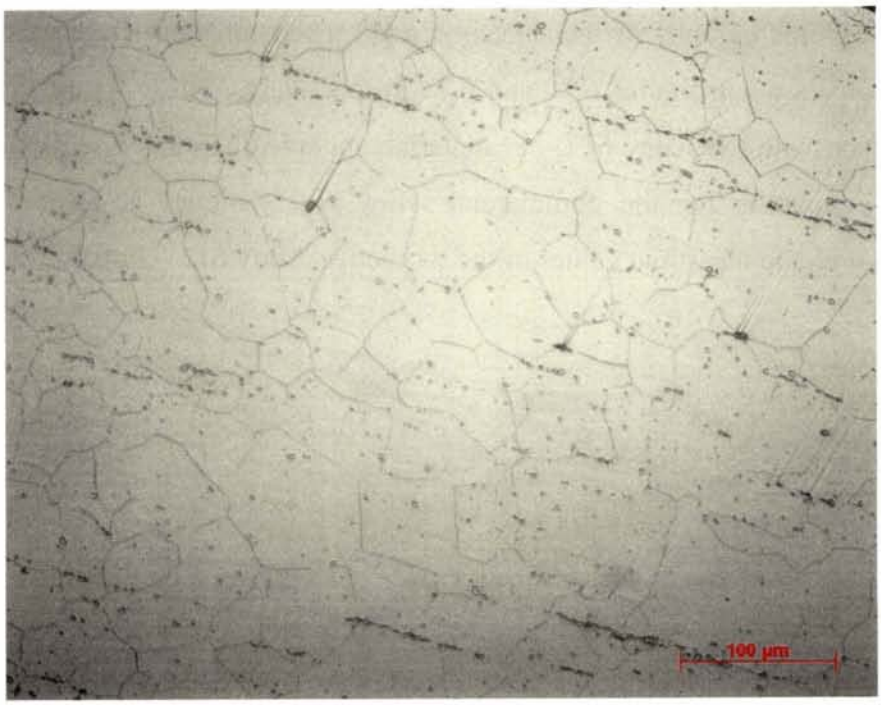

Fig 6.71: Alloy 617, 200 X, glyceregia - 1230 sec

6.6.2. Calculated Grain Size

The commercial wrought Alloy 617 material was measured to have a grain size of 110 microns. No grain size was specified by the manufacturer.

6.7. Alloy 617 – 2 wt% Pt

Table 6.9 shows the chemistry of the Alloy 617 – 2 wt% Pt alloy and indicates that all major alloying elements are within the specified compositional values for Alloy 617. With the exception of carbon, all minor alloying and tramp elements are within the specified compositional values for Alloy 617 as well. The carbon content of the Alloy 617 + 2 wt% Pt system is approximately 2.2 times higher than the maximum specified value for Alloy 617. Excessive carbide precipitation is expected to be a problem within the microstructure of this alloy system. Table 6.9 shows a platinum composition of 1.98 wt%, which is very close to the nominal composition of 2 wt%.

Figure 6.72 shows the results of the JMat Pro thermodynamic model for this material. At 1050 °C (1925 °F) the microstructure of the Alloy 617 – 2 wt% Pt system is predicted to be comprised of less than 6% $M_{23}C_6$ and 1% M_6C type carbides. The rest of the microstructure is predicted to be an austenite matrix. No γ' is predicted to precipitate.

An optical micrograph of the cast unetched structure at 200 X is shown in Figure 6.73. Two large features apparent in this micrograph were determined to be voids by altering the level of focus when viewing the structure in the laboratory. Additionally, a large 200 x 20 micron agglomeration of precipitates or tramp elements is also present. A fine distribution of 1 micron size precipitates is present within the cast microstructure along with a sparse distribution of coarsened 3 – 5 micron size precipitates. Some of the larger coarsened precipitates caused "comet tail" tracks through the matrix when they pulled due to mechanical polishing. This indicates that these larger precipitates are harder than the matrix material. Figure 6.74, a micrograph of the cast microstructure in the etched condition at 200 X, shows a much cleaner microstructure, which indicates that significant artifacts had been created due to polishing. Figure 6.74 shows a high density

of elongated inter and intra-dendritic precipitates. These precipitates have a camouflaging effect on the very large dendrite structure.

Optical micrographs of the unetched wrought structure at 200 X are shown in figures 6.75 – 6.77. These micrographs show precipitate stringing in the direction of rolling very clearly. Figures 6.78 – 6.80 show corresponding micrographs in the etched condition. These micrographs show a fine grain structure in each of the planes imaged along with a very profuse distribution of different precipitates. Precipitates that are strung in the direction of rolling appear to have a much darker contrast than the surrounding microstructure indicating that they were more aggressively attacked by the etching process. At the 200 X level of magnification it is difficult to determine whether or not smaller intra-granular features with a lighter contrast are pits or precipitates. Optical micrographs of the etched microstructure at 500 X are shown in figures 6.81 – 6.83. These micrographs reveal that inter-granular carbides have a pinning effect on the grain boundaries. Additionally, these inter-granular precipitates appear to be nearly as large as the surrounding grains. A minority of these larger strung precipitates appear to be very bright compared to others, which indicates that the etching procedure was not applied long enough to completely over-etch all of them. Figures 6.78 – 6.83 show a very symmetrical grain structure throughout the matrix.

Each wrought material was slightly over etched to adequately reveal the wrought grain structure for measurement. Table 6.10 shows the results of the grain size measurement calculations performed on the xy, xz, and yz planes. Grain size calculations indicated a very uniform grain structure throughout the microstructure with an average grain size of 14 microns. This value is very small compared to the calculated grain size of 110 microns for the specimen of commercial Alloy 617.

Figure 6.84, an SEI mode scanning electron micrograph at 3000 X, clearly reveals topological features of the Alloy 617 – 2 wt% Pt system. No depressed pitted regions appear within the microstructure. Figure 6.84 shows a high density of 1 – 4 micron size precipitate structures as raised features above the matrix. Very small sub micron size precipitates also appear to be evenly distributed through the matrix, though with a much lower density. Figure 6.85, a corresponding BEI mode scanning electron micrograph, shows relatively little contrast difference between the larger coarsened precipitates and

the matrix, which indicates relatively similar chemistry. Back scatter imaging shows a bright contrast relative to the matrix of the sub-micron precipitates initially viewed in Figure 6.84. Brighter contrast indicates a greater atomic weight than the matrix, which points to a (Ni, $Co)_3Mo_3C$ composition, where the molybdenum contributes to the increase in average atomic weight. The density ratio between the large coarsened precipitates with similar contrast to the matrix and the smaller brighter precipitates qualitatively appears to be equal to the ratio of $M_{23}C_6$ and M_6C carbides predicted by the JMat Pro model. The good agreement within the data further supports the proposed chemistry of the precipitates. No grain structure is revealed by the scanning electron micrographs.

Figures 6.86 and 6.87 show the results of EDS analysis performed on both the matrix and the lager 1 – 4 micron size precipitate features shown in Figure 6.84, respectively. EDS analysis of the matrix resulted in peak heights of major alloying elements that are consistent with the compositional analysis results reported in Table 6.9. EDS analysis performed on large precipitate structures shows significantly higher chromium and slightly higher molybdenum peaks compared to the EDS spectrum of the matrix. These results indicate that the precipitates are most likely $Cr_{21}Mo_2C_6$ type carbides.

6.7.1. Chemical Composition and JMat Pro Precipitate Model

Table 6.9			
Composition of Alloy 617 - 2 wt% Pt			
Element	**Wt %**	**Element**	**Wt%**
Carbon	0.336	Phosphorous	0.002
Titanium	0.28	Sulfur	0.004
Aluminum	0.94	Boron	0.001
Chromium	22.3	Iron	1.01
Cobalt	12.2	Copper	0.044
Molybdenum	8.58	Platinum	1.98
Manganese	0.030	Nickel	52.2
Silicon	0.021	Ref [44]	

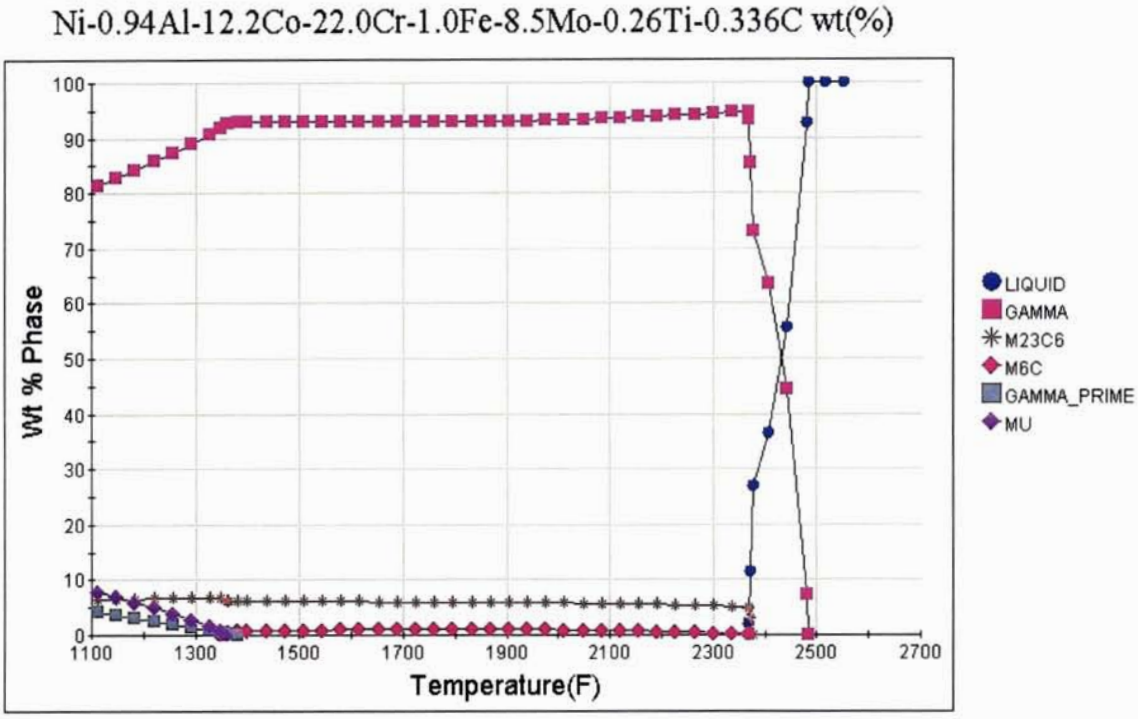

Fig 6.72: JMat Pro thermodynamic precipitate model for Alloy 617 – 2 wt% Pt alloyed system

6.7.2. Optical Micrographs of Cast Structure

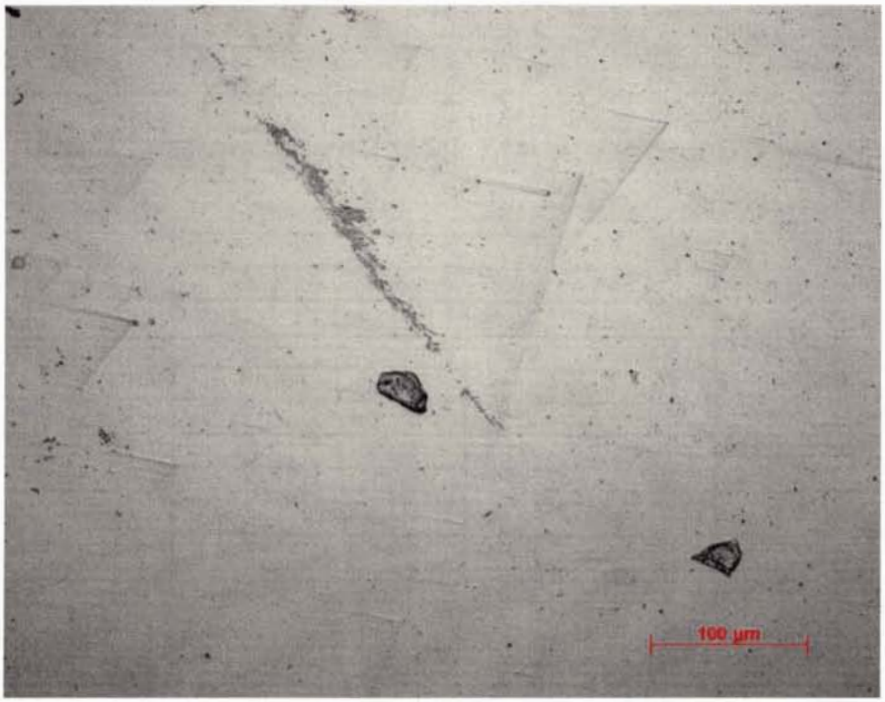

Fig 6.73: Precipitate features of cast Alloy 617 - 2 wt% Pt, 200 X

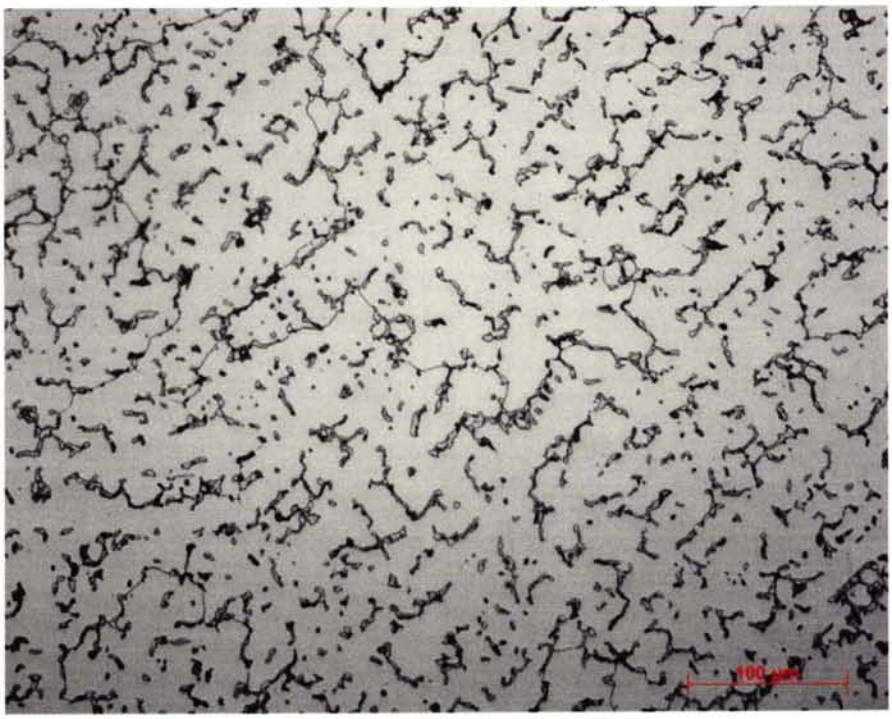

Fig 6.74: Precipitate features of cast Alloy 617 - 2 wt% Pt, 200 X, glyceregia - 780 sec

6.7.3. Optical Micrographs of Wrought Structure

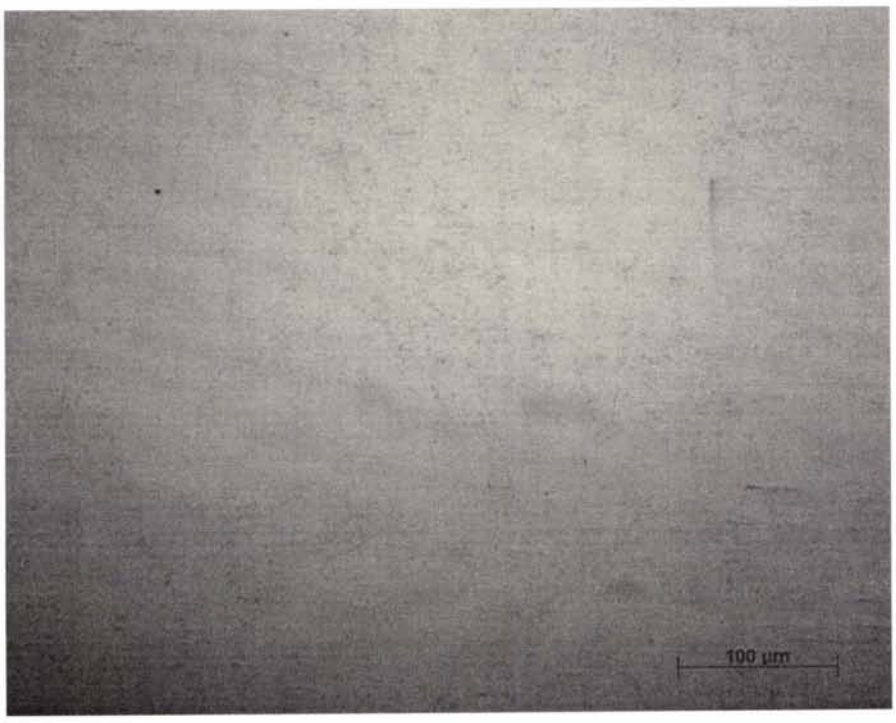

Fig 6.75: Precipitate features of wrought Alloy 617 – 2 wt% Pt, xy plane, 200 X

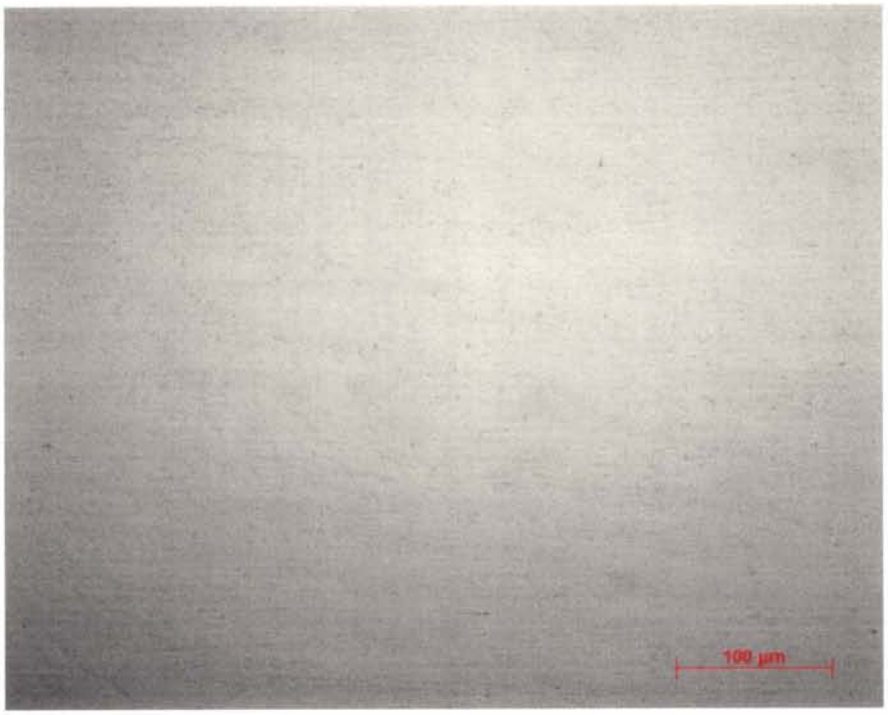

Fig 6.76: Precipitate features of wrought Alloy 617 – 2 wt% Pt, xz plane, 200 X

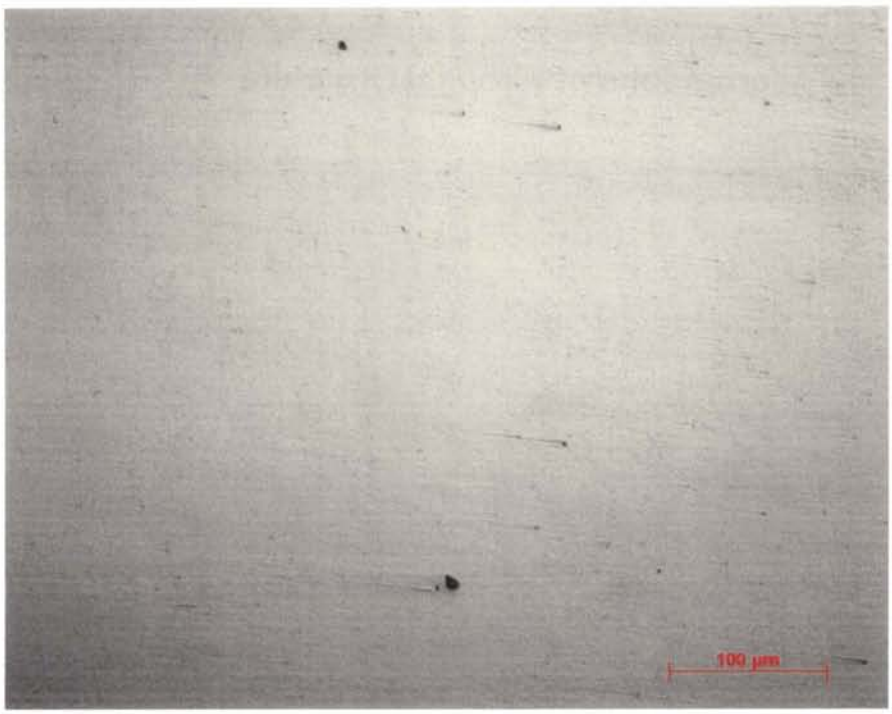

Fig 6.77: Precipitate features of wrought Alloy 617 – 2 wt% Pt, yz plane, 200 X

Fig 6.78: Grain structure and precipitate features of wrought Alloy 617 - 2 wt% Pt, xy plane, 200 X, 10ml Oxalic Acid 90ml H_2O, 3 VDC - 4 sec

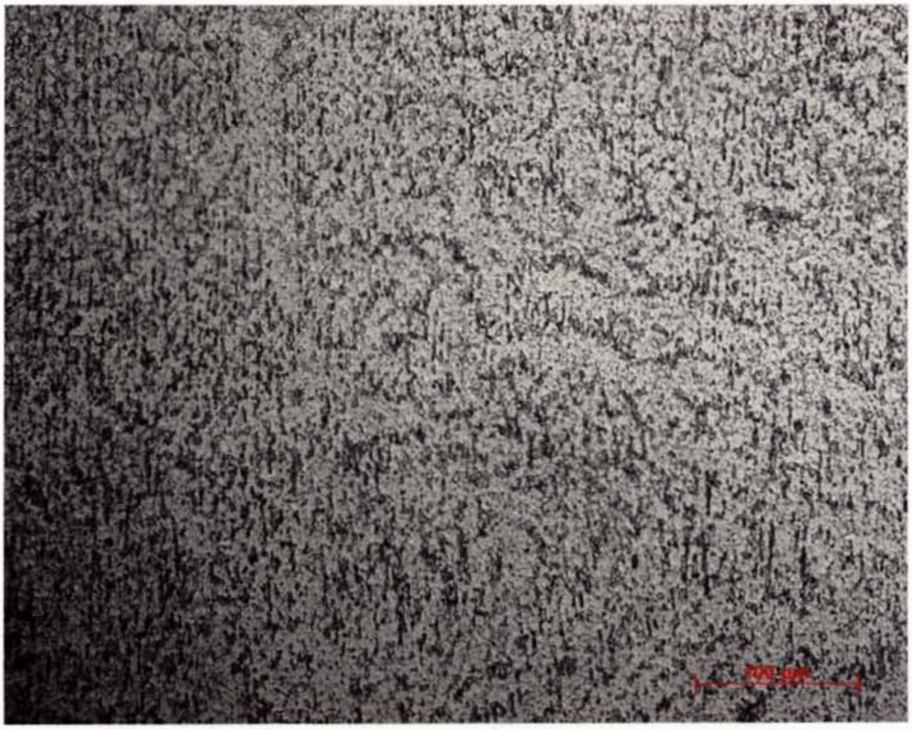

Fig 6.79: Grain structure and precipitate features of wrought Alloy 617 - 2 wt% Pt, xz plane, 200 X, 10ml Oxalic Acid 90ml H_2O, 1.5 VDC - 6 sec

Fig 6.80: Grain structure and precipitate features of wrought Alloy 617 - 2 wt% Pt, yz plane, 200 X, 10ml Oxalic Acid 90ml H_2O, 1.5 VDC - 4 sec

Fig 6.81: Grain structure and precipitate features of wrought Alloy 617 - 2 wt% Pt, xy plane, 500 X, 10ml Oxalic Acid 90ml H_2O, 3 VDC - 4 sec

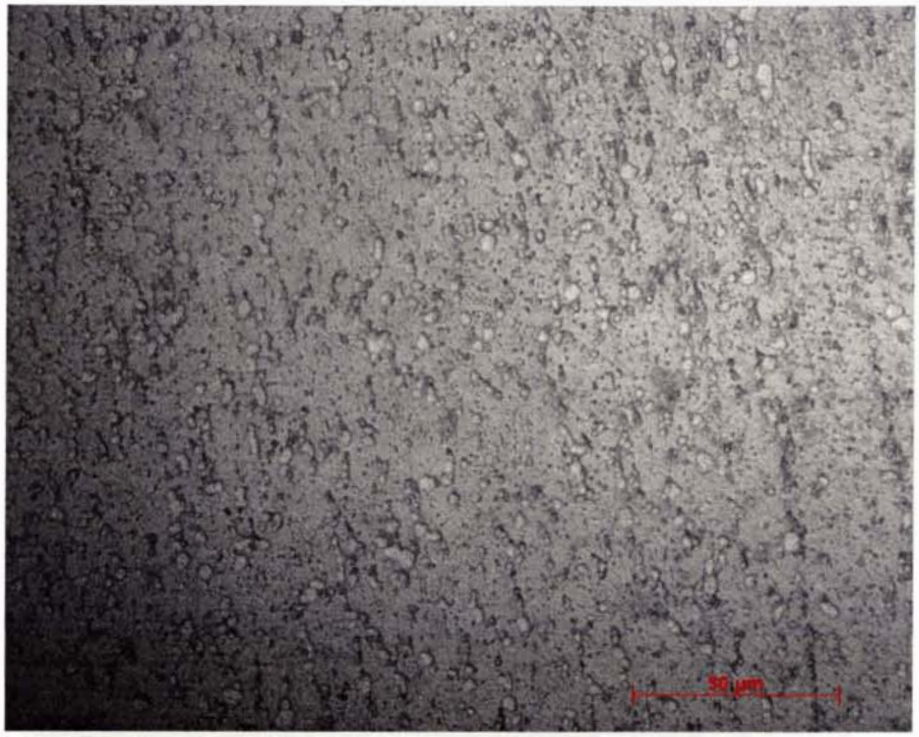

Fig 6.82: Grain structure and precipitate features of wrought Alloy 617 - 2 wt% Pt, xz plane, 500 X, 10ml Oxalic Acid 90ml H_2O, 1.5 VDC - 6 sec

Fig 6.83: Grain structure and precipitate features of wrought Alloy 617 - 2 wt% Pt, yz plane, 500 X, 10ml Oxalic Acid 90ml H_2O, 1.5 VDC - 4 sec

6.7.4. Calculated Grain Size

Table 6.10	
Calculated grain sizes for Alloy 617 - 2 Wt % Pt	
Plane	**Diameter (microns)**
xy	14
xz	13
yz	14
Average	**14**

6.7.5. Scanning Electron Micrographs of Wrought Structure

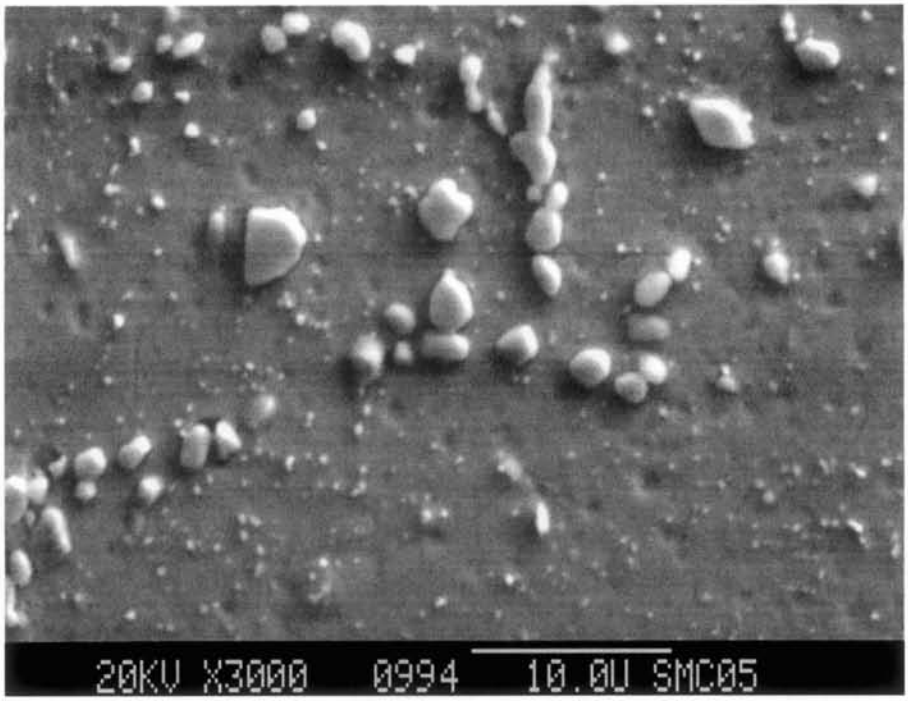

Fig 6.84: Topographical contrast of coarsened precipitate and sub-micron size precipitates in wrought Alloy 617 - 2 wt% Pt, Secondary Electron Image, 3000 X

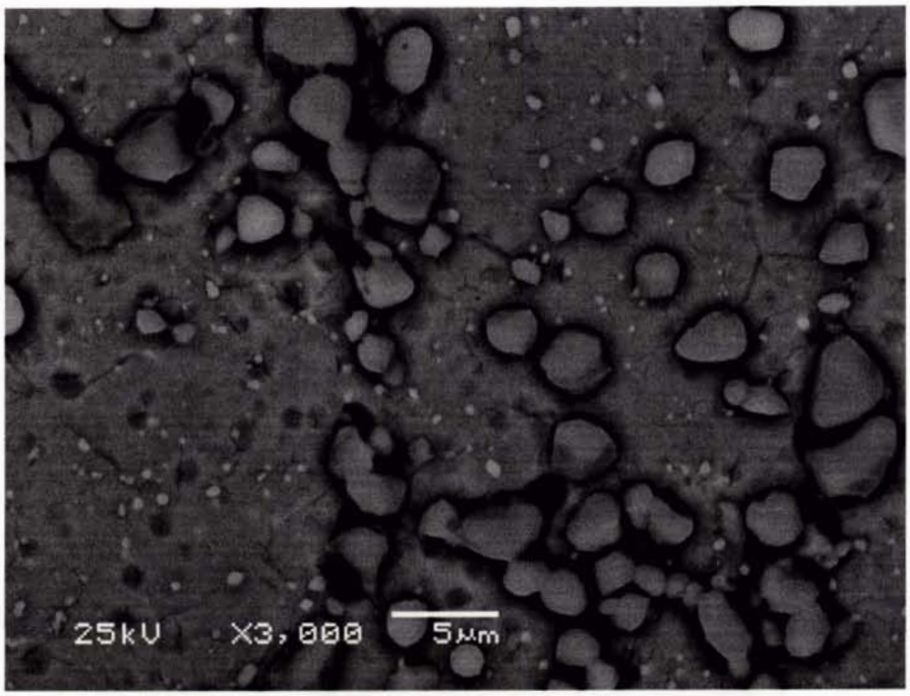

Fig 6.85: Low contrast of coarsened inter-granular precipitates with the matrix and bright contrast of sub-micron intra-granular precipitates with the matrix in wrought Alloy 617 - 2 wt% Pt, Backscatter Electron Image, 3000X

6.7.6. Electron Dispersive Spectrometry of Wrought Structure Features

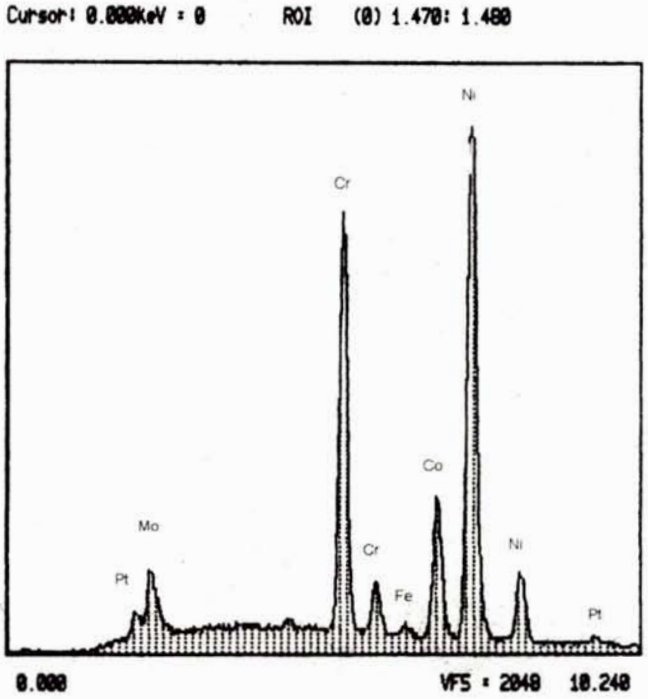

Fig 6.86: Element peak heights for matrix are consistent with compositional analysis of wrought Alloy 617 – 2 wt% Pt

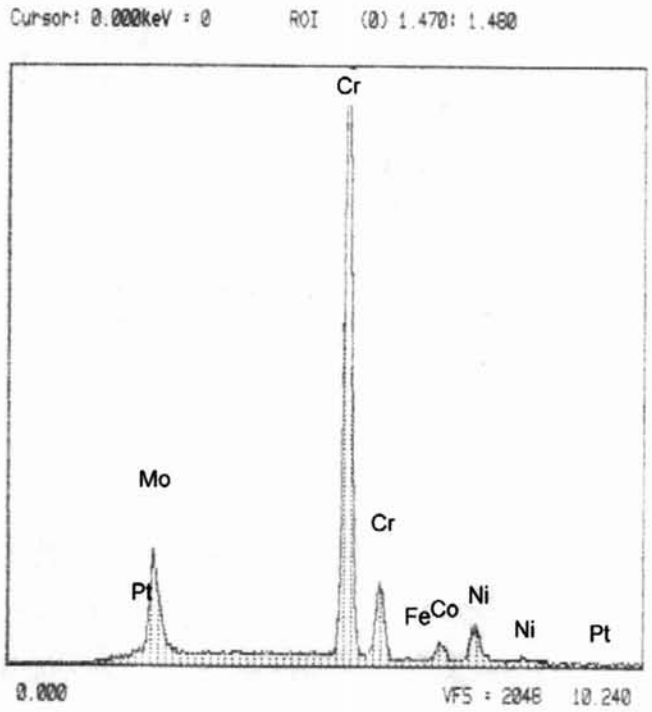

Fig 6.87: High chromium peak for precipitate relative to the matrix for wrought Alloy 617 – 2 wt% Pt

6.8. *Alloy 617 – 5 wt% Pt*

Table 6.11 shows the chemistry of the Alloy 617 – 5 wt% Pt alloy and indicates that only the nickel and cobalt major alloying elements are within the specified compositional values for Alloy 617. The chromium and molybdenum contents of the Alloy 617 – 5 wt% Pt system are only 1.9 wt% and 0.13 wt% below their minimum specified values for Alloy 617, respectively. This compositional discrepancy is acceptable considering the alloy system contains an additional 4.76 wt% platinum. With the exception of carbon, all minor alloying and tramp element compositions are below their minimum specified values for Alloy 617. The carbon content of this alloy system, however, is approximately 3.5 times higher than the maximum value for Alloy 617. Excessive carbide precipitation is therefore expected to be a problem.

Figure 6.88 shows the results of the JMat Pro thermodynamic model for this material. At 1050 °C (1925 °F) the microstructure of the Alloy 617 – 5 wt% Pt system is predicted to be comprised of less than 10% $M_{23}C_6$ and less than 1% M_6C type carbides.

The rest of the microstructure is predicted to be an austenite matrix. No γ' is predicted to precipitate.

Figure 6.89, an optical micrograph of the cast unetched microstructure at 200 X, shows a large volume fraction of 2-5 micron size precipitates that are clustered in elongated patterns. These precipitates appear to have a slightly lighter contrast than the matrix. A very few number of darker larger precipitates are also present within the cast microstructure. Some of these precipitates have pulled out during mechanical polishing. Comet tails left in the tracks of the pulled precipitates indicate that they are harder than the matrix. Figure 6.89, an optical micrograph of the etched cast microstructure at 200 X, does not show any dendritic boundaries due to insufficient etching. The lightly contrasted precipitates with high volume fraction viewed in Figure 6.89 appear to have etched to various degrees in Figure 6.90.

Optical micrographs of the unetched wrought microstructure at 200 X are shown for the xy, xz, and yz planes in figures 6.91 – 6.93. These micrographs adequately reveal precipitate stringing in the direction of rolling. Figures 6.94 6.96 are corresponding micrographs of the etched microstructure at 200 X. These micrographs indicate that each imaged plane of the Alloy 617 – 5 wt% Pt system was over etched. Additionally, these micrographs reveal a very fine grain structure and precipitates that appear to be much lighter in contrast compared to the matrix. At 200 X very fine details are visible, but are too small to be viewed in detail. Optical micrographs of the etched wrought microstructure at 500 X are shown in figures 6.97 – 6.99. The grain structure is not adequately revealed in figures 6.97 – 6.99. However, these micrographs do show a profuse distribution of strung out precipitates that appear lighter than the over-etched matrix as well as a profuse distribution of smaller precipitates or pits that are probably intra-granular. The coarsened inter-granular precipitates viewed in figures 6.97 – 6.99 very likely have a pinning effect on the grain boundaries due to their profuse distribution throughout the microstructure. Though the definite grain structure is difficult to distinguish in figures 6.94 – 6.99, it is possible to make an approximate grain size measurement due to the high density of intra-granular precipitates and partially developed grain boundaries. Micrographs of each imaged plane at both 200 and 500 X indicate a uniform grain structure throughout the matrix.

In order to adequately reveal the grain structure for measurement, each sample was slightly over etched and 3 ml of hydrochloric acid was added to the electrolyte. Unfortunately, only precipitate structures could be developed using this etching technique. In some cases grain boundaries were completely decorated with intra-granular precipitates and in other cases they simply did not develop. From the micrographs shown above, the poor results of etching can be attributed to microstructural features that camouflaged the grain structure rather than the etching technique itself. Despite these problems, enough microstructural detail was revealed to perform grain size calculations on each imaged plane. Table 6.12 indicates a very fine uniform grain size throughout the microstructure. The overall grain size was measured to be approximately 12 microns. There may be significant error associated with this result due to microstructural features; however, despite any such error the measured grain size is still very small compared to the measured value of 110 microns for the commercial Alloy 617 sample.

Figure 6.100, an SEI mode scanning electron micrograph at 1300 X, reveals the nature of precipitate structures much more accurately than optical micrographs. Coarsened precipitates that are 1 – 4 microns in diameter appear to be raised above the matrix. A distribution of sub-micron size precipitates is also present within the microstructure. Though the grain structure is not adequately revealed, these smaller precipitates are probably intra-granular because of their high density and homogenous distribution throughout the microstructure. A BEI mode scanning electron micrograph, shown in Figure 6.101, reveals a small percentage of precipitates with brighter contrast than the matrix while the majority of precipitates are shown with darker contrast. Precipitates with brighter contrast most probably have an overall higher atomic weight than the matrix, which points to a $(Ni,Co)_3Mo_3C$ composition. Darker precipitates have lower atomic weight than the matrix, which points to a $Cr_{21}Mo_2C_6$ composition. The ratio of darker to brighter precipitate densities qualitatively appears to be close to the ratio of $M_{23}C_6$ to M_6C predicted by the JMat Pro model. The agreement between these results further supports the proposed precipitate chemistries. No grain structure is revealed in by either scanning electron micrograph.

Figures 6.102 and 6.103 give the results of EDS analysis performed on the matrix as well as on the larger coarsened precipitate features shown in figures 6.100 and 6.101.

The spot was moved to the area of lowest small precipitate distribution possible to mitigate their effect on the results for EDS analysis of the matrix. The results of matrix EDS analysis indicate peak heights that are consistent with the compositional results reported in Table 6.11. EDS analysis of the coarsened precipitate features indicates a very high chromium peak and a slightly higher molybdenum peak than the corresponding peaks of the matrix spectrum. This result points to a $Cr_{21}Mo_2C_6$ type carbide precipitate structure.

To confirm precipitate composition elemental mapping was performed for the precipitate structures viewed in the scanning electron micrographs. Figure 6.104 shows the X-Ray elemental dot map for each major alloying element within the Alloy 617 – 5 wt% Pt system along with a corresponding BEI scanning electron micrograph at 10000 X. The BEI micrograph shows some precipitates that have a brighter and darker contrast. The included X-ray dot maps show that molybdenum segregates to the brighter precipitates, while chromium segregates to the darker precipitates. These results indicate that there are two definite types of precipitates. The darker chromium rich precipitates are most probably $Cr_{21}Mo_2C_6$ carbides that precipitated on the brighter molybdenum rich precipitates, which are probably $(Ni, Co)_3Mo_3C$ carbides.

6.8.1. Chemical Composition and JMat Pro precipitate model

Table 6.11			
Composition of Alloy 617 - 5 wt% Pt			
Element	**Wt %**	**Element**	**Wt%**
Carbon	0.525	Phosphorous	0.005
Titanium	0.28	Sulfur	0.005
Aluminum	0.84	Boron	0.004
Chromium	18.9	Iron	0.85
Cobalt	11.3	Copper	0.13
Molybdenum	7.87	Platinum	4.76
Manganese	0.032	Nickel	51.9
Silicon	0.050	Ref [44]	

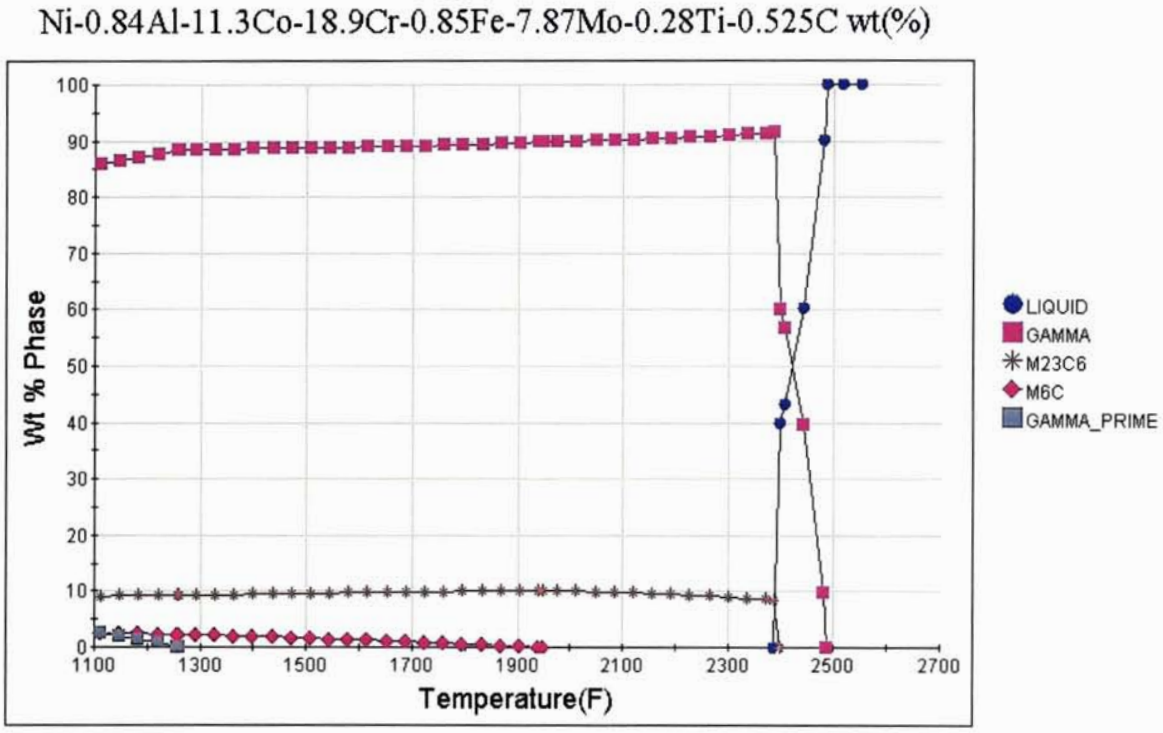

Fig 6.88: JMat Pro thermodynamic precipitate model for Alloy 617 – 5 wt% Pt alloyed system

6.8.2. Optical Micrographs of Cast Structure

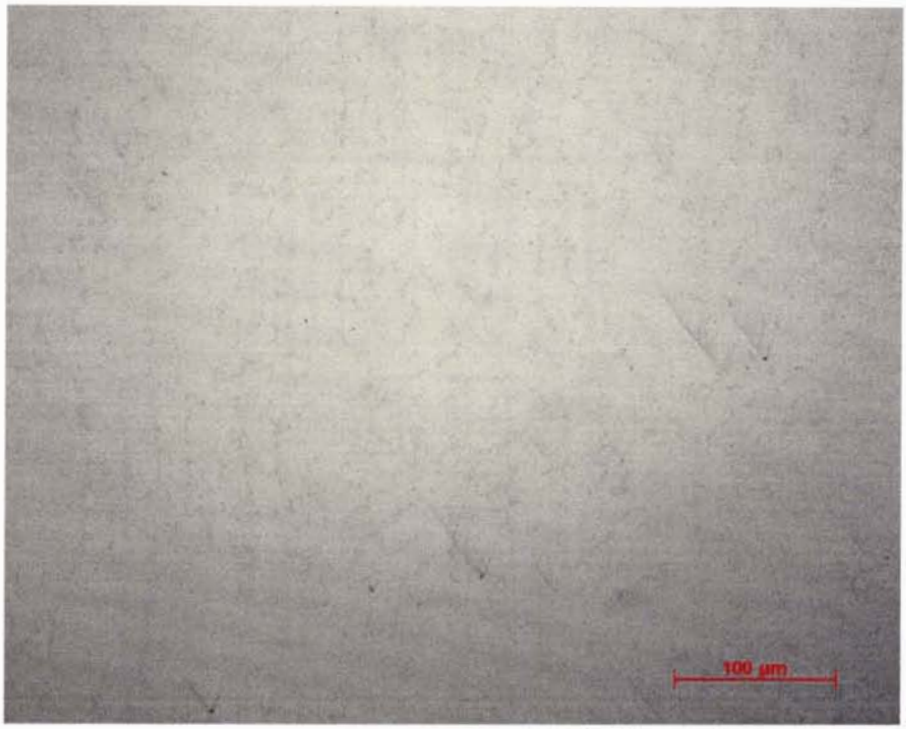

Fig 6.89: Precipitate features of cast Alloy 617 - 5 wt% Pt, 200 X

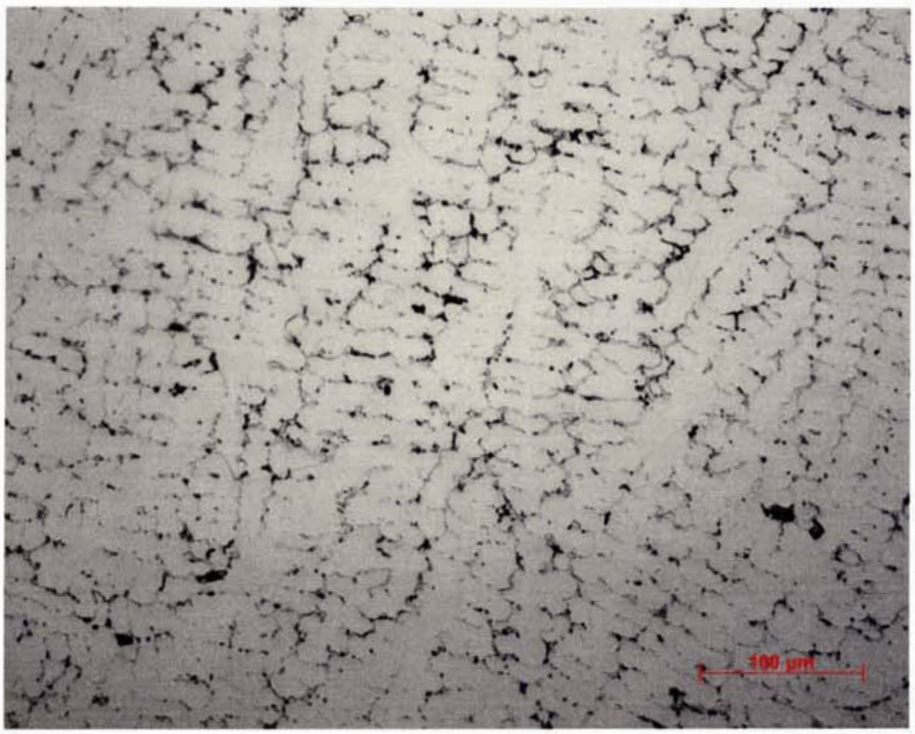

Fig 6.90: Precipitate features of cast Alloy 617 – 5 wt% Pt, 200X, glyceregia - 1020 sec

6.8.3. Optical Micrographs of Wrought Structure

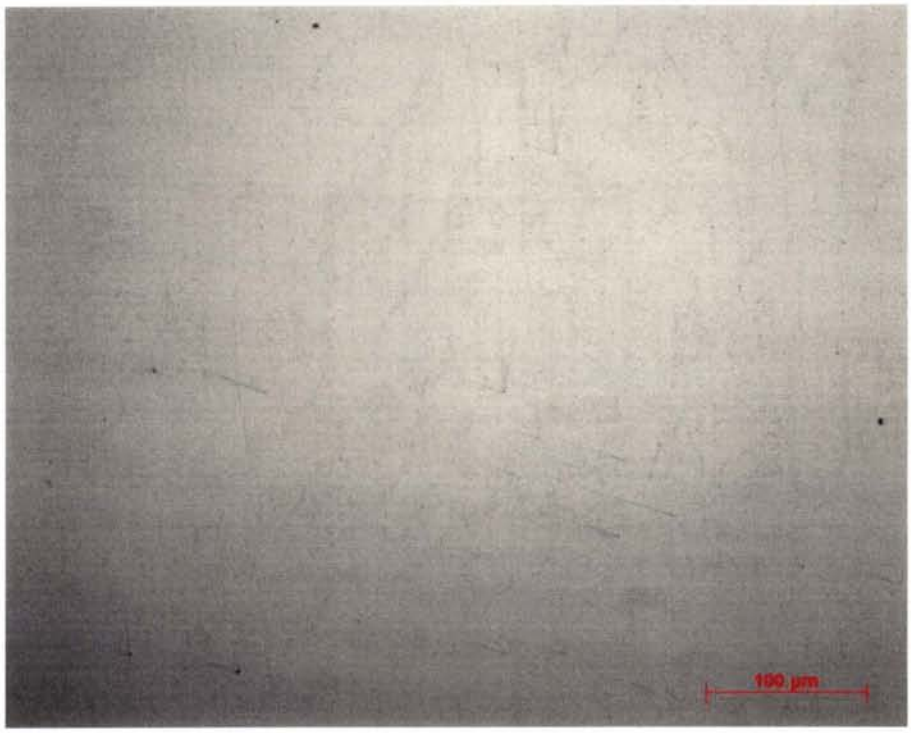

Fig 6.91: Precipitate features of wrought Alloy 617 – 5 wt% Pt, xy plane, 200 X

Fig 6.92: Precipitate features of wrought Alloy 617 – 5 wt% Pt, xz plane, 200 X

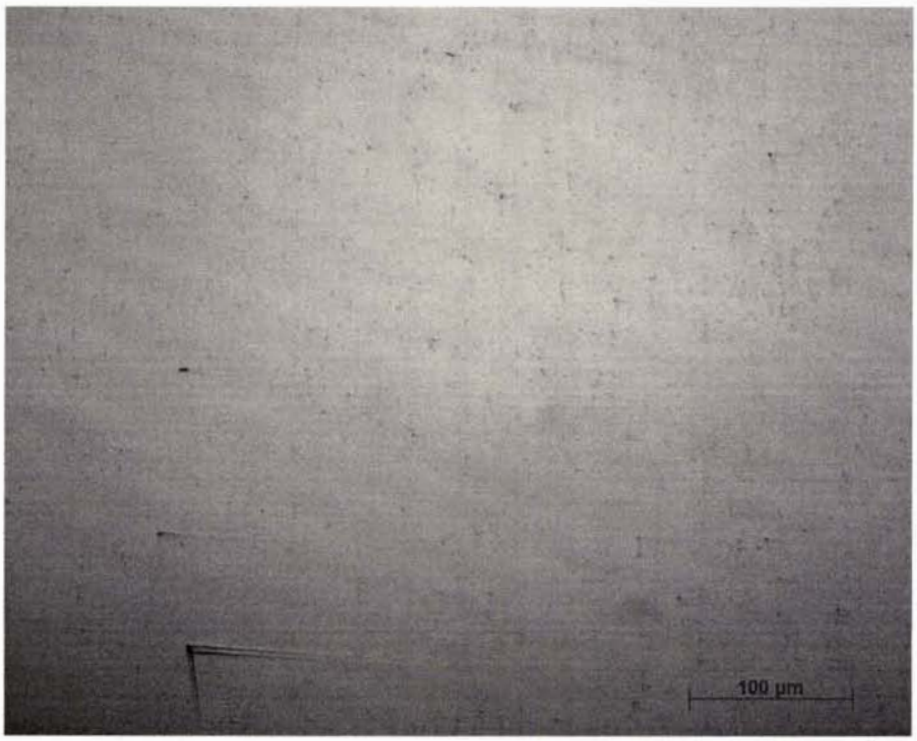

Fig 6.93: Precipitate features of wrought Alloy 617 – 5 wt% Pt, yz plane, 200 X

Fig 6.94: Grain structure and precipitate features of wrought Alloy 617 - 5 wt% Pt, xy plane, 200 X, 10ml Oxalic Acid 90ml H_2O 3ml HCl, 1.5 VDC - 4 sec

Fig 6.95: Grain structure and precipitate features of wrought Alloy 617 - 5 wt% Pt, xz plane, 200 X, 10ml Oxalic Acid 90ml H_2O 3ml HCl, 1 VDC - 3 sec

Fig 6.96: Grain structure and precipitate features of wrought Alloy 617 - 5 wt% Pt, yz plane, 200 X, 10ml Oxalic Acid 90ml H_2O 3ml HCl, 1 VDC - 3 sec

Fig 6.97: Grain structure and precipitate features of wrought Alloy 617 - 5 wt% Pt, xy plane, 500 X, 10ml Oxalic Acid 90ml H_2O 3ml HCl, 1.5 VDC - 4 sec

Fig 6.98: Grain structure and precipitate features of wrought Alloy 617 - 5 wt% Pt, xz plane, 500 X, 10ml Oxalic Acid 90ml H_2O 3ml HCl, 1 VDC - 3 sec

Fig 6.99: Grain structure and precipitate features of wrought Alloy 617 - 5 wt% Pt, yz plane, 500 X, 10ml Oxalic Acid 90ml H_2O 3ml HCl, 1 VDC - 3 sec

6.8.4. Calculated Grain Size

Table 6.12	
Calculated grain sizes for Alloy 617 - 5 Wt % Pt	
Plane	**Diameter (microns)**
xy	12
xz	12
yz	13
Average	**12**

6.8.5. Scanning Electron Micrographs of Wrought Structure

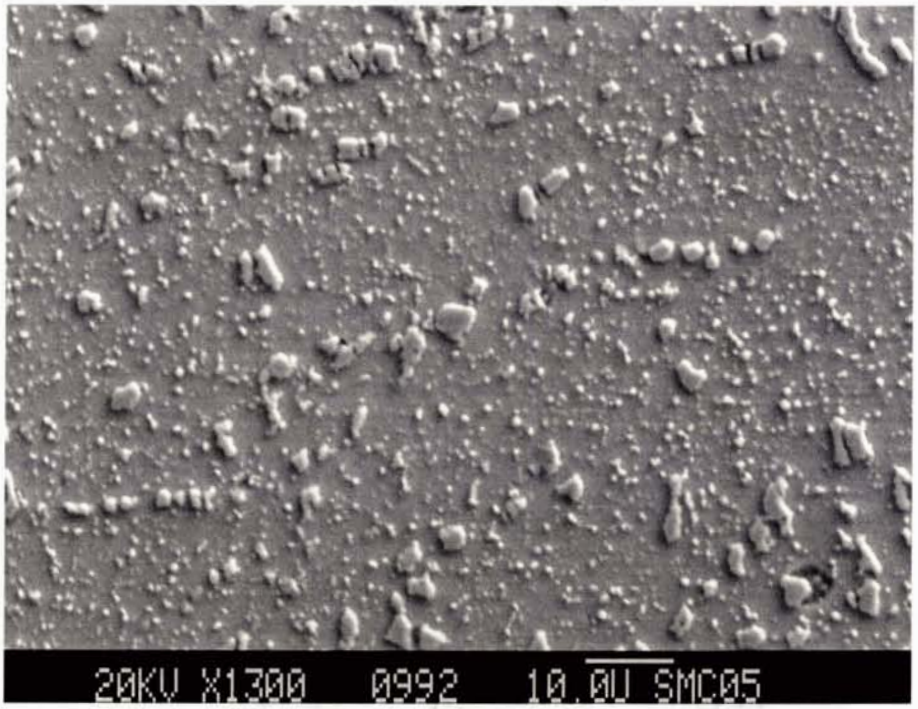

Fig 6.100: Topographical contrast of coarsened precipitates and sub-micron intra-granular precipitates in wrought Alloy 617 - 5 wt% Pt, Secondary Electron Image, 1300 X

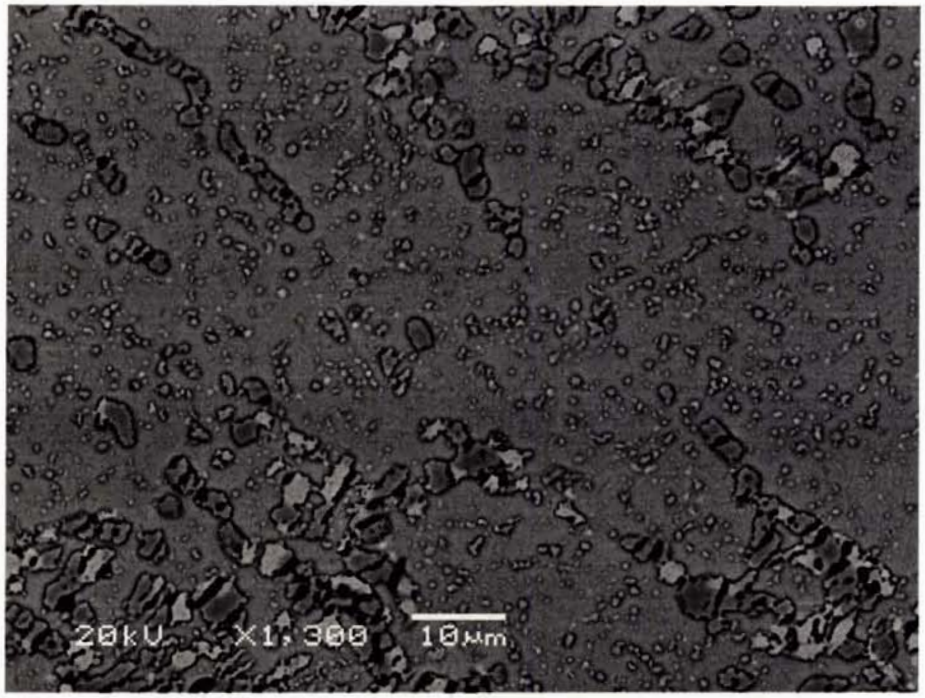

Fig 6.101: Precipitate composition differences determined by contrast within wrought Alloy 617 - 5 wt% Pt, Backscatter Electron Image, 1300 X

6.8.6. Electron Dispersive Spectrometry of Wrought Structure Features

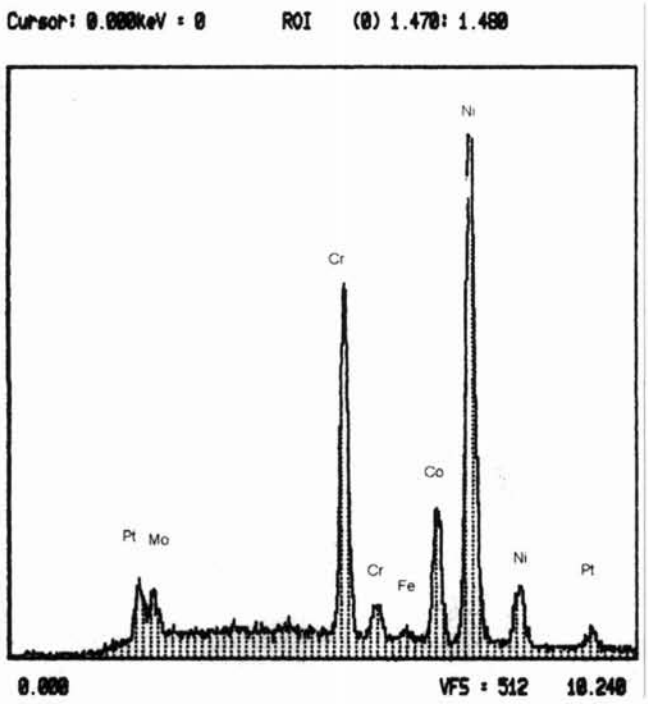

Fig 6.102: Element peak heights for matrix are consistent with compositional analysis of wrought alloy 617 – 5 wt% Pt

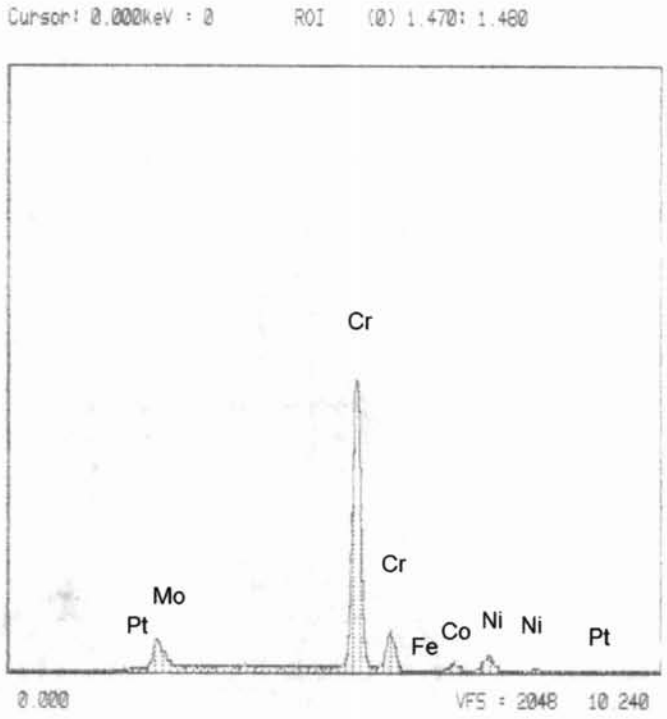

Fig 6.103: High chromium peak for precipitate relative to the matrix for wrought Alloy 617 – 5 wt%

6.8.7. EDS Elemental Dot Map of Precipitates

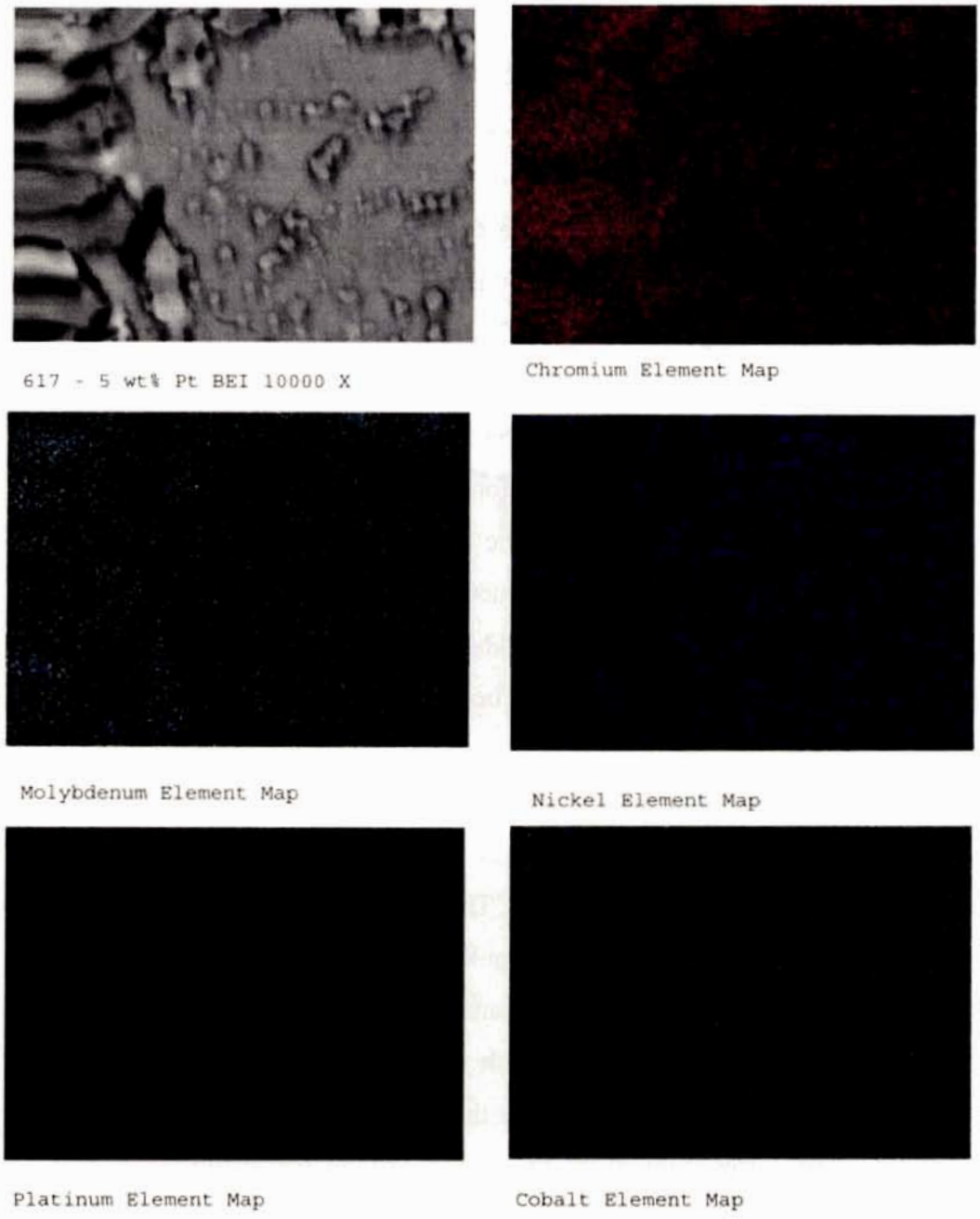

Fig 6.104: Chromium segregation to dark precipitates and molybdenum segregation to bright precipitates in corresponding BEI micrograph of wrought Alloy 617 – 5 wt% Pt, 10000 X, EDS dot map

6.9. Alloy 617 – 15 wt% Pt

Table 6.13 shows the chemistry of the Alloy 617 – 15 wt% Pt alloy and indicates that with the exception of chromium and molybdenum, all major alloying elements are within the compositional specifications for Alloy 617. The chromium and molybdenum composition of this alloy system are only 1.2 wt% and 0.19 wt % below the minimum specified values for Alloy 617, respectively. The platinum composition of this alloy system is only 11.5 wt%, which is low considering the nominal composition is specified as 15 wt%. With the exceptions of aluminum and carbon, all other minor alloying and tramp elements meet compositional specification requirements for Alloy 617. The Aluminum content is only 0.01 wt% below the specified value for Alloy 617. The carbon content is approximately 3.6 times higher than the maximum specified value for Alloy 617. Excessive carbide precipitation is therefore expected to be a problem.

Figure 6.105 shows the results of the JMat Pro thermodynamic model for this material. At 1050 °C (1925 °F) the microstructure of the Alloy 617 – 15 wt% Pt system is predicted to be comprised of less than 10% $M_{23}C_6$ and less than 1% M_6C type carbides. The rest of the microstructure is predicted to be an austenite matrix. No γ' is predicted to precipitate.

Figure 6.106, an optical micrograph of the cast unetched microstructure at 200 X, shows a high volume fraction of 2 – 5 micron size precipitates that have clustered into elongated structures throughout the matrix. These precipitate structures have a slightly darker contrast than the matrix and have pulled during mechanical polishing leaving behind artifacts that indicate their greater hardness relative to the matrix. A very few number of larger coarsened precipitates with significantly darker contrast are present. These precipitates appear to be harder than the matrix for the same reasons described above. Figure 6.107, a micrograph of the etched cast microstructure at 200 X, shows significant preferential etching between large dendrites. This may have occurred due to platinum segregation between dendrites induced by exceeded solubility limits. The effects of etching reveal a greater density of the 2 – 5 micron size precipitates that are present in figure 6.106. The artifacts induced by mechanical polishing have been removed by the etching process.

Optical micrographs of the unetched wrought microstructure are shown for the xy, xz, and yz planes in figures 6.108 – 5.110. These micrographs show precipitate stringing in the direction of rolling. Optical micrographs of the etched wrought structure at 200 X are shown in figures 6.111 – 6.113. These figures show strung out precipitates as well. The strung precipitates in the xy and yz planes generally appear to be much lighter that the microstructure. At 200 X it is very difficult to see the grain structure due to a very high density of extremely fine features. These features may either be precipitates or pits. Figures 6.114 – 6.116 show the same microstructure at 500 X. These micrographs confirm that the grain structure was not adequately developed by the implemented etching technique even though the matrix surrounding precipitates appears to be over etched in each imaged plane. Figure 6.115, a micrograph of the xz plane, shows regions within the matrix that are darker than others. These regions may be grains, but no clearly defined grain structure is apparent. A high volume fraction of precipitates is visible throughout the microstructure in figures 6.111 – 6.113. Many of these precipitates appear to be inter-granular despite the lack of clarity of the grain structure. These precipitates probably have a strong pinning effect on the grain boundaries due to their inter-granular nature and high volume fraction.

In order to adequately reveal the grain structure for measurement, each sample was slightly over-etched and a small amount of hydrochloric acid was added to the electrolyte. Unfortunately, only precipitate features were adequately revealed by the etching process. The high density of inter-granular precipitates made it possible to perform a grain size calculation on the microstructure. Table 6.14 indicates a uniform fine grain size throughout the microstructure. The average grain size for the Alloy 617 – 15 wt% Pt system is 15 microns. There is a significant amount of error associated with this calculated value due to an inadequately revealed grain structure. Nevertheless, a calculated grain size of 15 microns is significantly smaller than the calculated grain size of 110 microns for the specimen of commercial Alloy 617.

Figure 6.117, an SEI mode scanning electron micrograph of the wrought structure at 1300 X, reveals precipitate features with greater clarity than optical microscopy. Coarsened precipitates that are 1 – 7 microns in diameter appear to be raised above the matrix. A homogenous and dense distribution of sub-micron size precipitates is also

present. These precipitates are probably intra-granular due to their distribution features. No grain structure is revealed with SEM techniques. A very few number of pits are visible in Figure 6.116. The pits that are present appear to have formed at precipitate sites. This is a good indication that precipitates are anodic compared to the matrix. A corresponding BEI model scanning electron micrograph, shown in Figure 6.118, reveals some precipitate features with darker contrast than the matrix while others are shown with nearly equal contrast to the matrix. The darker contrasted precipitates have an overall lower atomic weight than the matrix, which points to a $Cr_{21}Mo_2C_6$ composition. The brighter precipitates may have a composition of $(Ni,Co)_3Mo_3C$, due relatively higher atomic weight induced by the molybdenum content. However, the ratio of darker to lighter precipitates in Figure 6.118 does not appear to be equal to the ratio of $M_{23}C_6$ to M_6C precipitates predicted by the JMat Pro model. This result cannot be explained at this time. No grain structures are revealed by either SEM micrograph.

Figures 6.119 and 6.120 show the results of EDS analysis performed on both the matrix and larger coarsened precipitate features. For EDS analysis of the matrix the spot was adjusted to a region of the matrix with a relatively few number of intra-dendritic sub-micron size precipitates in order to reduce the error associated with the results. EDS analysis results of the matrix shows peaks that are consistent with the composition reported in Table 6.13. EDS analysis of the coarsened precipitates shows very high chromium and slightly higher molybdenum peaks compared to the corresponding peaks of the matrix spectrum. These results indicate that the precipitates are most likely $Cr_{21}Mo_2C_6$ type carbides.

EDS elemental dot mapping was performed on the precipitates within the Alloy 617 – 15 wt% Pt microstructure in order to verify their compositions. The results of EDS mapping are shown with a corresponding BEI mode scanning electron micrograph in Figure 6.121. Mapping shows that chromium segregated to darker precipitate features in the corresponding BEI micrograph, while molybdenum segregated to the brighter precipitate features. The darker chromium rich precipitates are most probably $Cr_{21}Mo_2C_6$ carbides that precipitated on the brighter molybdenum rich precipitates, which are probably $(Ni, Co)_3Mo_3C$ carbides.

6.9.1. Chemical Composition and JMat Pro Precipitate Model

Table 6.13			
Composition of Alloy 617 - 15 wt% Pt			
Element	**Wt %**	**Element**	**Wt%**
Carbon	0.534	Phosphorous	0.003
Titanium	0.26	Sulfur	0.003
Aluminum	0.79	Boron	0.003
Chromium	18.2	Iron	0.75
Cobalt	10.6	Copper	0.041
Molybdenum	7.81	Platinum	11.5
Manganese	0.041	Nickel	46.8
Silicon	0.058	Ref [44]	

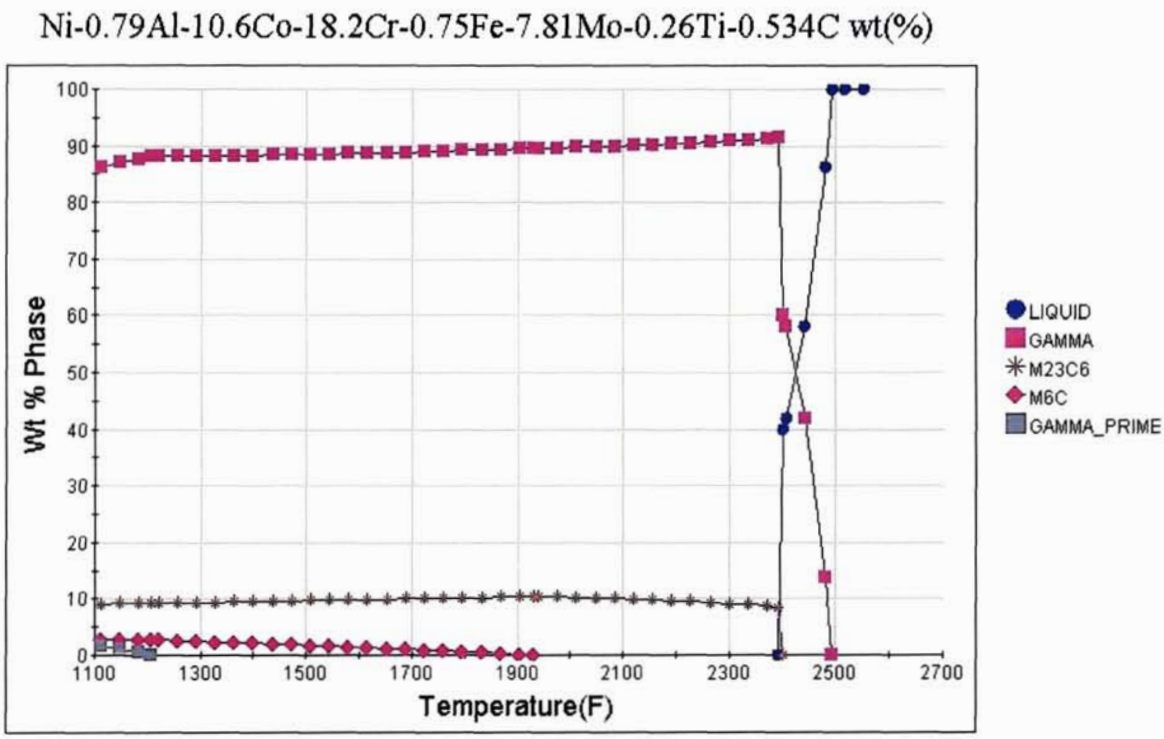

Fig 6.105: JMat Pro thermodynamic precipitate model for Alloy 617 – 15 wt% Pt alloyed system

6.9.2. Optical Micrographs of Cast Structure

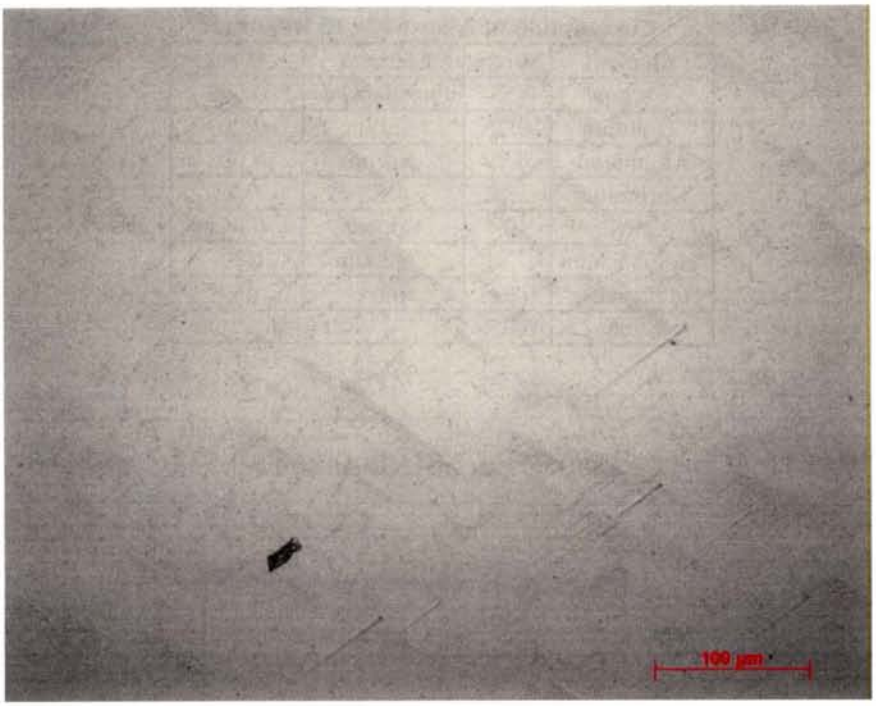

Fig 6.106: Precipitate features of cast Alloy 617 - 15 wt% Pt, 200 X

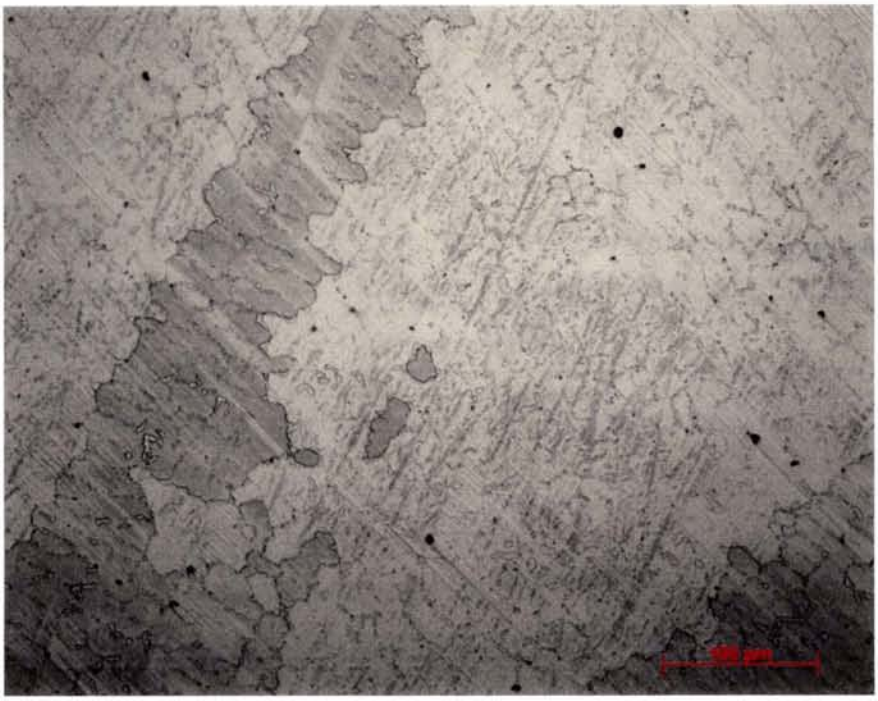

Fig 6.107: Precipitate features of cast Alloy 617 - 15 wt% Pt, 200 X, glyceregia - 1500 sec

6.9.3. Optical Micrographs of Wrought Structure

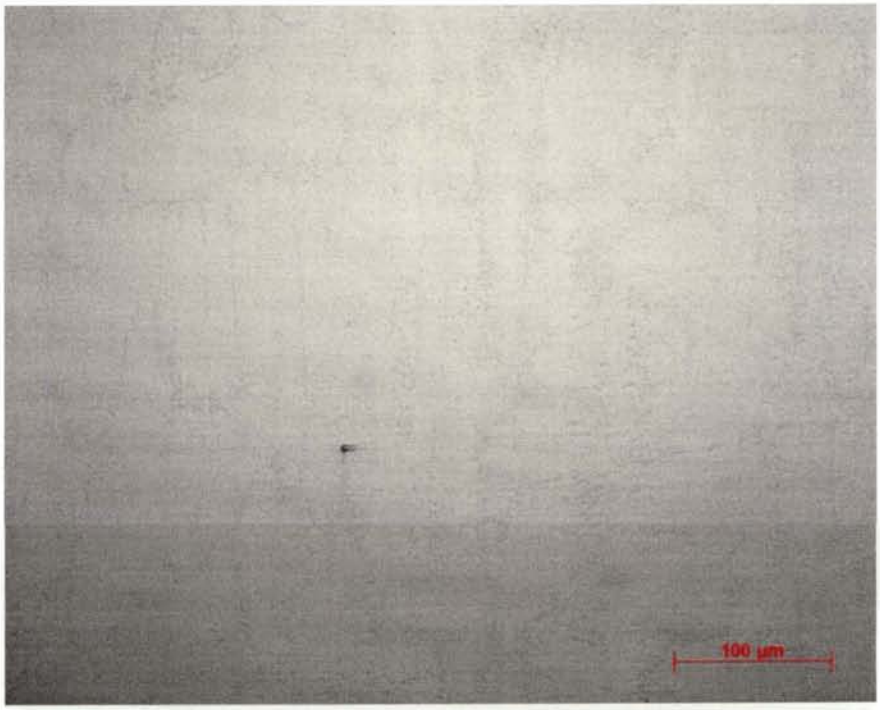

Fig 6.108: Precipitate features of wrought Alloy 617 – 15 wt% Pt, xy plane, 200 X

Fig 6.109: Precipitate features of wrought Alloy 617 – 15 wt% Pt, xz plane, 200 X

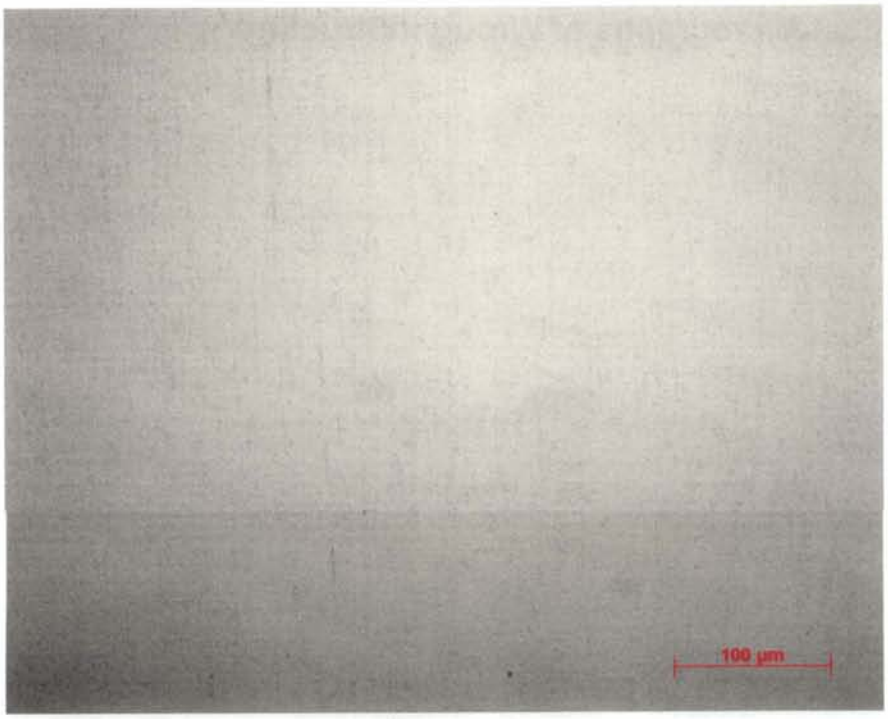

Fig 6.110: Precipitate features of wrought Alloy 617 – 15 wt% Pt, yz plane, 200 X

Fig 6.111: Grain structure and precipitate features of wrought Alloy 617 - 15 wt% Pt, xy plane, 200 X, 10ml Oxalic Acid 90ml H_2O 3ml HCl, 1.5 VDC - 6 sec

Fig 6.112: Grain structure and precipitate features of wrought Alloy 617 - 15 wt% Pt, xz plane, 200 X, 10ml Oxalic Acid 90ml H_2O 3ml HCl, 1 VDC - 7 sec

Fig 6.113: Grain structure and precipitate features of wrought Alloy 617 - 15 wt% Pt, yz plane, 200 X, 10ml Oxalic Acid 90ml H_2O 3ml HCl, 1 VDC - 4 sec

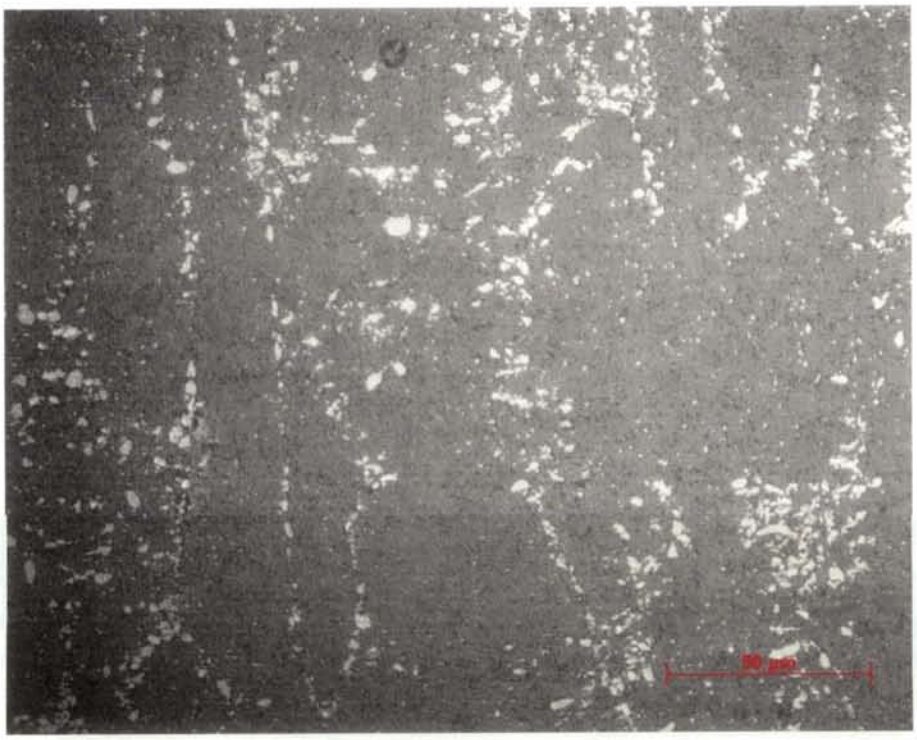

Fig 6.114: Grain structure and precipitate features of wrought Alloy 617 - 15 wt% Pt, xy plane, 500 X, 10ml Oxalic Acid 90ml H_2O 3ml HCl, 1.5 VDC - 6 sec

Fig 6.115: Grain structure and precipitate features of wrought Alloy 617 - 15 wt% Pt, xz plane, 500 X, 10ml Oxalic Acid 90ml H_2O 3ml HCl, 1 VDC - 7 sec

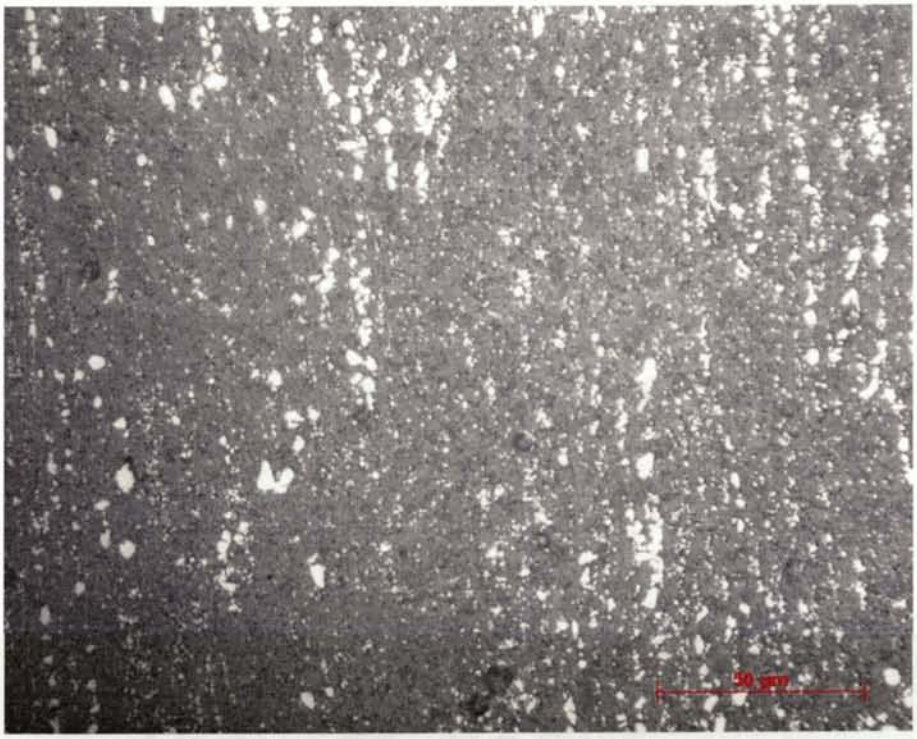

Fig 6.116: Grain structure and precipitate features of wrought Alloy 617 - 15 wt% Pt, yz plane, 500 X, 10ml Oxalic Acid 90ml H_2O 3ml HCl, 1 VDC - 4 sec

6.9.4. Calculated Grain Size

Table 6.14	
Calculated grain sizes for Alloy 617 - 15 Wt % Pt	
Plane	**Diameter (microns)**
xy	16
xz	14
yz	14
Average	**15**

6.9.5. Scanning Electron Micrographs of Wrought Structure

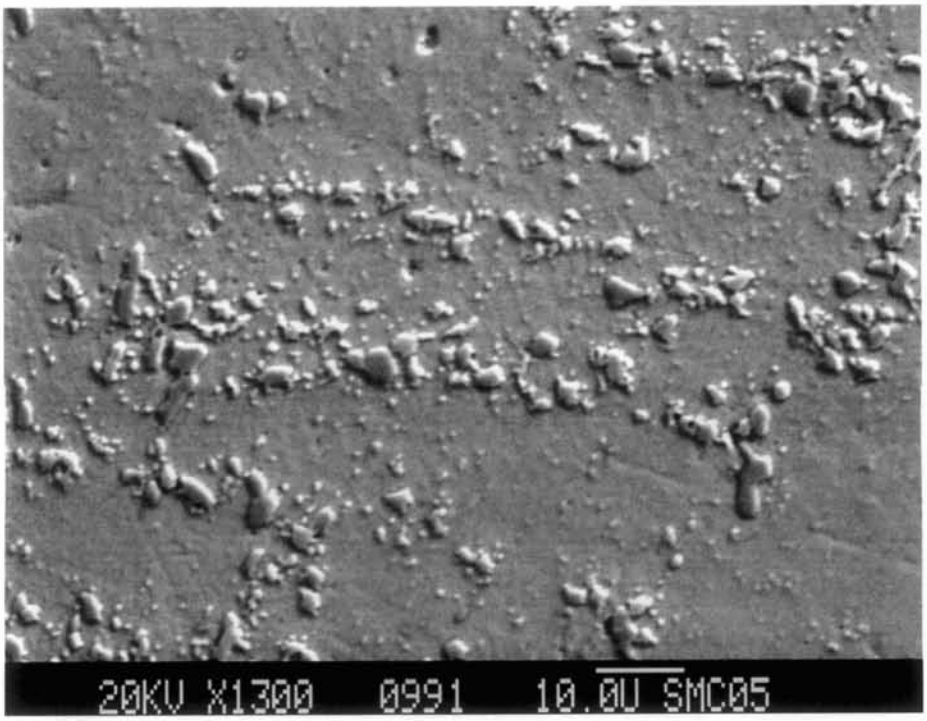

Fig 6.117: Topographical contrast of coarsened and sub-micron precipitates in wrought Alloy 617 - 15 wt% Pt, Secondary Electron Image, 1300 X

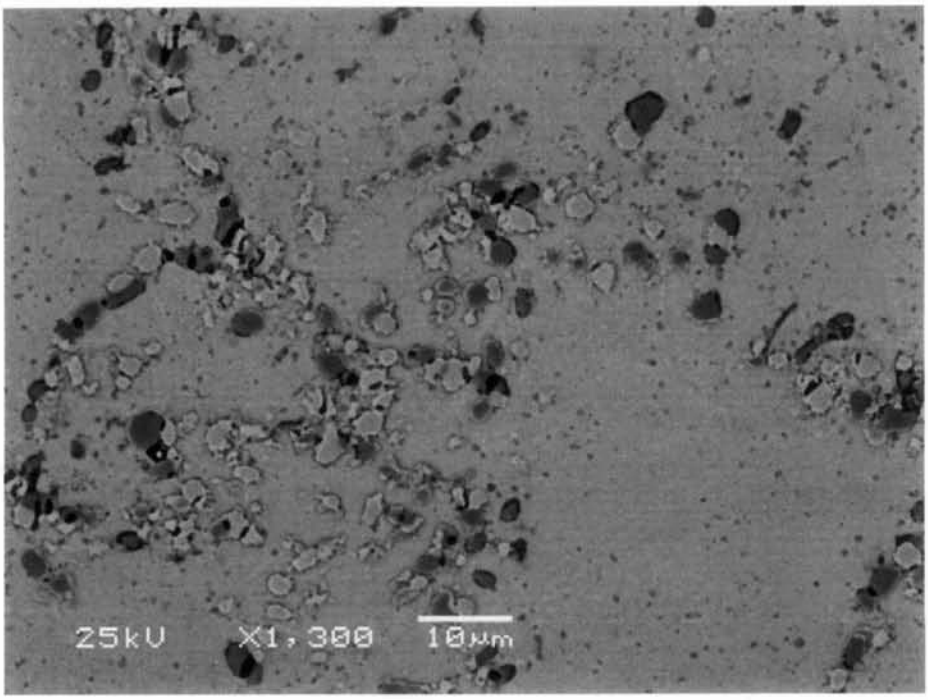

Fig 6.118: Precipitate composition differences distinguished by contrast in wrought Alloy 617 - 15 wt% Pt, Backscatter Electron Image, 1300 X

6.9.6. Electron Dispersive Spectrometry of Wrought Structure Features

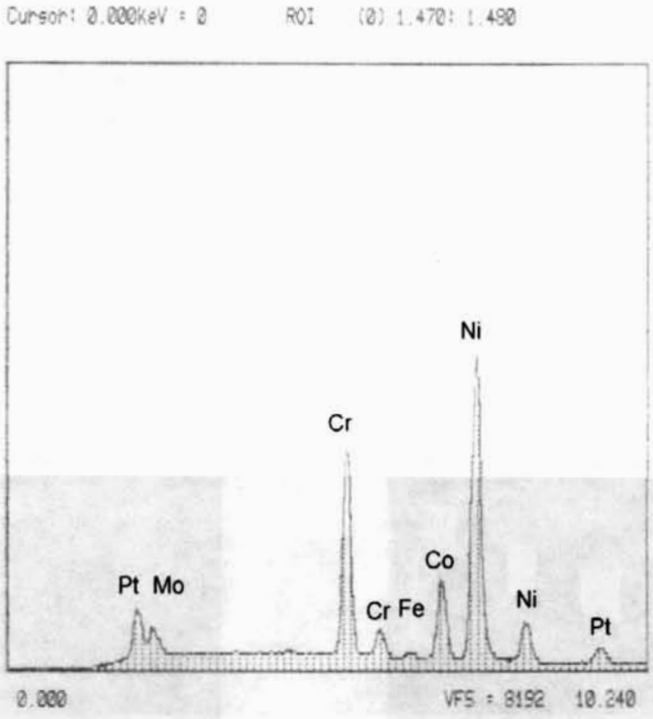

Fig 6.119: Element peak heights for matrix are consistent with compositional analysis of wrought Alloy 617 – 15 wt% Pt

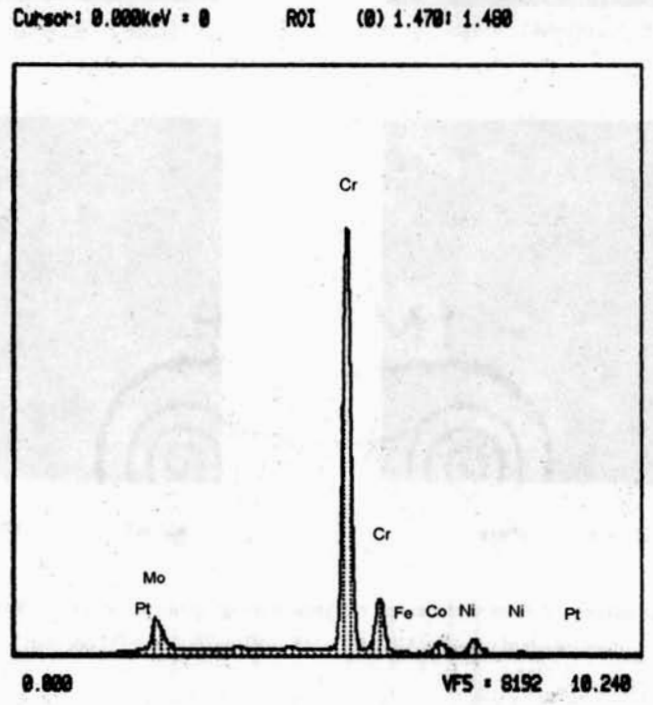

Fig 6.120: High chromium peak for precipitate relative to the matrix for wrought Alloy 617 – 15 wt% Pt

6.9.7 EDS Elemental Dot Map of Precipitates

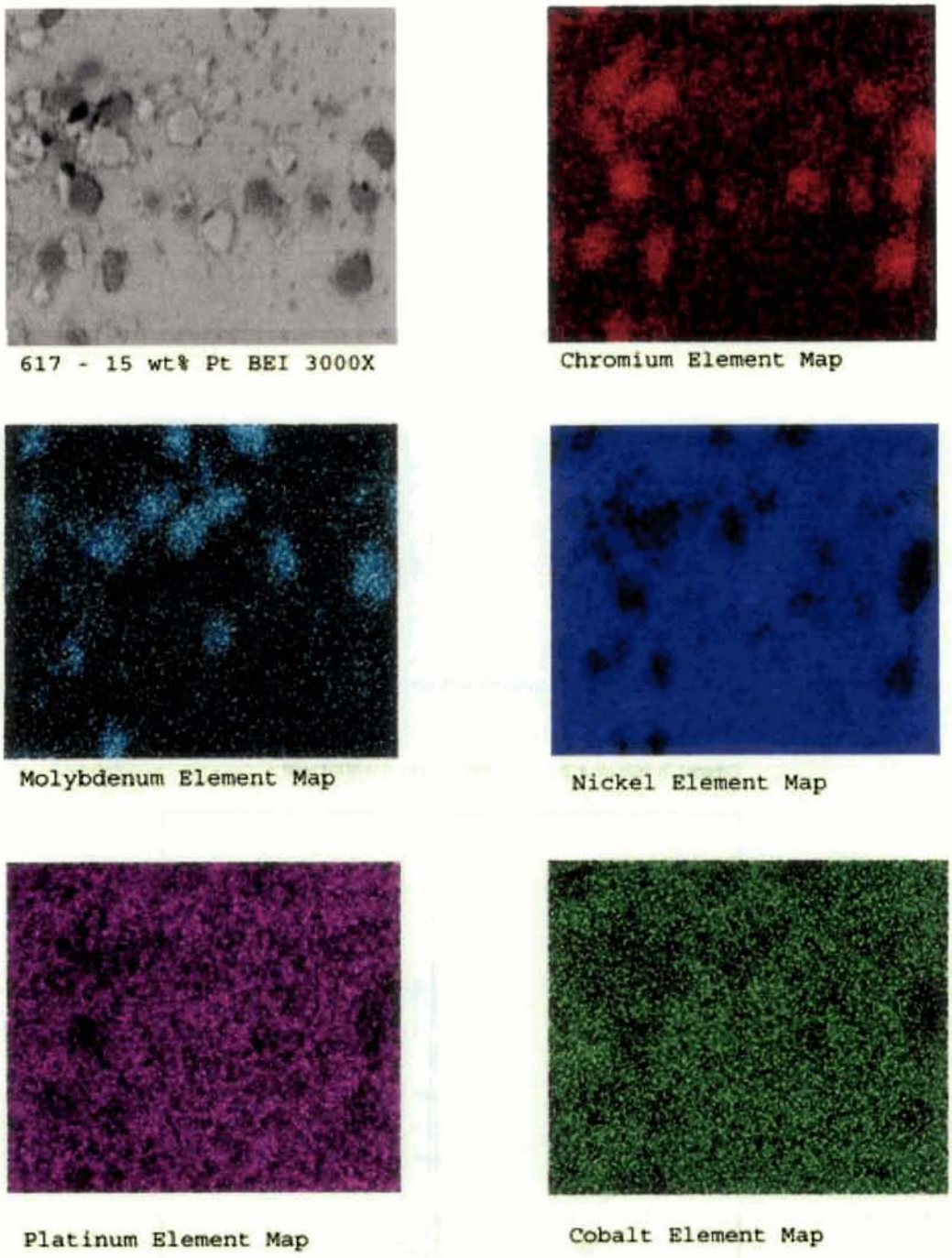

Fig 6.121: Chromium segregation to dark precipitates and molybdenum segregation to bright precipitates in corresponding BEI micrograph of wrought Alloy 617 – 15 wt% Pt, 3000 X, EDS dot map

6.10. Alloy 617 – 30 wt% Pt

Table 6.15 shows the chemistry of the Alloy 617 – 30 wt% Pt alloy and indicates a uniform compositional reduction of major alloying elements below their specified values for Alloy 617. This result is acceptable in light of the high platinum addition to this alloy. The platinum composition is reported as 26 wt %, which is somewhat low considering a nominal composition of 30 wt %. With the exception of aluminum and carbon, all minor alloying and tramp element compositions are within the specified limits for Alloy 617. The aluminum composition of this alloy is 0.19% lower than the minimum for Alloy 617. The carbon content of this alloy is 1.16 times higher than the maximum specified value for Alloy 617, which, in light of the other alloy systems studied herein, is only marginally unacceptable. Nevertheless, a carbon content that is higher than the maximum specified limit is expected to cause greater carbide precipitation than what is normally present in Alloy 617.

Figure 6.122 shows the results of the JMat Pro thermodynamic model for this material. At 1050 °C (1925 °F) the microstructure of the Alloy 617 – 30 wt% Pt system is predicted to be comprised of 3% $M_{23}C_6$. The rest of the microstructure is predicted to be an austenite matrix. No γ' is predicted to precipitate.

Figure 6.123, an optical micrograph of the cast unetched microstructure at 200 X, shows a distribution of very fine 1 micron size precipitates. Some of these precipitates have pulled from the matrix during mechanical polishing leaving behind 50 – 100 micron "comet tails". This indicates that these small precipitates are harder than the matrix. Figure 6.124, a micrograph of the cast microstructure in the etched condition at 200 X, clearly reveals the presence of fine precipitates that have agglomerated into 20 – 50 micron elongated patterns. A few number of relatively darker 2 – 7 micron size coarsened spherical precipitates are also visible in Figure 6.124.

Optical micrographs of the un-etched wrought structure at 200 X are shown for the xy, xz, and yz planes in figures 6.125 – 6.127. These micrographs barely show precipitate stringing in the direction of rolling. Precipitates in these micrographs are not easily visible due to low contrast difference from the matrix and low volume fraction

compared to the other alloys studied herein. Corresponding micrographs in the etched condition at 200 X are shown in figures 6.128 – 6.130. These micrographs more clearly reveal precipitate features. Figures 6.128 – 6.130 show a structure throughout the matrix consisting of fine blocky grains of varying contrast. True grain boundaries may actually be camouflaged by annealing twins. Figures 6.131 – 6.133 show corresponding optical micrographs at 500 X. These micrographs indicate that the grain structure was not adequately revealed by the applied etching technique. Figures 6.131 – 6.133 are most useful for revealing the presence of annealing twins throughout the microstructure.

Each wrought structure was slightly over etched in an attempt to reveal the grain structure for measurement. The addition of 3 milliliters hydrochloric acid to the electrolyte had negligible beneficial effects on revealing the grain structure for measurement. Fortunately, the resistance of the Alloy 617 – 30 wt% Pt system to the applied etching technique indicates good resistance to corrosive environments. Only annealing twins were adequately revealed by the applied etching technique. These features enabled a measurement of the average grain size in each imaged plane. Table 6.16 indicates a very fine uniform grain structure throughout the microstructure. The average grain size was measured to be 17 microns. This value is inaccurate due to errors associated a poorly developed grain structure. Nevertheless, the measured grain size is extremely fine compared to the measured value of 110 microns for the commercial Alloy 617 sample.

Figure 6.134, an SEI mode scanning electron micrograph of the wrought structure at 1300 X, indicates that all precipitates have pitted from the matrix. All pit sites appear to have very discrete boundaries, which indicate that the matrix itself was very well cathodically protected during the etching process. Figure 6.132 also shows a dense homogeneous distribution of pits where fine sub micron-sized precipitates were once present. Due to their distribution features, these precipitates were probably intra-granular. Figure 6.135, an SEI mode scanning electron micrograph at 3000 X, reveals a fine lamellar structure with inter-lamellar spacing of approximately 0.2 – 0.3 microns. A BEI mode scanning electron micrograph shown in Figure 6.136 reveals the inter-lamellar boundaries with dark contrast. This indicates that a second phase may have precipitated within the microstructure. The orientation of the lamellar two phase structure shown in

figures 6.135 and 6.136 changes between individual grains. Figure 6.135 also shows a few 3 – 5 micron size precipitates that did not pit during the etching process. One of these precipitates appears to have cracked as a result of the cold working process. This serves as further evidence that the precipitates were present within the microstructure prior to annealing.

Figures 6.137 and 6.138 show the results of EDS analysis performed on the matrix and on pitted precipitate features. Figure 6.137 shows elemental peak heights for the matrix that are consistent with the compositional analysis results reported in Table 6.15. Figure 6.136 shows an elemental spectrum that is identical to the matrix, which indicates that the features analyzed are indeed pits.

6.10.1. Chemical Composition and JMat Pro Precipitate Model

Table 6.15			
Composition of Alloy 617 - 30 wt% Pt			
Element	**Wt %**	**Element**	**Wt%**
Carbon	0.174	Phosphorous	0.006
Titanium	0.22	Sulfur	0.006
Aluminum	0.61	Boron	0.004
Chromium	15.7	Iron	0.66
Cobalt	8.39	Copper	0.11
Molybdenum	6.60	Platinum	26.0
Manganese	0.022	Nickel	37.3
Silicon	0.26	Ref [44]	

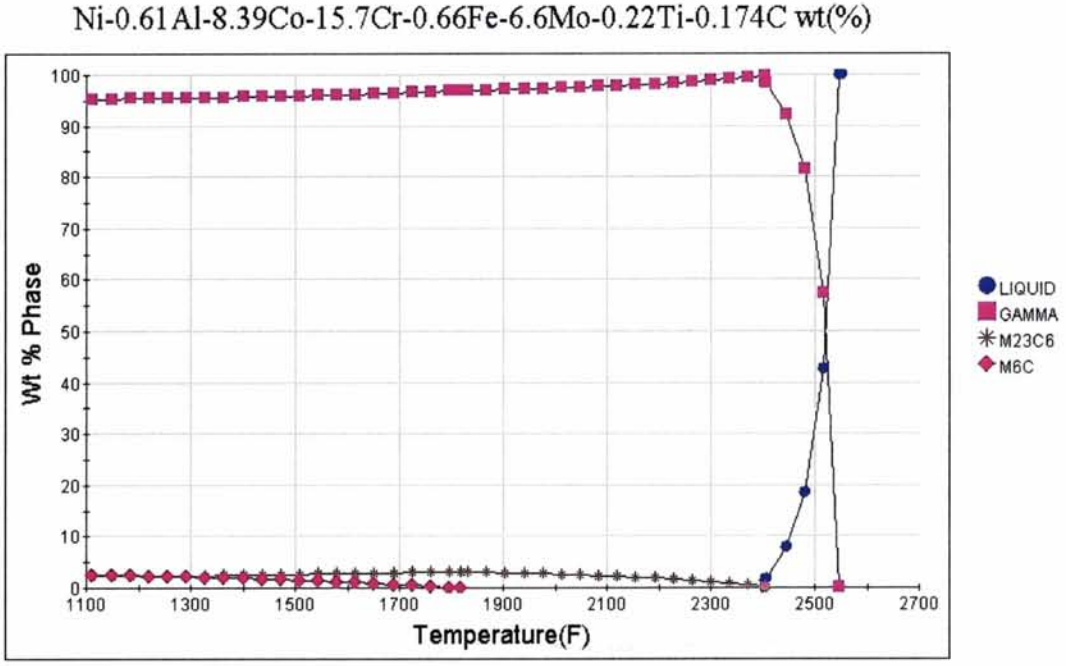

Fig 6.122: JMat Pro thermodynamic precipitate model for Alloy 617 – 30 wt% Pt alloyed system

6.10.2. Optical Micrographs of Cast Structure

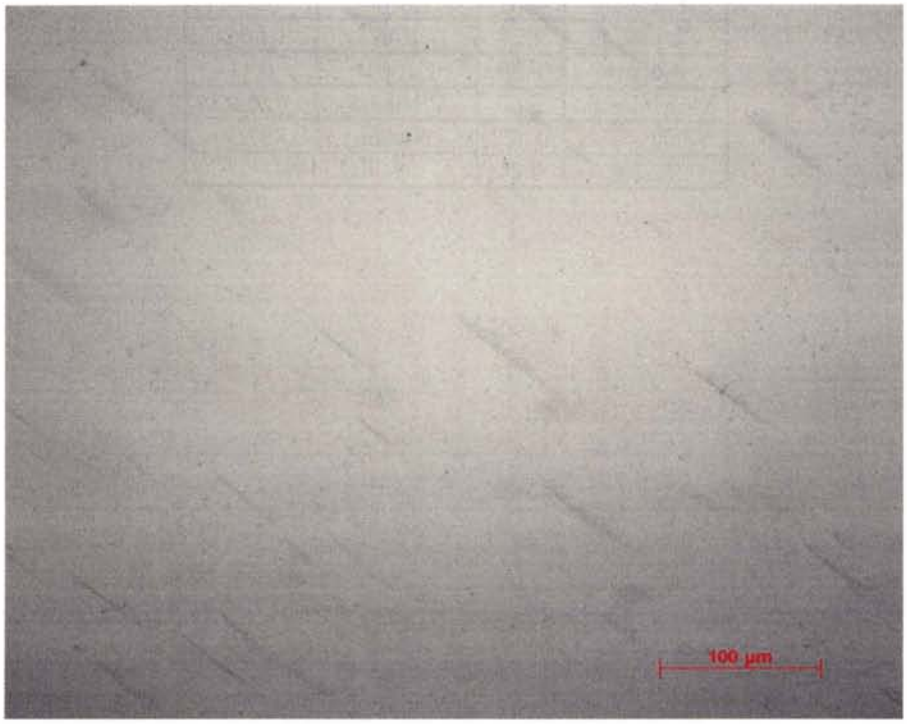

Fig 6.123: Precipitate features of cast Alloy 617 - 30 wt% Pt, 200 X

Fig 6.124: Precipitate features of cast Alloy 617 - 30 wt% Pt, 200 X, glyceregia - 480 sec

6.10.3. Optical Micrographs of Wrought Structure

Fig 6.125: Precipitate features of wrought Alloy 617 – 30 wt% Pt, xy plane, 200 X

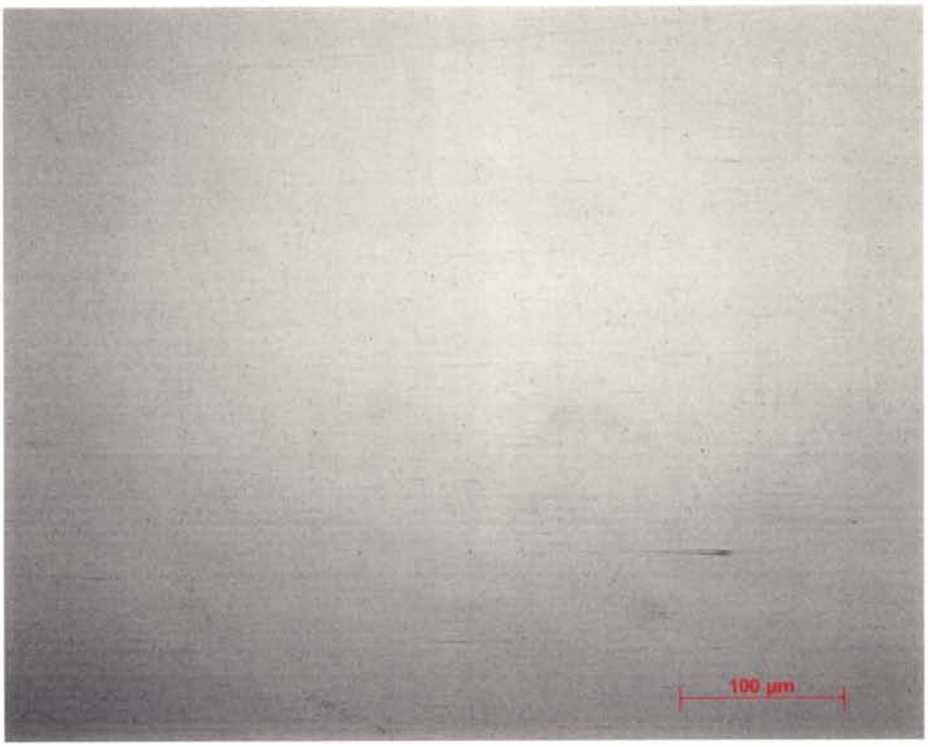

Fig 6.126: Precipitate features of wrought Alloy 617 – 30 wt% Pt, xz plane, 200 X

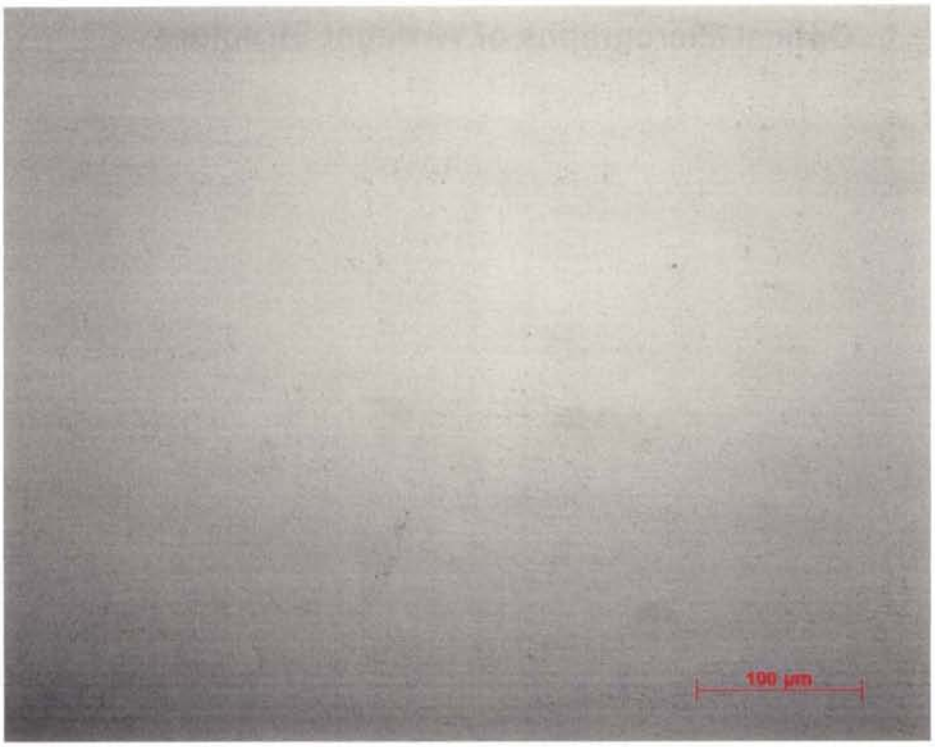

Fig 6.127: Precipitate features of wrought Alloy 617 – 30 wt% Pt, yz plane, 200 X

Fig 6.128: Grain structure, annealing twins, and precipitate features of wrought Alloy 617 - 30 wt% Pt, xy plane, 200 X, 10ml Oxalic Acid 90ml H_2O 3ml HCl, 1.5 VDC - 12 sec

Fig 6.129: Grain structure, annealing twins, and precipitate features of wrought Alloy 617 - 30 wt% Pt, xz plane, 200 X, 10ml Oxalic Acid 90ml H_2O 3ml HCl, 1.5 VDC - 8 sec

Fig 6.130: Grain structure, annealing twins, and precipitate features of wrought Alloy 617 - 30 wt% Pt, yz plane, 200 X, 10ml Oxalic Acid 90ml H_2O 3ml HCl, 1.5 VDC - 6 sec

Fig 6.131: Grain structure, annealing twins, and precipitate features of wrought Alloy 617 - 30 wt% Pt, xy plane, 500 X, 10ml Oxalic Acid 90ml H_2O 3ml HCl, 1.5 VDC - 12 sec

Fig 6.132: Grain structure, annealing twins, and precipitate features of wrought Alloy 617 - 30 wt% Pt, xz plane, 500 X, 10ml Oxalic Acid 90ml H_2O 3ml HCl, 1.5 VDC - 8 sec

Fig 6.133: Grain structure, annealing twins, and precipitate features of wrought Alloy 617 - 30 wt% Pt, yz plane, 500 X, 10ml Oxalic Acid 90ml H_2O 3ml HCl, 1.5 VDC - 6 sec

6.10.4. Calculated Grain Size

Table 6.16	
Calculated grain sizes for Alloy 617 - 30 Wt % Pt	
Plane	**Diameter (microns)**
xy	18
xz	17
yz	16
Average	**17**

6.10.5. Scanning Electron Micrographs of Wrought Structure

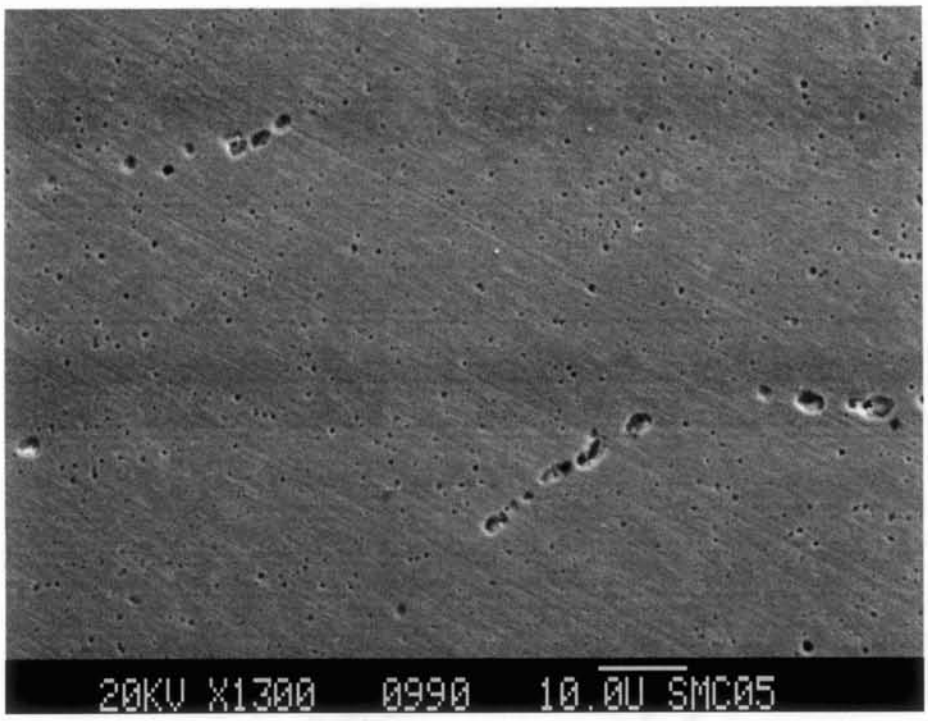

Fig 6.134: Pitted precipitate sites in wrought Alloy 617 - 30 wt% Pt, Secondary Electron Image, 1300 X

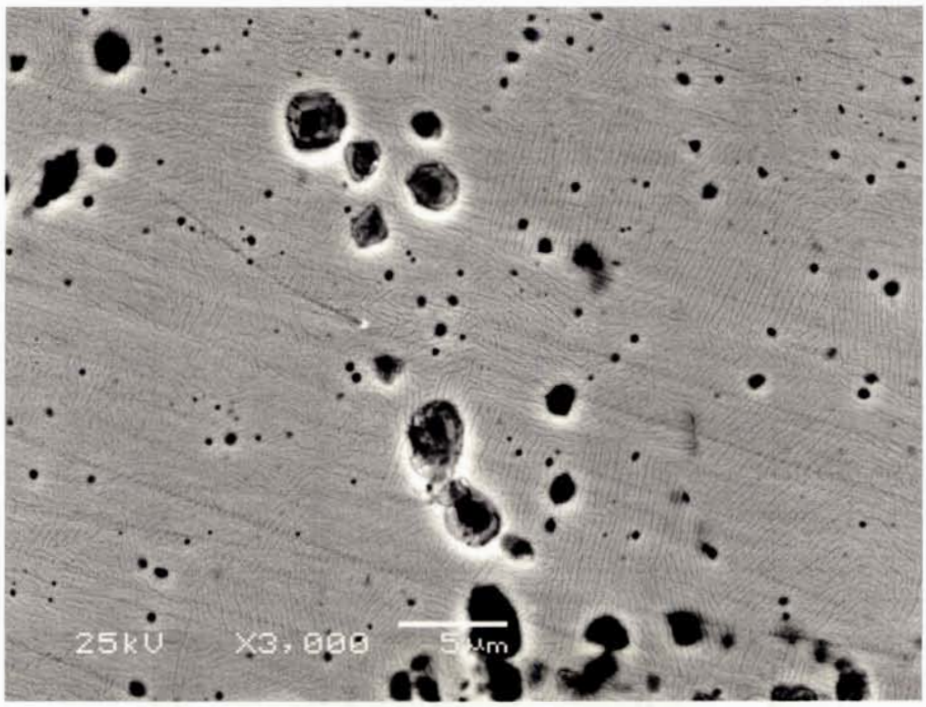

Fig 6.135: Lamellar structure of two phase system and cracked carbides in wrought Alloy 617 - 30 wt% Pt, Secondary Electron Image, 6000 X

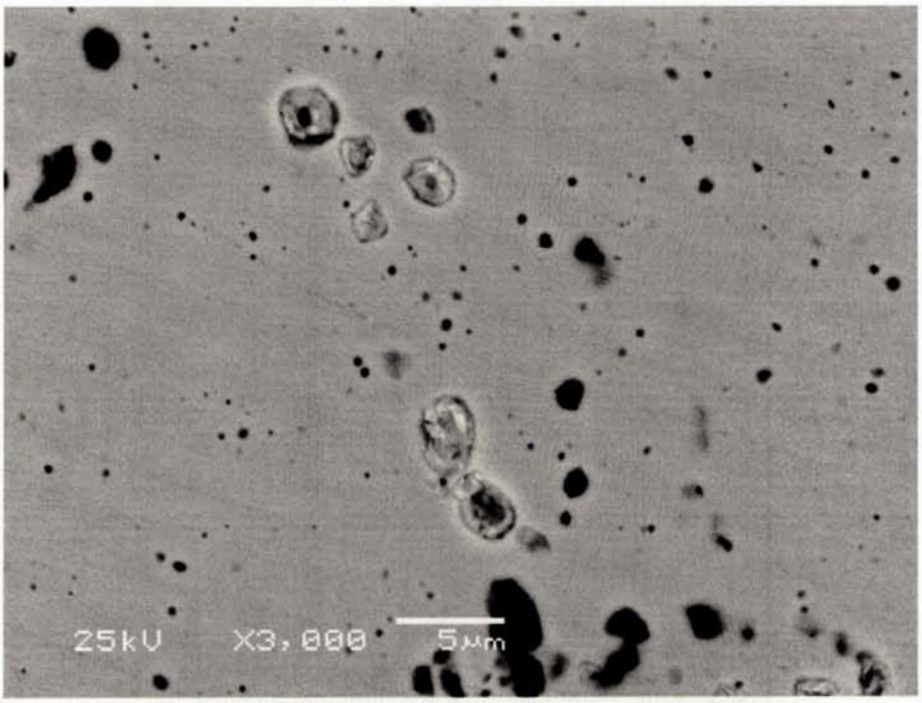

Fig 6.136: Compositional differences between lamellar phases are shown by contrast difference in the wrought Alloy 617 - 30 wt% Pt, Backscatter Electron Image, 6000 X

6.10.6 Electron Dispersive Spectrometry of Wrought Structure Features

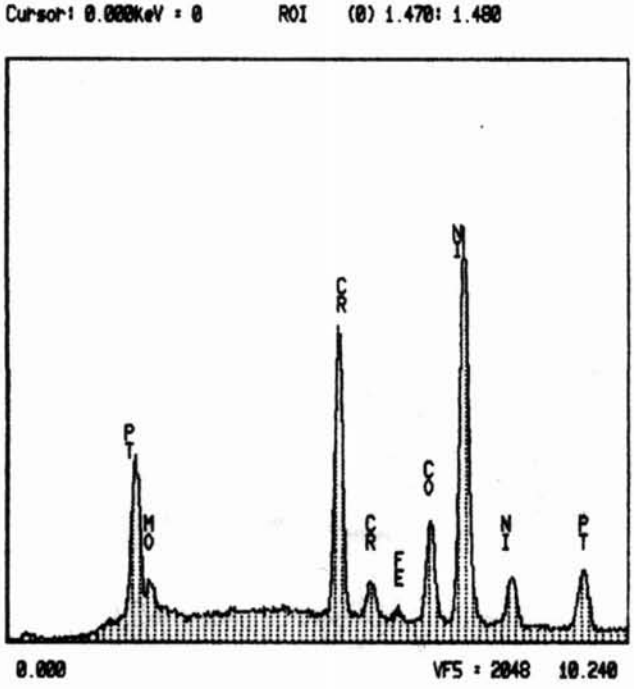

Fig 6.137: Element peak heights for matrix are consistent with compositional analysis of wrought Alloy 617 – 30 wt% Pt

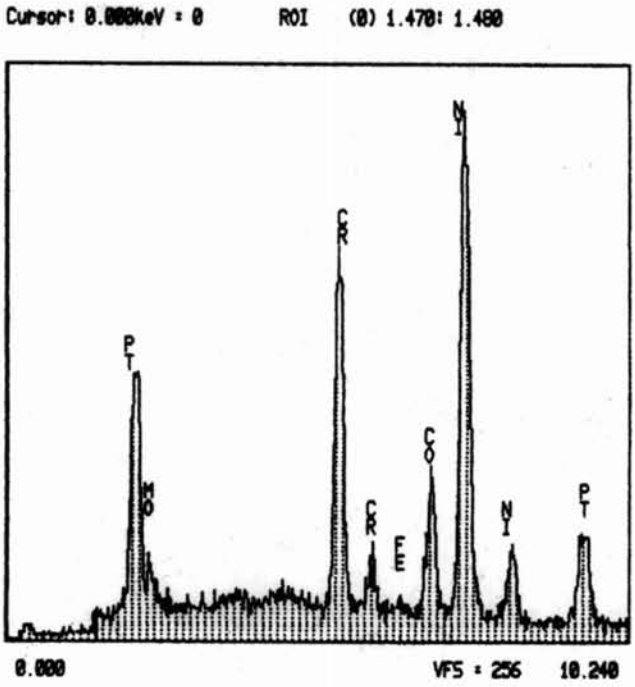

Fig 6.138: Elemental peak heights for pit / precipitate features are identical to elemental peak heights for the matrix of wrought Alloy 617 – 30 wt% Pt

7. Discussion

7.1 Overview of General Observations

The most significant factors affecting the microstructural stability of each alloy system characterized herein are related to carbon and platinum composition. Platinum composition had the strongest effect on resistance to the etching techniques and the formation of annealing twins. With the exception of the Alloy 617 – 30 wt% Pt material, elemental segregation of platinum due to compositions above solubility limits is unlikely. All of the optical and SEM micrographs of alloy systems with higher platinum compositions indicate good solubility within the matrix because no obvious second phases precipitate, except for within the above mentioned system. Trends observed across each alloy system show that carbon content has a strong effect on grain structure and precipitate characteristics. The effects of both platinum and carbon content are found to be very important to microstructural stability.

7.2 Etching Results

Electrolytic etching was performed on wrought samples to save the excessive amount of time that was required to chemically etch cast samples. The applied etching technique for each wrought alloy required much lower voltage than the typical 5 VDC that is used to etch commercial samples of wrought Alloys 800 HT and 617. Lower voltages were necessary due to small sample sizes and because of the short amount of time required to develop microstructural features. The etched microstructures of alloy systems with nominal platinum compositions of 2 and 5 wt% Pt showed adequate grain structure features at the expense of slight over-etching. For alloy systems with nominal platinum compositions of 15 and 30 wt % the applied etching techniques did not reveal the grain structures to the desired level of clarity required for accurate grain size determination. Grain size measurements for these systems were carried out with a large

amount of subjectivity aided by inter-granular precipitate distribution and annealing twin features.

7.3 Grain Structure

Grain measurements of the orthogonal xy, xz, and yz planes indicate a uniform grain structure within each alloy system. Therefore, the annealing process was performed for sufficient time to fully develop wrought structures with no grain orientation relative to the rolling direction. The grain structure of each alloy system characterized herein was measured to be extremely fine relative to the respective grain structures of Alloys 800 HT and 617. The grain structures of the Alloy 800 HT – Pt systems were, on the whole, somewhat larger than those of the Alloy 617 – Pt systems. This can be attributed to the grain refining effect of carbide precipitation, which was less prevalent within the Alloy 800 HT – Pt systems. Fine grain structures have a negative effect on high temperature mechanical properties. Microstructures with smaller grain sizes have an overall larger grain boundary area, which renders them more susceptible to creep deformation by grain boundary sliding.

7.4 Platinum Composition Effects

Micrographs of the etched cast structures of alloy systems with higher platinum compositions show preferential corrosion between dendrites as well as rings of unetched material around some precipitates. Some limited degree of platinum segregation may have occurred within these respective cast microstructures. Optical micrographs of wrought structures with the same platinum compositions do not show any sign of elemental segregation. This may indicate that the development of wrought structures has a homogenizing effect on any platinum that may have segregated in the cast condition. Upon initial observation the Alloy 800 HT – 15 wt% Pt appears to be an exception to this observation. Figure 6.50, a BEI micrograph, indicates that a heavier element segregated to the grain boundaries of the Alloy 800 HT – 15 wt% Pt system. The apparent

segregation appears in the form of decorated grain boundaries characterized by a discrete interface with the matrix inside grains. This behavior is not characteristic of elemental segregation due to compositions above solubility limits. If platinum had exceeded the solubility limit within the base chemistry of Alloy 800 HT, either a second phase would have precipitated with an intra-granular pearlite-like structure, or there would be a gradually increasing platinum enrichment from the interior of grains to grain boundaries. Furthermore, scanning electron micrographs of the Alloy 800 HT – 30 wt% Pt system show a homogenous matrix with no apparent contrast difference by backscatter imaging, which indicates that no segregation occurred within this sample. These results indicate that segregation in the 15 wt% Pt system may not have occurred due to a platinum composition greater than the solubility limits. The reason for the apparent segregation is not understood at this time. Despite this un-explainable phenomenon, scanning electron microscopy indicates that platinum is soluble in the base Alloy 800 HT chemistry up to 30 wt%. These results are in good agreement with the Hume-Rothery rules for solubility within solid solutions.

With the exception of the 30 wt% Pt sample, scanning electron micrographs indicate that the matrix of each base Alloy 617 sample consists of a single phase. Figure 6.135, an SEI mode scanning electron micrograph at 3000 X, shows that the Alloy 617 – 30 wt% Pt system has a two phase microstructure that resembles pearlite. Figure 6.136 shows by contrast difference with backscatter electrons that the observed microstructure is composed of two different compositions. This result indicates that the observed structure consists of two distinct phases rather than needle-like grains. It is very likely that the two phase structure formed due to a platinum composition above the solubility limits of the base Alloy 617 chemistry. It is also possible that the high carbon content is not soluble in the chemistry of the alloy system due to high platinum composition. Hume-Rothery rules do not explain the observed results well. According to these rules, if any element were to segregate due to high size factor difference it would be molybdenum because its metallic radius has the largest size difference (10.69%) from the average metallic radius of the alloy system. Platinum, however, only has a size difference of 3.05%. Segregation of platinum could have occurred due to its high electro-negativity (2.28 eV); however, if it had segregated from the matrix for this reason it should also

have done so in the Alloy 800 HT – 30 wt% Pt system. A survey of binary phase diagrams for each of the major alloying elements in Alloy 617 with platinum indicates that platinum could form a two phase system with chromium. The binary Pt-Cr phase diagram shows that 30 wt% platinum in a pure chromium matrix may consist of approximately 37.6% Cr and 62.4% Cr_3Pt at the annealing temperature of 1050 °C. If such a system did form, it should also have been visible within the Alloy 800 HT – 30 wt% Pt system since both systems have nearly equal chromium and platinum compositions. At present, the observed segregation in the Alloy 617 – 30 wt% Pt system cannot be fully explained. The microstructure of this system will not have favorable mechanical properties, and is expected to exhibit poor corrosion resistance properties.

Initially increasing platinum compositions within each base alloy system appear to have an effect of producing larger grain sizes. High platinum compositions, however, have a camouflaging effect on the etched grain structure. This camouflaging effect may indicate that the above observation is not real. For instance, as shown in figures B.42 – B.44, grain size measurements performed on the Alloy 800 HT – 15 wt% Pt system indicate a grain size of 25 microns. Figures 6.49 and 6.50 show elemental segregation to grain boundaries within the Alloy 800 HT – 15 wt% Pt system, which by qualitative inspection indicates a finer grain size than 25 microns.

The base alloy systems with higher platinum compositions exhibit greater corrosion resistance to the applied etching techniques. Over-etching of these systems produces a uniform darkening of the surface rather than over-development of grain boundary features.

Platinum composition is found to have a strong effect on the formation of annealing twins within both of the Alloy 800 HT – Pt and Alloy 617 – Pt systems. In general, as platinum composition is increased so does the formation of annealing twins. Annealing twins are first present within the Alloy 800 HT – 5 wt% Pt system and become the dominant microstructural feature in the 30 wt% Pt system. Annealing twins are not visible in the Alloy 617 – Pt system until the platinum composition reaches the nominal value of 30 wt%. The width of a twin in a material is inversely proportional to its stacking fault energy [3, 47]. As evidenced by the increase in twinning density, increasing platinum composition within the base alloy chemistries has the effect of

lowering the stacking fault energy of the respective alloy system. This effect is much more prevalent in the base Alloy 800 HT systems than in the Alloy 617 systems. FCC structures with low stacking fault energies have been found to possess somewhat higher creep strength due to their greater tendency to work harden during the initial stage of creep [47]. Therefore, the Alloy 800 HT – Pt and Alloy 617 – Pt systems with higher platinum compositions may show higher creep strength in future mechanical testing.

Figure 6.66 shows that precipitates pitted with very discrete boundaries from the matrix within the Alloy 800 HT – 30 wt% Pt system due to the applied etching technique. The matrix of the Alloy 800 HT – 30 wt% Pt system appears to be relatively unaffected by the applied etching techniques because no microstructural details are revealed. This indicates that the high platinum composition of this alloy system cathodically protects the matrix very well, which is indicative of favorable corrosion resistance properties. Figure 6.135 shows that precipitate pitting occurs in nearly the same manner from the microstructure of the Alloy 617 – 30 wt% Pt system; however, significant microstructural details of the matrix were revealed by the applied etching technique. This indicates that the high platinum composition of this alloy system did not cathodically protect the matrix from the applied etching technique as well as it did for the Alloy 800 HT – 30 wt% Pt system. The corrosion resistance properties of the Alloy 617 – 30 wt % Pt system are therefore expected to be reduced compared to the Alloy 800 HT – 30 wt% Pt system.

7.5 Carbon and Precipitates

With the exception of the Alloy 800 HT – 30 wt% Pt system, the carbon content of each alloy is much higher than the maximum specified compositional value for the respective base alloy chemistry. As predicted by the JMat Pro thermodynamic models for precipitate density, high carbon content results in excessive carbide precipitation.

EDS results indicate that all precipitates large enough for analysis with the 3 micron spot size had very high chromium content. In the case of Alloy 617 – Pt systems, the EDS spectrum of these precipitates also had slightly higher molybdenum peaks than the matrix. These results point to $Cr_{23}C_6$ and $Cr_{21}Mo_2C_6$ carbide structures for the large precipitates within the Alloy 800 HT – Pt and Alloy 617 – Pt systems, respectively.

These larger precipitates have blocky shapes that seem to have formed inter-granularly. These characteristics match well with $M_{23}C_6$ type carbides. EDS performed on smaller intra-granular precipitates did not show any spectral differences from the matrix due to their small size relative to the spot. The best explanation of the nature of these smaller precipitates is provided by the JMat Pro thermodynamic precipitate density model results, as well as by EDS mapping for the case of the Alloy 617 – 5, and 15 wt% Pt systems. The results of the JMat Pro model show that each of the Alloy 617 – Pt systems could have formed approximately 1 wt% or less of M_6C type carbides. This result is further confirmed by SEI micrographs that show a distribution of intra-granular precipitates that appears to be on the order of 1% of the matrix for each Alloy 617 – Pt system. BEI micrographs of the Alloy 617 – 5, and 15 wt% Pt systems show some precipitate features with brighter contrast than others, which indicates that these precipitates have an overall higher atomic weight. Additionally many of the brighter and darker precipitate features are connected, which indicates that one type of precipitate may have nucleated on the other. EDS dot mapping of BEI micrographs of the Alloy 617 – 5 and 15 wt% Pt systems indicate that molybdenum segregated to precipitates with brighter contrast and chromium segregated to precipitates with darker contrast. The brighter molybdenum rich precipitates are probably therefore $(Ni, Co)_3Mo_3C$ carbides, while the darker chromium rich precipitates are probably $Cr_{21}Mo_2C_6$ carbides. Due to a lower temperature range of stability for the $Cr_{21}Mo_2C_6$ type carbides and the ability of $(Ni, Co)_3Mo_3C$ carbides to provide carbon, it is likely that $Cr_{21}Mo_2C_6$ carbides precipitated on $(Ni, Co)_3Mo_3C$ carbides as temperature decreased within the alloy system.

Overall, each alloy system had similar density and size of precipitates in the cast and wrought conditions. Furthermore, figure 6.135 shows that some precipitates are cracked, which indicate that they were cracked during cold working. These results show that the precipitates identified in the wrought structures were formed at some point during the melting process rather than during post cold work annealing.

Excessive carbide precipitation is detrimental to the microstructural integrity of the alloy systems characterized herein. The fine grain structure of each alloy system is primarily caused by excessive carbide precipitation. The combination of high carbide concentration and a fine grain structure is expected to greatly reduce the quality of

mechanical properties, including ductility and high temperature creep strength. Corrosion resistance properties can be compromised by excessive carbide precipitation as well. Inter-granular precipitation of $M_{23}C_6$ and M_3C_7 carbides can lead to sensitization. SEI micrographs of the wrought Alloy 800 HT – 2 and 5 wt% Pt systems show that sensitization caused the beginning of inter-granular attack induced by the etching process. SEI micrographs of the Alloy 617 – 2, 5, 15 wt% Pt systems show carbides above the surface of the matrix. This indicates that these alloy systems are less prone to inter-granular attack by the applied etching process.

Carbon is much more soluble in iron than in the other major alloying elements found in the base chemistries of Alloys 800 HT and 617. The higher iron and lower carbon content of the Alloy 800 HT – Pt systems is responsible for the overall lower carbide precipitation in these systems than in the Alloy 617 – Pt systems. Nevertheless, despite higher carbide precipitation, SEI micrographs of the Alloy 617 systems did not show sensitization. With the exception of the Alloy 617 – 30 wt% Pt system, micrographs show that carbides in the Alloy 617 – Pt systems were not attacked by the etching process. These alloy systems may therefore be more resistant than the Alloy 800 HT – Pt systems to inter-granular environmental attack.

Due to the lack of high temperature ageing treatments and low aluminum and titanium compositions, no γ' is expected to have formed in any of the microstructures characterized herein.

7.6 Recommendations for Microstructure Refinement

The microstructural properties of the Alloy 800 HT – Pt and Alloy 617 – Pt systems show promise for use as self catalytic structural materials for sulfuric acid decomposition. The materials characterized herein would not be suitable for such use in their present condition due to excessive carbide precipitation and inadequate grain size. Fortunately, platinum is shown to be soluble in these alloy systems and the above identified problems are easily surmountable.

These materials should be manufactured with carbon contents that are within the limits for their respective base alloy specifications (0.06 – 0.10wt% for Alloy 800 HT, and 0.05 – 0.15 wt% for Alloy 617). Reduced carbon content will result in a reduction of inter-granular $M_{23}C_6$ carbides that are present within both Alloy 800 HT – Pt and Alloy 617 – Pt systems. A corresponding reduction will also occur for inter-granular M_3C_7 carbides that are present within the Alloy 800 HT – Pt systems. Fewer inter-granular carbides will reduce the possibility of sensitization and consequent inter-granular attack induced by high temperature service in aggressive environments. Due to a lower pinning effect on grain boundaries during coarsening, the maximum possible grain size will also be increased with fewer inter-granular carbides.

Due to the formation of an unfavorable second phase, the Alloy 617 – 30 wt% Pt system should be excluded from further evaluation for application to sulfuric acid decomposition service. This material is expected to exhibit poor mechanical and corrosion resistance properties.

Larger grain size is very important to maintaining high temperature creep strength during material service. To further increase the grain size of the Alloy 800 HT – Pt and Alloy 617 – Pt systems to values consistent with respective base alloy specifications, the final annealing process should be extended from 30 minutes to 1 – 2 hours.

8. Conclusion

The microstructures of eight heats of Alloy 800 HT and 617 with various platinum additions were characterized in the cast and wrought conditions. Characterization techniques included optical microscopy, SEI and BEI scanning electron microscopy, EDS spectral analysis and dot mapping, JMat Pro precipitate density thermodynamic modeling, and chemical composition analysis. The goals of characterization were successful in determining microstructural features related to metallurgical performance in service conditions for sulfuric acid decomposition. Platinum and carbon compositions were found to have the most pronounced effects on microstructure development.

Optical microscopy shows that increasing platinum composition enhances the development of annealing twin features within the microstructure of the base Alloy 800 HT and 617 systems. Increasing platinum composition may also increase the effective grain size within both alloy systems; however, this effect is more prevalent in the Alloy 800 HT system. Corrosion resistance properties appear to be enhanced by increasing platinum composition as well. Alloy systems with higher platinum compositions do not show grain structure features very well with the applied etching techniques. SE microscopy indicates platinum solubility in base Alloys 800 HT up to 30 wt%. These results are in good agreement with initial predictions of high solubility based on Hume-Rothery rules. Scanning electron microscopy shows the development of a two phase structure in the Alloy 617 – 30 wt% system. This result indicates a poor microstructure for further development of a self catalytic constructional alloy.

Optical microscopy shows a significant amount of annealing twin formation in Alloy 800 HT – 15, and 30 wt% Pt and Alloy 617 – 30 wt% Pt systems. These results show that platinum addition to the base alloy chemistry has the effect of lowering the system's stacking fault energy. Lower stacking fault energy in FCC can enhance creep strength due to increased work hardening in the initial stages of creep.

Chemical composition analysis indicates very high carbon contents for all but one of the alloy systems characterized. The Alloy 800 HT – 30 wt% system was found to have carbon content below the minimum specified value for Alloy 800 HT. Optical and

SEM microscopy revealed very high carbide precipitation in each alloy system except the Alloy 800 HT – 30 wt% Pt system. The Alloy 617 – Pt systems exhibited higher carbide precipitation than the Alloy 800 HT – Pt systems due to higher carbon and lower iron contents. Carbide precipitation density was predicted for each alloy system by JMat Pro thermodynamic precipitate models. Carbide chemistry relative to the matrix was verified by EDS spectral analysis and BEI imaging. Results show that $Cr_{23}C_6$ and Cr_3C_7 formed inter-granularly within the Alloy 800 HT – Pt systems, which caused in sensitization of the 2 and 5 wt% Pt systems. JMat Pro precipitate density models indicate that MC type carbides precipitated intra-granularly within the Alloy 800 HT – Pt systems. A significant amount of $Cr_{21}Mo_2C_6$, and $(Ni, Co)_3Mo_3C$ type carbides formed within the Alloy 617 – Pt systems. BEI imaging and corresponding EDS dot mapping of the Alloy 617 – 5 and 15 wt% Pt systems shows that $Cr_{21}Mo_2C_6$ and $(Ni, Co)_3Mo_3C$ type carbides formed near each other, which indicates that the former type may have precipitated on the latter type. SEI micrographs of the Alloy 617 – 2, 5, 15 wt% Pt systems show carbides above the surface of the matrix, which indicates that these alloy systems are less prone to inter-granular attack by the applied etching process. Comparisons of corresponding optical micrographs of cast and wrought structures indicate that carbide formation occurred at some point during the melting process rather than during post cold work annealing.

SE microscopy indicates that the Alloy 617 – 30 wt % Pt system formed a two phase structure. Such a microstructure is expected to exhibit poor mechanical and corrosion resistance properties.

Due to the lack of high temperature ageing treatments and low aluminum and titanium compositions no γ' is expected to have formed in any of the microstructures characterized herein.

The grain structure of each alloy system characterized herein was found to be uniform across each of the three orthogonal planes measured indicating no preferential orientation relative to the rolling direction. The Alloy 800 HT – Pt systems developed larger grains than the Alloy 617 – Pt systems, which can be attributed to the more pronounced pinning effect of inter-granular carbides observed in the Alloy 617 – Pt

systems. The overall grain size of each alloy system, however, was much smaller than the minimum specified grain size for the respective base alloys.

The formation of inter-granular carbides, particularly $M_{23}C_6$ and M_3C_7, results in chromium depletion of grain boundary regions. Chromium depleted grain boundaries are sensitized to inter-granular corrosion, especially in sulfur bearing environments [45]. Additionally, high carbide precipitation is expected to exhibit a negative effect on high temperature mechanical properties. Ductility and high temperature creep strength, in particular, is reduced by excessive carbide formation. These properties are also adversely affected by the relatively fine grain size apparent within the microstructures characterized herein. High temperature creep strength is of particular importance to the development of these materials. Creep occurs in part by the action of grains migrating under the application of constant sub-yield stress for extended periods of time. Grain size is important to the creep phenomenon in that larger grain structures have smaller net grain boundary area, which reduces the amount of grain sliding that can occur. The materials characterized herein would have good microstructural stability for sulfuric acid decomposition service with a reduction in carbon content and an increase in grain size to values consistent with those of the respective base alloys included herein. Furthermore, the Alloy 617 – 30 wt% Pt system should be omitted from further characterization for sulfuric acid decomposition applications due to the formation of an unfavorable two phase microstructure.

9. Future Work

Initial microstructural characterization goals for several heats of material have been effectively met. Additional characterization is required to determine optimum chemistry for the development of self catalytic materials for the construction of a sulfuric acid decomposition process heat exchanger. With the exception of the Alloy 617 – 30 wt% Pt system, remaining samples of wrought base alloy – - Pt chemistries should be mechanically worked into foil form for testing of catalytic activity. Alloy systems that show appreciable catalytic conversion of sulfuric acid to decomposition products should be developed in moderately larger heats for further characterization of mechanical, and corrosion resistance properties. Research experience shows that careful control of carbon content and grain size will be important variables in the development of these larger heats. Mechanical testing should include tensile and creep rupture tests in order to verify that the materials in question retain the minimum acceptable standards for the respective base alloy systems.

If no appreciable conversion is shown in the tested alloy systems, powder metallurgy processing will be necessary to develop materials with sufficient catalytic activity. Higher platinum compositions would be directly alloyed into Alloys 800 HT and 617 and then atomized into powder form. This powder would then be partially consolidated and co-processed onto the respective base alloy in order to create a catalytic surface with high surface area to volume ratio. It is hoped that powder metallurgy will not be necessary due to predicted substandard mechanical properties; however, the process will be pursued in order to verify or discount such predictions.

Eventually four small heat exchangers must be constructed for benchmark testing. Two heat exchangers will be constructed from materials developed by powder metallurgy techniques and two will be constructed from materials developed by conventional direct alloying techniques. Within these sub-categories, one heat exchanger will have a unit shell and tube type configuration while the other will have a unit plate or printed circuit type configuration. All prototype heat exchangers will be characterized with respect to their mechanical and catalytic properties.

Appendix A: Catalysis Effectiveness System

A system must be designed to measure the catalytic effectiveness of several base alloy + Pt chemistry materials for the decomposition of sulfuric acid. This decomposition reaction is a two step process that proceeds as follows:

$$H_2SO_4 \rightarrow SO_3 + H_2O \quad (1)$$

$$SO_3 + H_2O \rightarrow SO_2 + H_2O + \tfrac{1}{2}O_2 \quad (2)$$

The decomposition of sulfuric acid is an endothermic process. Nearly 100% conversion of reaction (1) is possible with a reaction temperature between 350 - 500°C. Reaction (2) has been identified as the rate limiting step because the presence of a solid catalyst and a reaction temperature between 800 - 900°C are required to achieve appreciable conversion. The required system may be designed to measure either the conversion of SO_3 or H_2SO_4 to the final reaction products in order to determine the catalytic effectiveness of the materials in question.

A.1 Flow rate calculations and reactant selection

A system design analysis has been undertaken of possible reactant species of both sulfur trioxide and sulfuric acid as reactive species for decomposition to sulfur dioxide, oxygen and water. As a starting point, the weighted hourly space velocity (WHSV) of a successful catalysis effectiveness system designed at INL was used to calculate preliminary mass flow rates of both possible reactant species. The INL system, headed by Dr. Daniel Ginosar, measured between 20 – 50 mol% conversion of sulfuric acid to sulfur dioxide and oxygen with a WHSV of 265.13 mol reactant / m^2 – hr [41]. The three catalysts tested by the INL research group contain 0.1 wt% Pt over approximately 2 m^2 of surface area embedded in 1 gram samples of porous Alumina Oxide (Al_2O_3), titanium oxide (TiO_2), and zirconium oxide (ZrO_2). The materials to be tested herein contain between 20 to 300 times higher platinum concentration (2 – 30% Pt); however, due to a lack of porosity, the surface areas of these materials are approximately 730 times smaller

(.002741 m^2) than the catalysts tested at INL. The resulting disparity translates to much lower calculated molar flow rates of reactant over the base alloy + Pt chemistry than those utilized at INL.

The mass flow rates of reactants expected to produce similar mol% conversion as those observed by the INL group were calculated accordingly:

$$WHSV = \frac{mol_{reactant}}{m^2_{catalyst} - hr}$$

The INL research group reports 20-50 mol% conversion with $52 \frac{grams_{H2SO4}}{gram_{catalyst} - hr}$

$$(52 \frac{grams_{H2SO4}}{gram_{catalyst} - hr}) * (\frac{1 gram_{catalyst}}{2 m^2_{catalyst}}) * (\frac{1 m^2_{catalyst}}{.001 m^2_{Pt}}) * (\frac{1 mol_{H2SO4}}{98.066 grams_{H2SO4}}) = 265.13 \frac{mol_{H2SO4}}{m^2_{Pt} - hr}$$

Base alloy + Pt chemistry alloys will be tested for catalytic effectiveness in the following dimensions with the resulting surface area:

L = 6 inch, W = 0.25 inch, T = 0.1inch

$$2(6in * .25in) + 2(6in * 0.1in) + 2(.1in * .25in) * (\frac{0.0254^2 m^2}{1 in^2}) = .002741 m^2$$

Sample calculation of SO_3 mass flow rate for base alloy + 2 wt% Pt sample:

$$(265.13 \frac{mol_{SO3}}{m^2_{Pt} - hr}) * (\frac{80.064 grams_{SO3}}{mol_{SO3}}) * (\frac{.02 m^2_{Pt}}{m^2_{catalyst}}) * (\frac{1 hr}{60 \min}) * (.002741 m^2_{catalyst})$$

$$= 0.0194 \frac{grams_{SO3}}{\min}$$

Sample calculation of 96 wt% H_2SO_4 aqueous solution mass flow rate for base alloy + 2 wt% Pt sample:

$$(265.13 \frac{mol_{H2SO4}}{m^2_{Pt} - hr}) * (\frac{98.066 grams_{H2SO4}}{mol_{H2SO4}}) * (\frac{.02 m^2_{Pt}}{m^2_{catalyst}}) * (\frac{1 hr}{60 \min}) * (.002741 m^2_{catalyst})$$

$$* (\frac{100 grams_{total}}{96 grams_{H2SO4}}) = 0.02475 \frac{grams_{96 wt\% H2SO4}}{\min}$$

Table A.1				
Alloy (wt% Pt)	**SO3 mass flow rate (g/min)**	**96 wt% aqueous H2SO4 mass flow rate (g/min)**	**75 wt% aqueous H2SO4 mass flow rate (g/min)**	**50 wt% aqueous H2SO4 mass flow rate (g/min)**
2	0.0194	0.0247	0.0317	0.0475
5	0.0485	0.0619	0.0792	0.1188
15	0.1455	0.1856	0.2376	0.3563
30	0.2909	0.3712	0.4751	0.7127

Mass flow rates for sulfur trioxide and three different concentrations of sulfuric acid in aqueous solution have been calculated and are shown above in table 1. The resulting low values dictate that a carrier gas will be needed to maintain a sufficient flow rate within the high temperature quartz reactor. Such a carrier gas will also have a pressure spike moderating effect that could be associated with boiling the reactant species in the gas stream if injected as a liquid. Helium and nitrogen are possible options for a carrier gas medium. Nitrogen is less expensive than helium; however, helium will provide the highest carrier gas flow rate because of its relatively lower density. Helium also eliminates the problem of oxygen detection in the gas chromatograph due to overlapping nitrogen and oxygen peaks. The required reactant flow rate will be much lower for the 2 and 5 wt% Pt samples than for the 15 and 30 wt% Pt samples. Therefore, helium may be added to the gas stream in variable molar concentration as needed in order to maintain an appreciable flow rate through the system.

Volumetric flow rate calculations for each reactant species have been performed at 10/90 and 50/50 molar concentrations with helium carrier gas at three different temperatures: 25 ºC, 70 ºC (SO_3) 125 ºC (H_2SO_4 aq solutions), and 850 ºC. SO_3 and H_2SO_4 aqueous solution reactants boil at 44.7 ºC and 100 ºC, respectively. SO_3 gas and H_2SO_4 gas could be treated as ideal gases for calculation purposes above 70ºC and 125 ºC, respectively, due to sufficient superheating above their respective boiling points. The low and respective intermediate temperatures were chosen in order to explore two different reactant and carrier gas supply options. The first option involves metered liquid injection of the reactant species at 25ºC. The second option involves metering the boiled reactant species into the flow stream at the respective intermediate temperatures listed above. At these temperatures there would be sufficient reactant gas pressure to ensure steady flow through the metering device into the system. If selected, the SO_3 reactant

would require a higher back pressure due to the need for a head of water utilized for scrubbing the residual sulfur trioxide from the flow stream prior to analysis within the gas chromatograph. Volumetric flow rate calculations were performed at 850 ºC to determine total gas flow rates through the quartz reaction chamber. A summary of volumetric flow rates are appended to this report in tables 4 and 5. Sample calculations for SO_3 over 2 wt% Pt catalyst and helium carrier gas are included below:

Back pressure induced by 20 cm head of water required for scrubbing SO_3 (SO_3 reactant only):

$$(20cm_{H2O}) * (\frac{1gram_{H20}}{1cm^3_{H20}}) * (\frac{1kg}{1000grams}) * (\frac{100^2 cm^2}{m^2}) * (9.81\frac{m}{s^2}) * (\frac{1KPa}{1000Pa}) * (\frac{1psi}{6.895KPa})$$
$$= 0.285psig$$

SO_3 molar flow rate for base alloy + 2 wt% Pt sample:

$$(.019395\frac{gram_{SO3}}{\min}) * (\frac{1mol}{80.064grams_{SO3}}) = .00024224\frac{mol_{SO3}}{\min}$$

Volumetric flow rates at 25 °C

SO_3 (liquid):

$$(.019395\frac{grams_{SO3}}{\min}) * (1.97\frac{cc}{gram_{SO3}}) = .00984\frac{cc_{SO3}}{\min}$$

Helium (10 mol% SO_3 – 90 mol% He):

$$\frac{(0.00024224\frac{mol_{SO3}}{\min}) * (9\frac{mol_{He}}{mol_{SO3}}) * (0.0083143\frac{KN-m}{mol-\circ K}) * (298.15\circ K)}{(\frac{1m^3_{He}}{10^6 cc_{He}}) * (101.325\frac{KN}{m^2})} = 53.34\frac{cc_{He}}{\min}$$

Helium (50 mol% SO_3 – 50 mol% He):

$$\frac{(0.00024224\frac{mol_{SO3}}{\min}) * (4\frac{mol_{He}}{mol_{SO3}}) * (0.0083143\frac{KN-m}{mol-\circ K}) * (298.15\circ K)}{(\frac{1m^3_{He}}{10^6 cc_{He}}) * (101.325\frac{KN}{m^2})} = 23.71\frac{cc_{He}}{\min}$$

Volumetric flow rates at 70 °C

SO_3 (gas):

$$\frac{(.019395\frac{grams_{SO3}}{\min})*(10^6\frac{cc}{m^3})*(0.0083143\frac{KN-m}{mol-\circ K})*(343.15\circ K)}{(80.064\frac{grams_{SO3}}{mol_{SO3}})*(101.325\frac{KN}{m^2})}=6.82\frac{cc_{SO3}}{\min}$$

Helium (10 mol% SO_3 – 90 mol% He):

$$\frac{(0.00024224\frac{mol_{SO3}}{\min})*(9\frac{mol_{He}}{mol_{SO3}})*(0.0083143\frac{KN-m}{mol-\circ K})*(343.15\circ K)}{(\frac{1m^3_{He}}{10^6 cc_{He}})*(101.325\frac{KN}{m^2})}=61.38\frac{cc_{He}}{\min}$$

Total gas flow rate (10 mol% SO_3 – 90 mol% He):

$$6.82\frac{cc_{SO3}}{\min}+61.38\frac{cc_{He}}{\min}=68.20\frac{cc_{tot}}{\min}$$

Helium (50 mol% SO_3 – 50 mol% He):

$$\frac{(0.00024224\frac{mol_{SO3}}{\min})*(4\frac{mol_{He}}{mol_{SO3}})*(0.0083143\frac{KN-m}{mol-\circ K})*(343.15\circ K)}{(\frac{1m^3_{He}}{10^6 cc_{He}})*(101.325\frac{KN}{m^2})}=27.28\frac{cc_{He}}{\min}$$

Total gas flow rate (50 mol% SO_3 – 50 mol% He):

$$7.91\frac{cc_{SO3}}{\min}+27.28\frac{cc_{He}}{\min}=34.10\frac{cc_{tot}}{\min}$$

SO_3 gas maximum back pressure upstream of flow metering device:

$$[(343.15\circ K)*(\frac{101.325KPa}{317.85\circ K})-101.325KPa]*(\frac{1psi}{6.895KPa})=1.17psig$$

Volumetric flow rates at 850 °C

SO_3 (gas):

$$\frac{(.019395\frac{grams_{SO3}}{\min})*(10^6\frac{cc}{m^3})*(0.0083143\frac{KN-m}{mol-\circ K})*(1123.15\circ K)}{(80.064\frac{grams_{SO3}}{mol_{SO3}})*(101.325\frac{KN}{m^2})}=22.33\frac{cc_{SO3}}{\min}$$

Helium (10 mol% SO_3 – 90 mol% He):

$$\frac{(0.00024224\frac{mol_{SO3}}{\min})*(9\frac{mol_{He}}{mol_{SO3}})*(0.0083143\frac{KN-m}{mol-\circ K})*(1123.15\circ K)}{(\frac{1m^3_{He}}{10^6 cc_{He}})*(101.325\frac{KN}{m^2})}=200.91\frac{cc_{He}}{\min}$$

Total gas flow rate (10 mol% SO_3 – 90 mol% He):

$$22.33\frac{cc_{SO3}}{\min}+200.91\frac{cc_{He}}{\min}=223.24\frac{cc_{tot}}{\min}$$

Helium (50 mol% SO_3 – 50 mol% He):

$$\frac{(0.00024224\frac{mol_{SO3}}{\min})*(4\frac{mol_{He}}{mol_{SO3}})*(0.0083143\frac{KN-m}{mol-\circ K})*(1123.15\circ K)}{(\frac{1m^3_{He}}{10^6 cc_{He}})*(101.325\frac{KN}{m^2})}=89.30\frac{cc_{He}}{\min}$$

Total gas flow rate (50 mol% SO_3 – 50 mol% He):

$$22.33\frac{cc_{SO3}}{\min}+89.30\frac{cc_{He}}{\min}=111.63\frac{cc_{tot}}{\min}$$

The tabulated results show that optimal flow rates will be maintained with different molar concentrations of reactant species in the helium carrier gas for the various wt% Pt alloy samples. A 10-90 molar concentration of reactant species in carrier gas will be best suited for the 2 wt% Pt and 5 wt% Pt samples. A 50-50 molar concentration of

reactant species in carrier gas will be best suited for the 15 wt% Pt and 30 wt% Pt samples.

The low surface area of the alloy samples tested herein generally limits the flow rates of all possible reactant species to very low values. The compiled data shows that the reactant with the highest flow rates in variable concentration with helium gas is 50 wt% H_2SO_4 aqueous solution. A favorable property of sulfuric acid is that it is hygroscopic. Any sulfuric acid that does not decompose will adsorb any water and drop out of the flow stream in a collection vessel upstream of the gas chromatograph. If 50 wt% H_2SO_4 aqueous solution is used, and appreciable decomposition occurs, there may not be enough sulfuric acid in the flow stream to adsorb all of the residual water prior to entering the gas chromatograph. If 75 wt% H_2SO_4 aqueous solution is used as a reactant species, there should be enough sulfuric acid remaining in the flow stream after the reaction chamber to adsorb all remaining water. Calculated volumetric flow rates of 75 wt% H_2SO_4 aqueous solution are the next highest of all the four reactant species analyzed. This reactant option appears to be best suited to our application.

Sulfur trioxide was examined as a possible reactant species and was found to be inadequate. This reactant readily forms sulfuric acid vapor if exposed to water vapor in air and can be lethal if inhaled. This danger is substantial only during initial handling of the reactant during the system construction phase of the project. The danger may be mitigated with the use of a fume hood and cumbersome protective clothing. However, the system construction will be labor intensive, and an exposure incident may occur that would jeopardize safety of the individual working at the site. In addition to the safety concerns, sulfur trioxide will have the lowest maximum flow rate of all reactants analyzed for this project. This means that it will be the most difficult reactant to regulate in precise quantities. If sulfur trioxide is used, good catalytic effectiveness properties may be found for the alloys in question; however, the data collected will only give precise catalytic effectiveness properties for sulfur trioxide decomposition and not sulfuric acid decomposition. Testing for catalytic effectiveness properties with a sulfuric acid solution may give more reliable data for the alloys in question.

A.2 Reactant and carrier gas feed configuration

Option 1:

As mentioned previously, there are two possible reactant plus carrier gas supply options that are investigated in this report. One option involves directly pumping an accurately controlled low flow rate of liquid reactant entrained by helium gas into the quartz reaction chamber located within the tube furnace. The required low flow rates of either SO_3 or variable wt% H_2SO_4 aqueous solution may be provided with a positive displacement peristaltic pump manufactured by Cole Parmer. This pump operates via rollers compressing a Teflon tube at variable speeds. The Teflon tube is the only wetted component of the pump thereby ensuring that the pump will not fail due to corrosion. This pump has a rated capacity between .003 – 50 ml/min. The wide capacity range of this pump may prove to be advantageous in the event that the calculated flow rates are too low for what is actually required to observe appreciable sulfur dioxide generation. In addition, should it become necessary to develop porous catalytic materials from the alloys tested herein; this pump will be able to provide the necessary flow rates to test their catalytic effectiveness. The reactant feed configuration at the point of entry into the quartz reaction chamber should provide for efficient boiling and mixing with the helium carrier gas in such a way as to minimize pressure spikes that are typically associated with liquid to vapor phase transfer. In order to meet these criteria it is proposed that the liquid feed pass through a 1/16"OD, 1/32" ID tube into the reaction chamber. For the range of flow rates calculated and listed in table 5 the reactant species would form a small bubble at the end of the tube, boil off, and mix with the entraining helium gas as it is heated to the reaction temperature of 850 °C. Additionally, the high temperature at the point of entry into the reaction chamber will preclude the option of using a Teflon feed tube. The tube may therefore be constructed of Titanium, which would easily withstand the corrosive medium at temperature. The major costs associated with this feed option are listed in the table 2 below:

Table A.2						
Component	**Manufacturer**	**Model Number**	**Capacity (ml/min)**	**QTY**	**Price ($)**	**Misc Info**
Pump	Cole Parmer	EW-78017-35	0.003-50	1	$2,360.00	31 day wait
Helium mass flow controller	MKS	1179	2-100% full scale	2	$2,290.00	
Mass flow controller read out	MKS	247C	N/A	N/A	$1,425.00	4 channels
Titanium feed tube	Microgroup Inc	Custom Order	N/A	1	$147.84	
Total Price					**$6222.84**	

Option 2:

The second reactant supply option involves boiling the liquid reactant prior to metering into the flow stream with helium gas. Both gasses would be metered with MKS mass flow controllers. The models selected are resistant to upstream pressure changes caused by boiling, and are able to withstand up to 150 ºC. Despite manufacturer assurance, their environmental resistance to sulfur compound environments is questionable due to product failures experienced by the INL catalysis research group. The wetted components of the MKS mass flow controllers are constructed of SUS-316L stainless steel. This material may be corrosion resistant to sulfur trioxide gas at 70 ºC; however, it is very doubtful that the material will withstand sulfuric acid gas at 125 ºC. Sulfinert coated 316 L SS tubing would be needed for the SO_3 supply to the mass flow controller and along the entire mixed gas stream supplying the hot zone of the system. The inflexible nature of steel tubing would make it difficult to configure the feed system within the hood. The major costs associated with the gas reactant supply option are listed in the table 3 below:

Table A.3						
Component	**Manufacturer**	**Model Number**	**Capacity (ml/min)**	**QTY**	**Price ($)**	**Misc Info**
Reactant mass flow controller	MKS	M330AH	2-100% full scale	1	$4,900.00	150 deg C max temp, 6-8 week lead time
Helium mass flow controller	MKS	1179	2-100% full scale	2	$2,290.00	
Mass flow controller read out	MKS	247D	N/A	1	$1,425.00	4 channels
Total Price					**$8,615.00**	

Option 1 appears to be the best configuration for our application. The major costs associated with the liquid feed option are approximately 65% of the major costs associated with the gas feed option. The first option will also be easier to configure because all of the supply tubing before the boiling chamber may be constructed from Teflon. Furthermore, based on INL experience, sulfur bearing compounds will probably destroy the mass flow controller needed for the reactant gas supply option.

A.3 Reactant and supply configuration summary

75 wt% H_2SO_4 aqueous solution is the reactant of choice from those considered for the catalysis effectiveness loop. The reactant solution should be mixed with 90 mol % helium concentration for testing of the 2 and 5 wt% Pt concentration samples, and 50 mol % helium concentration for testing the 15 and 30 wt% Pt samples. The feed system should be configured according to option 1 described above. Tables 4 and 5 included below show all flow rate calculation results. The numbers indicated in bold apply to the selected flow parameters. A detailed system configuration is proposed in Figures 1 and 2. The components of these diagrams are numerous and are therefore referenced numerically to table 6, which also includes vendor and pricing information for future design work.

TableA.4	Flow rate calculations for various reactant mixtures, 10 mol % concentration in Helium gas									
96 wt% H2SO4 in aqueous solution			**10 mol % reactant solution - 90 mol% He**							
Catalyst (% Pt)	Reactant [g/min]	Reactant [mol/min]	Reactant [cc/min] (liq, 25 deg C)	He [cc/min] (gas, 25 deg C)	Reactant [cc/min] (gas, 125 deg C)	He [cc/min] (gas, 125 deg C)	Total flow [cc/min] (gas, 125 deg C)	Reactant [cc/min] (gas, 850 deg C)	He [cc/min] (gas, 850 deg C)	Total flow [cc/min](gas, 850 deg C)
2	0.02475	0.0002972	0.01351	65.45	8.52	87.39	95.92	24.04	246.56	270.61
5	0.06186	0.0007431	0.03379	163.62	21.31	218.48	239.79	60.10	616.41	676.51
15	0.18559	0.0022292	0.10136	490.85	63.92	655.45	719.37	180.30	1849.24	2029.54
30	0.37118	0.0044585	0.20272	981.69	127.83	1310.90	1438.73	360.61	3698.47	4059.08
75 wt% H2SO4 in aqueous solution			**10 mol % reactant solution - 90 mol% He**							
Catalyst (% Pt)	Reactant [g/min]	Reactant [mol/min]	Reactant [cc/min] (liq, 25 deg C)	He [cc/min] (gas, 25 deg C)	Reactant [cc/min] (gas, 125 deg C)	He [cc/min] (gas, 125 deg C)	Total flow [cc/min] (gas, 125 deg C)	Reactant [cc/min] (gas, 850 deg C)	He [cc/min] (gas, 850 deg C)	Total flow [cc/min](gas, 850 deg C)
2	**0.03167**	**0.0006822**	**0.01903**	**150.20**	**13.26**	**200.57**	**213.83**	**37.40**	**565.88**	**603.28**
5	**0.07919**	**0.0017054**	**0.04759**	**375.51**	**33.15**	**501.43**	**534.58**	**93.50**	**1414.70**	**1508.20**
15	0.23756	0.0051162	0.14276	1126.52	99.44	1504.29	1603.73	280.51	4244.09	4524.60
30	0.47511	0.0102324	0.28552	2253.04	198.88	3008.58	3207.46	561.01	8488.18	9049.19
50 wt% H2SO4 in aqueous solution			**10 mol % reactant solution - 90 mol% He**							
Catalyst (% Pt)	Reactant [g/min]	Reactant [mol/min]	Reactant [cc/min] (liq, 25 deg C)	He [cc/min] (gas, 25 deg C)	Reactant [cc/min] (gas, 125 deg C)	He [cc/min] (gas, 125 deg C)	Total flow [cc/min] (gas, 125 deg C)	Reactant [cc/min] (gas, 850 deg C)	He [cc/min] (gas, 850 deg C)	Total flow [cc/min](gas, 850 deg C)
2	0.04751	0.0015620	0.03416	343.93	26.75	459.27	486.01	75.45	1295.74	1371.19
5	0.11878	0.0039050	0.08539	859.83	66.87	1148.17	1215.03	188.63	3239.35	3427.98
15	0.35633	0.0117149	0.25617	2579.48	200.60	3444.50	3645.10	565.89	9718.04	10283.93
30	0.71267	0.0234299	0.51234	5158.96	401.21	6889.00	7290.20	1131.77	19436.08	20567.85
SO3 99% purity liquid			**10 mol% SO3 - 90 mol% He**							
Catalyst (% Pt)	SO3 [g/min]	SO3 [mol/min]	SO3 [cc/min] (liq, 25 deg C)	He [cc/min] (gas, 25 deg C)	SO3 [cc/min] (gas, 70 deg C)	He [cc/min] (gas, 70 deg C)	Total flow [cc/min] (gas, 70 deg C)	SO3 [cc/min] (gas, 850 deg C)	He [cc/min] (gas, 850 deg C)	Total flow [cc/min](gas, 850 deg C)
2	0.019395	0.00024224	0.00984	53.34	6.82	61.38	68.20	22.33	200.91	223.24
5	0.048486	0.00060559	0.02461	133.34	17.05	153.46	170.51	55.81	502.28	558.09
15	0.145459	0.00181678	0.07384	400.03	51.16	460.40	511.56	167.44	1506.92	1674.36
30	0.290918	0.00363357	0.14767	800.05	102.31	920.80	1023.11	334.87	3013.85	3348.72

Table A.5	Flow rate calculations for various reactant mixtures, 50 mol % concentration in Helium gas									
96 wt% H2SO4 in aqueous solution			**50 mol % reactant solution - 50 mol% He**							
Catalyst (% Pt)	Reactant [g/min]	Reactant [mol/min]	Reactant [cc/min] (liq, 25 deg C)	He [cc/min] (gas, 25 deg C)	Reactant [cc/min] (gas, 125 deg C)	He [cc/min] (gas, 125 deg C)	Total flow [cc/min] (gas, 125 deg C)	Reactant [cc/min] (gas, 850 deg C)	He [cc/min] (gas, 850 deg C)	Total flow [cc/min](gas, 850 deg C)
2	0.02475	0.0002972	0.01351	29.09	8.52	38.84	47.36	24.04	109.58	133.62
5	0.06186	0.0007431	0.03379	72.72	21.31	97.10	118.41	60.10	273.96	334.06
15	0.18559	0.0022292	0.10136	218.15	63.92	291.31	355.23	180.30	821.88	1002.19
30	0.37118	0.0044585	0.20272	436.31	127.83	582.62	710.46	360.61	1643.77	2004.37
75 wt% H2SO4 in aqueous solution			**50 mol % reactant solution - 50 mol% He**							
Catalyst (% Pt)	Reactant [g/min]	Reactant [mol/min]	Reactant [cc/min] (liq, 25 deg C)	He [cc/min] (gas, 25 deg C)	Reactant [cc/min] (gas, 125 deg C)	He [cc/min] (gas, 125 deg C)	Total flow [cc/min] (gas, 125 deg C)	Reactant [cc/min] (gas, 850 deg C)	He [cc/min] (gas, 850 deg C)	Total flow [cc/min](gas, 850 deg C)
2	0.03167	0.0006822	0.01903	66.76	13.26	89.14	102.40	37.40	251.50	288.90
5	0.07919	0.0017054	0.04759	166.89	33.15	222.86	256.00	93.50	628.75	722.26
15	**0.23756**	**0.0051162**	**0.14276**	**500.67**	**99.44**	**668.57**	**768.01**	**280.51**	**1886.26**	**2166.77**
30	**0.47511**	**0.0102324**	**0.28552**	**1001.35**	**198.88**	**1337.15**	**1536.02**	**561.01**	**3772.52**	**4333.54**
50 wt% H2SO4 in aqueous solution			**50 mol % reactant solution - 50 mol% He**							
Catalyst (% Pt)	Reactant [g/min]	Reactant [mol/min]	Reactant [cc/min] (liq, 25 deg C)	He [cc/min] (gas, 25 deg C)	Reactant [cc/min] (gas, 125 deg C)	He [cc/min] (gas, 125 deg C)	Total flow [cc/min] (gas, 125 deg C)	Reactant [cc/min] (gas, 850 deg C)	He [cc/min] (gas, 850 deg C)	Total flow [cc/min](gas, 850 deg C)
2	0.04751	0.0015620	0.03416	152.86	26.75	204.12	230.87	75.45	575.88	651.34
5	0.11878	0.0039050	0.08539	382.15	66.87	510.30	577.16	188.63	1439.71	1628.34
15	0.35633	0.0117149	0.25617	1146.44	200.60	1530.89	1731.49	565.89	4319.13	4885.01
30	0.71267	0.0234299	0.51234	2292.87	401.21	3061.78	3462.98	1131.77	8638.26	9770.03
SO3			**50 mol% SO3 – 50 mol% He**							
Catalyst (% Pt)	SO3 [g/min]	SO3 [mol/min]	SO3 [cc/min] (liq, 25 deg C)	He [cc/min] (gas, 25 deg C)	SO3 [cc/min] (gas, 70 deg C)	He [cc/min] (gas, 70 deg C)	Total flow [cc/min] (gas, 70 deg C)	SO3 [cc/min] (gas, 850 deg C)	He [cc/min] (gas, 850 deg C)	Total flow [cc/min](gas, 850 deg C)
2	0.019395	0.00024224	0.00984	23.71	6.82	27.28	34.10	22.33	89.30	111.63
5	0.048486	0.00060559	0.02461	59.26	17.05	68.21	85.26	55.81	223.25	279.06
15	0.145459	0.00181678	0.07384	177.79	51.16	240.62	291.78	167.44	669.74	837.18
30	0.290918	0.00363357	0.14767	355.58	102.31	409.20	511.51	334.87	1339.33	1674.20

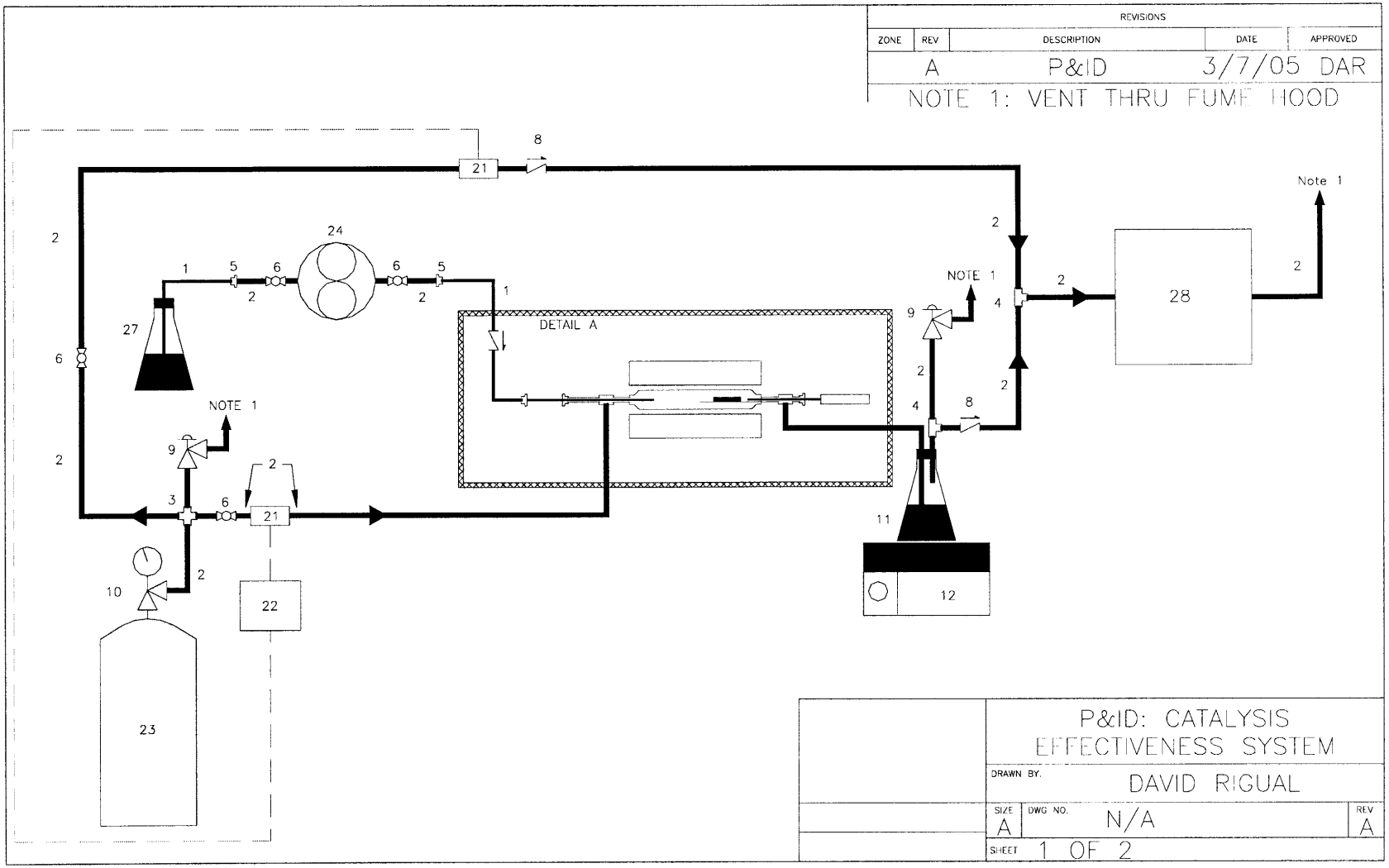

Fig. A.1: CAD drawing of proposed catalysis effectiveness loop

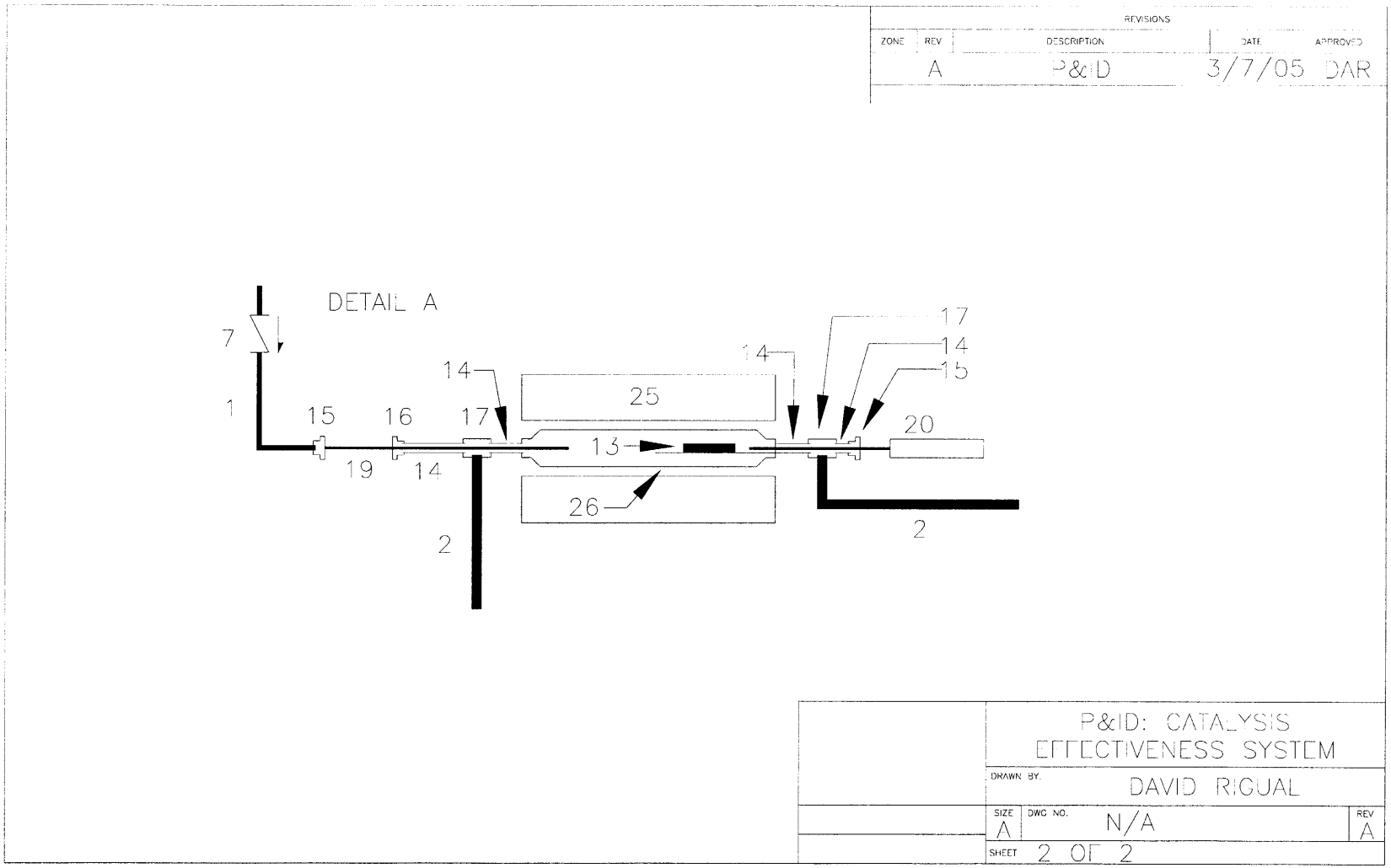

Fig. A.2: CAD drawing of Detail A from Fig A.1

Table A.6							
Catalysis Effectiveness System Component List							
Dwg Ref No.	**Component**	**Vendor**	**Ordering Number**	**Contact Info**	**QTY**	**Price / Unit**	**Price**
1	1/8" OD, 1/16" ID, Teflon TFE tubing	Teqcom	FT-125-030	(714) 979-7024	35 ft	$1.00 / ft	$35.00
2	¼" OD, 3/16" ID, Teflon TFE tubing	Teqcom	FT-250-030	(714) 979-7024	25 ft	$1.25 / ft	$31.25
3	1/4" tubing Union Cross	Teqcom	UC-F-4-HA	(714) 979-7024	1	$45.00	$45.00
4	1/4" tubing Union Tee	Teqcom	UT-F-4-HA	(714) 979-7024	2	$35.00	$70.00
5	¼"-1/8" Teflon Reducing Union	Teqcom	RU-F-42-HA	(714) 979-7024	2	$23.00	$46.00
6	1/4" Teflon Ball Valve	Teqcom	BV-4-4-T	(714) 979-7024	4	$340.00	$1360.00
7	1/8" Teflon Check Valve	Teqcom	TA-CV-1202	(714) 979-7024	1	$84.00	$84.00
8	1/4" Teflon Check Valve	Teqcom	TA-CV-1302	(714) 979-7024	2	$88.00	$176.00
9	¼" Teflon Pressure Relief Valve	Teqcom	RV-4T-KA	(714) 979-7024	2	$190.00	$380.00
10	Regulator	Lab	N/A	N/A	1	N/A	$0.00
11	H2SO4 collection beaker	Lab	N/A	N/A	1	N/A	$0.00
12	Hot plate	Lab	N/A	N/A	1	N/A	$0.00
13	Test specimen	Lab	N/A	N/A	1	N/A	$0.00
14	1/4" OD, .18" ID, 316 L Silcosteel-CR tubing	Restek	22897	(800) 356-1688	5 ft	$18.75 / ft	$93.75
15	1/4"-1/8" Silcosteel-CR tubing reducer	Restek	22871	(800) 356-1688	1	$66.00	$66.00
16	1/16"-1/4" Silcosteel-CR tubing reducer	Restek	22870	(800) 356-1688	1	$66.00	$66.00
17	1/4" Silcosteel-CR Tee	Restek	22868	(800) 356-1688	2	$82.00	$82.00
18	1/16"-1/8" Silcosteel-CR tubing reducer	Restek	22869	(800) 356-1688	1	$70.00	$70.00
19	1/16" OD, .0305" ID Titanium tubing	Microgroup Inc.	Not Specified	(800) ALL-TUBE	2 ft	$73.92 / ft	$147.84
20	1/8" OD, 18" L, type K, PFA coated, Thermocouple	Omega	CASS-18G-18-PFA	(888) TC-OMEGA	1	$52.90	$52.90
21	General Purpose Mass Flow Controller	MKS	1179 A	(978) 284-4000	2	$1,145.00	$2,290.00
22	4-channel Digital Readout	MKS	247C	(978) 284-4000	1	$1,425.00	$1,425.00
23	He tank	BOC			1		
24	Ismatec Compact Multichannel Pump	Cole Parmer	EW-78017-35	(800) 323-4340	1	$2,360.00	$2,360.00
25	Lindberg/Blue M Mini-Mite tube furnace	Cole Parmer	EW33850-05	(800) 323-4340	1	$1,905.00	$1,905.00
26	Quartz reaction chamber and Specimen tray	Tech. Glass	Custom Order	(440) 639-6399	1	$200	$200.00
27	ACS grade 99.999% H2SO4 (mixed to 75 wt%)	Aldrich	339741	(800) 325-3010	2 L	$191 / 0.5 L	$764.00
28	Gas Chromatograph	Agilent	G1540N	(302) 633-8569	1	$31,947	$31,947
Total Price							**$43,496.74**

Appendix B: Additional Micrographs and Grain Size Measurement Data

B.1. Alloy 800 HT Grain Size Calculation Data

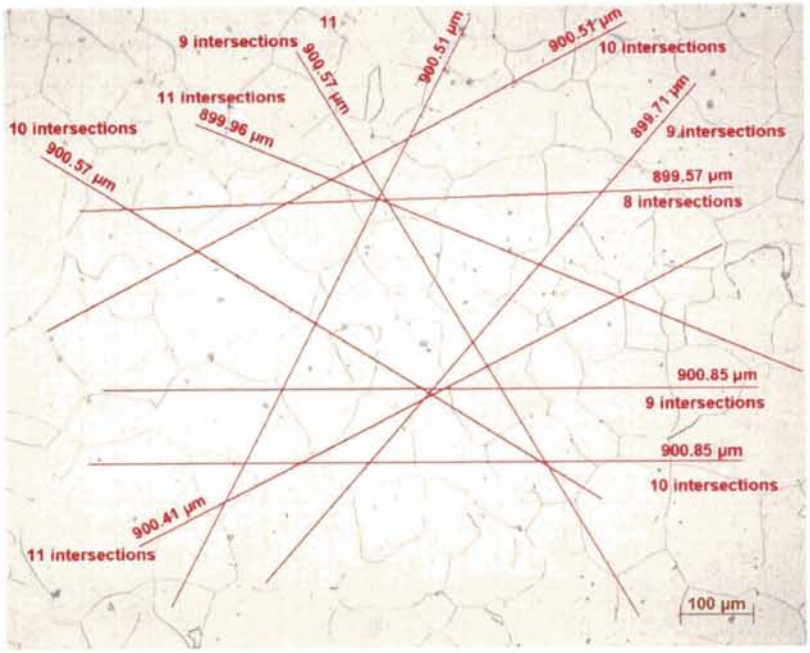

Fig B.1: Alloy 800 HT, 100 X, grain size measurement

Table B.1			
Grain size calculation for Alloy 800 HT			
Projection	Length (microns)	# intercepts	Grain size (microns)
1	900.57	10	270
2	899.96	11	240
3	900.57	9	300
4	900.51	11	250
5	900.51	10	270
6	899.71	9	300
7	899.57	8	340
8	900.85	9	300
9	900.85	10	270
10	900.41	11	250
AVG grain size			**280**

B.2. Alloy 800 HT – 2 wt% Pt

B.2.1. Micrographs of Cast Structure

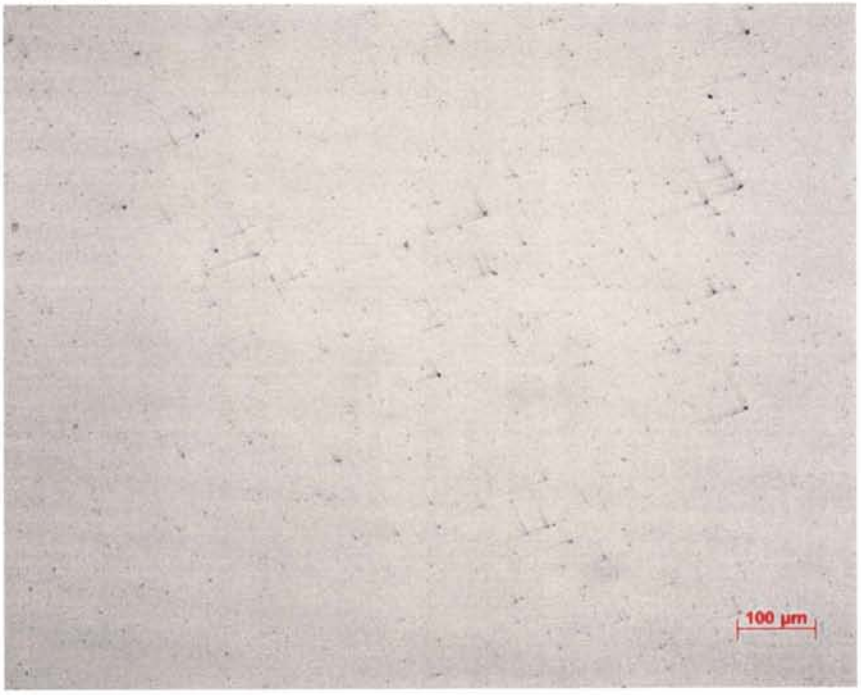

Fig B.2: Cast Alloy 800 HT – 2 wt% Pt, 100 X

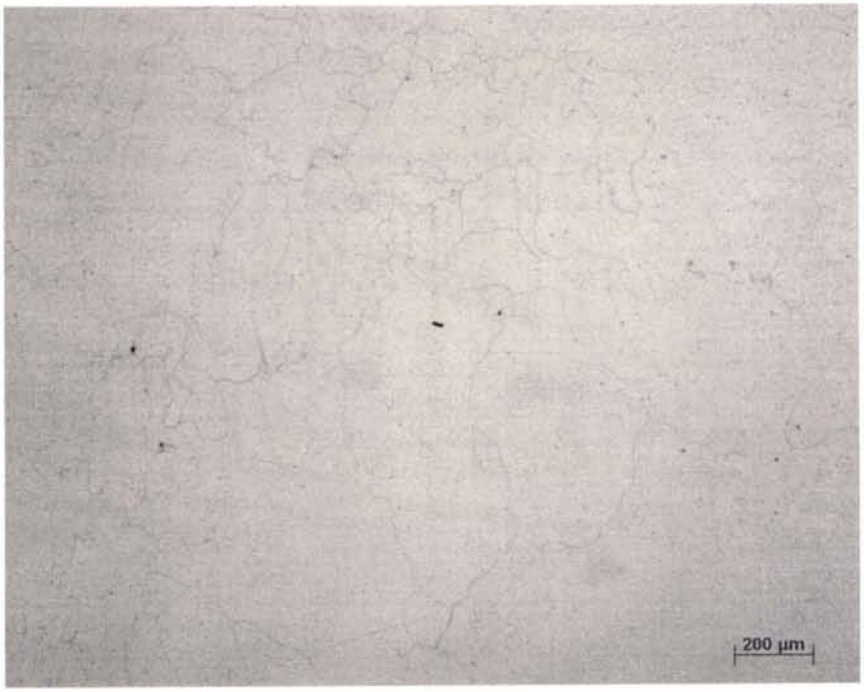

Fig B.3: Cast Alloy 800 HT - 2 wt% Pt, 50 X, weak glyceregia - 210 sec

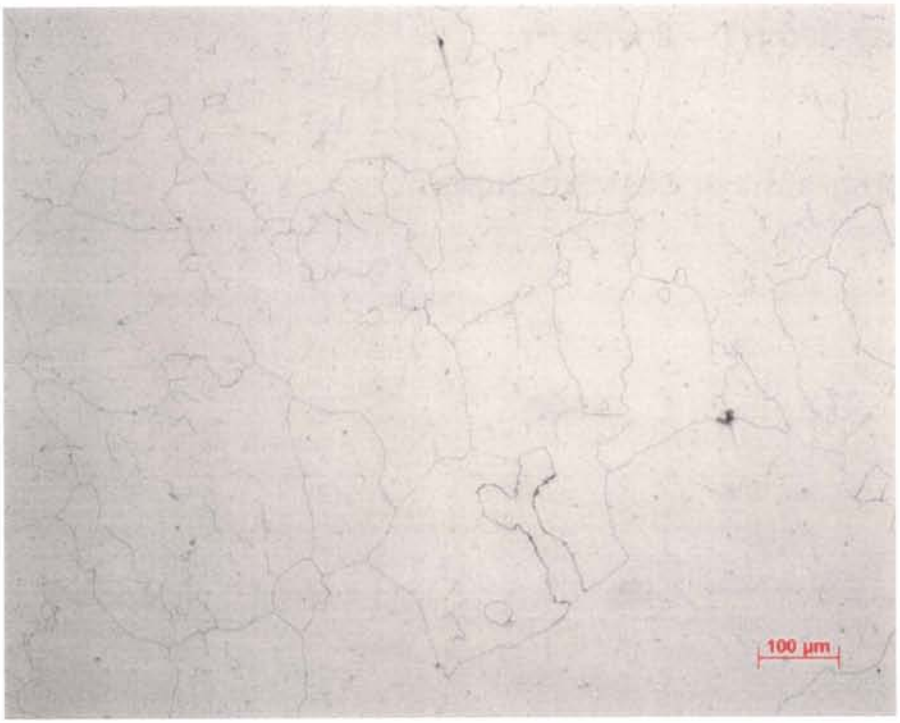

Fig B.4: Cast Alloy 800 HT - 2 wt% Pt, 100 X, weak glyceregia - 210 sec

B.2.2. Micrographs of Wrought Structure

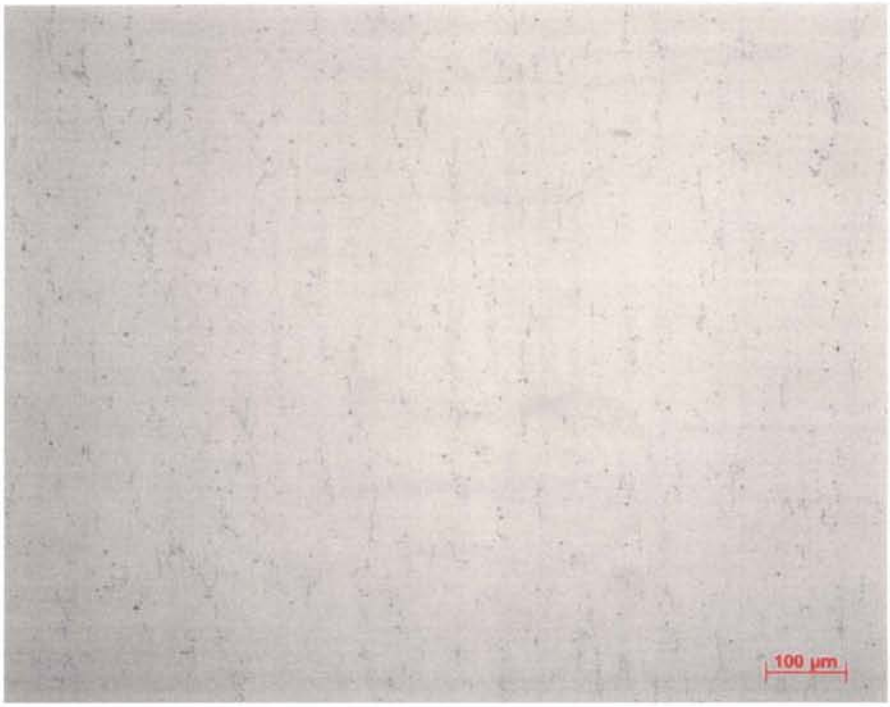

Fig B.5: Wrought Alloy 800 HT – 2 wt% Pt, xy plane, 100 X

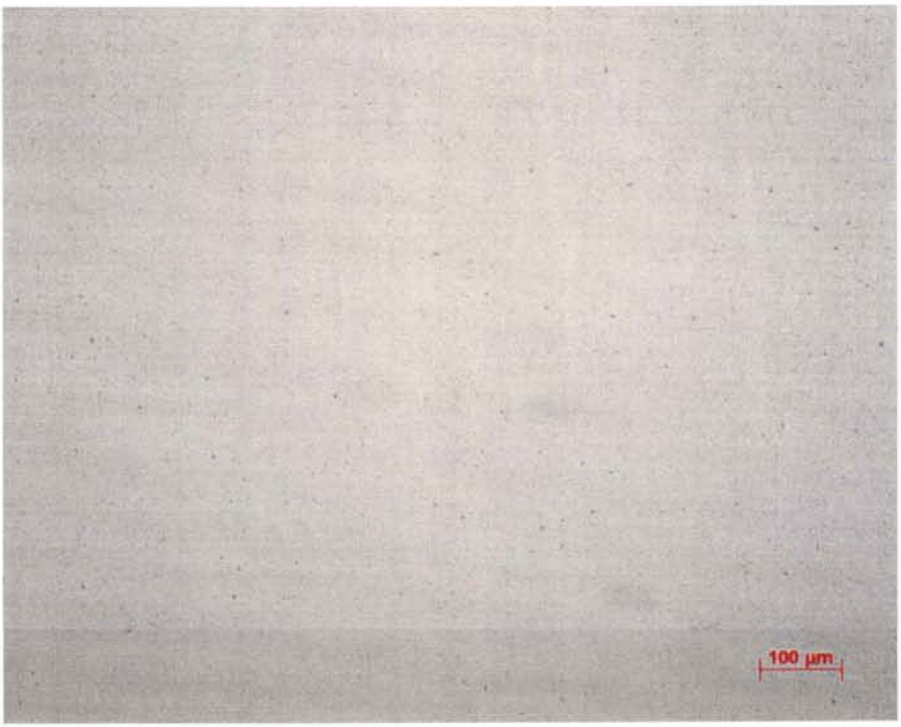

Fig B.6: Wrought Alloy 800 HT – 2 wt% Pt, xz plane, 100 X

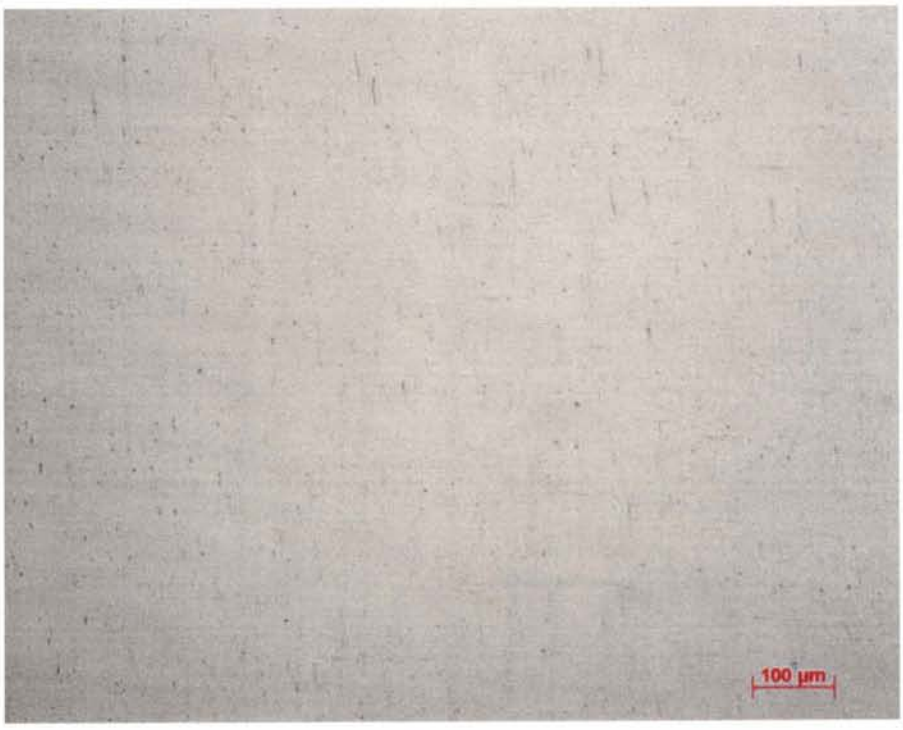

Fig B.7: Wrought Alloy 800 HT – 2 wt% Pt, yz plane, 100 X

Fig B.8: Wrought Alloy 800 HT - 2 wt% Pt, xy plane, 100 X, Nital, 3 VDC - 6 sec

Fig B.9: Wrought Alloy 800 HT - 2 wt% Pt, xz plane, 100 X, Nital, 1.5 VDC – 8 sec, 1 VDC – 15 sec

Fig B.10: Wrought Alloy 800 HT - 2 wt% Pt, yz plane, 100 X, Nital, 1.5 VDC – 4 sec, 1 VDC – 10 sec

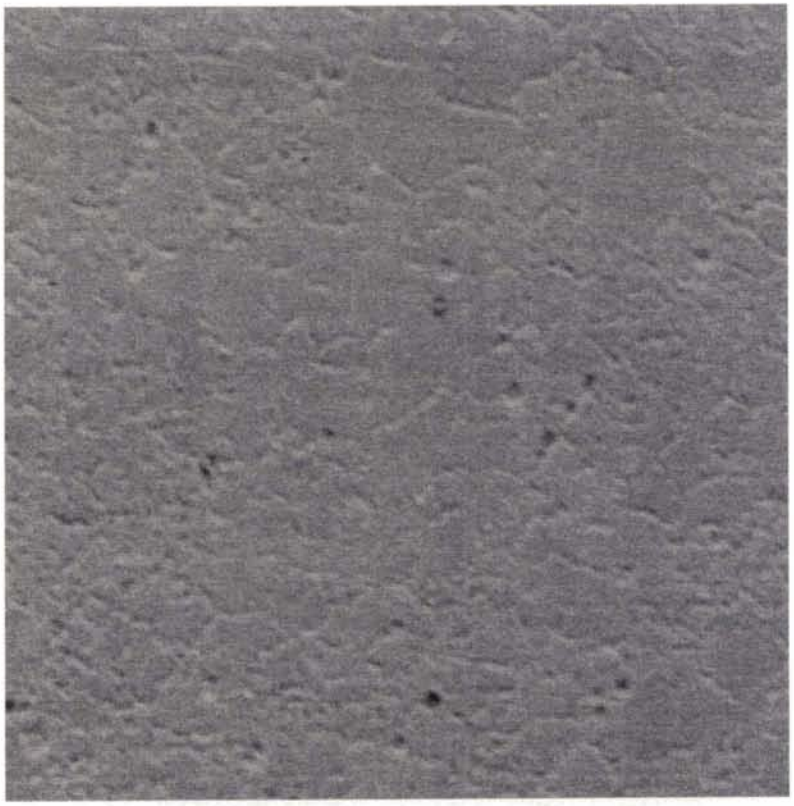

Fig B.11: Wrought Alloy 800 HT – 2 wt% Pt, Secondary Electron Image, 500 X

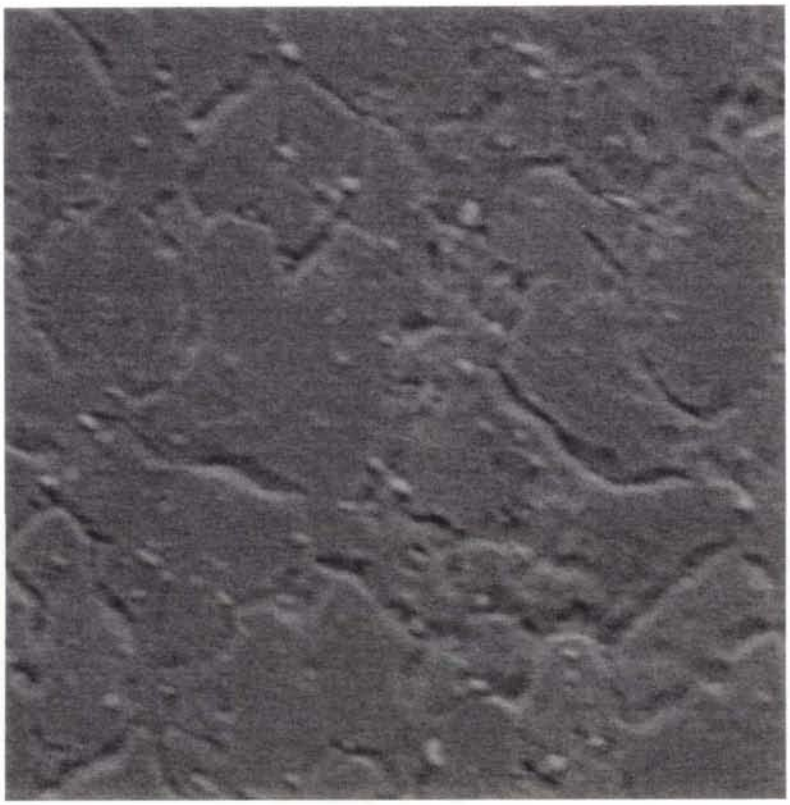

Fig B.12: Wrought Alloy 800 HT – 2 wt% Pt, Secondary Electron Image, 1500 X

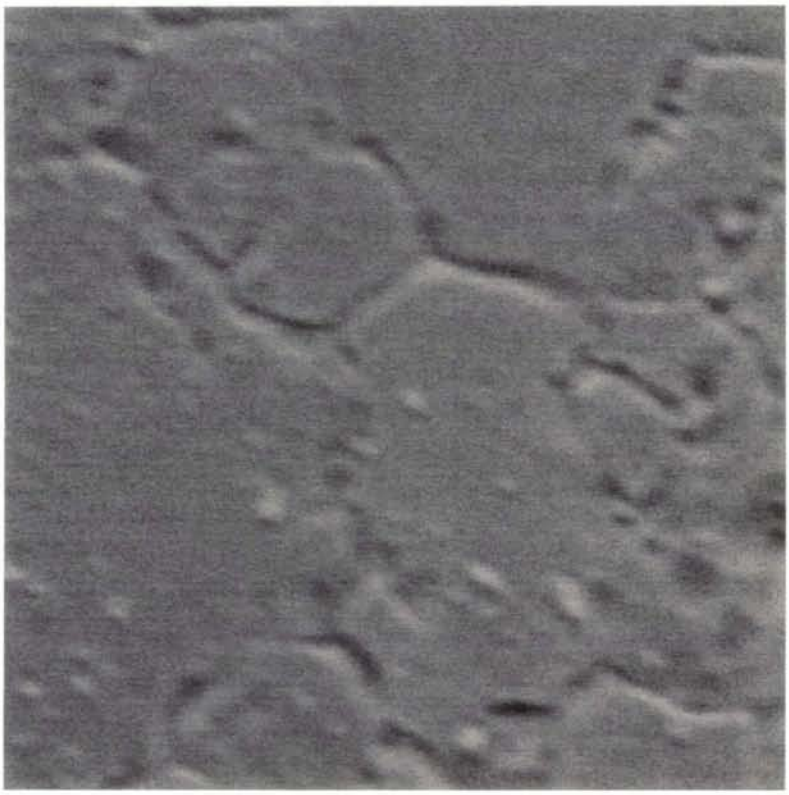

Fig B.13: Wrought Alloy 800 HT – 2 wt% Pt, Secondary Electron Image, 2500 X

B.2.3. Grain Size Calculation Data

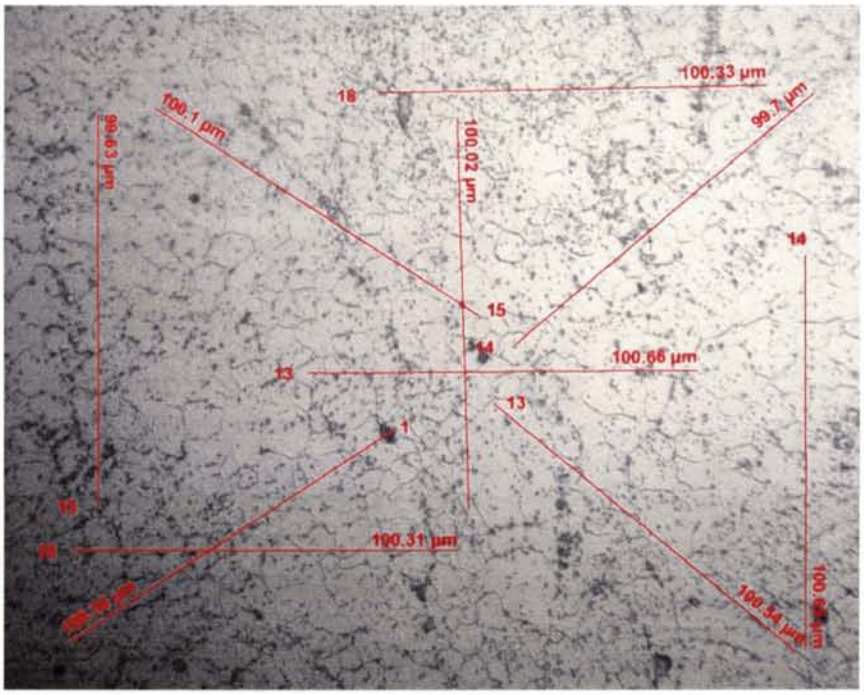

Fig B.14: Wrought Alloy 800 HT – 2 wt% Pt, xy plane, 500 X, grain size measurement

Table B.2			
Grain size calculation for Alloy 800 HT + 2 wt% Pt xy plane			
Projection	**Length (microns)**	**# intercepts**	**Grain size (microns)**
1	99.63	15	20
2	100.31	18	17
3	100.36	14	22
4	100.1	15	20
5	99.7	14	21
6	100.02	15	20
7	100.66	13	23
8	100.33	18	17
9	100.54	13	23
10	100.65	14	22
AVG grain size			**21**

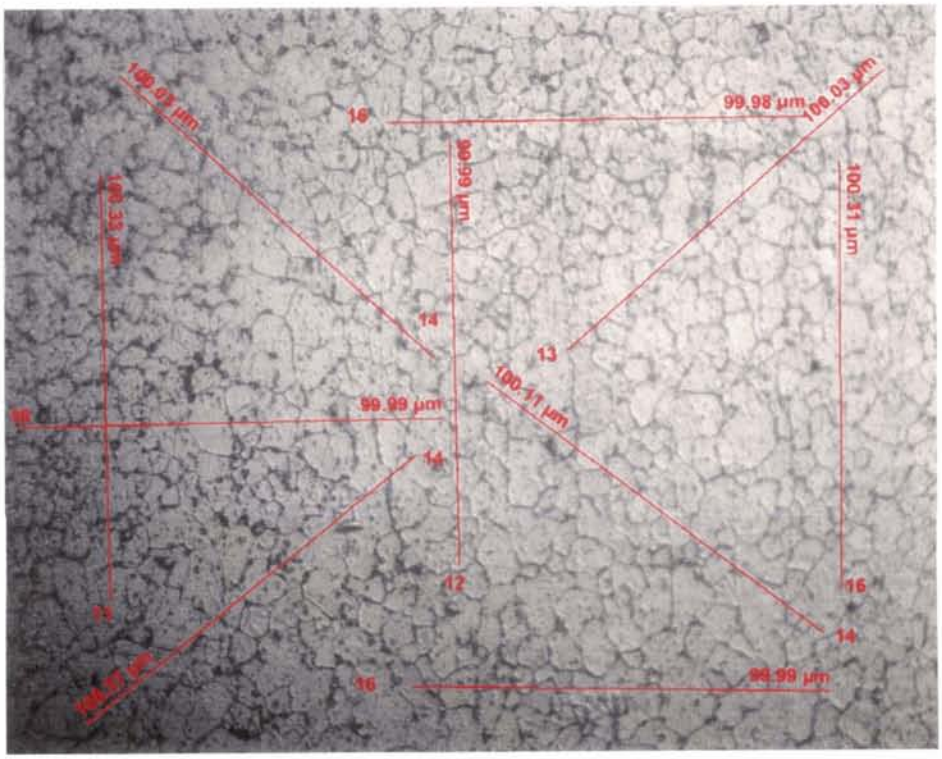

Fig B.15: Wrought Alloy 800 HT – 2 wt% Pt, xz plane, 500 X, grain size measurement

Table B.3			
Grain size calculation for Alloy 800 HT + 2 wt% Pt xz plane			
Projection	**Length (microns)**	**# intercepts**	**Grain size (microns)**
1	100.33	11	27
2	99.99	12	25
3	100.31	16	19
4	99.98	16	19
5	99.99	16	19
6	99.99	16	19
7	100.03	14	21
8	100.11	14	21
9	100.03	13	23
10	100.37	14	22
AVG grain size			**22**

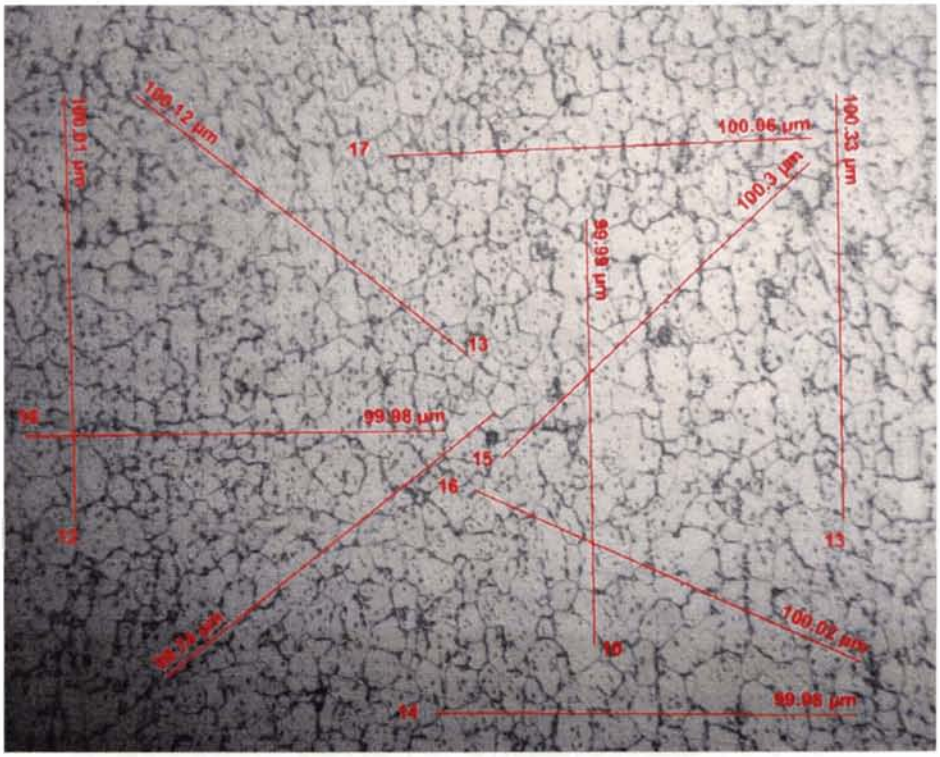

Fig B.16: Wrought Alloy 800 HT – 2 wt% Pt, yz plane, 500 X, grain size measurement

Table B.4			
Grain size calculation for Alloy 800 HT + 2 wt% Pt yz plane			
Projection	**Length (microns)**	**# intercepts**	**Grain size (microns)**
1	100.01	12	25
2	99.99	10	30
3	100.33	13	23
4	100.06	17	18
5	99.98	16	19
6	99.98	14	21
7	100.12	13	23
8	100.02	16	19
9	100.3	15	20
10	99.74	16	19
AVG grain size			**22**

B.3. Alloy 800 HT – 5 wt% Pt

B.3.1. Micrographs of Cast Structure

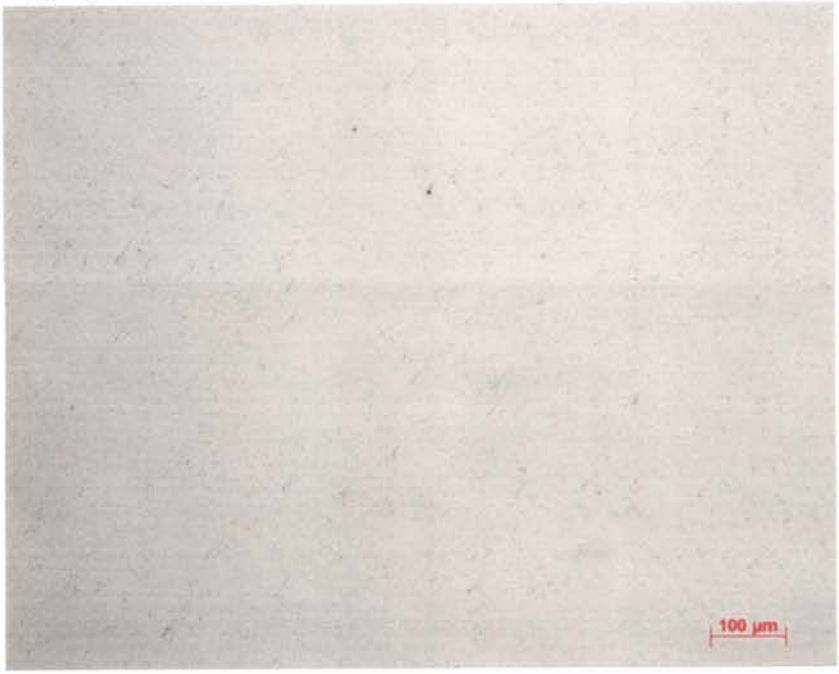

Fig B.17: Cast Alloy 800 HT – 5 wt% Pt, 100 X

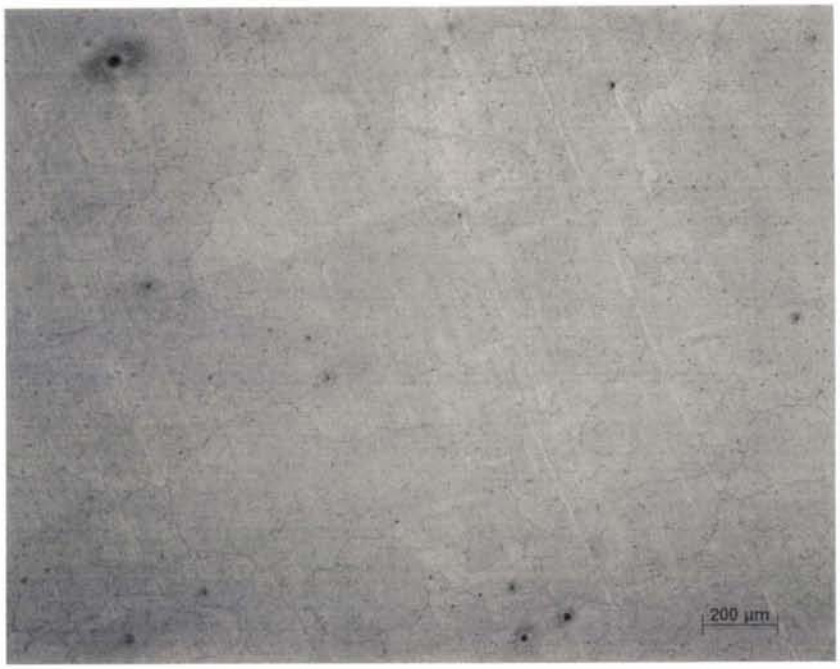

Fig B.18: Cast Alloy 800 HT - 5 wt% Pt, 50 X, weak glyceregia - 200 sec

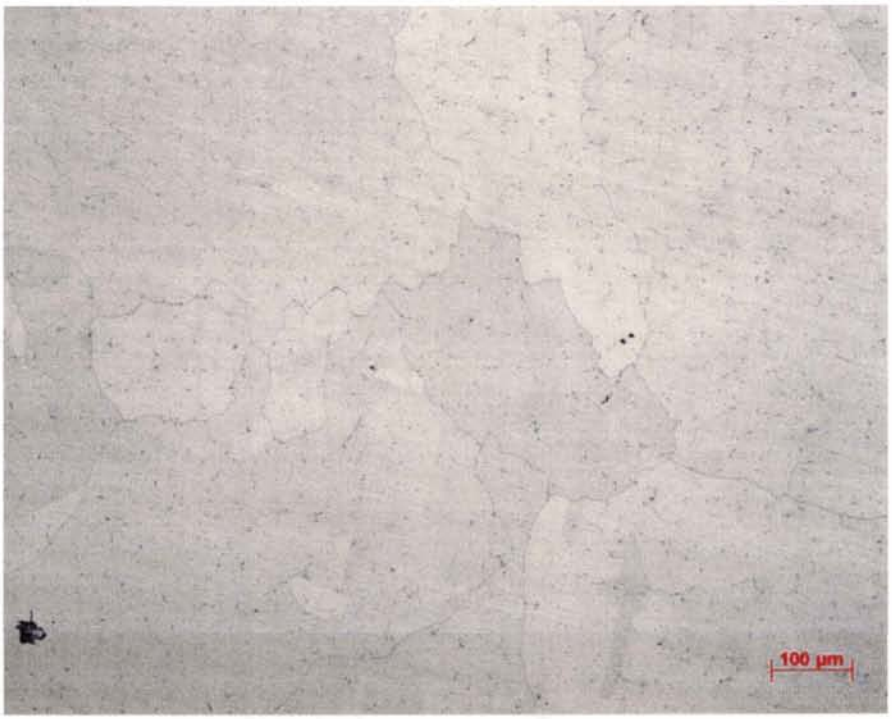

Fig B.19: Cast Alloy 800 HT - 5 wt% Pt, 100 X, weak glyceregia - 200 sec

B.3.2. Micrographs of Wrought Structure

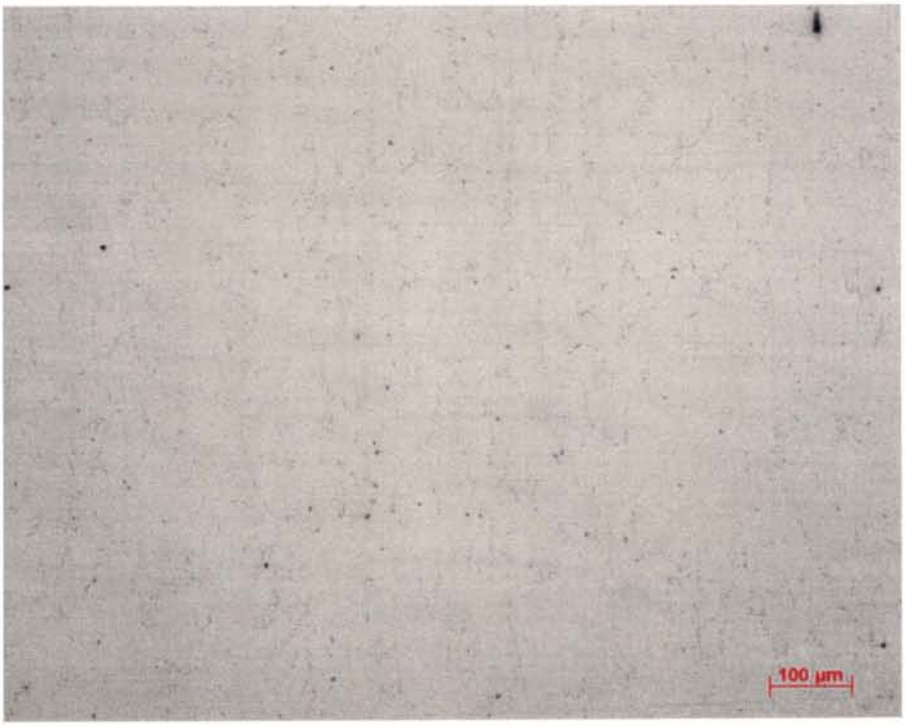

Fig B.20: Wrought Alloy 800 HT – 5 wt% Pt, xy plane, 100 X

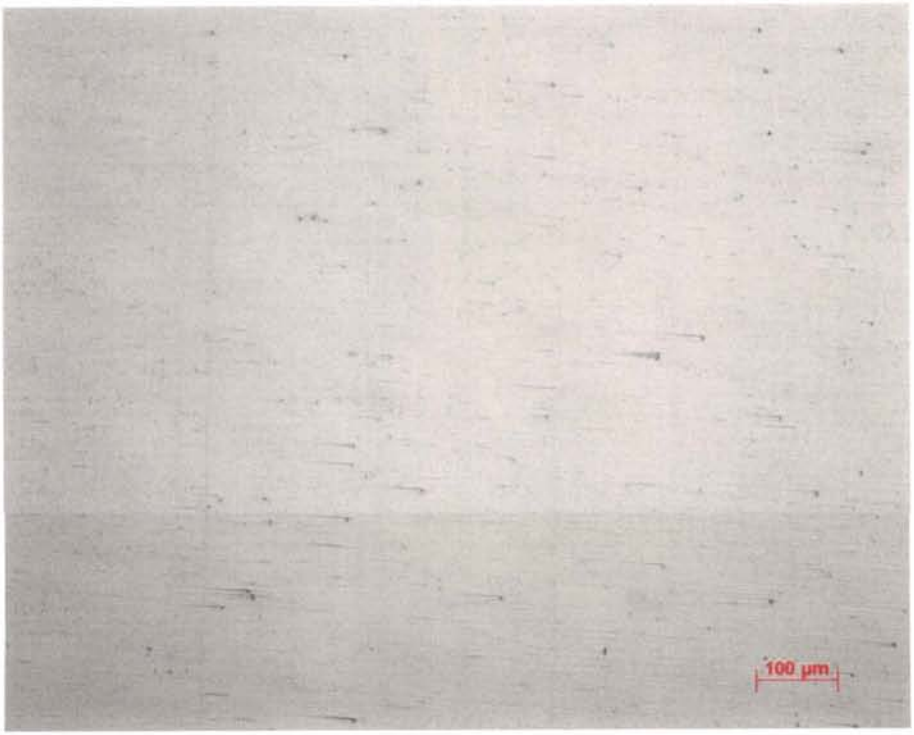

Fig B.21: Wrought Alloy 800 HT – 5 wt% Pt, xz plane, 100 X

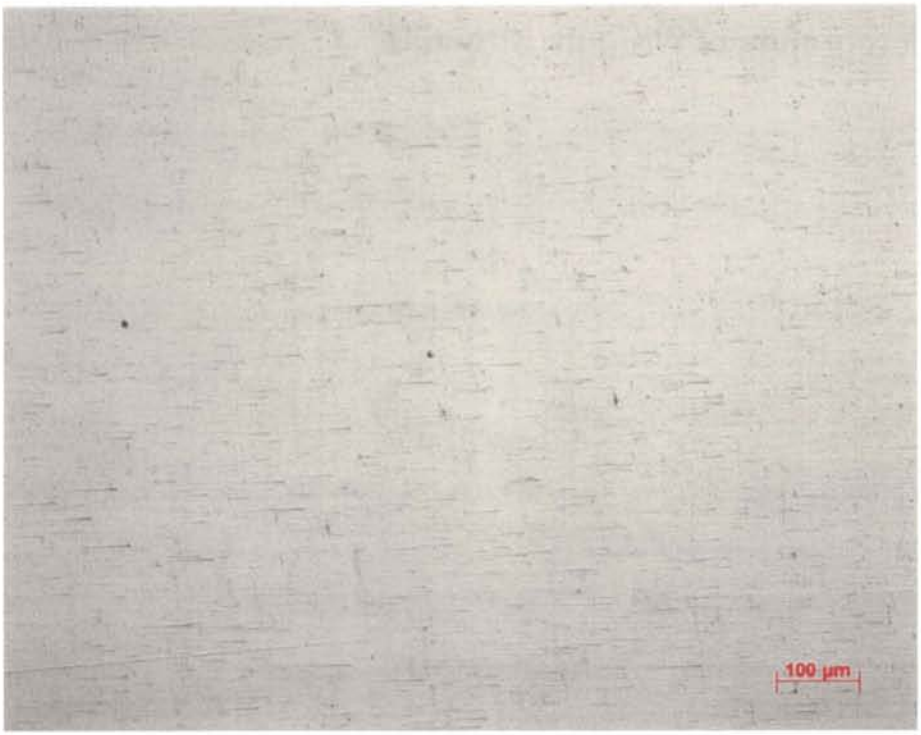

Fig B.22: Wrought Alloy 800 HT – 5 wt% Pt, yz plane, 100 X

Fig B.23: Wrought Alloy 800 HT – 5 wt% Pt, xy plane, 100 X, Nital, 3 VDC – 6 sec, 1.5 VDC – 10 sec

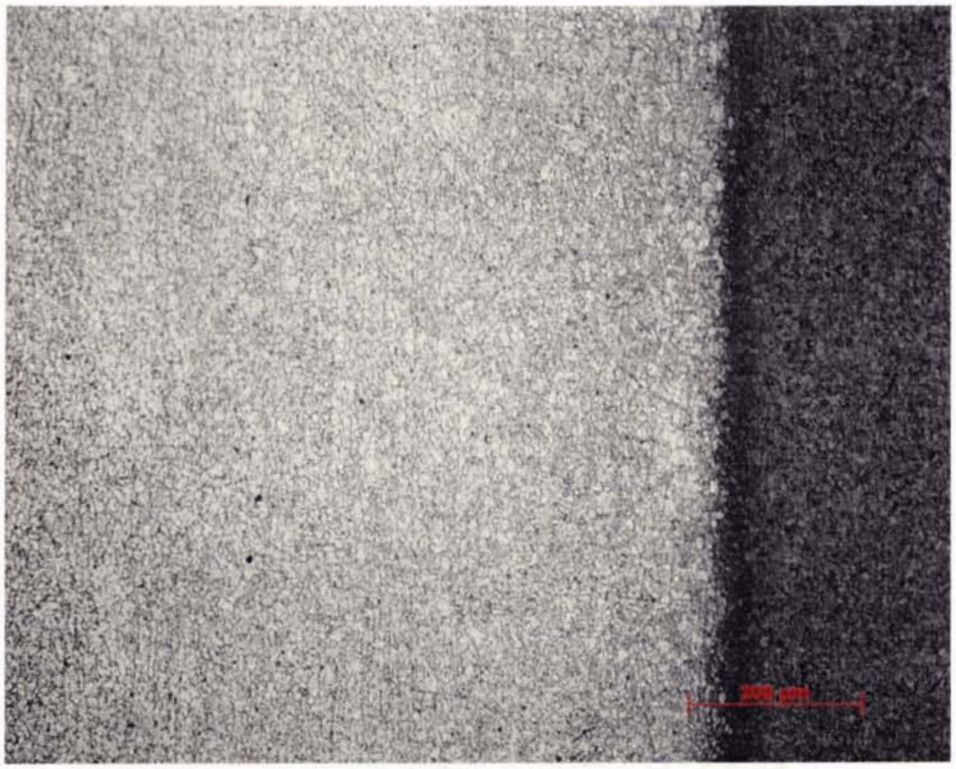

Fig B.24: Wrought Alloy 800 HT – 5 wt% Pt, xz plane, 100 X, Nital, 1.5 VDC – 5 sec, 1 VDC – 5 sec

Fig B.25: Wrought Alloy 800 HT – 5 wt% Pt, yz plane, 100 X, Nital, 1.5 VDC – 5 sec, 1 VDC – 4 sec

Fig B.26: Wrought Alloy 800 HT – 5 wt% Pt, Secondary Electron Image, 500 X

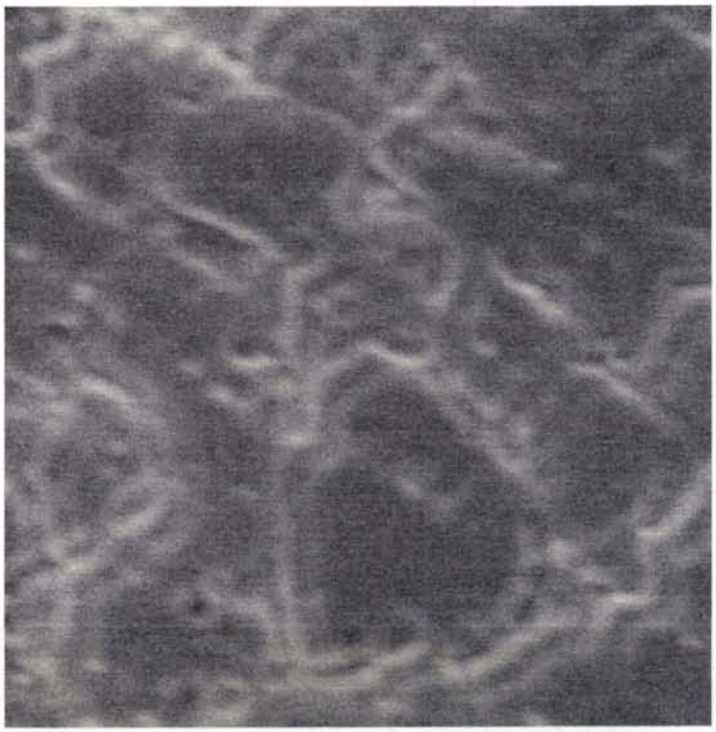

Fig B.27: Wrought Alloy 800 HT – 5 wt% Pt, Secondary Electron Image, 2500 X

B.3.3. Grain Size Calculation Data

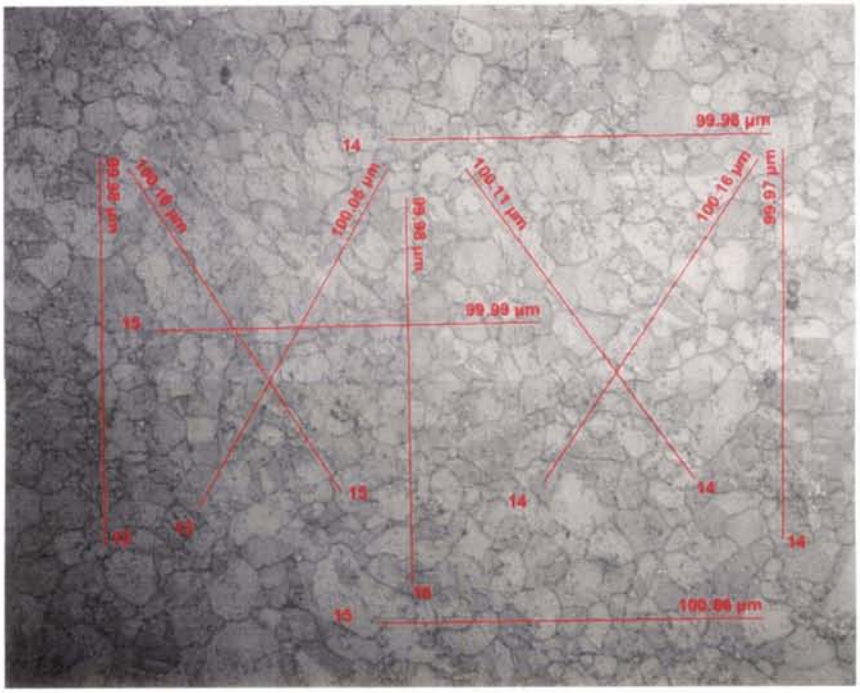

Fig B.28: Wrought Alloy 800 HT – 5 wt% Pt, xy plane, 500 X, grain size measurement

Table B.5			
Grain size calculation for Alloy 800 HT + 5 wt% Pt xy plane			
Projection	**Length (microns)**	**# intercepts**	**Grain size (microns)**
1	99.98	12	25
2	99.98	16	19
3	99.97	14	21
4	99.98	14	21
5	99.99	15	20
6	100.66	15	20
7	100.16	15	20
8	100.05	13	23
9	100.11	14	21
10	100.16	14	21
AVG grain size			**21**

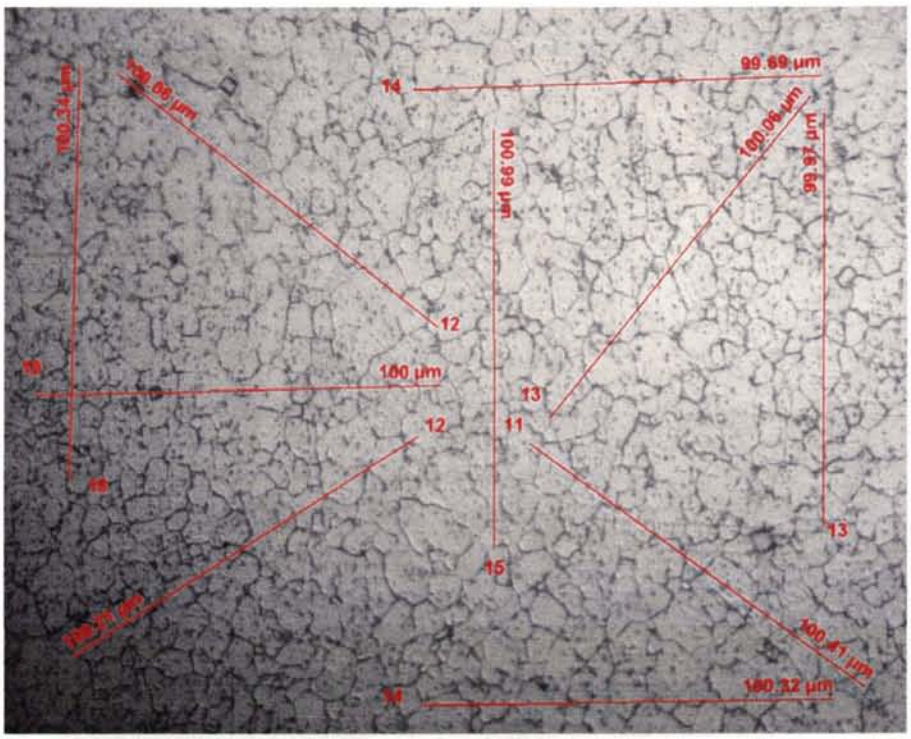

Fig B.29: Wrought Alloy 800 HT – 5 wt% Pt, xz plane, 500 X, grain size measurement

Table B.6			
Grain size calculation for Alloy 800 HT + 5 wt% Pt xz plane			
Projection	**Length (microns)**	**# intercepts**	**Grain size (microns)**
1	100.34	18	17
2	100.99	15	20
3	99.97	13	23
4	99.59	14	21
5	100	19	16
6	100.32	14	22
7	100.21	12	25
8	100.06	13	23
9	100.06	12	25
10	100.41	11	27
AVG grain size			**22**

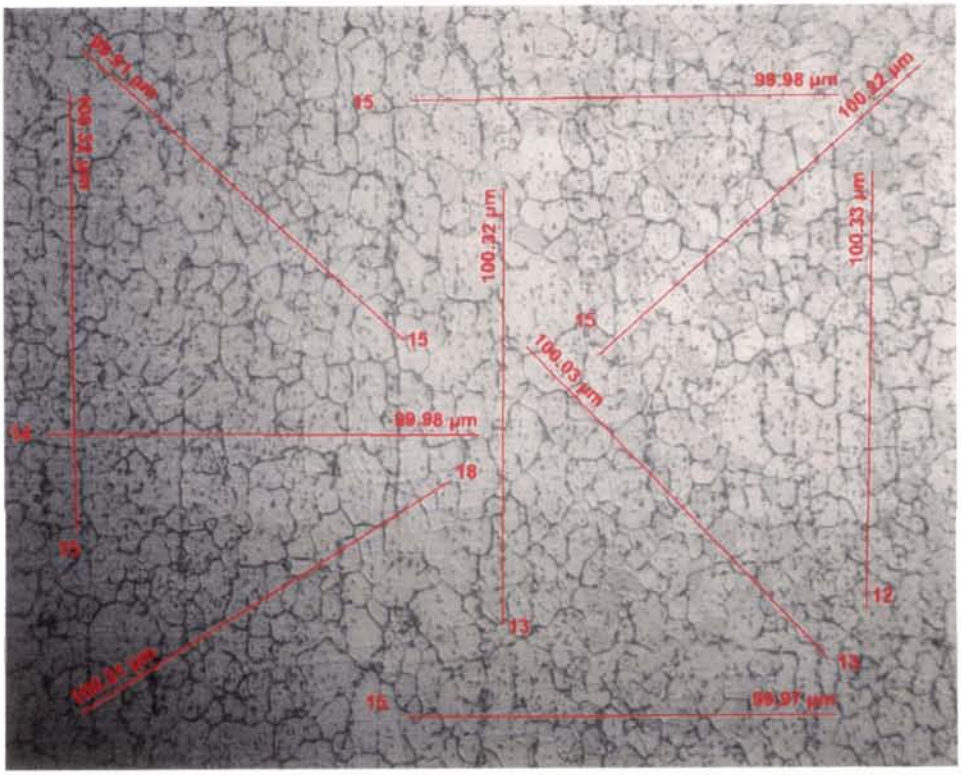

Fig B.30: Wrought Alloy 800 HT – 5 wt% Pt, yz plane, 500 X, grain size measurement

Table B.7			
Grain size calculation for Alloy 800 HT + 5 wt% Pt yz plane			
Projection	**Length (microns)**	**# intercepts**	**Grain size (microns)**
1	100.32	15	20
2	100.32	13	23
3	100.33	12	25
4	99.98	15	20
5	99.98	14	21
6	99.97	15	20
7	99.91	15	20
8	100.03	13	23
9	100.31	18	17
10	100.22	15	20
AVG grain size			**21**

B.4. Alloy 800 HT – 15 wt% Pt

B.4.1. Micrographs of Cast Structure

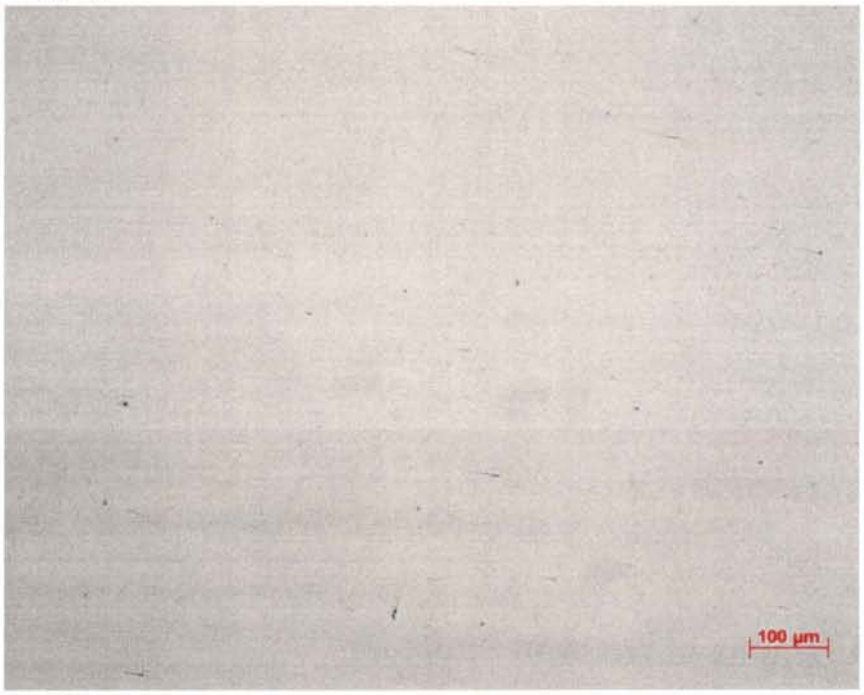

Fig B.31: Cast Alloy 800 HT – 15 wt% Pt, 100 X

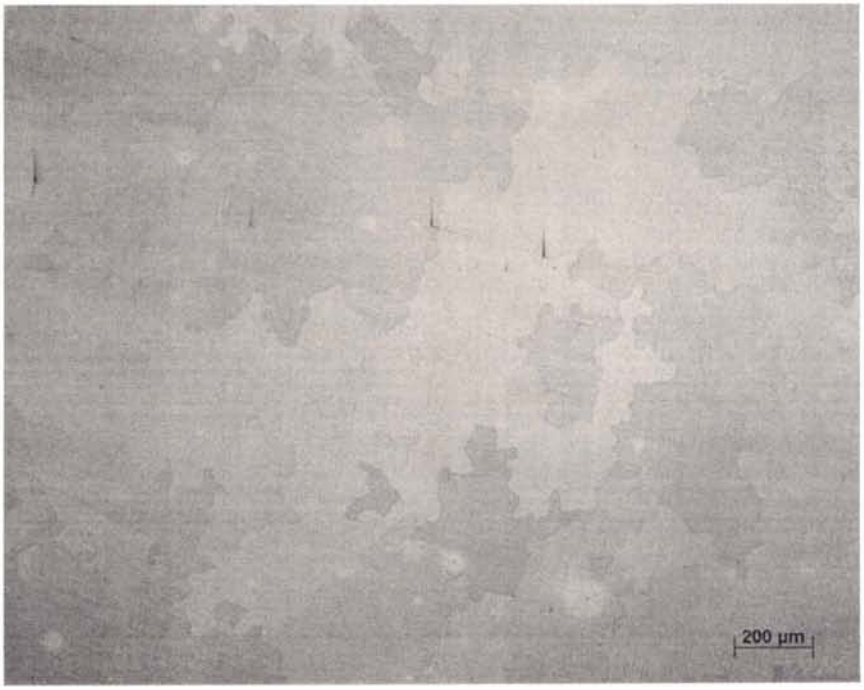

Fig B.32: Cast Alloy 800 HT – 15 wt% Pt, 50 X, weaker glyceregia – 510 sec

Fig B.33: Cast Alloy 800 HT – 15 wt% Pt, 100 X, weaker glyceregia – 510 sec

B.4.2. Micrographs of Wrought Structure

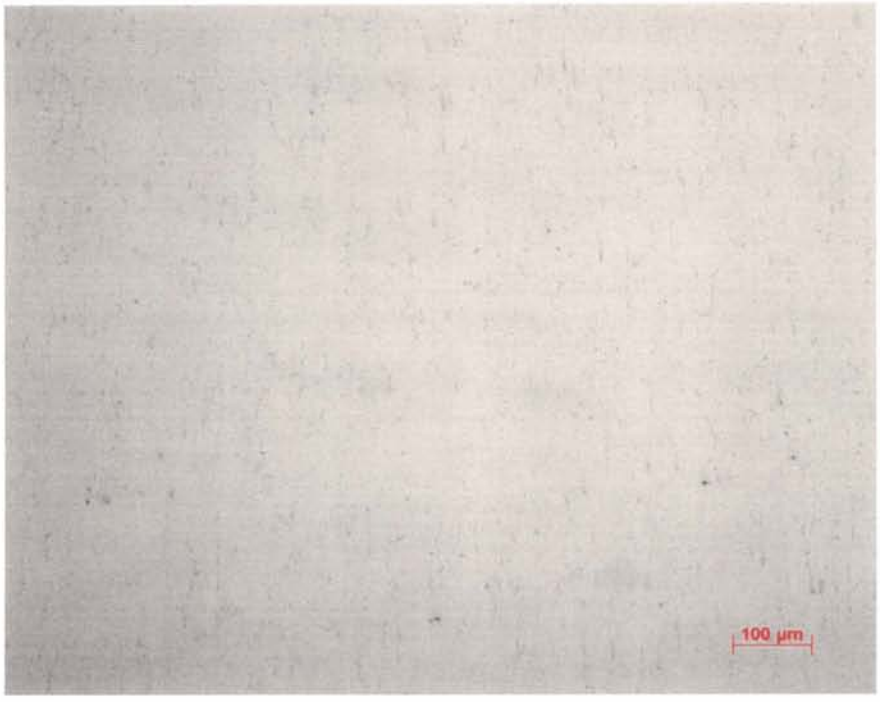

Fig B.34: Wrought Alloy 800 HT – 15 wt% Pt, xy plane, 100 X

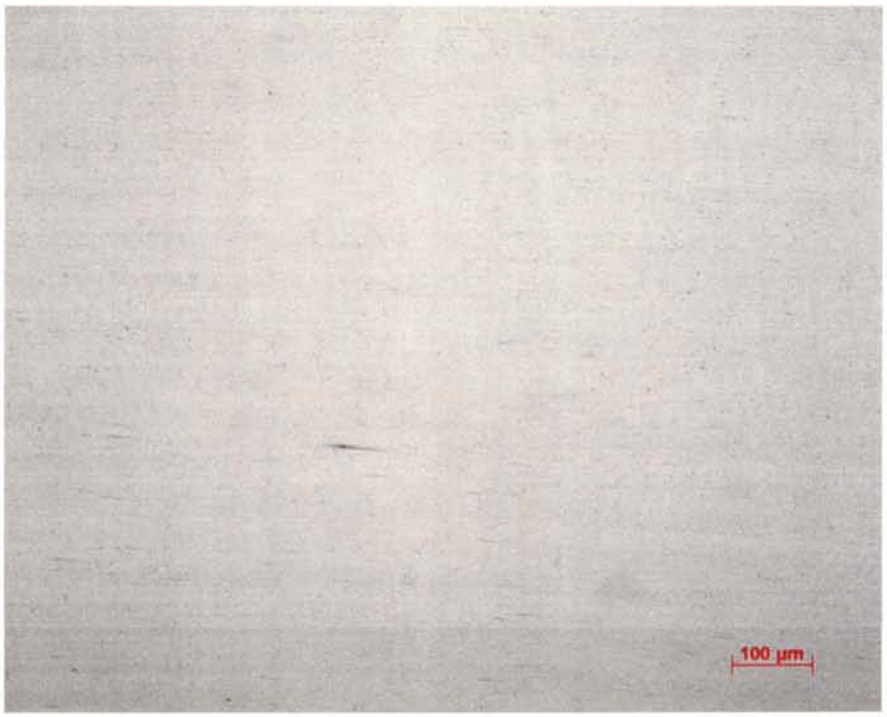

Fig B.35: Wrought Alloy 800 HT – 15 wt% Pt, xz plane, 100 X

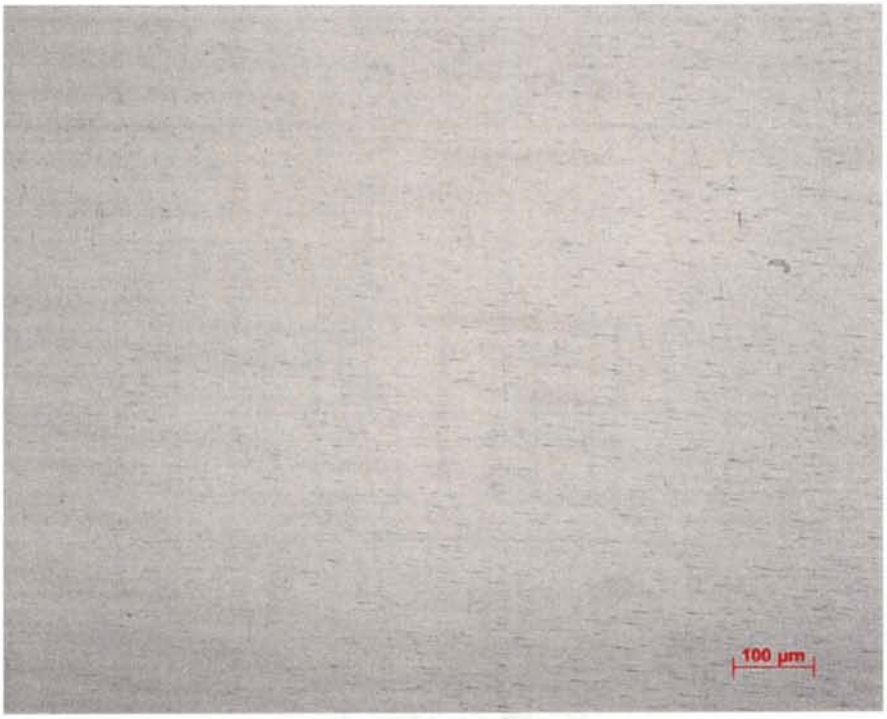

Fig B.36: Wrought Alloy 800 HT – 15 wt% Pt, yz plane, 100 X

Fig B.37: Wrought Alloy 800 HT – 15 wt% Pt, xy plane, 100 X, Nital, 3 VDC – 5 sec, 1.5 VDC – 15 sec

Fig B.38: Wrought Alloy 800 HT – 15 wt% Pt, xz plane, 100 X, Nital, 1.5 VDC – 4 sec, 1 VDC – 5 sec

Fig B.39: Wrought Alloy 800 HT – 15 wt% Pt, yz plane, 100 X, Nital, 1.5 VDC – 4 sec, 1 VDC – 5 sec

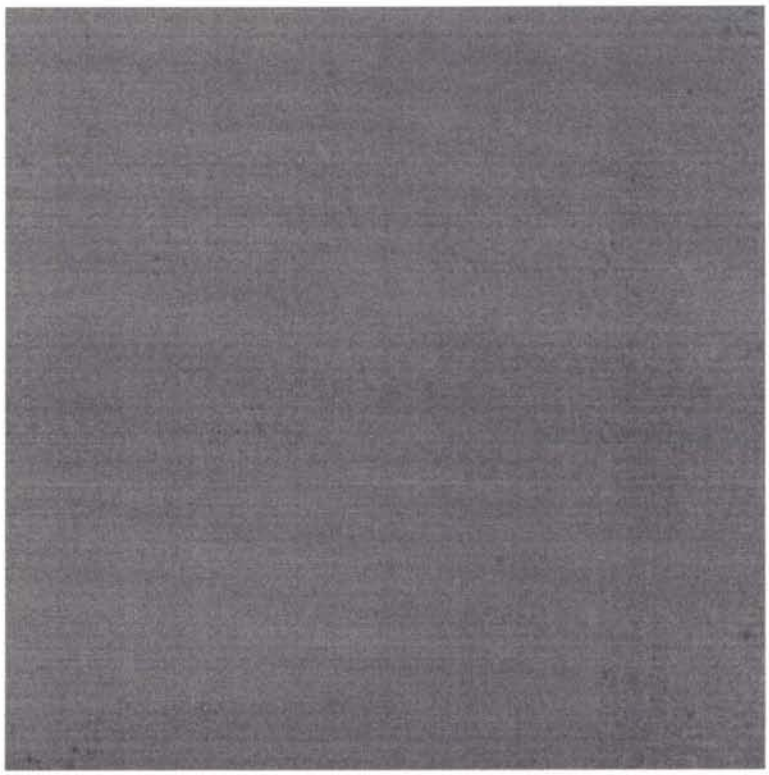

Fig B.40: Wrought Alloy 800 HT – 15 wt% Pt, Secondary Electron Image, 500 X

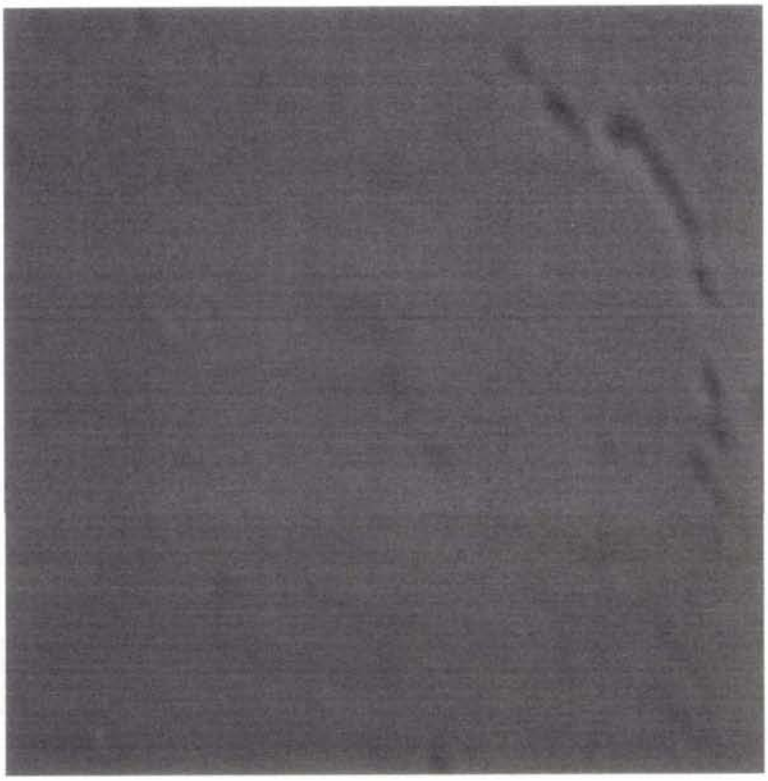

Fig B.41: Wrought Alloy 800 HT – 15 wt% Pt, Secondary Electron Image, 2500 X

B.4.3. Grain Size Calculation Data

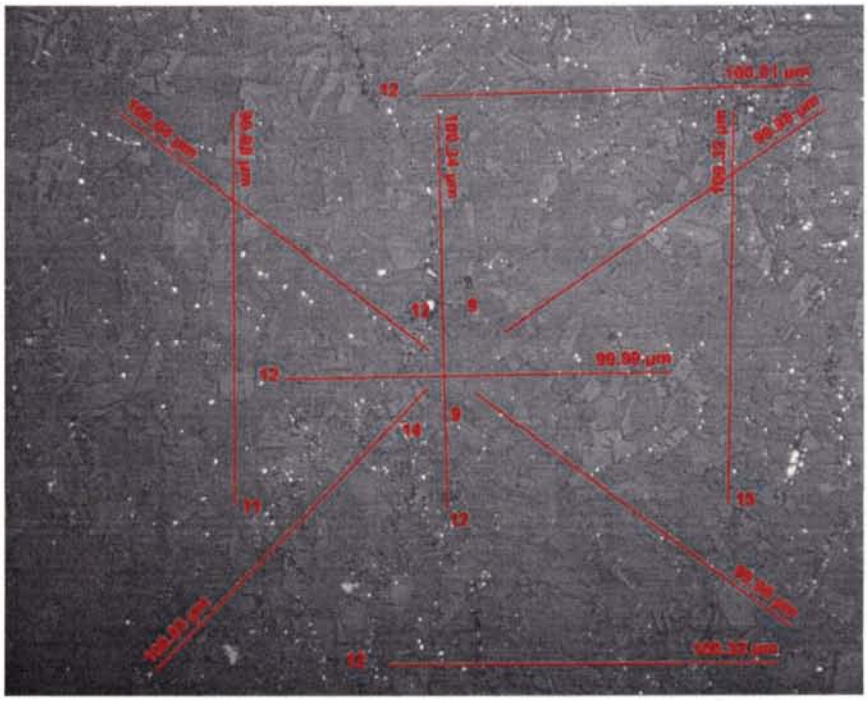

Fig B.42: Wrought Alloy 800 HT – 15 wt% Pt, xy plane, 500 X, grain size measurement

Table B.8			
Grain size calculation for Alloy 800 HT + 15 wt% Pt xy plane			
Projection	**Length (microns)**	**# intercepts**	**Grain size (microns)**
1	99.98	11	27
2	100.34	12	25
3	100.32	15	20
4	100.01	12	25
5	99.99	12	25
6	100.32	12	25
7	100.04	12	25
8	99.98	9	33
9	100.03	14	21
10	99.98	9	33
AVG grain size			**26**

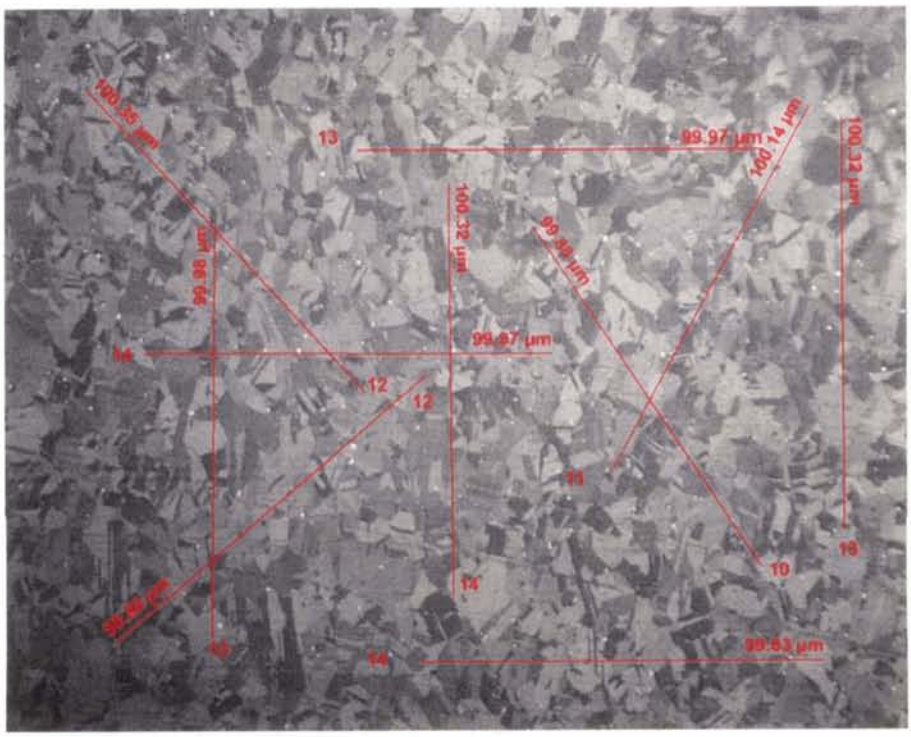

Fig B.43: Wrought Alloy 800 HT – 15 wt% Pt, xz plane, 500 X, grain size measurement

Table B.9			
Grain size calculation for Alloy 800 HT + 15 wt% Pt xz plane			
Projection	**Length (microns)**	**# intercepts**	**Grain size (microns)**
1	100.35	12	20
2	99.88	12	25
3	100.12	11	27
4	99.88	10	30
5	99.98	13	23
6	100.32	14	22
7	100.32	13	23
8	99.97	13	23
9	99.97	14	21
10	99.63	14	21
AVG grain size			**24**

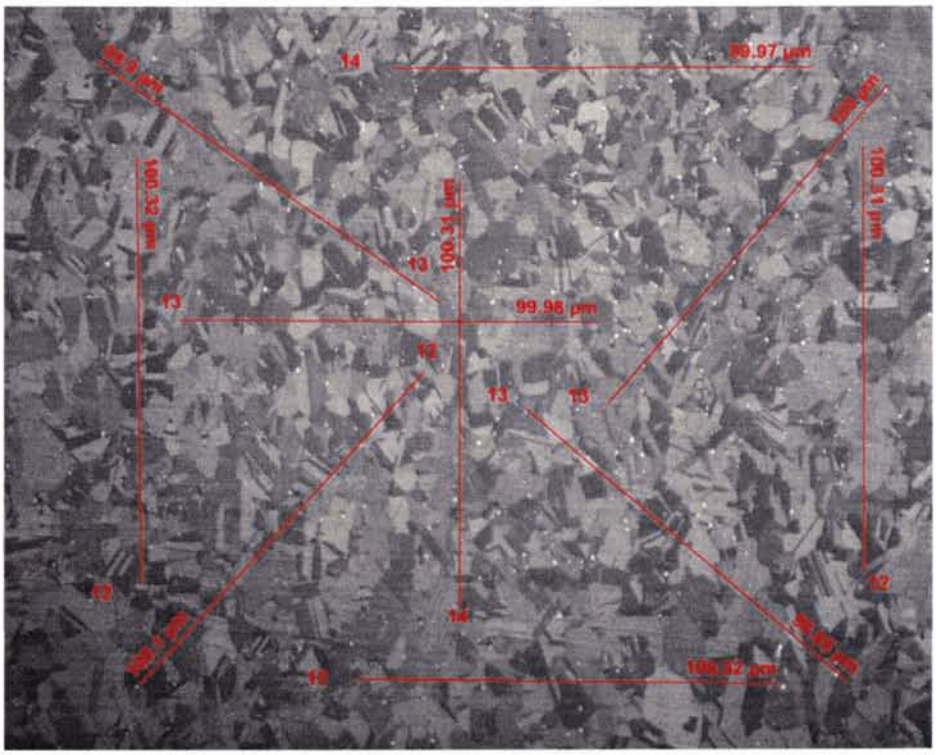

Fig B.44: Wrought Alloy 800 HT – 15 wt% Pt, yz plane, 500 X, grain size measurement

Table B.10			
Grain size calculation for Alloy 800 HT + 15 wt% Pt yz plane			
Projection	**Length (microns)**	**# intercepts**	**Grain size (microns)**
1	99.97	14	21
2	99.98	13	23
3	100.32	12	25
4	100.32	12	25
5	100.31	14	22
6	100.31	12	25
7	99.9	13	23
8	99.66	13	23
9	100	13	23
10	100.1	12	25
AVG grain size			**24**

B.5. Alloy 800 HT – 30 wt% Pt

B.5.1. Micrographs of Cast Structure

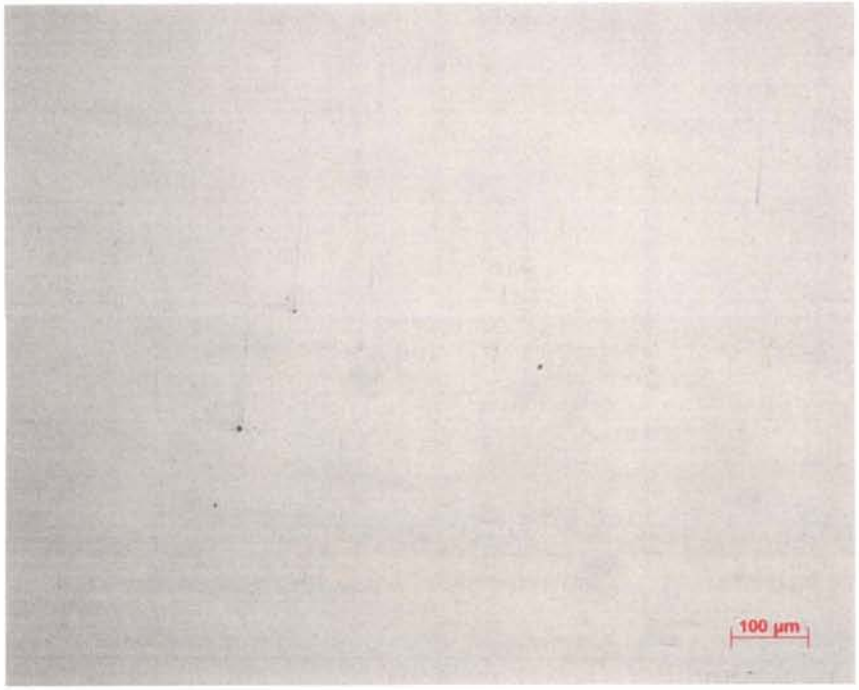

Fig B.45: Cast Alloy 800 HT – 30 wt% Pt, 100 X

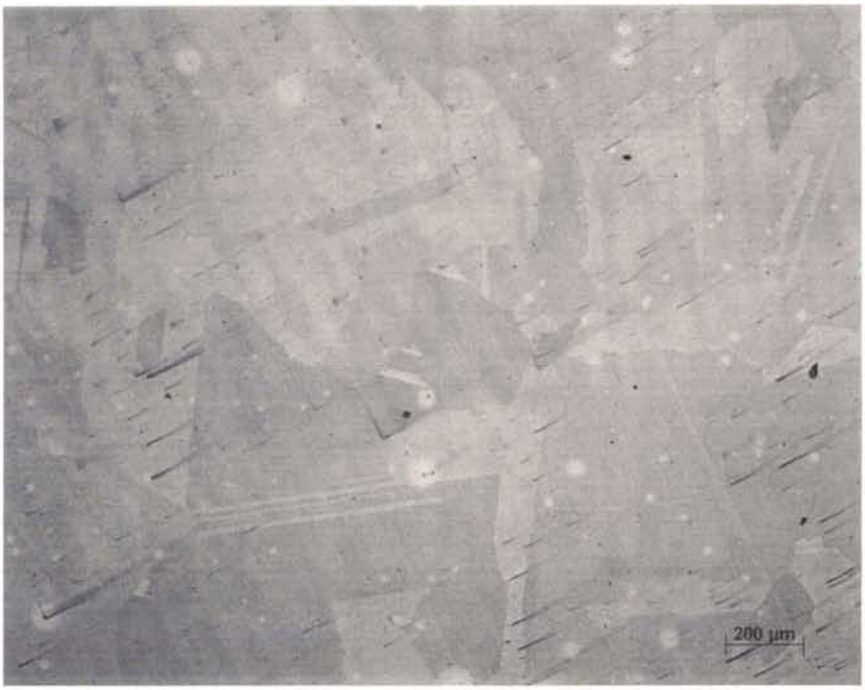

Fig B.46: Cast Alloy 800 HT - 30 wt% Pt, 50 X, weak glyceregia - 1380 sec

Fig B.47: Cast Alloy 800 HT - 30 wt% Pt, 100 X, weak glyceregia - 1380 sec

B.5.2. Micrographs of Wrought Structure

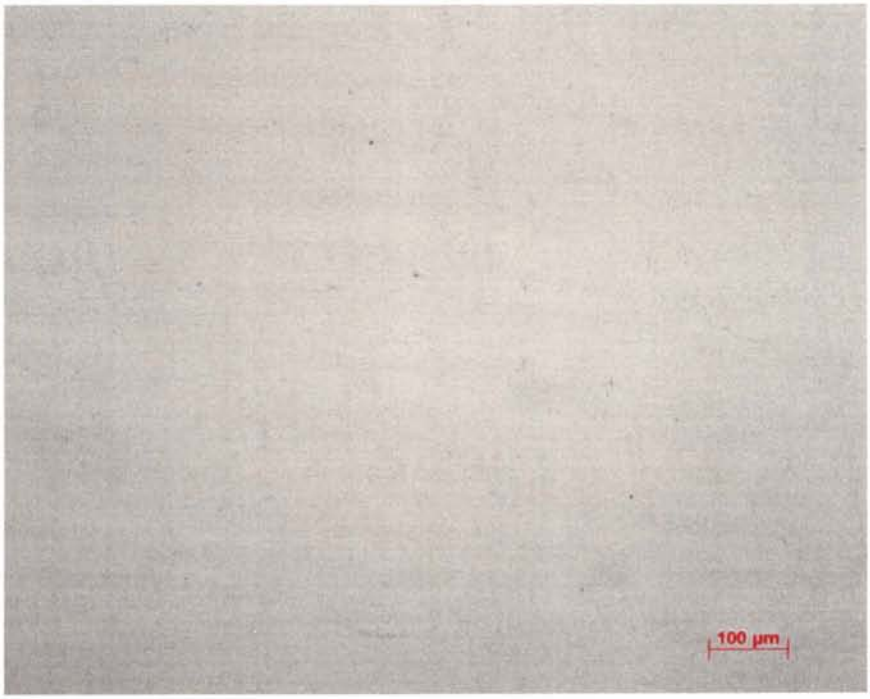

Fig B.48: Wrought Alloy 800 HT – 30 wt% Pt, xy plane, 100 X

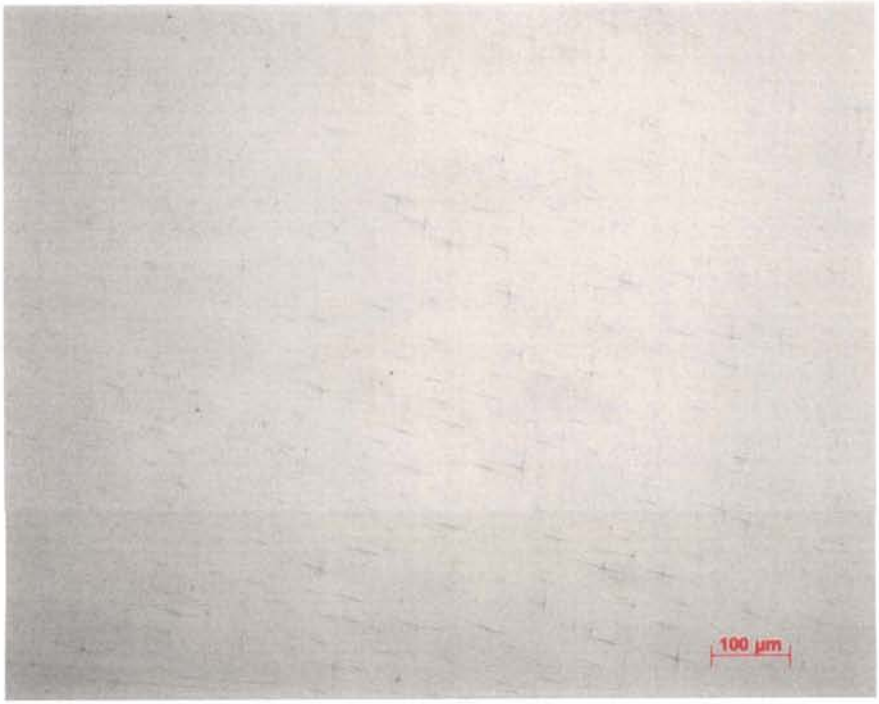

Fig B.49: Wrought Alloy 800 HT – 30 wt% Pt, xz plane, 100 X

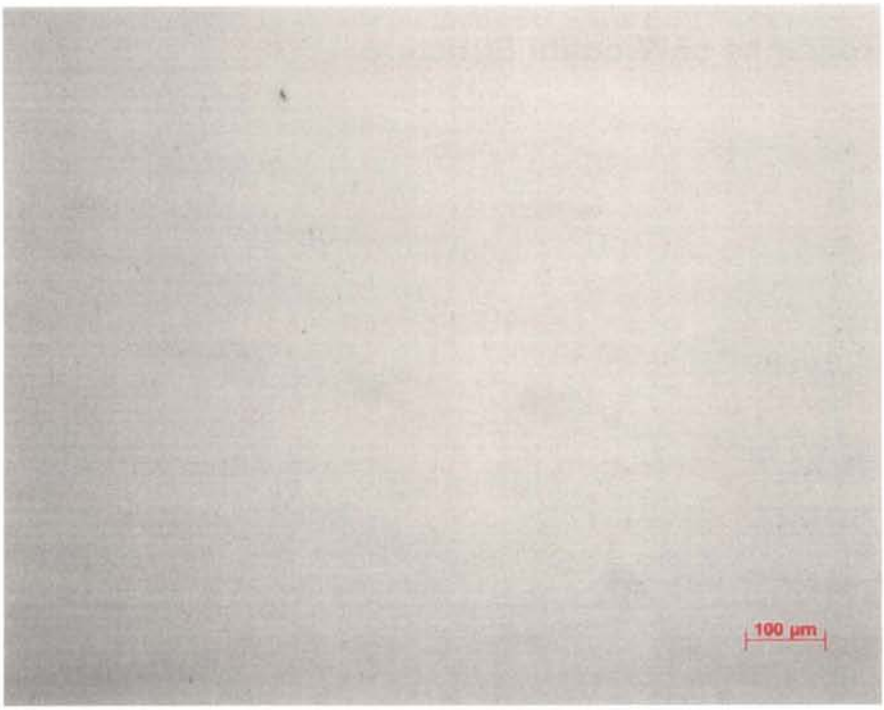

Fig B.50: Wrought Alloy 800 HT – 30 wt% Pt, yz plane, 100 X

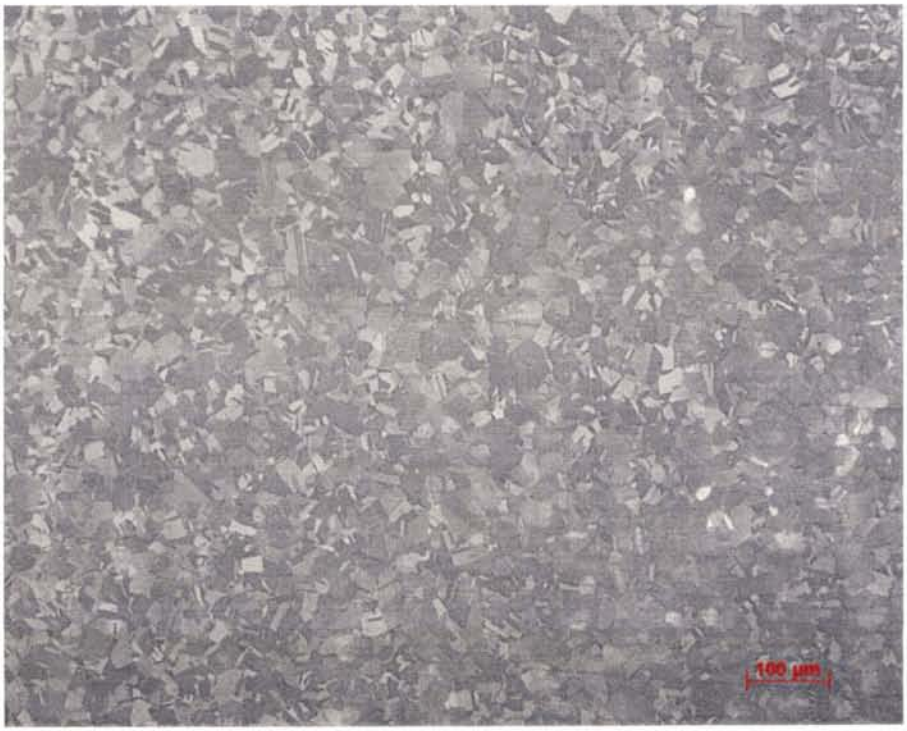

Fig B.51: Wrought Alloy 800 HT - 30 wt% Pt, xy plane, 100 X, Nital, 3 VDC - 5 sec

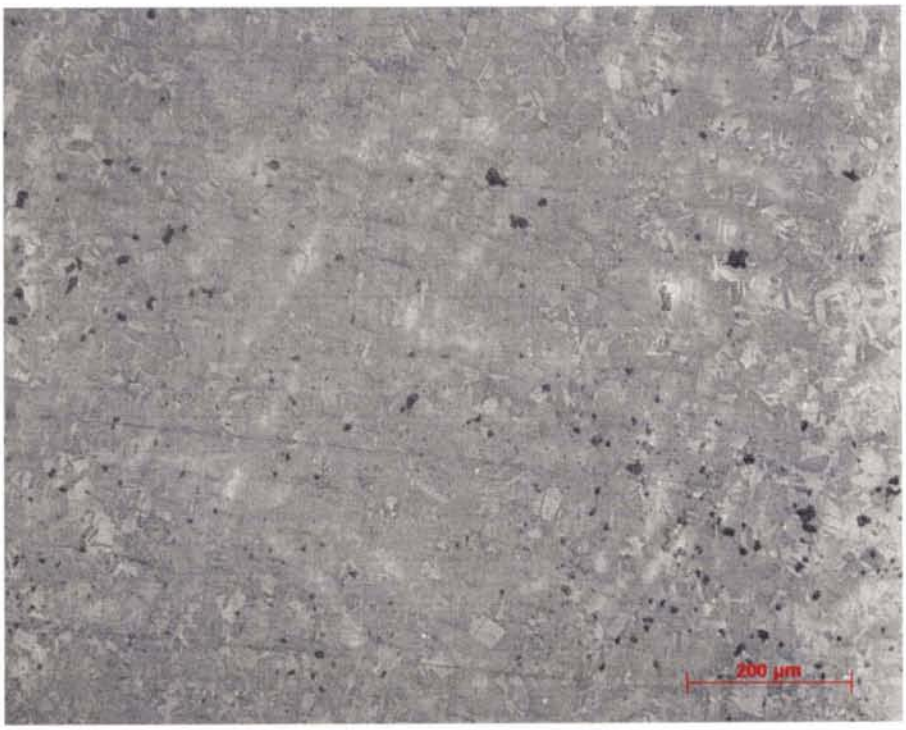

Fig B.52: Wrought Alloy 800 HT - 30 wt% Pt, xz plane, 100 X, Nital, 1.5 VDC - 15 sec

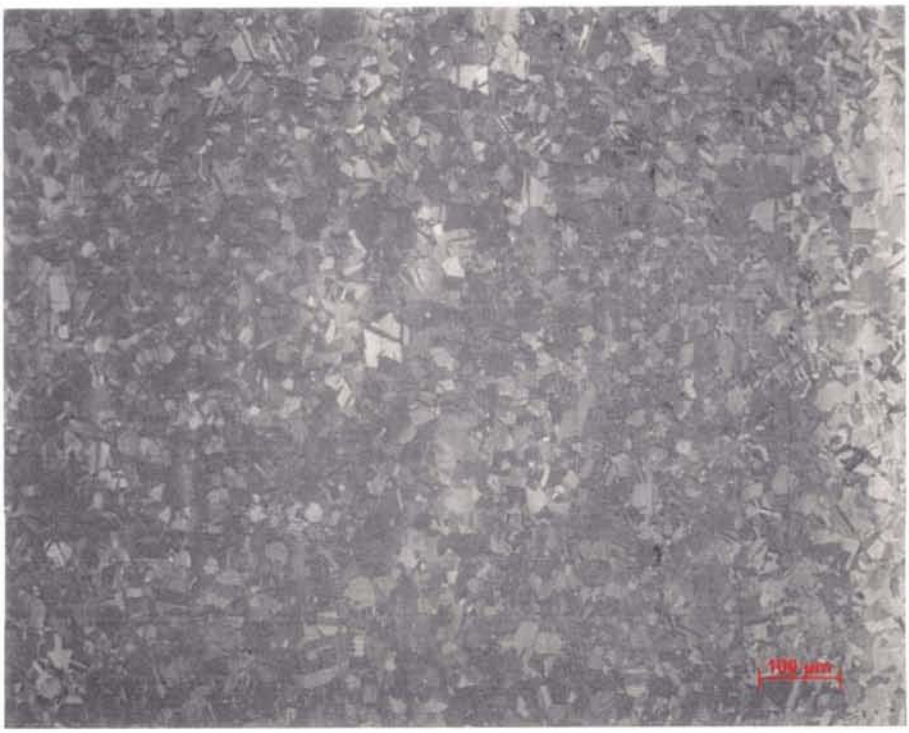

Fig B.53: Wrought Alloy 800 HT - 30 wt% Pt, yz plane, 100 X, Nital, 1 VDC - 4 sec

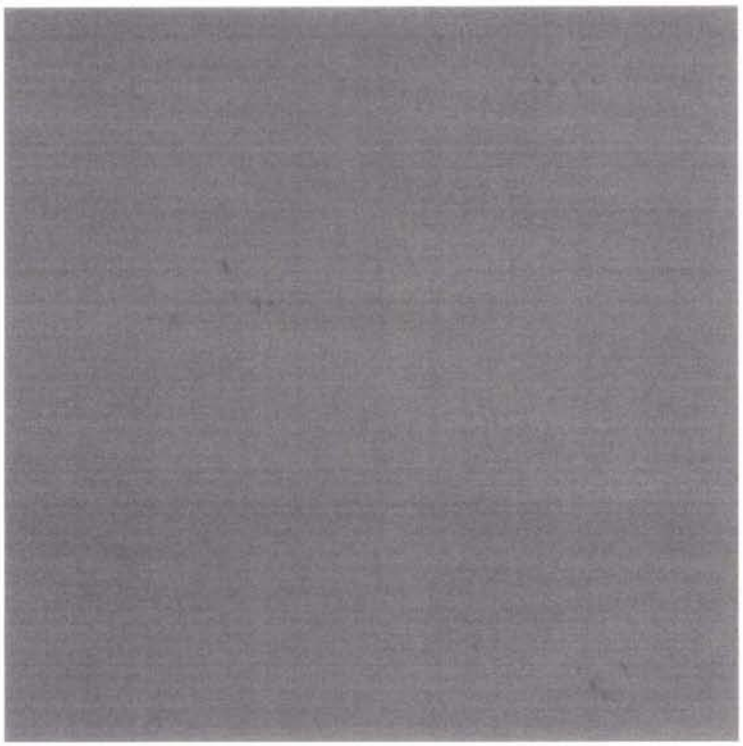

Fig B.54: Wrought Alloy 800 HT – 30 wt% Pt, Secondary Electron Image, 500 X

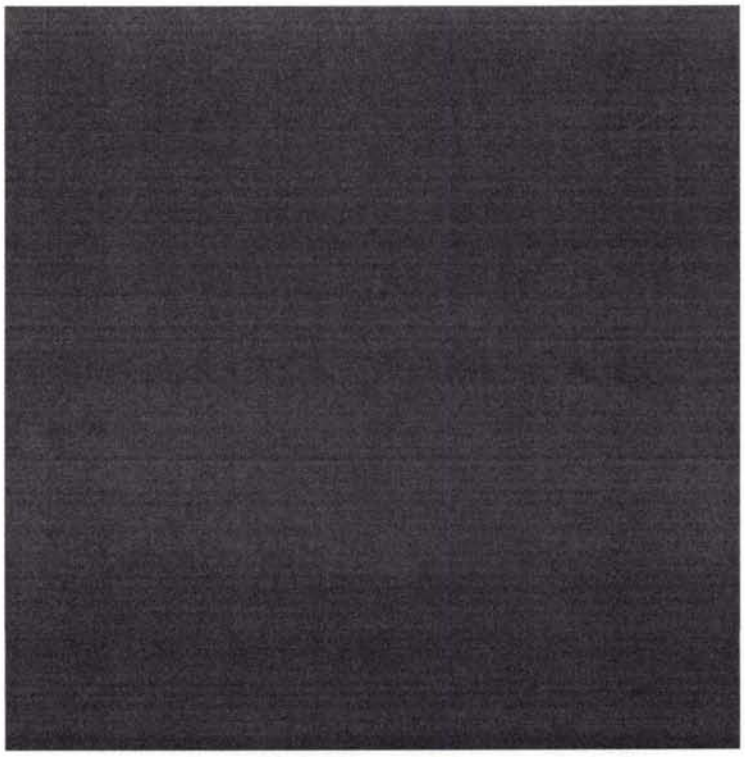

Fig B.55: Wrought Alloy 800 HT – 30 wt% Pt, Secondary Electron Image, 2500 X

B.5.3. Grain Size Calculation Data

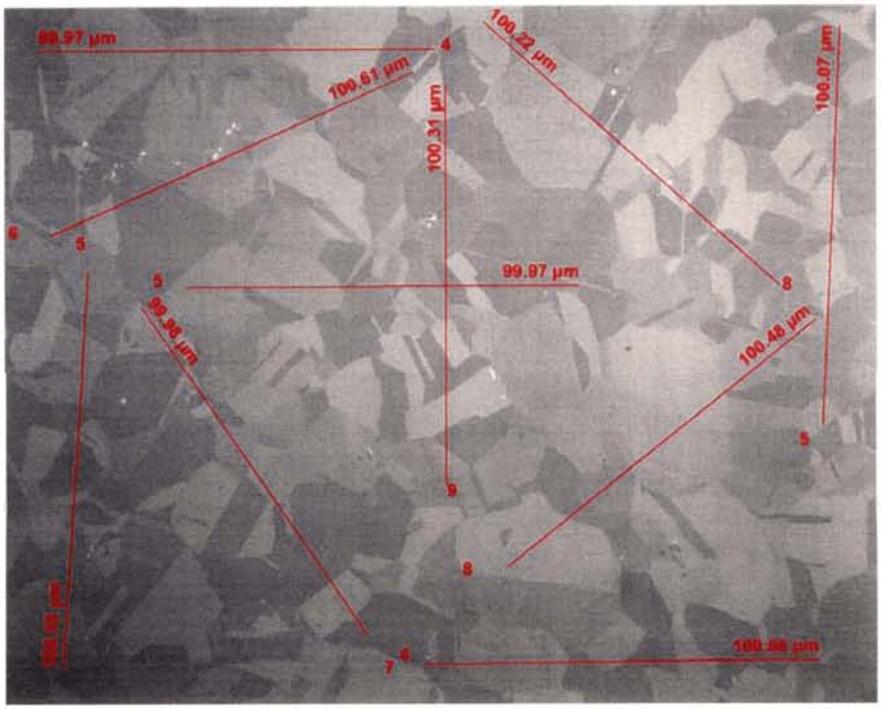

Fig B.56: Wrought Alloy 800 HT – 30 wt% Pt, xy plane, 500 X, grain size measurement

Table B.11			
Grain size calculation for Alloy 800 HT + 30 wt% Pt xy plane			
Projection	**Length (microns)**	**# intercepts**	**Grain size (microns)**
1	99.97	4	75
2	99.97	5	60
3	100.66	6	50
4	100.18	5	60
5	100.31	9	33
6	100.07	5	60
7	100.61	6	50
8	99.98	7	43
9	100.48	8	38
10	100.22	8	38
AVG grain size			**51**

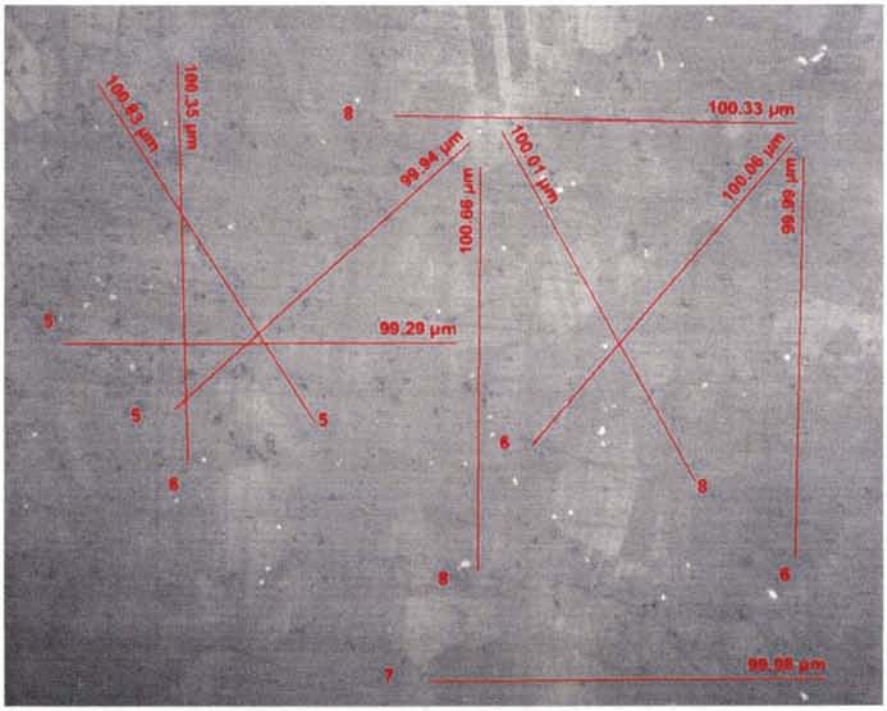

Fig B.57: Wrought Alloy 800 HT – 30 wt% Pt, xz plane, 500 X, grain size measurement

Table B.12			
Grain size calculation for Alloy 800 HT + 30 wt% Pt xz plane			
Projection	**Length (microns)**	**# intercepts**	**Grain size (microns)**
1	100.33	8	38
2	99.29	5	60
3	99.98	7	43
4	100.35	6	50
5	100.66	8	38
6	99.99	6	50
7	100.83	5	60
8	99.94	5	60
9	100.01	8	38
10	100.06	6	50
AVG grain size			**49**

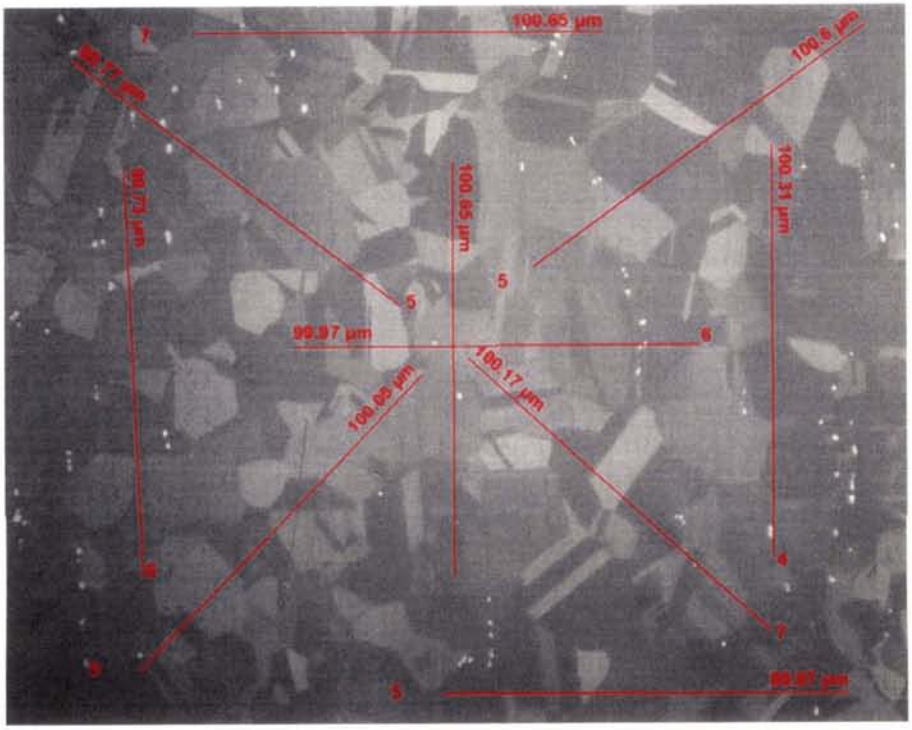

Fig B.58: Wrought Alloy 800 HT – 30 wt% Pt, yz plane, 500 X, grain size measurement

Table B.13			
Grain size calculation for Alloy 800 HT + 30 wt% Pt yz plane			
Projection	**Length (microns)**	**# intercepts**	**Grain size (microns)**
1	100.65	7	43
2	99.97	6	50
3	99.97	5	60
4	99.73	6	50
5	100.65	7	43
6	100.31	4	75
7	99.77	5	60
8	100.6	5	60
9	100.05	5	60
10	100.17	7	43
AVG grain size			**54**

B.6. Alloy 617 Grain Size Calculation Data

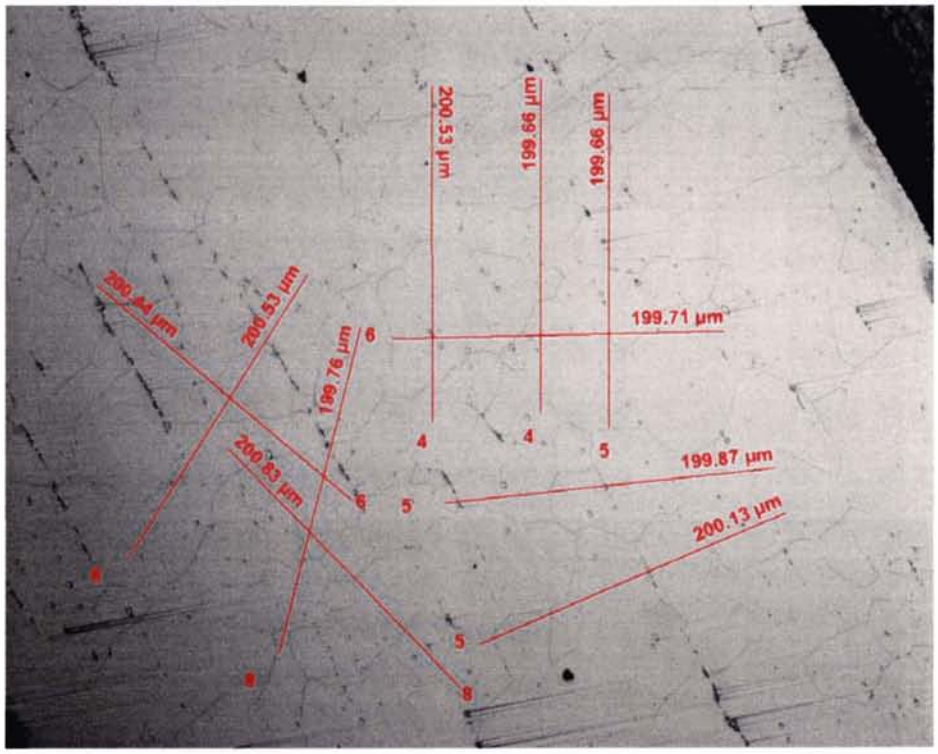

Fig B.59: Alloy 617, 200 X, grain size measurement

Table B.14			
Grain size calculation for Alloy 617			
Projection	Length (microns)	# intercepts	Grain size (microns)
1	200.13	5	120
2	199.87	5	120
3	199.71	6	100
4	200.53	4	150
5	199.66	4	150
6	199.66	5	120
7	200.44	6	100
8	200.83	8	80
9	199.76	8	80
10	200.53	6	100
AVG grain size			**110**

B.7. Alloy 617 – 2 wt% Pt

B.7.1. Micrographs of Cast Structure

Fig B.60: Cast Alloy 617 – 2 wt% Pt, 50 X

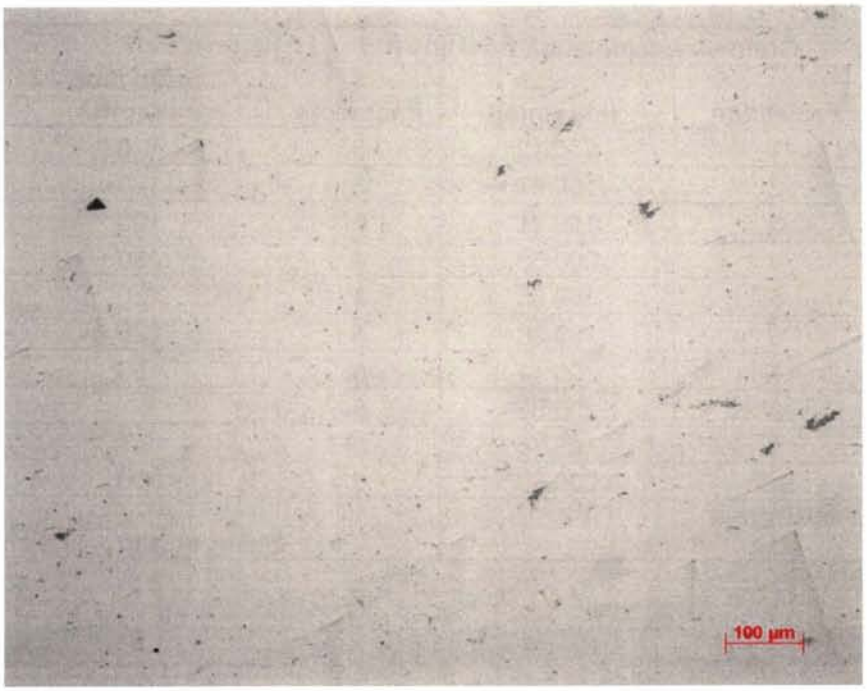

Fig B.61: Cast Alloy 617 – 2 wt% Pt, 100 X

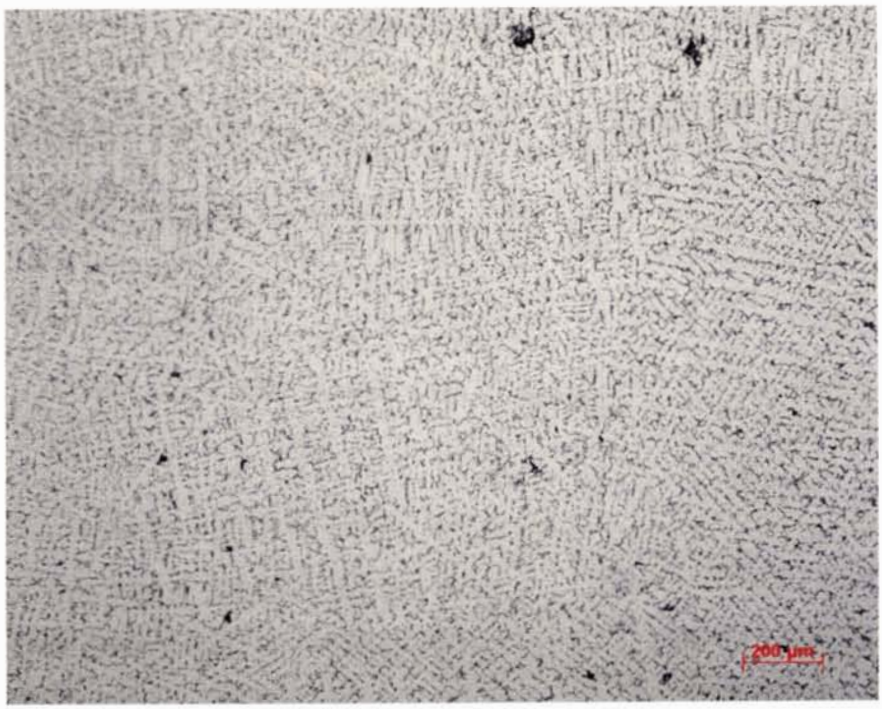

Fig B.62: Cast Alloy 617 – 2 wt% Pt, 50 X, glyceregia – 780 sec

Fig B.63: Cast Alloy 617 – 2 wt% Pt, 100 X, glyceregia – 780 sec

B.7.2. Micrographs of Wrought Structure

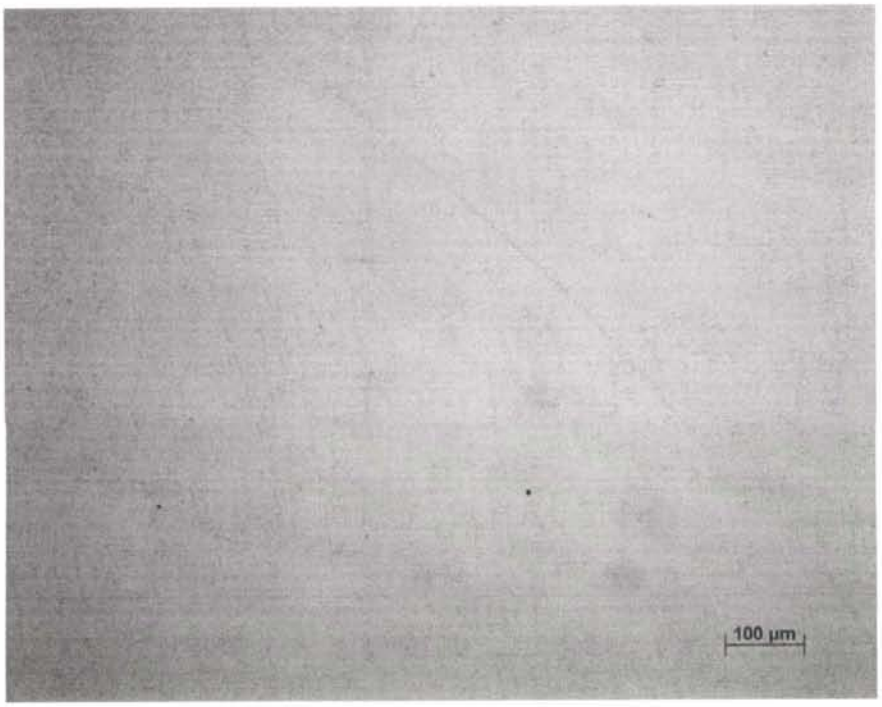

Fig B.64: Wrought Alloy 617 – 2 wt% Pt, xy plane, 100 X

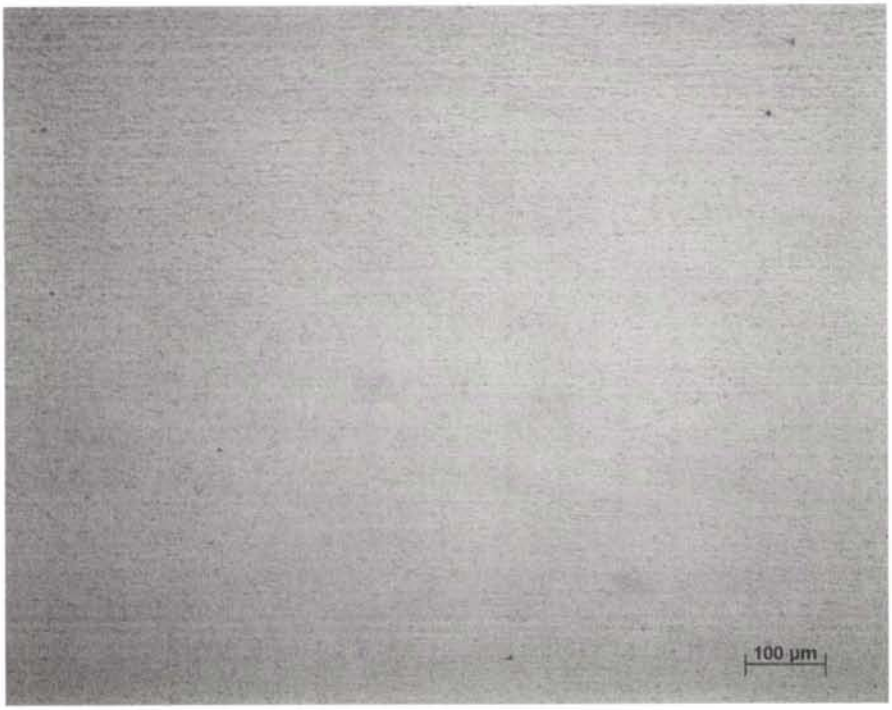

Fig B.65: Wrought Alloy 617 – 2 wt% Pt, xz plane, 100 X

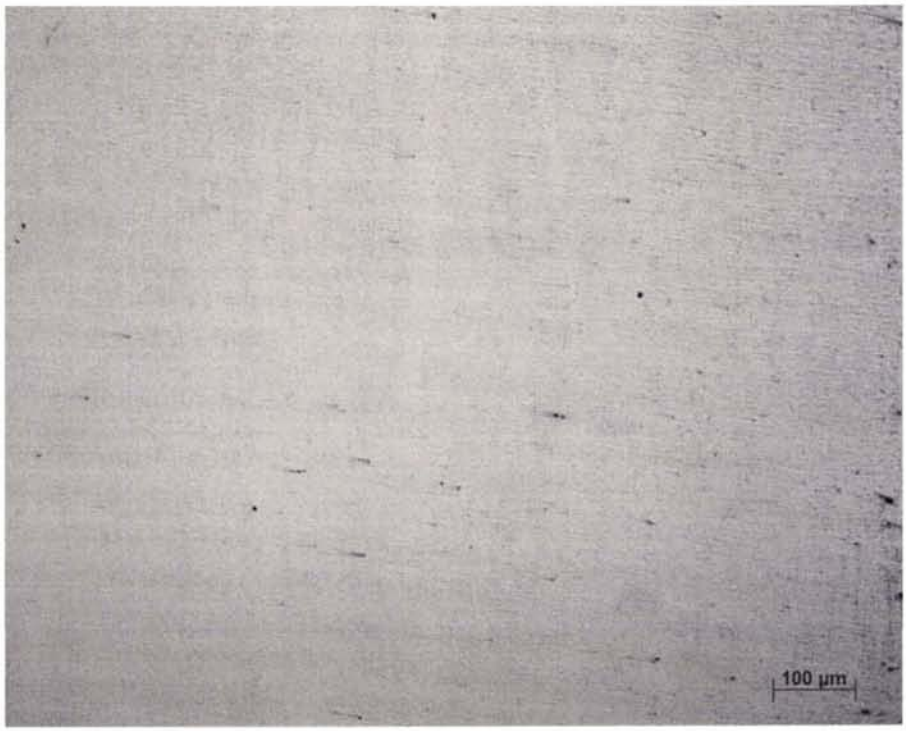

Fig B.66: Wrought Alloy 617 – 2 wt% Pt, yz plane, 100 X

Fig B.67: Wrought Alloy 617 – 2 wt% Pt, xy plane, 100 X, 10ml Oxalic Acid 90ml H_2O, 3VDC – 4 sec

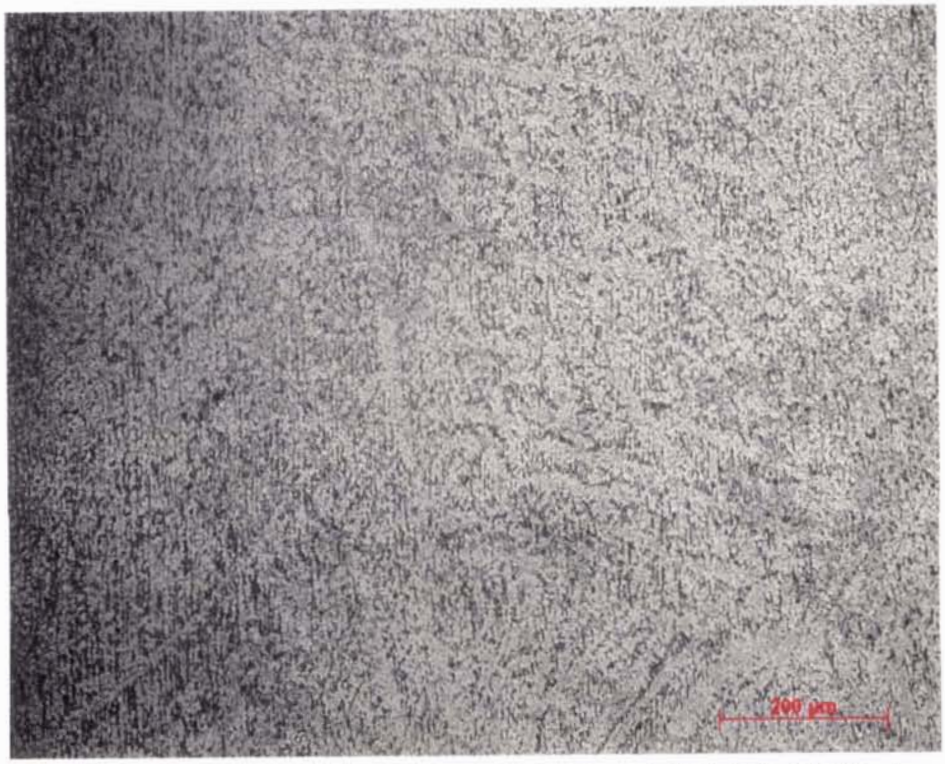

Fig B.68: Wrought Alloy 617 – 2 wt% Pt, xz plane, 100 X, 10ml Oxalic Acid 90ml H_2O, 1.5 VDC – 6 sec

Fig B.69: Wrought Alloy 617 – 2 wt% Pt, yz plane, 100 X, 10ml Oxalic Acid 90ml H_2O, 1.5 VDC – 4 sec

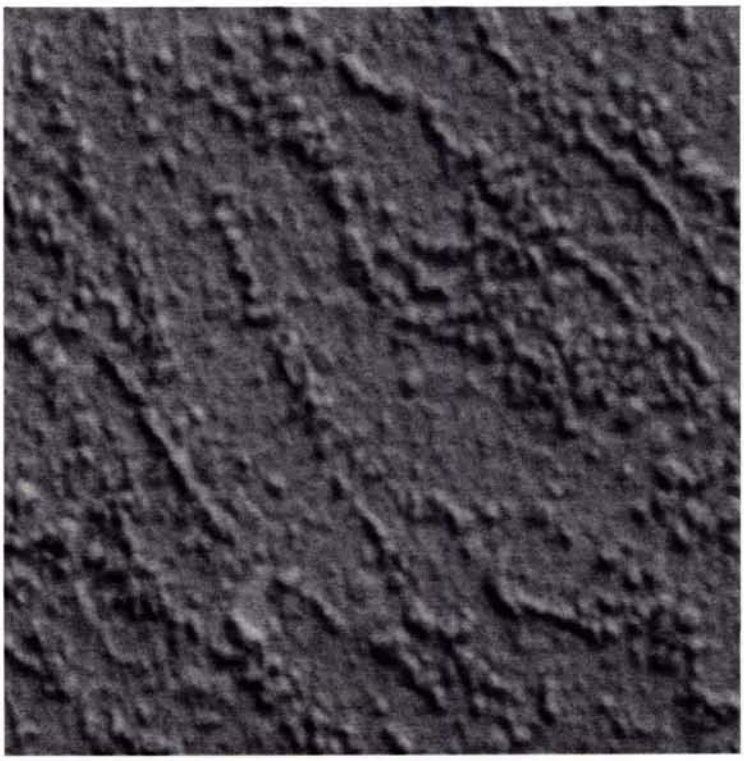

Fig B.70: Wrought Alloy 617 – 2 wt% Pt, Secondary Electron Image, 500 X

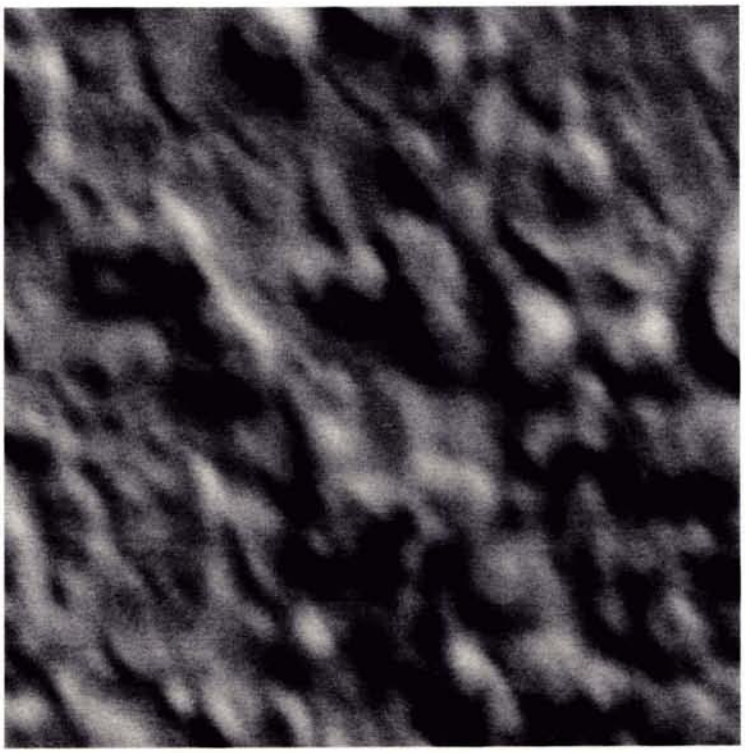

Fig B.71: Wrought Alloy 617 – 2 wt% Pt, Secondary Electron Image, 2500 X

B.7.3. Grain Size Calculation Data

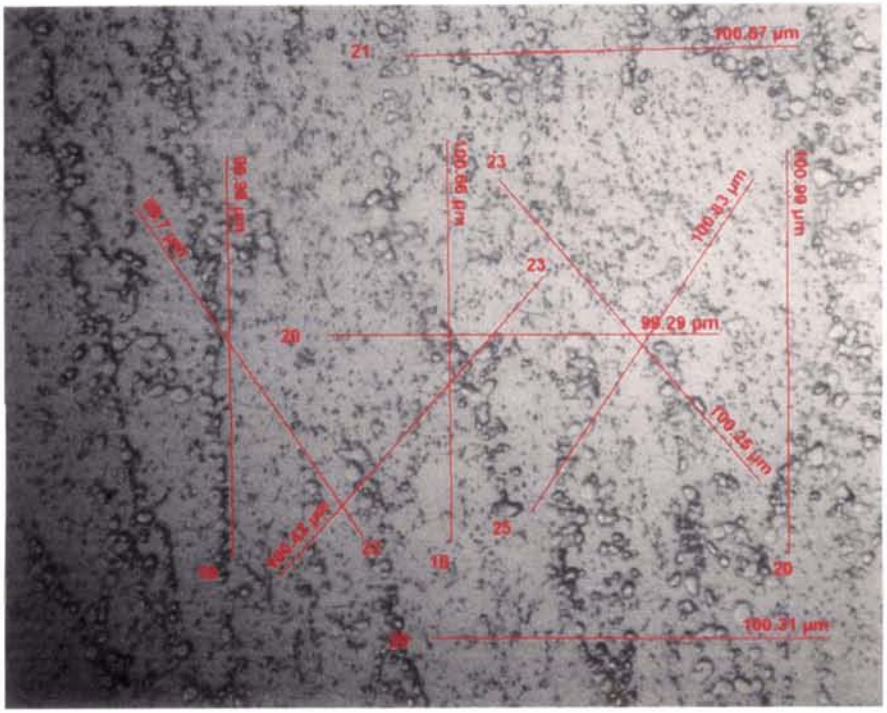

Fig B.72: Wrought Alloy 617 – 2 wt% Pt, xy plane, 500 X, grain size measurement

Table B.15			
Grain size calculation for Alloy 617 + 2 wt% Pt xy plane			
Projection	**Length (microns)**	**# intercepts**	**Grain size (microns)**
1	99.98	19	16
2	100.66	18	17
3	100.99	20	15
4	100.31	20	15
5	99.29	20	15
6	100.67	21	14
7	99.97	22	14
8	100.42	23	13
9	100.25	23	13
10	100.83	25	12
AVG grain size			**14**

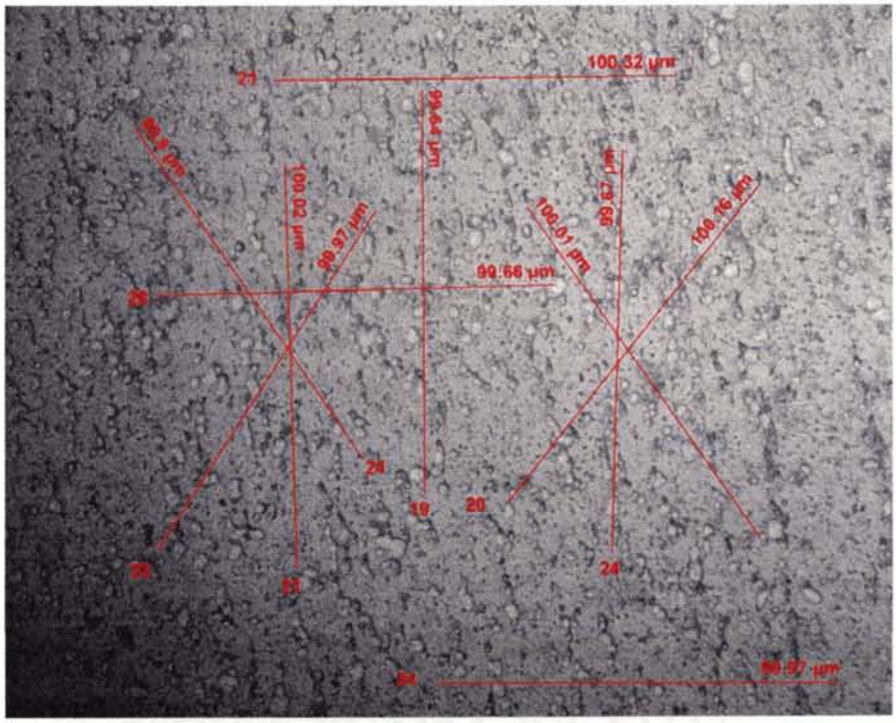

Fig B.73: Wrought Alloy 617 – 2 wt% Pt, xz plane, 500 X, grain size measurement

Table B.16			
Grain size calculation for Alloy 617 + 2 wt% Pt xz plane			
Projection	**Length (microns)**	**# intercepts**	**Grain size (microns)**
1	100.02	21	14
2	99.64	19	16
3	99.67	24	12
4	99.97	24	12
5	99.66	28	11
6	100.32	21	14
7	99.9	24	12
8	99.97	23	13
9	100.01	22	14
10	100.16	20	15
AVG grain size			**13**

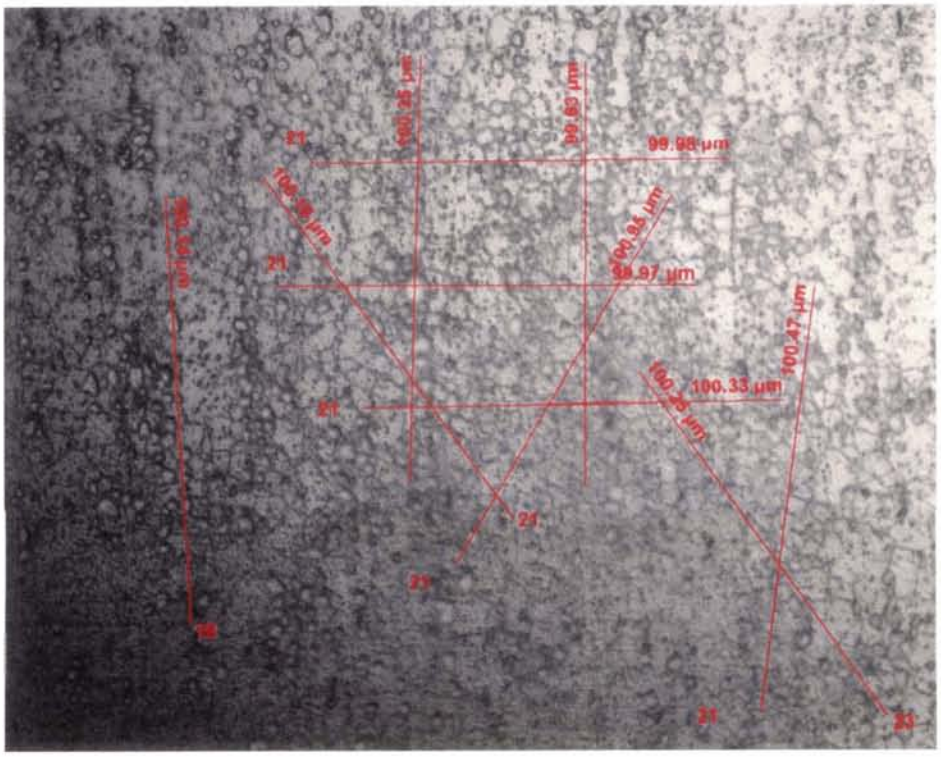

Fig B.74: Wrought Alloy 617 – 2 wt% Pt, yz plane, 500 X, grain size measurement

Table B.17			
Grain size calculation for Alloy 617 + 2 wt% Pt yz plane			
Projection	**Length (microns)**	**# intercepts**	**Grain size (microns)**
1	100.35	25	12
2	99.63	20	15
3	100.14	18	17
4	100.33	21	14
5	99.97	21	14
6	99.98	21	14
7	100.18	21	14
8	100.95	21	14
9	100.25	23	13
10	100.47	21	14
AVG grain size			**14**

B.8. Alloy 617 – 5 wt% Pt

B.8.1. Micrographs of Cast Structure

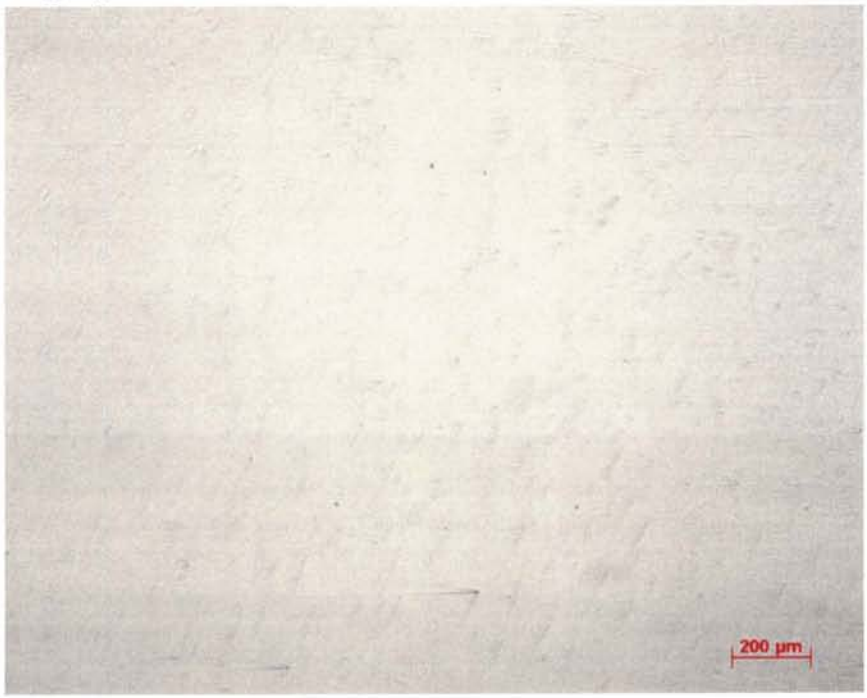

Fig B.75: Cast Alloy 617 – 5 wt% Pt, 50 X

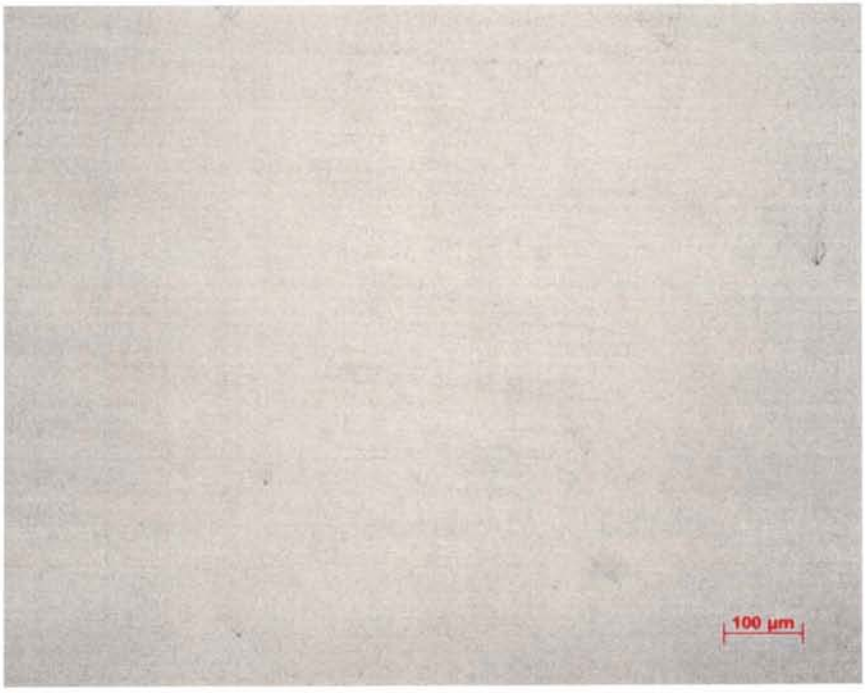

Fig B.76: Cast Alloy 617 – 5 wt% Pt, 100 X

Fig B.77: Cast Alloy 617 – 5 wt% Pt, 50 X, glyceregia – 1020 sec

Fig B.78: Cast Alloy 617 – 5 wt% Pt, 100 X, glyceregia – 1020 sec

B.8.2. Micrographs of Wrought Structure

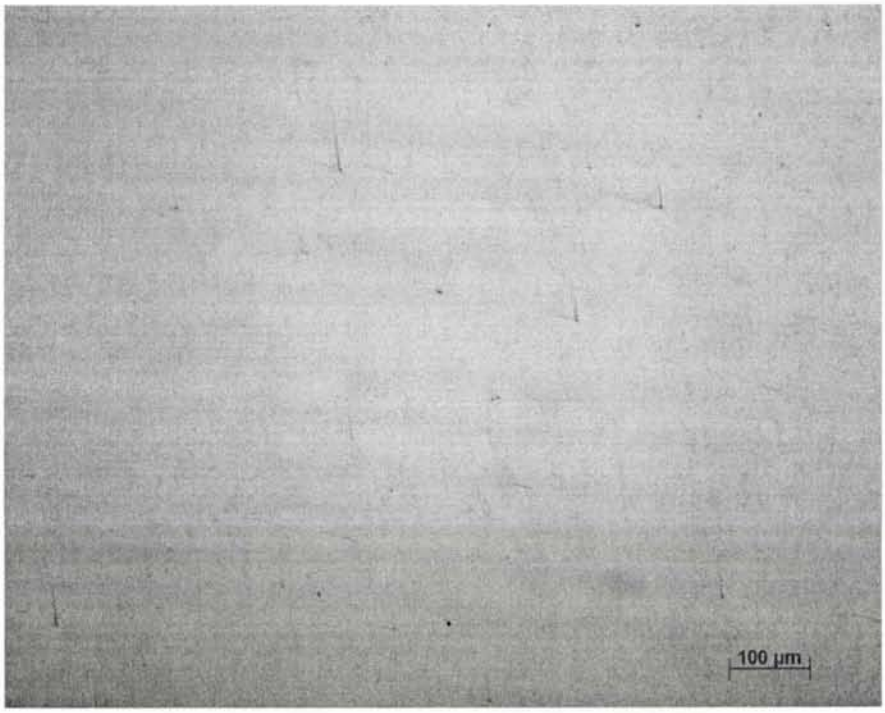

Fig B.79: Wrought Alloy 617 – 5 wt% Pt, xy plane, 100 X

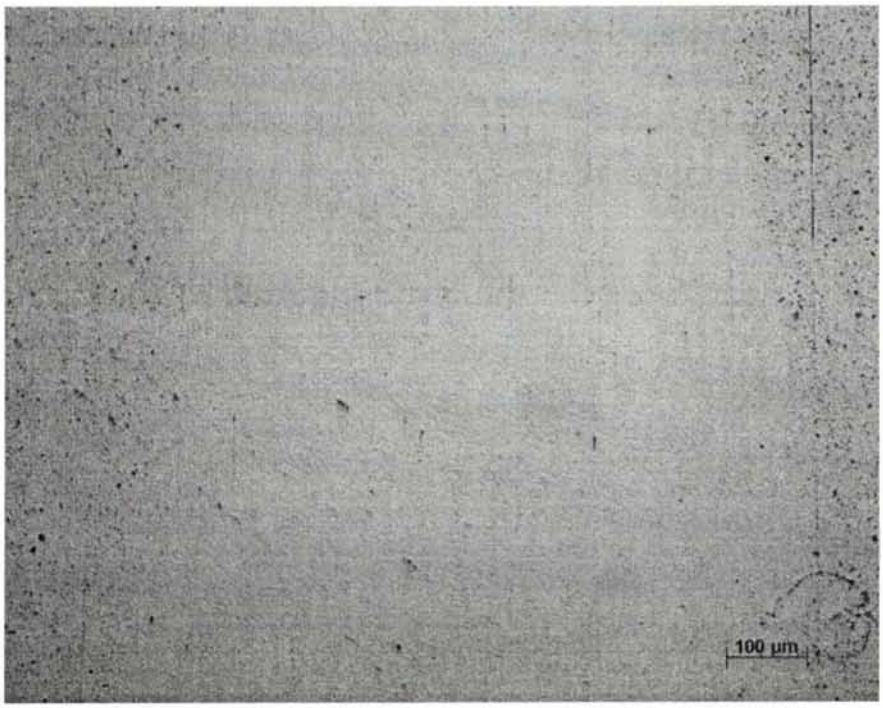

Fig B.80: Wrought Alloy 617 – 5 wt% Pt, xz plane, 100 X

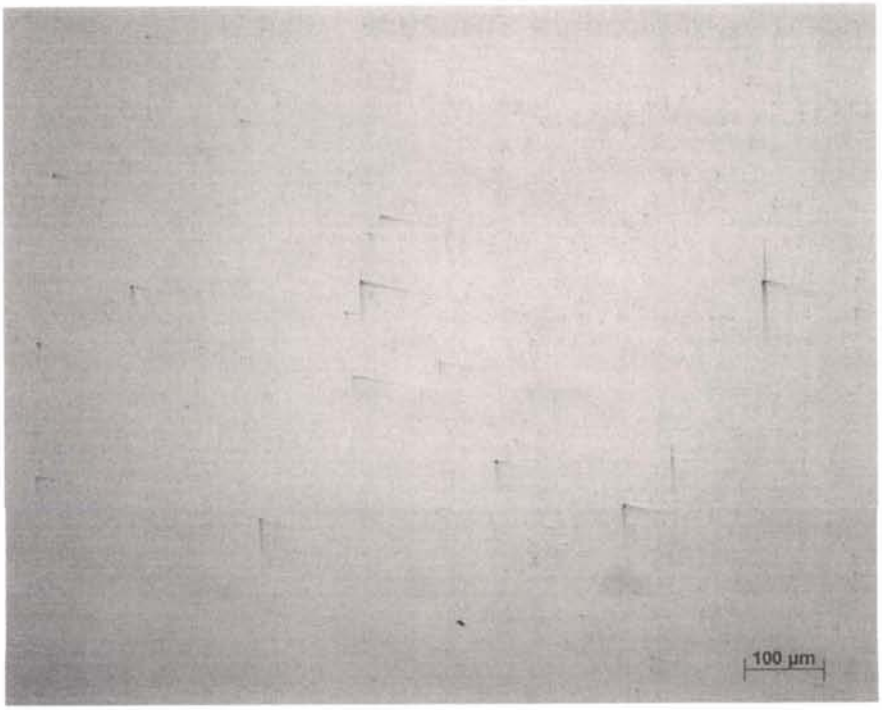

Fig B.81: Wrought Alloy 617 –5 wt% Pt, yz plane, 100 X

Fig B.82: Wrought Alloy 617 –5 wt% Pt, xy plane, 100 X, 10ml Oxalic Acid 90ml H_2O 3 ml HCl, 1.5 VDC – 6 sec

Fig B.83: Wrought Alloy 617 –5 wt% Pt, xz plane, 100 X, 10ml Oxalic Acid 90ml H_2O 3 ml HCl, 1 VDC – 3 sec

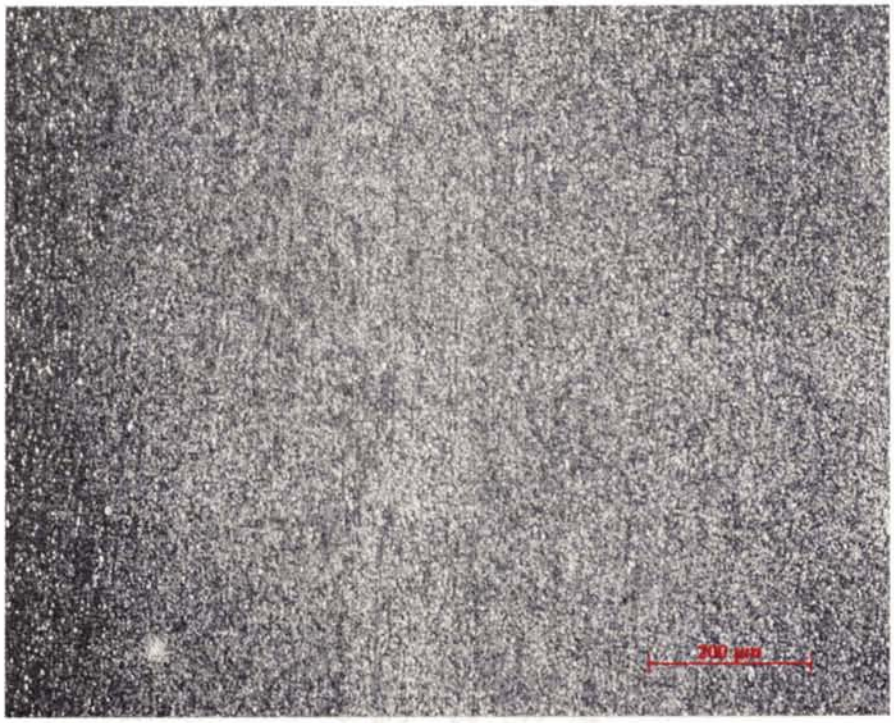

Fig B.84: Wrought Alloy 617 –5 wt% Pt, yz plane, 100 X, 10ml Oxalic Acid 90ml H_2O 3 ml HCl, 1 VDC – 3 sec

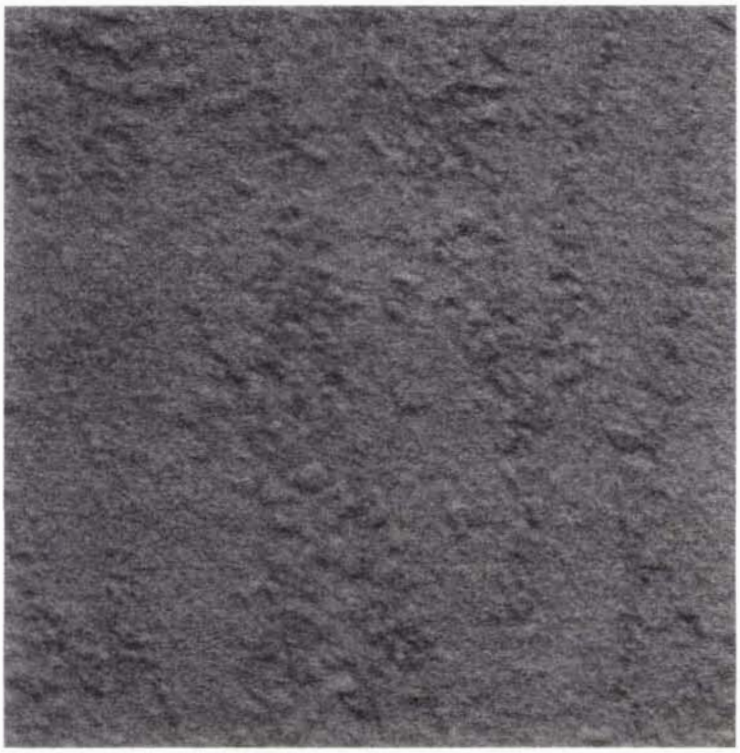

Fig B.85: Wrought Alloy 617 – 5 wt% Pt, Secondary Electron Image, 500 X

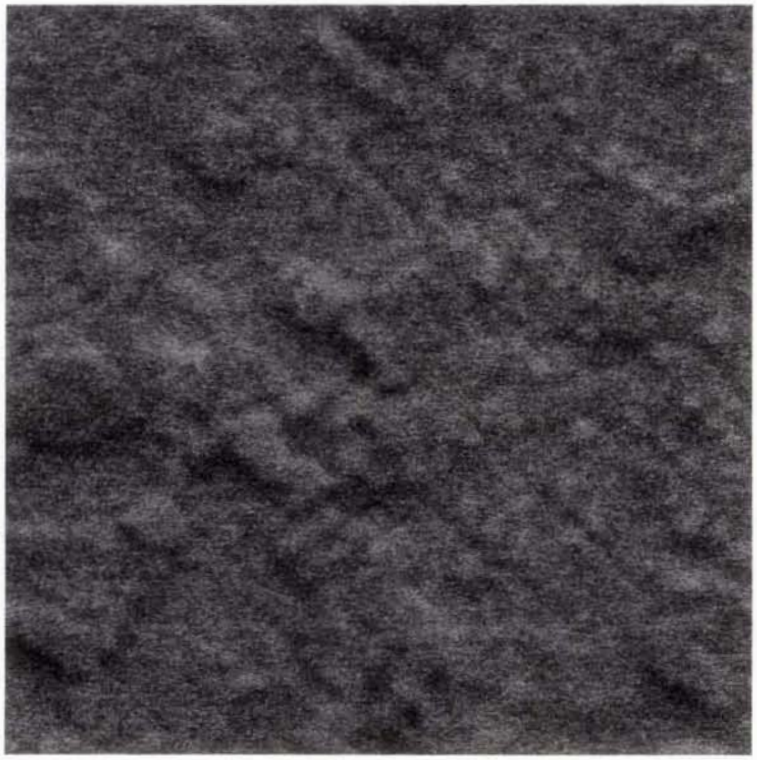

Fig B.86: Wrought Alloy 617 – 5 wt% Pt, Secondary Electron Image, 2500 X

B.8.3. Grain Size Calculation Data

Fig B.87: Wrought Alloy 617 – 5 wt% Pt, xy plane, 500 X, grain size measurement

Table B.18			
Grain size calculation for Alloy 617 + 5 wt% Pt xy plane			
Projection	**Length (microns)**	**# intercepts**	**Grain size (microns)**
1	100.21	25	12
2	99.97	25	12
3	100.99	23	13
4	99.63	26	11
5	99.66	25	12
6	100.32	21	14
7	100.1	27	11
8	100.74	27	11
9	100.08	26	12
10	100.01	27	11
AVG grain size			**12**

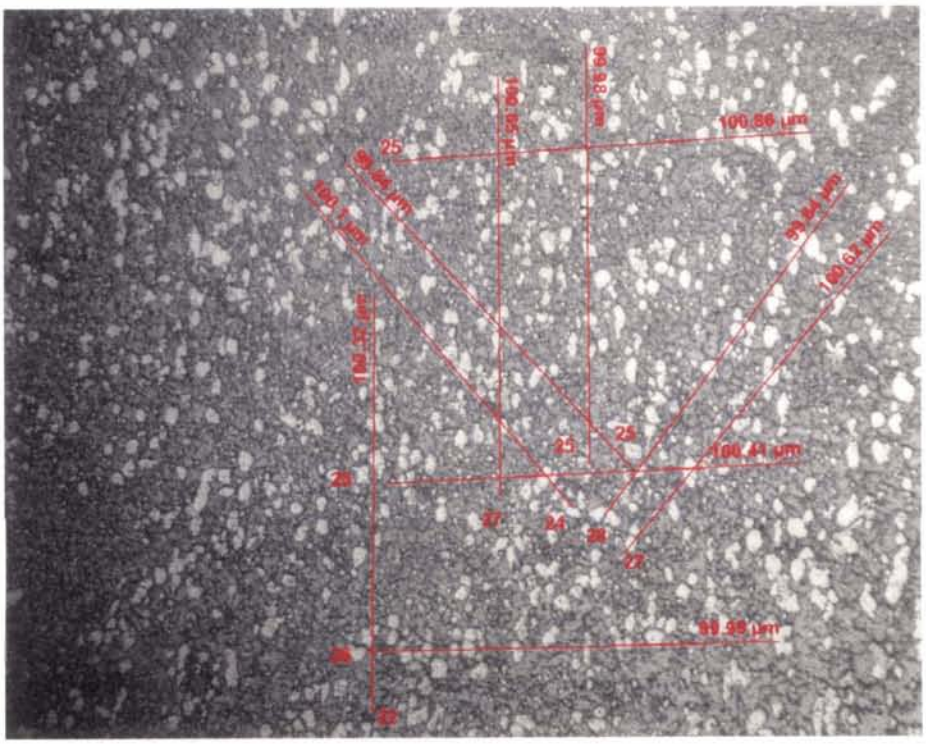

Fig B.88: Wrought Alloy 617 – 5 wt% Pt, xz plane, 500 X, grain size measurement

Table B.19			
Grain size calculation for Alloy 617 + 5 wt% Pt xz plane			
Projection	**Length (microns)**	**# intercepts**	**Grain size (microns)**
1	100.86	26	12
2	100.41	25	12
3	99.99	26	12
4	100.32	22	14
5	100.65	27	11
6	99.98	25	12
7	100.1	24	13
8	99.84	25	12
9	99.84	28	11
10	100.62	27	11
AVG grain size			**12**

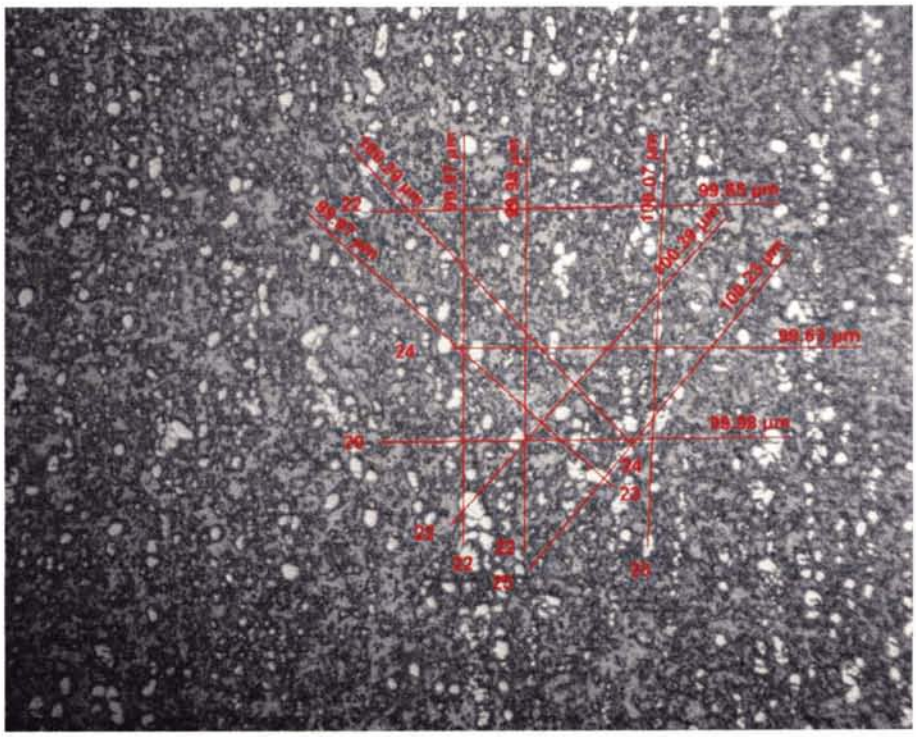

Fig B.89: Wrought Alloy 617 – 5 wt% Pt, yz plane, 500 X, grain size measurement

Table B.20			
Grain size calculation for Alloy 617 + 5 wt% Pt yz plane			
Projection	Length (microns)	# intercepts	Grain size (microns)
1	99.98	20	15
2	99.63	24	12
3	99.65	22	14
4	99.97	22	14
5	99.98	22	14
6	100.07	23	13
7	99.97	23	13
8	100.29	24	13
9	100.39	22	14
10	100.23	25	12
AVG grain size			**13**

B.9. Alloy 617 – 15 wt% Pt

B.9.1. Micrographs of Cast Structure

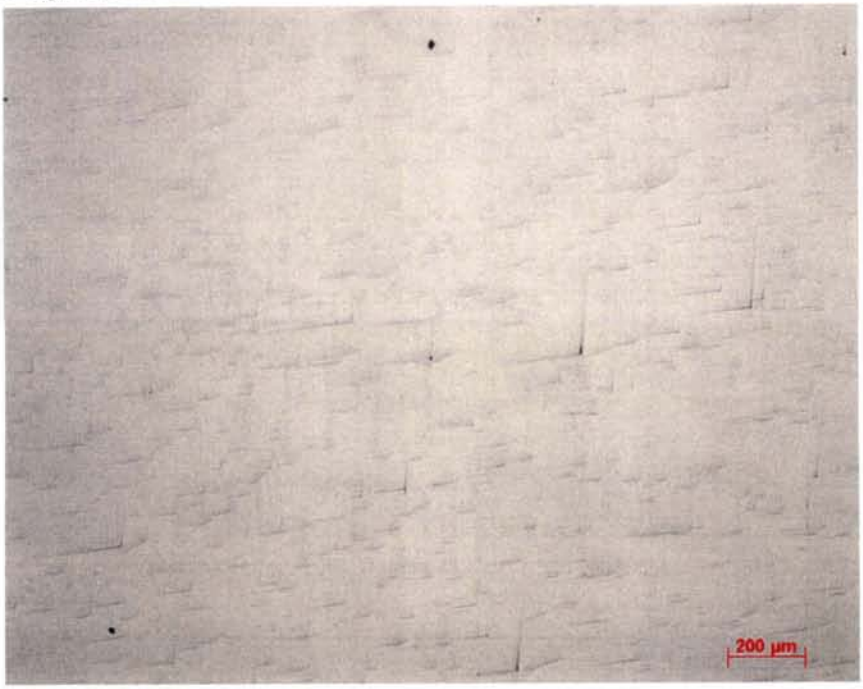

Fig B.90: Cast Alloy 617 – 15 wt% Pt, 50 X

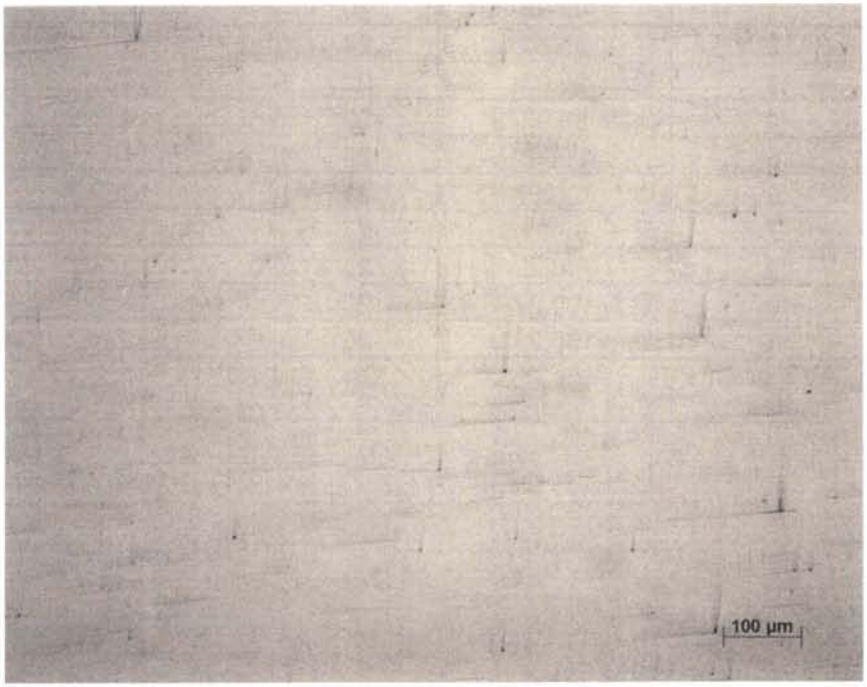

Fig B.91: Cast Alloy 617 – 15 wt% Pt, 100 X

Fig B.92: Cast Alloy 617 – 15 wt% Pt, 50 X, glyceregia – 1500 sec

Fig B.93: Cast Alloy 617 – 15 wt% Pt, 100 X, glyceregia – 1500 sec

B.9.2. Micrographs of Wrought Structure

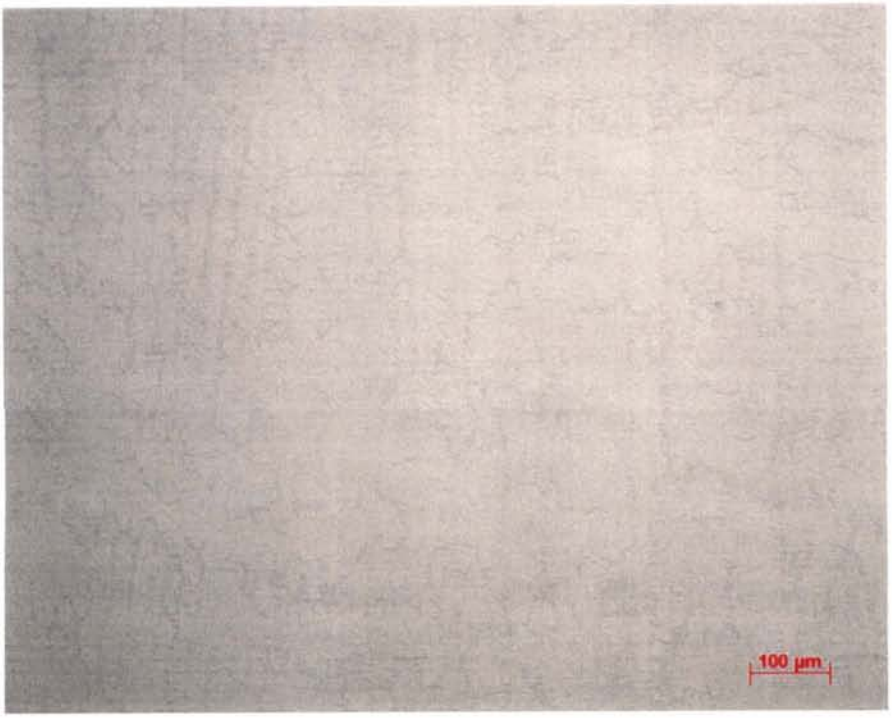

Fig B.94: Wrought Alloy 617 – 15 wt% Pt, xy plane, 100 X

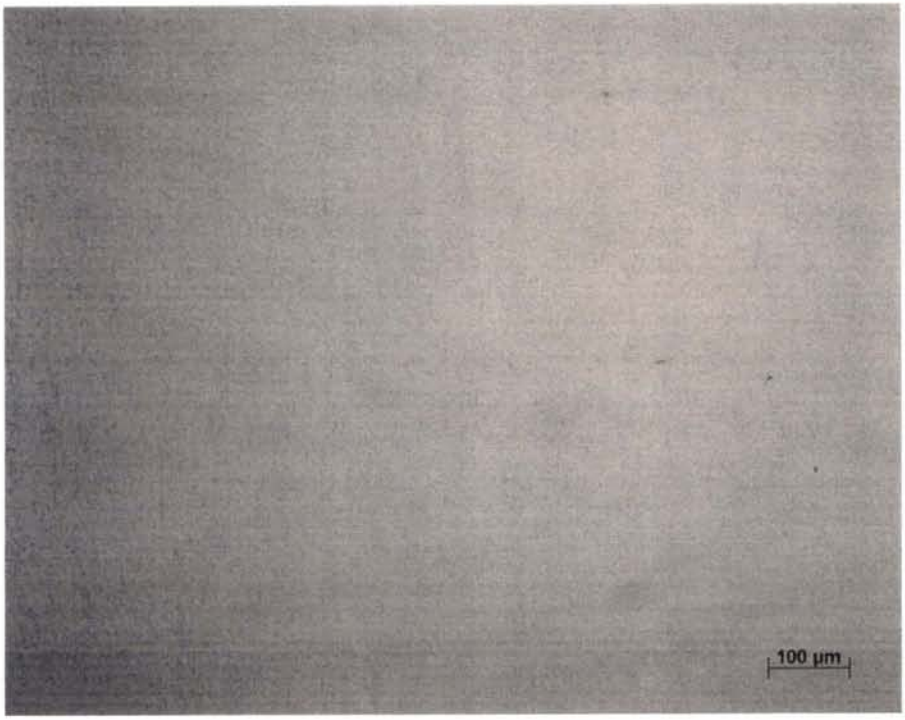

Fig B.95: Wrought Alloy 617 – 15 wt% Pt, xz plane, 100 X

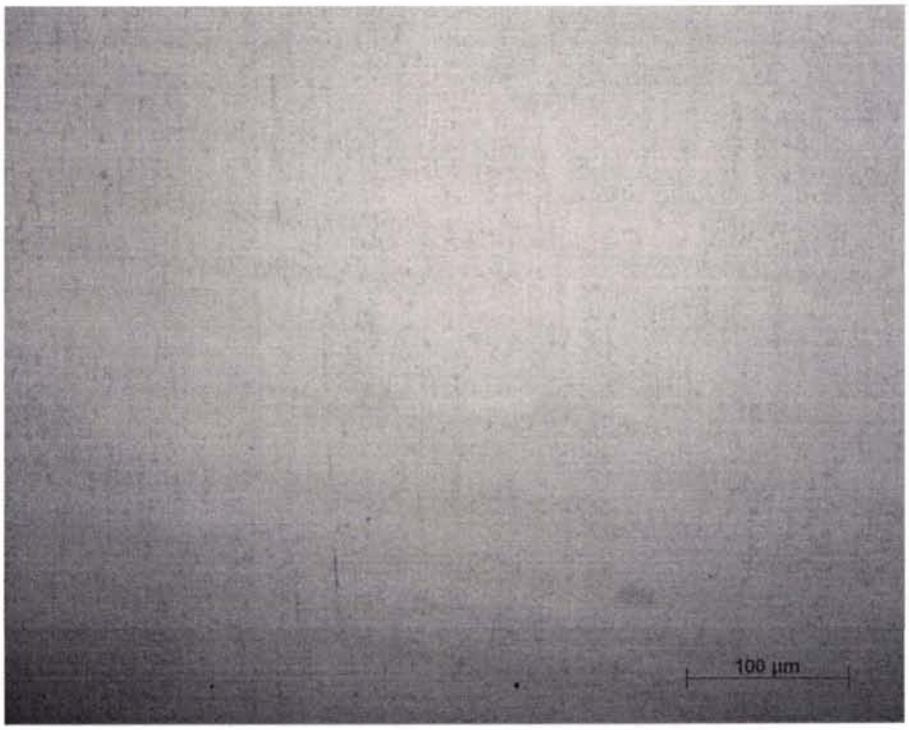

Fig B.96: Wrought Alloy 617 – 15 wt% Pt, yz plane, 100 X

Fig B.97: Wrought Alloy 617 – 15 wt% Pt, xy plane, 100 X, 10ml Oxalic Acid 90ml H_2O 3ml HCl, 1.5 VDC – 6 sec

Fig B.98: Wrought Alloy 617 – 15 wt% Pt, xz plane, 100 X, 10ml Oxalic Acid 90ml H_2O 3ml HCl, 1 VDC – 7 sec

Fig B.99: Wrought Alloy 617 – 15 wt% Pt, yz plane, 100 X, 10ml Oxalic Acid 90ml H_2O 3ml HCl, 1 VDC – 4 sec

Fig B.100: Wrought Alloy 617 – 15 wt% Pt, Secondary Electron Image, 500 X

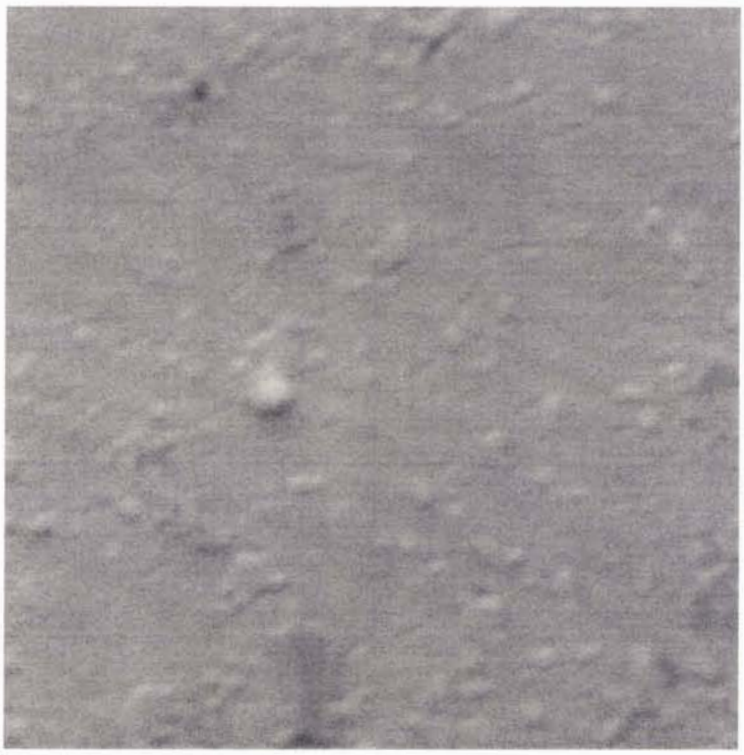

Fig B.101: Wrought Alloy 617 – 15 wt% Pt, Secondary Electron Image, 2500 X

B.9.3. Grain Size Calculation Data

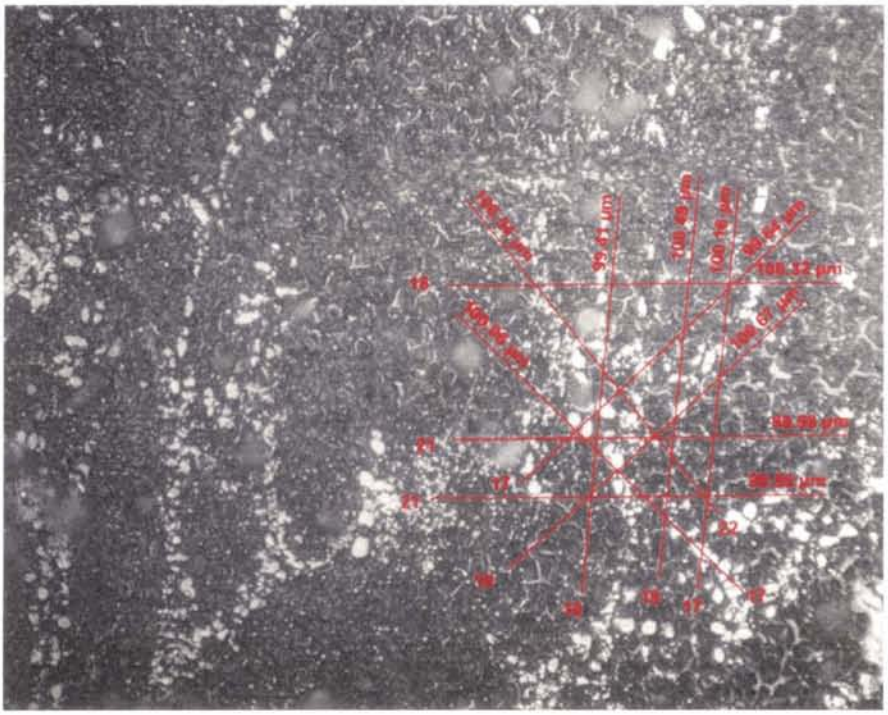

Fig B.102: Wrought Alloy 617 – 15 wt% Pt, xy plane, 500 X, grain size measurement

Table B.21			
Grain size calculation for Alloy 617 + 15 wt% Pt xy plane			
Projection	**Length (microns)**	**# intercepts**	**Grain size (microns)**
1	100.32	18	17
2	99.98	21	14
3	99.98	21	14
4	99.41	18	17
5	100.49	19	16
6	100.16	17	18
7	100.54	22	14
8	100.06	17	18
9	99.64	17	18
10	100.67	19	16
AVG grain size			**16**

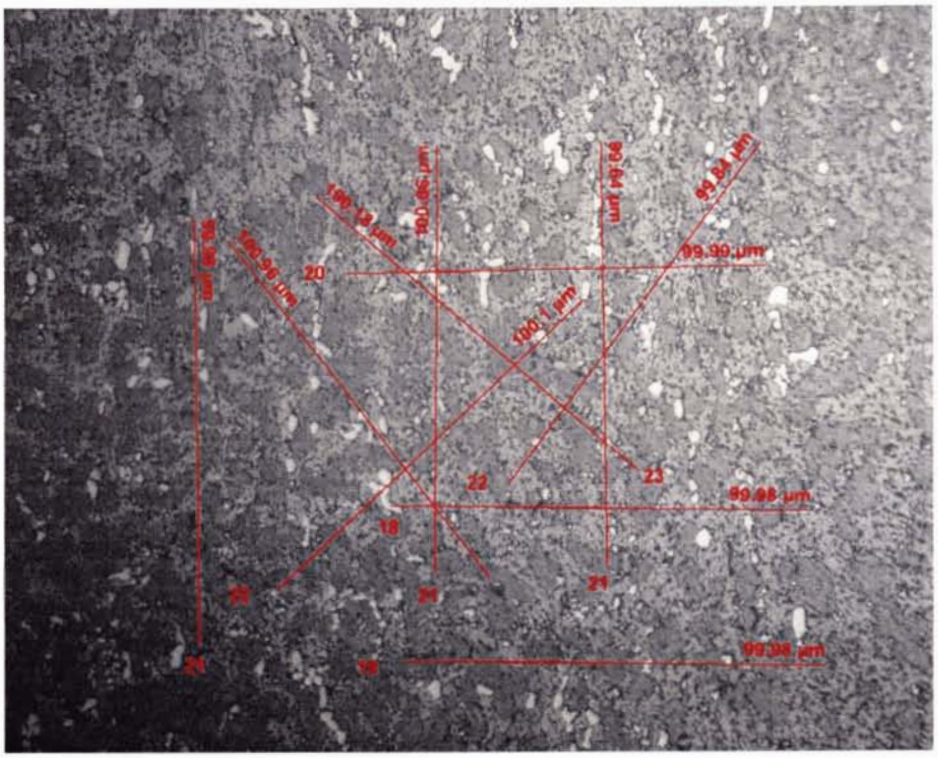

Fig B.103: Wrought Alloy 617 – 15 wt% Pt, xz plane, 500 X, grain size measurement

Table B.22			
Grain size calculation for Alloy 617 + 15 wt% Pt xz plane			
Projection	**Length (microns)**	**# intercepts**	**Grain size (microns)**
1	99.98	21	14
2	100.66	21	14
3	99.64	21	14
4	99.99	20	15
5	99.98	18	17
6	99.98	19	16
7	100.96	22	14
8	100.1	22	14
9	100.18	23	13
10	99.84	22	14
AVG grain size			**14**

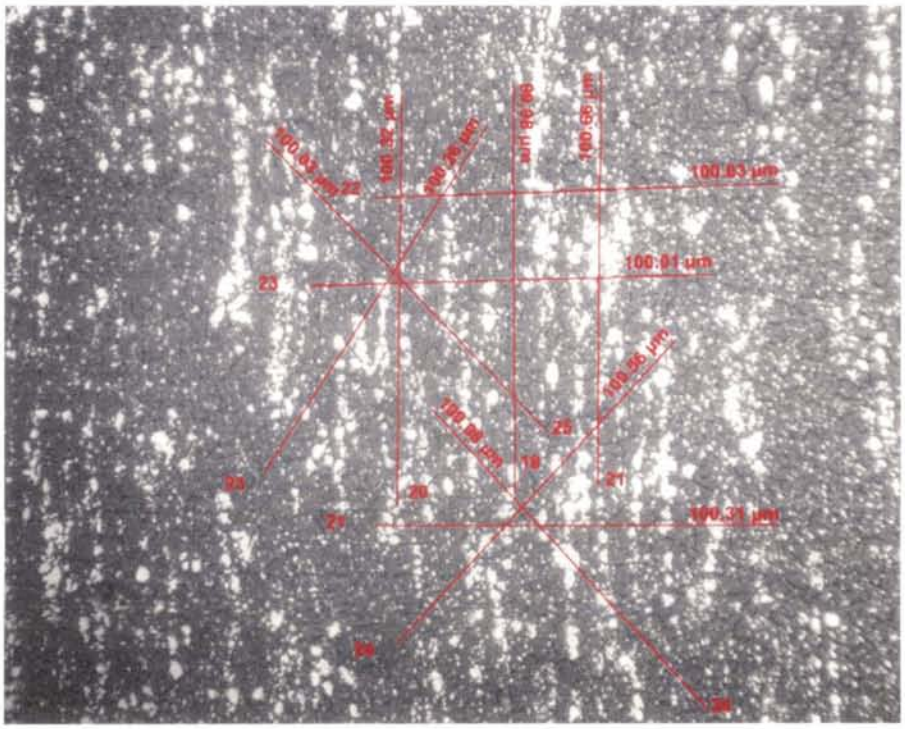

Fig B.104: Wrought Alloy 617 – 15 wt% Pt, yz plane, 500 X, grain size measurement

Table B.23			
Grain size calculation for Alloy 617 + 15 wt% Pt yz plane			
Projection	**Length (microns)**	**# intercepts**	**Grain size (microns)**
1	100.32	20	15
2	99.98	18	17
3	100.66	21	14
4	100.31	21	14
5	100.01	23	13
6	100.03	22	14
7	100.03	25	12
8	100.26	23	13
9	100.08	24	13
10	100.56	21	14
AVG grain size			**14**

B.10. Alloy 617 – 30 wt% Pt

B.10.1. Micrographs of Cast Structure

Fig B.105: Cast Alloy 617 – 30 wt% Pt, 50 X

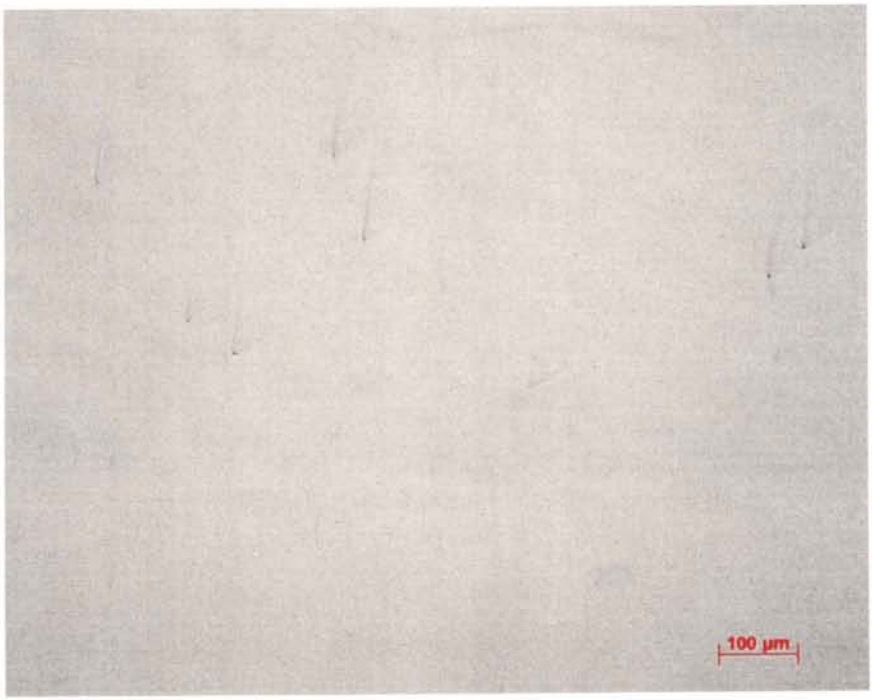

Fig B.106: Cast Alloy 617 – 30 wt% Pt, 100 X

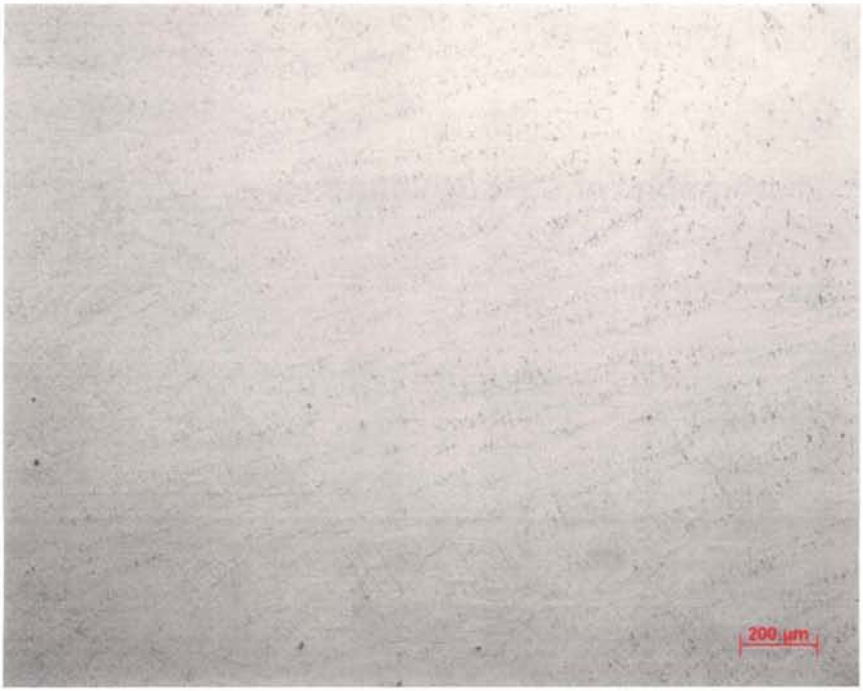

Fig B.107: Cast Alloy 617 – 30 wt% Pt, 50 X, glyceregia – 480 sec

Fig B.108: Cast Alloy 617 – 30 wt% Pt, 100 X, glyceregia – 480 sec

B.10.2. Micrographs of Wrought Structure

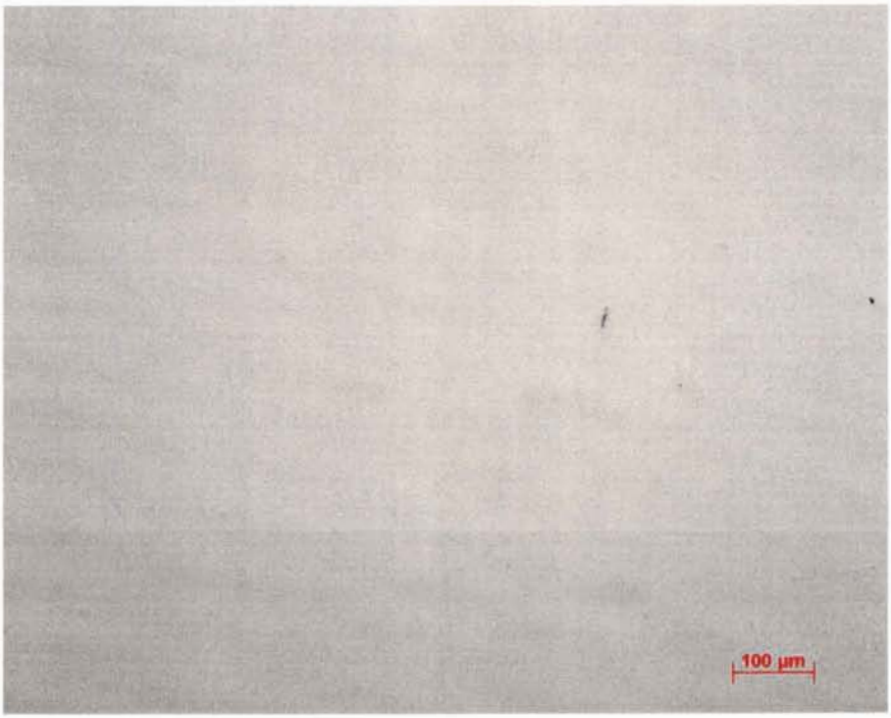

Fig B.109: Wrought Alloy 617 – 30 wt% Pt, xy plane, 100 X

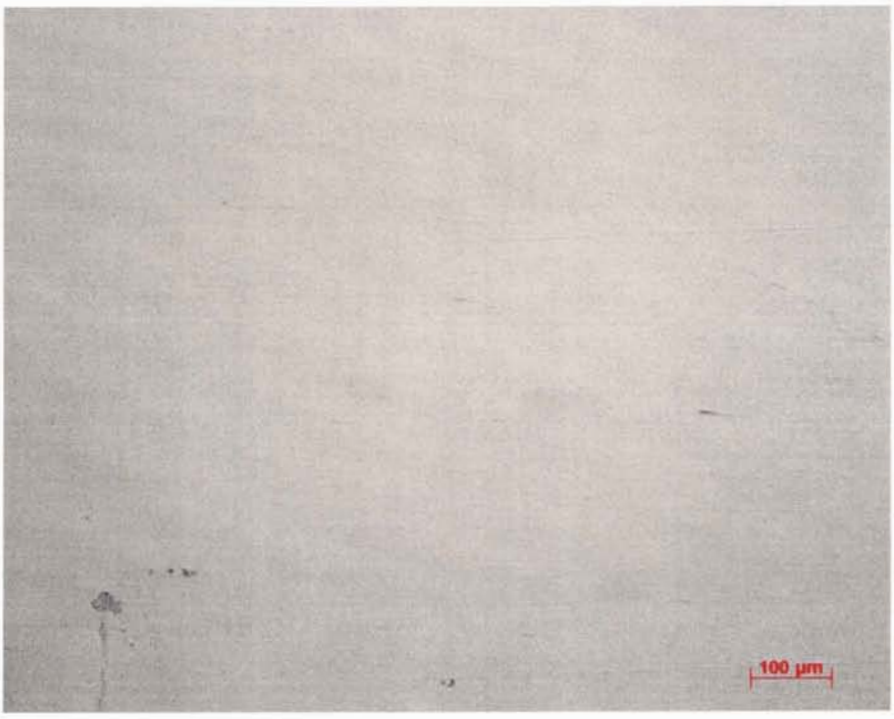

Fig B.110: Wrought Alloy 617 – 30 wt% Pt, xz plane, 100 X

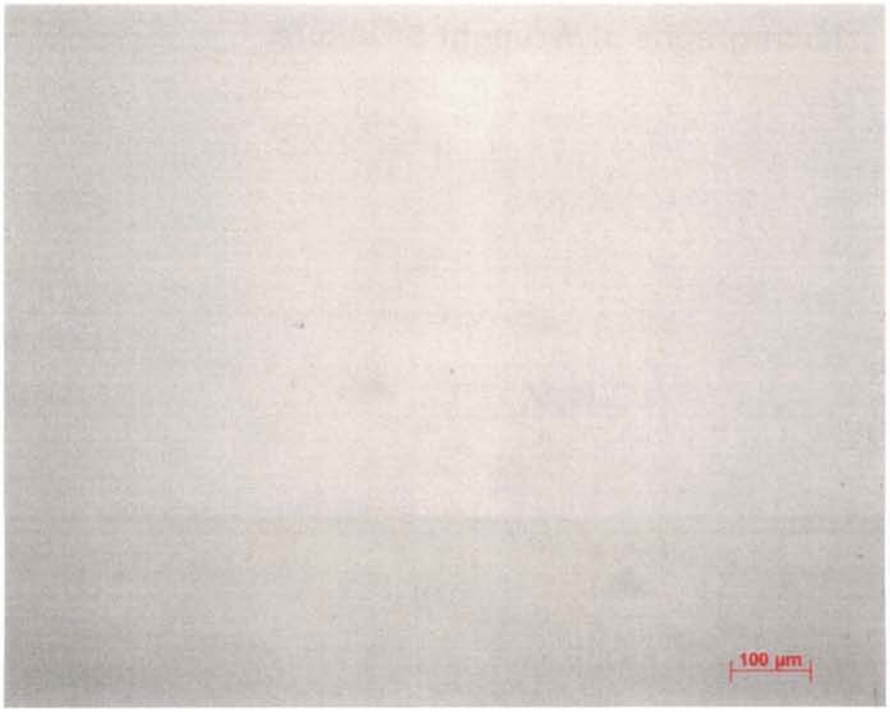

Fig B.111: Wrought Alloy 617 – 30 wt% Pt, yz plane, 100 X

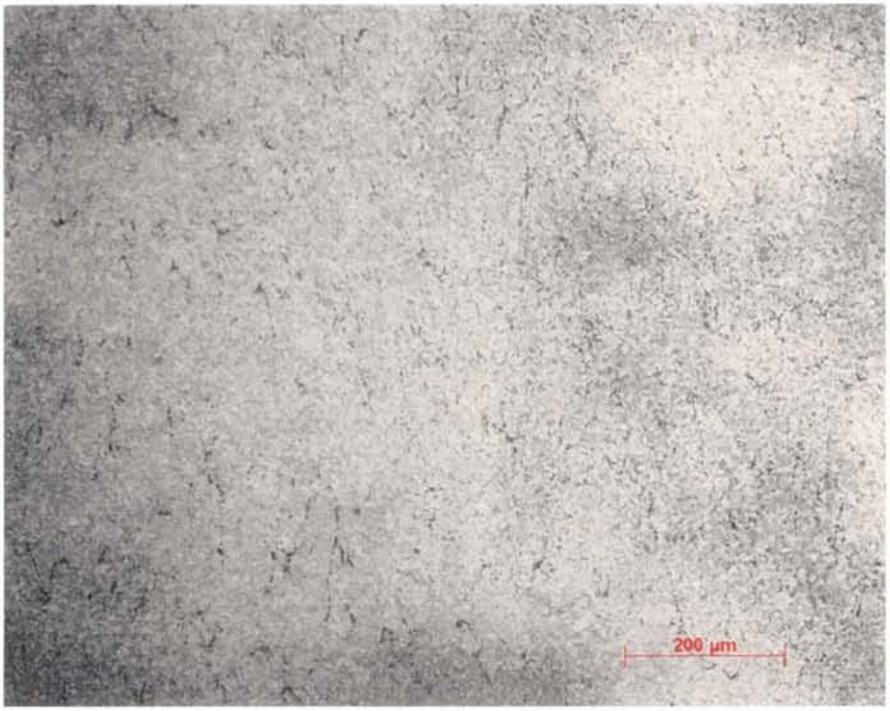

Fig B.112: Wrought Alloy 617 – 30 wt% Pt, xy plane, 100 X, 10ml Oxalic Acid 90ml H_2O 3ml HCl, 1.5 VDC – 12 sec

Fig B.113: Wrought Alloy 617 – 30 wt% Pt, xz plane, 100 X, 10ml Oxalic Acid 90ml H_2O 3ml HCl, 1.5 VDC – 8 sec

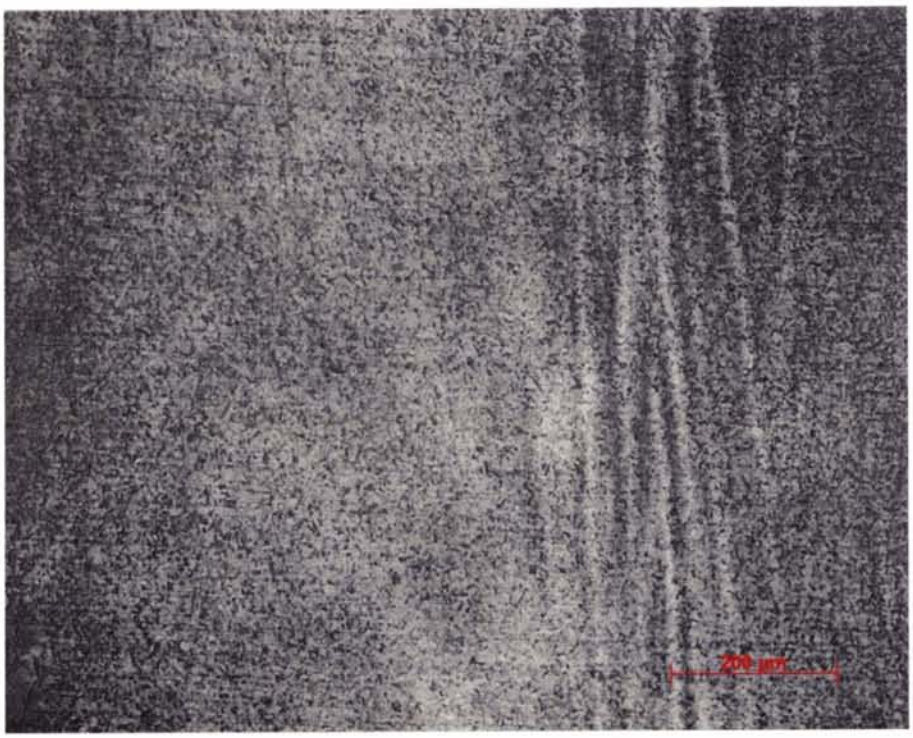

Fig B.114: Wrought Alloy 617 – 30 wt% Pt, yz plane, 100 X, 10ml Oxalic Acid 90ml H_2O 3ml HCl, 1.5 VDC – 6 sec

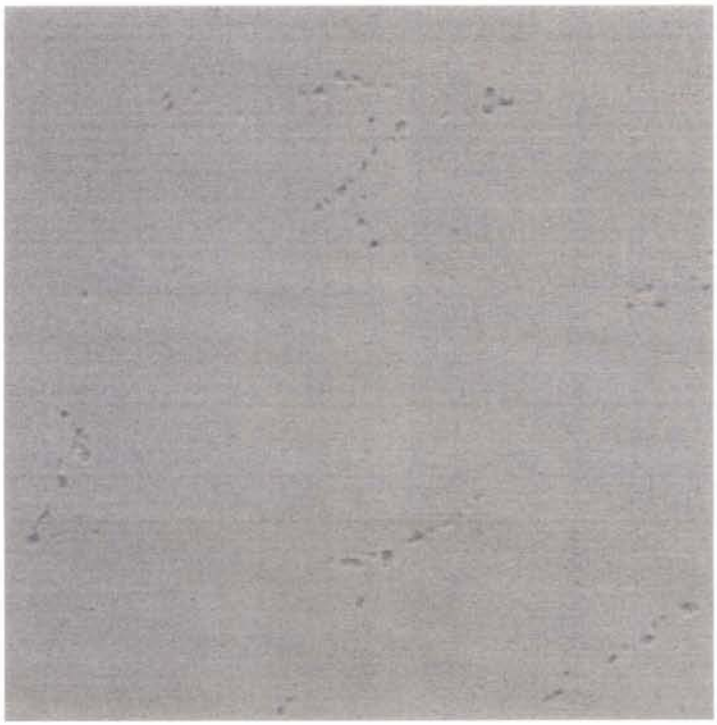

Fig B.115: Wrought Alloy 617 – 30 wt% Pt, Secondary Electron Image, 500 X

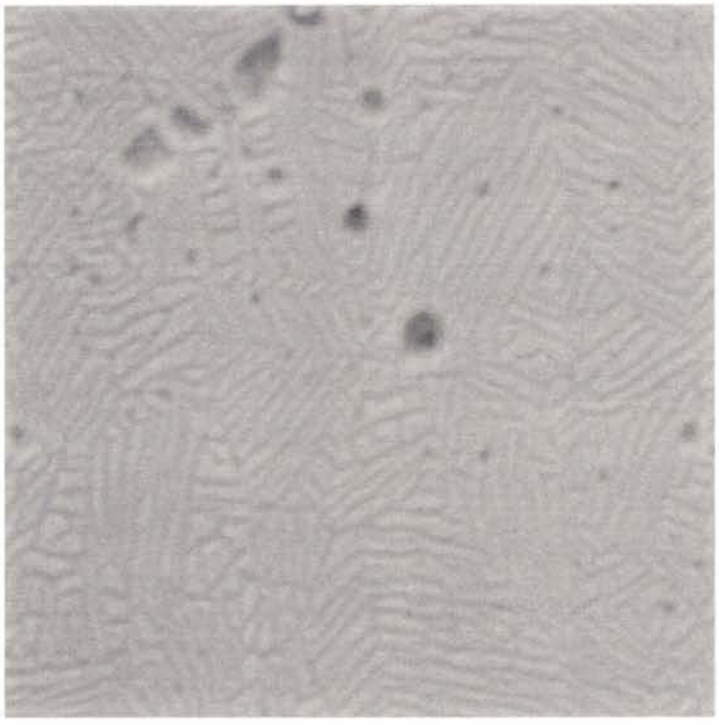

Fig B.116: Wrought Alloy 617 – 30 wt% Pt, Secondary Electron Image, 2500 X

B.10.3. Grain Size Calculation Data

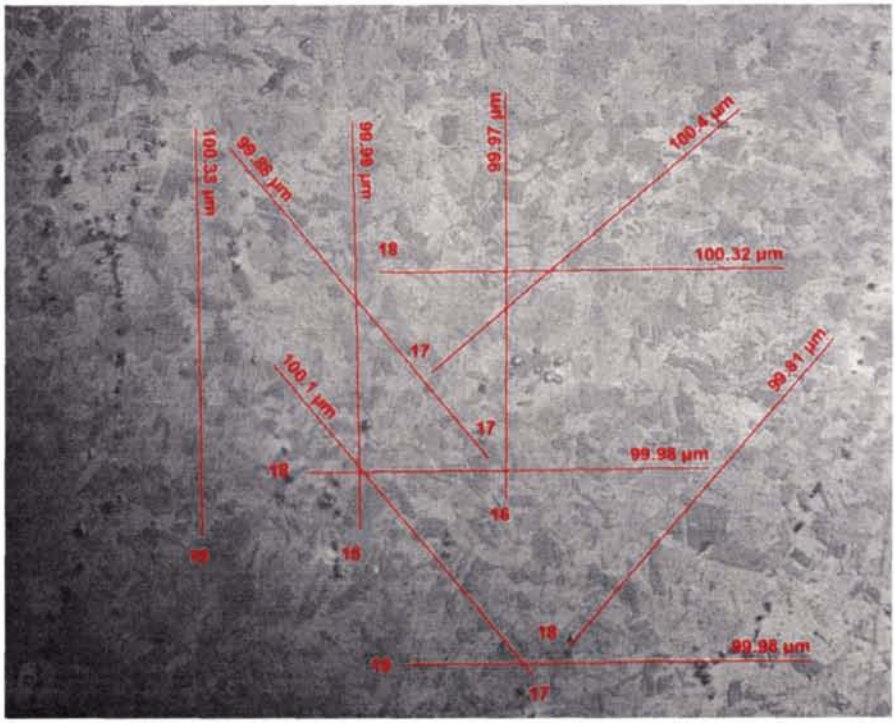

Fig B.117: Wrought Alloy 617 – 30 wt% Pt, xy plane, 500 X, grain size measurement

Table B.24			
Grain size calculation for Alloy 617 + 30 wt% Pt xy plane			
Projection	**Length (microns)**	**# intercepts**	**Grain size (microns)**
1	100.33	16	19
2	99.99	16	19
3	99.97	16	19
4	100.32	18	17
5	99.98	18	17
6	99.98	19	16
7	99.88	17	18
8	100.4	17	18
9	100.1	17	18
10	99.81	18	17
AVG grain size			**18**

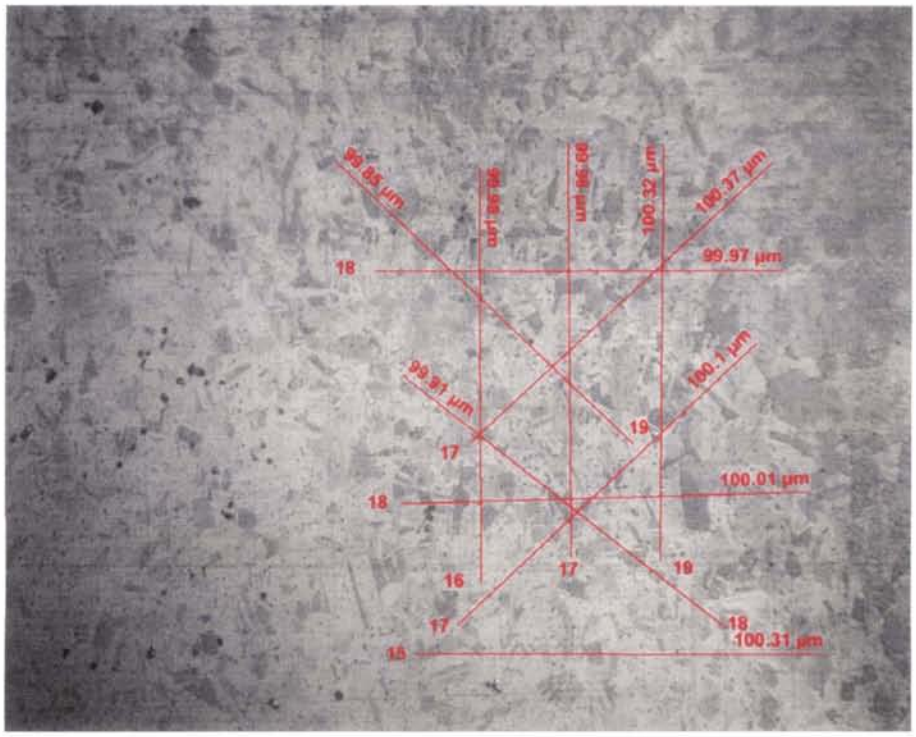

Fig B.118: Wrought Alloy 617 – 30 wt% Pt, xz plane, 500 X, grain size measurement

Table B.25			
Grain size calculation for Alloy 617 + 30 wt% Pt xz plane			
Projection	**Length (microns)**	**# intercepts**	**Grain size (microns)**
1	99.98	16	19
2	99.98	17	18
3	100.32	19	16
4	99.97	18	17
5	100.01	18	17
6	100.31	15	20
7	99.85	19	16
8	100.37	17	18
9	100.1	17	18
10	99.91	18	17
AVG grain size			**17**

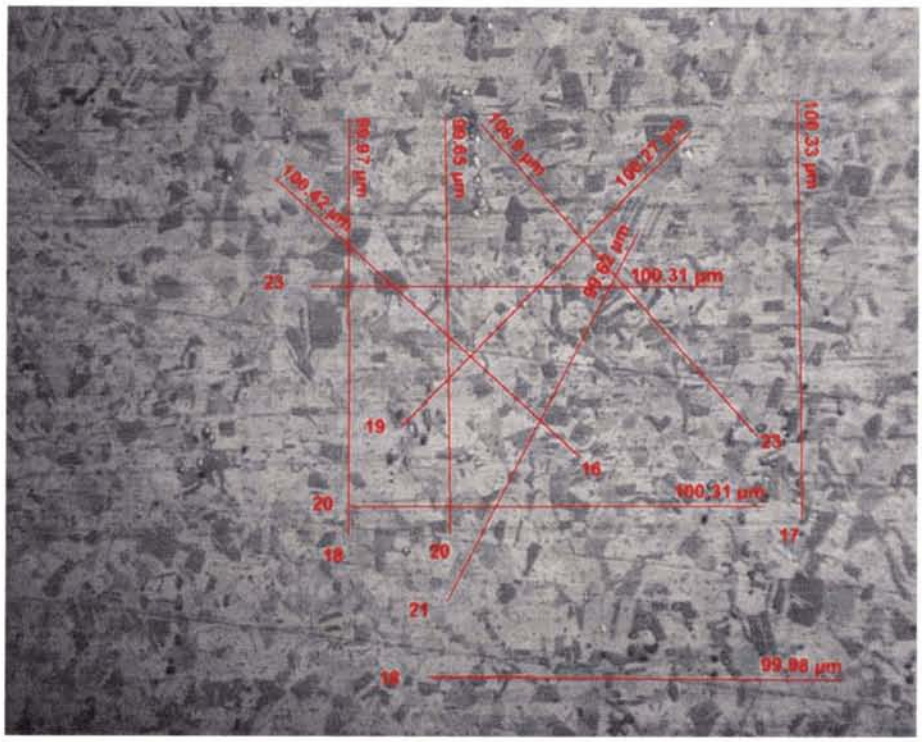

Fig B.119: Wrought Alloy 617 – 30 wt% Pt, yz plane, 500 X, grain size measurement

Table B.26			
Grain size calculation for Alloy 617 + 30 wt% Pt yz plane			
Projection	**Length (microns)**	**# intercepts**	**Grain size (microns)**
1	99.97	18	17
2	99.65	20	15
3	100.33	17	18
4	100.31	23	13
5	100.31	20	15
6	99.98	18	17
7	100.27	19	16
8	99.62	21	14
9	100.42	16	19
10	100.9	23	13
AVG grain size			**16**

References

[1] Kurz, W. Fundamentals of Solidification. Switzerland: Trans Tech Publications Ltd., 1998.

[2] Massalski, T.B. Binary Alloy Phase Diagrams. 2nd Ed. Vol. I – III. Materials Park OH: ASM International, 1990.

[3] Reed-Hill, R. and R. Abbaschian. Physical Metallurgy Principles. 3rd Ed. Boston: PWS Publishing Company, 1994.

[4] Smallman, R.E., W. Hume-Rothery, and C.W. Haworth. The Structure of Metals and Alloys. London: The Institute of Metals, 1985.

[5] Kloop, W.D. Aerospace Structural Metals Handbook. Code 4215. West Lafayette IN: Purdue Research Foundation, Jan 1994.

[6] Aerospace Structural Metals Handbook. Code 1615. West Lafayette IN: Purdue Research Foundation, 1980.

[7] "Inconel® Alloy 617." Special Metals Corp. Pub No SMC-029. © 2004. 10 March 2005. [http://www.specialmetals.com/documents/Inconel%20alloy%20617.pdf].

[8] "Incoloy® Alloy 800H & 800HT." Special Metals Corp. Pub No SMC-047. © 2004. 10 March 2005. [http://www.specialmetals.com/documents/Incoloy%20alloys%20800H%20800HT.pdf].

[9] Cornish, L.A., B. Fischer, and R. Völkl. "Development of Platinum-Group-Metal Superalloys for High-Temperature Use." MRS Bulletin. (Sept 2003): 632.

[10] Vorberg, S., et al. "Pt-Al-Cr-Ni Superalloys: Heat Treatment and Microstructure." JOM. (Sept 2004): 40.

[11] Yamabe-Mitarai, Y., et al. "Platinum-Group-Metal-Based Intermetallics as High-Temperature Structural Materials." JOM. (Sept 2004): 34.

[12] Hill, P.J., et al. "An assessment of ternary precipitation-strengthened Pt alloys for ultra-high temperature applications." Mat Sci Eng [A]. 301 (2001): 167.

[13] Biggs, T., M.J. Witcomb, and L.A. Cornish. "Martensitic-type transformations in platinum alloys." Mat Sci Eng [A]. 273-275 (1999): 204.

[14] Hill, P. J., et al. "Platinum alloys based on Pt – Pt_3Al for ultra-high temperature use." Mat Sci Eng [A]. 329-331 (2002): 295.

[15] Bertolini, J.C., et al. "$Pt_{10}Ni_{90}$ (111) SINGLE CRYSTAL ALLOY: DETERMINATION OF THE SURFACE COMPOSITION BY AES, XPS, AND ISS." Surf Sci. 119 (1982): 95.

[16] Gauthier, Y., et al. "Pt_xNi_{1-x} (111) ALLOY SURFACES: STRUCTURE AND COMPOSITION IN RELATION TO SOME CATALYTIC PROPERTIES." Surf Sci. 162 (1985): 342.

[17] Gauthier, Y., et al. "Influence of the transition metal and of order on the composition profile of $Pt_{80}M_{20}$ (111) (M = Ni, Co, Fe) alloy surfaces: LEED study of $Pt_{80}Co_{20}$ (111)." Surf Sci. 276 (1992): 1.

[18] "The Cu_3Au ($L1_2$) structure." Crystal Lattice Structures. Naval Research Laboratory. 21 Oct. 2004. Center for Computational Materials Science. 15 March 2005. [http://cst-www.nrl.navy.mil/lattice/struk/l1_2.html].

[19] Sims, T., N.S. Stoloff, and W.C. Hagel. Superalloys II. New York: John Wiley and Sons Inc., 1987.

[20] Jones, D.A. Principles and Prevention of Corrosion. 2nd Ed. Upper Saddle River NJ: Prentice Hall, 1996.

[21] Prof. Ballinger, R.G. MIT. Personal Communication. 7 March 2005.

[22] Winter, M. "Metallic radius: Iron." www.webelements.com. University of Sheffield and Web Elements Ltd., UK. © 2003. 17 March 2005. [http://www.webelements.com/webelements/elements/text/Fe/radii.html].

[23] Metals Handbook. 9th Ed. Vol. 9. USA: American Society for Metals, 1985.

[24] Mathias, P.M., and L.C. Brown. "Thermodynamics of the Sulfur-Iodine Cycle for Thermochemical Hydrogen Production." Japan: 68th annual meeting of the Society of Chemical Engineers. 2003.

[25] Kubo S., et al. "R&D Program on Thermochemical Water-Splitting Iodine-Sulfur Process at JAERI." GENES4/ANP2003. (15 – 19 Sept. 2003): 1072.

[26] Tagawa, H., and E. Takayuki. "Catalytic Decomposition of Sulfuric Acid Using Metal Oxides as the Oxygen Generating Reaction In Thermochemical Water Splitting Process." Int. J. Hydrogen Energy. Vol. 14 No. 1 (1989): 11-17.

[27] Norman, J.H., et al. "Studies of the Sulfur-Iodine Thermochemical Water – Splitting Cycle." Int. J. Hydrogen Energy. Vol. 7 No. 7 (1982): 545-556.

[28] Ballinger, R.G. "The Development of Self Catalytic Materials for Thermochemical Water Splitting using the Sulfur-Iodine Process." Grant Proposal to the University of Nevada Las Vegas. 24 June 2004.

[29] Stewart, J., "ASTM Committee E-4 and Grain Size Measurements." www.metallography.com. 2 Feb 2005. [http://www.metallography.com/grain.htm].

[30] Winter, M. "Metallic radius: Nickel." www.webelements.com. University of Sheffield and Web Elements Ltd., UK. © 2003. 17 March 2005. [http://www.webelements.com/webelements/elements/text/Ni/radii.html].

[31] Winter, M. "Metallic radius: Chromium." www.webelements.com. University of Sheffield and Web Elements Ltd., UK. © 2003. 17 March 2005. [http://www.webelements.com/webelements/elements/text/Cr/radii.html].

[32] Winter, M. "Metallic radius: Cobalt." www.webelements.com. University of Sheffield and Web Elements Ltd., UK. © 2003. 17 March 2005. [http://www.webelements.com/webelements/elements/text/Co/radii.html].

[33] Winter, M. "Metallic radius: Molybdenum." www.webelements.com. University of Sheffield and Web Elements Ltd., UK. © 2003. 17 March 2005. [http://www.webelements.com/webelements/elements/text/Mo/radii.html].

[34] Winter, M. "Metallic radius: Platinum." www.webelements.com. University of Sheffield and Web Elements Ltd., UK. © 2003. 17 March 2005. [http://www.webelements.com/webelements/elements/text/Pt/radii.html].

[35] Winter, M. "Electronegativity: Iron." www.webelements.com. University of Sheffield and Web Elements Ltd., UK. © 2003. 17 March 2005. [http://www.webelements.com/webelements/elements/text/Fe/eneg.html].

[36] Winter, M. "Electronegativity: Nickel." www.webelements.com. University of Sheffield and Web Elements Ltd., UK. © 2003. 17 March 2005. [http://www.webelements.com/webelements/elements/text/Ni/eneg.html].

[37] Winter, M. "Electronegativity: Chromium." www.webelements.com. University of Sheffield and Web Elements Ltd., UK. © 2003. 17 March 2005. [http://www.webelements.com/webelements/elements/text/Cr/eneg.html].

[38] Winter, M. "Electronegativity: Cobalt." www.webelements.com. University of Sheffield and Web Elements Ltd., UK. © 2003. 17 March 2005. [http://www.webelements.com/webelements/elements/text/Co/eneg.html].

[39] Winter, M. "Electronegativity: Molybdenum." www.webelements.com. University of Sheffield and Web Elements Ltd., UK. © 2003. 17 March 2005. [http://www.webelements.com/webelements/elements/text/Mo/eneg.html].

[40] Winter, M. "Electronegativity: Platinum." www.webelements.com. University of Sheffield and Web Elements Ltd., UK. © 2003. 17 March 2005. [http://www.webelements.com/webelements/elements/text/Pt/eneg.html].

[41] Dr. Ginosar, D. INL. Personal Communication. 5 Feb 2005.

[42] Dr. Herring, S. INL. Personal Communication. 11 April 2005.

[43] Mr. Eisinger, N. Special Metals Corp. Personal Communication. 20 March 2005.

[44] Bell, T. "Chemical Composition Analysis." Analytical Report No 0-34669. Boylston MA: Luvak Inc. 17 March 2005

[45] Dechema, Corrosion Handbook. Vol 8. NYC: VCH, 1991.

[46] Course Notes. Physical Metallurgy (22.71J), MIT 2004

[47] Hertzberg, R. Deformation and Fracture Mechanics of Engineering Materials 4th Ed.USA: John Wiley & Sons, Inc., 1996

[48] JMat Pro. Version 3.0. UK: Sente Software Ltd., © 1999 – 2004 [contact information: email: jmatpro@sentesoftware.co.uk tel: 44 0 1483 685476]